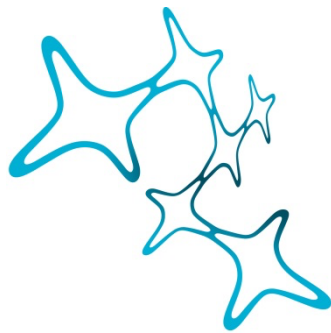

MOLECULAR PROFILING OF GLIAL REACTIVITY IN RESPONSE TO CNS INJURY

Christina Koupourtidou



Graduate School of
Systemic Neurosciences
LMU Munich



Dissertation der
Graduate School of Systemic Neurosciences der
Ludwig-Maximilians-Universität München

30th November, 2022

Supervisor

Prof. Dr. Jovica Ninkovic

Institute for Cell Biology and Anatomy

Biomedical Center (BMC)

Faculty of Medicine

LMU Munich

First Reviewer: Prof. Dr. Jovica Ninkovic

Second Reviewer: PD Dr. Florence Bareyre

External Reviewer: Dr. Ruth Beckervordersandforth-Bonk

Date of Submission: 30th November 2022

Date of Defense: 27th March 2023

Abstract

Traumatic brain injury (TBI) is a major contributor to death and disability and is considered a risk factor for developing neurodegenerative diseases. The initial trauma disrupts brain homeostasis leading to a highly orchestrated immune and glial cell response. Despite damages from the initial trauma, subsequent secondary cascades are thought to be a pivotal contributor to the subsequent detrimental outcomes. Glial cells are a critical contributor to secondary injury, having a dual role in TBI pathology. Initially, they associate with important protective aspects which promote recovery. However, during the disease progression, they promote further damage to the CNS via multiple processes, including neuroinflammation. This transition from a protective to a detrimental phenotype may present a time window for therapeutic interventions targeting glial cells, aiming to improve the adverse outcomes following TBI.

Understanding the mechanisms involved in the activation of specific cell types in response to TBI is necessary in order to manipulate their response. Thus, we developed a toolbox profiling the transcriptional changes across various cell types with providing spatial and temporal context. Our analysis profiles the transcriptomic signature of the injured murine cerebral cortex using spatial transcriptomics, which, combined with scRNA-seq analysis, revealed specific subpopulations of astrocytes, microglia, and oligodendrocyte precursor cells (OPCs) accumulating at injury sites. These cellular subpopulations had a shared inflammatory signature involving two innate immune pathways, the Tlr1/2 and Cxcr3. Interestingly, the two pathways have an essential role in OPCs proliferation and accumulation at the injury site in response to injury in zebrafish. Thus, I first addressed the role of the two pathways in OPCs *in vitro* with two approaches, generating a specific knockout cell line and using a pharmacological approach in primary OPC culture. Both approaches indicated a direct role of these receptors in regulating OPC proliferation. Then we aimed to address the role of Tlr1/2 and Cxcr3 in response to injury in mice using pharmacological inhibition. Manipulation of the two pathways systemically altered the transcription profile of glial cells, downregulating innate immune response in glial subpopulation and controlling specific aspects of their reactivity, like astrocytes proliferation and microglia morphology, without entirely restoring glial cell homeostasis.

Altogether, during my study, I generated a comprehensive tool profiling early events following traumatic brain injury with respect to changes in time, space, and cell type. This analysis enables the examination of the interplay between cells in response to injury. Thus, it allows a better understanding of the injury pathophysiology, which may open more opportunities for developing new therapeutic strategies.

Index

Abstract	iii
Index.....	v
1 Introduction.....	1
1.1 Traumatic brain injury	2
1.2 Inflammation and immune cell response	4
1.3 Glial cells in health and disease	5
1.3.1 Microglia	6
1.3.2 Oligodendrocytes progenitor cells.....	7
1.3.3 Astrocytes	9
1.4 Scarless regeneration of the zebrafish CNS and its implication for mammalian research.....	11
1.5 Innate immune pathways as a target to control glial reactivity.....	13
1.5.1 Toll-like receptor overview and Tlr2	13
1.5.2 Chemokine receptor overview and Cxcr3.....	14
1.6 Single-cell RNA-sequencing for studying glial reactivity	15
2 Results.....	19
2.1 Aim of study I	19
2.2 Aim of study II	65
2.3 Aim of study III	109
3 Discussion.....	160
3.1 Molecular mapping of the injury milieu using spatial transcriptomics.....	161
3.2 Specific glial subpopulations contribute to the injury milieu.....	162
3.3 Shared inflammatory signature of reactive glial cells	164
3.4 Cxcr3 and Tlr1/2 regulate distinct aspects of glial reactivity.....	167
3.5 Summary and conclusions	168

4	Bibliography	171
5	Curriculum Vitae	184
6	Publications	186
7	Eidesstattliche Versicherung/Affidavit	187
8	Declaration of author contributions	188
9	Acknowledgments	191

1 Introduction

The central nervous system (CNS) consists of the brain and the spinal cord. The brain, one of the most complex organs in our body, monitors and coordinates the activity of many other organs in addition to behavior, intelligence, emotions, consciousness, and response to environmental changes. As a fundamental organ that controls the whole organism, the brain is anatomically protected by the skull, the cerebrospinal fluid (CSF), and the meninges. The blood-brain barrier (BBB) is an additional protective barrier from pathogens, circulating immune cells, and factors within the blood. BBB consists of endothelial cells connected by continuous adhesive and tight junctions, pericytes, and astrocyte foot processes (endfeet) (Keaney & Campbell, 2015; Louveau et al., 2015; Thau et al., 2022).

The primary brain functions are the result of a highly integrated and interconnected cellular network of neurons and glial cells (or neuroglia). These two types of cells have distinct functions and physiology. Neurons are responsible for processing information and creating circuit-mediated behavior. At the same time, glial cells are responsible for the homeostatic and defense support of the nervous system, thus having an essential role in neuropathology (Ho et al., 2019; Verkhratsky & Parpura, 2014). Every insult to the nervous system triggers a glial response and initiates a specific glial defensive reaction. The degree of glial reactivity depends on the pathological condition of the brain as they react to various diseases, including psychiatric disorders, neurodegenerative diseases, and brain injuries. Glial contribution to brain pathological conditions often takes two faces which can be protective as well as harmful. A better understanding of the glial response to CNS insults could provide us with new tools to tackle those devastating disorders of our modern society.

Since my main focus lies on glial reactivity following brain injury, I will briefly summarize the events following traumatic brain injury (TBI) with an emphasis on glial cells, the key contributors to TBI pathophysiology. Additionally, I will describe the inflammatory response following TBI and introduce two innate immune pathways, Trl2 and Cxcr3, as targets of my research project. Finally, I will highlight how studying the regenerative capacity of zebrafish CNS and using new tools like single-cell transcriptomic analysis could

help us better identify the detrimental aspects of TBI-induced pathology and develop new therapeutic approaches.

1.1 Traumatic brain injury

Traumatic brain injury (TBI) is among the leading causes of death and disability worldwide, affecting approximately 69 million individuals of all ages each year (Blennow et al., 2016; Dewan et al., 2019; Majdan et al., 2017). TBI is an acute brain insult due to an external force which can be the action of a direct hit, acceleration/deceleration force or penetrating objects, which disrupts the physiological structure and function of the brain (Blennow et al., 2016; Finnie & Blumbergs, 2002). The outcome of TBI can be very heterogeneous depending on the affected area, the severity, and the mechanism, which can lead to acute disruption of brain function and long-term cognitive and behavioral changes (Mira et al., 2021; Xiong et al., 2018). It is also notable that TBI has emerged as a critical risk factor for multiple neurodegenerative diseases, including Alzheimer's disease (AD), Parkinson's disease, Amyotrophic lateral sclerosis (ALS), and Chronic Traumatic Encephalopathy (CTE) (Puntambekar et al., 2018).

TBI has a complex, progressive pathophysiology that leads to structural and functional changes and is classified into primary and secondary damage. (Mira et al., 2021). The external mechanical force triggers the direct damage at the time of injury, leading to cell death, axonal damage, and disruption of the BBB (Puntambekar et al., 2018). The initial insult is followed by progressive secondary damage, which develops over hours and days, including metabolic, neurochemical, cellular, and molecular changes (Maas et al., 2008; Puntambekar et al., 2018). Under the influence of the primary damage, astrocytes, microglia, and oligodendroglia precursors cells (OPCs, also often termed as NG2-glia) surrounding the lesioned site, alter their normal homeostasis and become reactive, resulting in changes in gene expression, morphology, and function (Batiuk et al., 2020; Robel et al., 2011; Sofroniew, 2009). These secondary changes are associated with important protective aspects which aim to isolate the damaged area and promote recovery (Anderson et al., 2016). However, they can also promote further neuronal damage, neuroinflammation, oxidative stress, and protein aggregation, mechanisms

responsible for the persistence of symptoms and increased vulnerability to other neurodegenerative disorders (Maas et al., 2008; Puntambekar et al., 2018).

After a TBI has occurred, the immediate neurological damage caused by the primary traumatic forces may not be reversible. In contrast, secondary neurologic damage is produced by a cascade of secondary events which evolve over time. An essential factor of the TBIs pathophysiology is the orchestrated response of glial cells accompanied by the infiltration of peripherally derived immune cell populations and their involvement in the inflammatory response (Figure 1) (Mira et al., 2021). A better understanding of the extended temporal profile of injury focusing on the interplay of glial cells and immune response may provide opportunities for new therapeutic interventions.

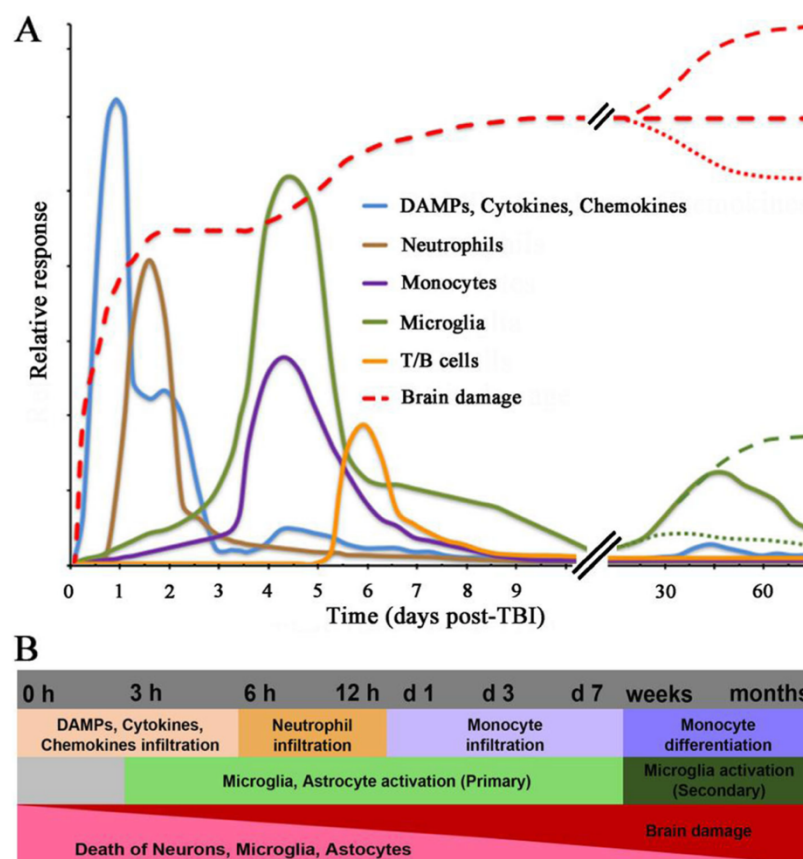


Figure 1. Timeline of cellular response (A) and schematic representation cellular behavior (B) in response to TBI (Alam et al., 2020. License CC-BY- NC 4.0)

In this line, the use of multiple animal models of TBI is essential to capture the heterogeneous nature of the clinical situation in TBI and characterize biomechanical, cellular, molecular, and behavioral aspects of the injury. Rodents are the most used animal models in TBI mainly due to their modest cost, small size, easy manipulation, and

standardized outcome measurements. The most widely used animal models are classified as closed-head injuries, as they do not involve skull fracture and include fluid percussion injury (FPI), controlled cortical impact (CCI) injury, weight-drop impact acceleration injury, and blast injury (Xiong et al., 2013). Another class is penetrating brain injury (PBI), resulting in skull fracture due to a gunshot or sharp object (Petersen et al., 2021). In my study, I used the stab-wound (SW) injury model in mice, a mild PBI model involving the breakdown of BBB and the activation of both glial and immune cells (Buffo et al., 2005; Friik et al., 2018; Scheller et al., 2017; Sirko et al., 2015; von Streitberg et al., 2021). The reproducibility of our model and the reactivity observed makes it perfect for studying the basic features of TBI pathophysiology.

1.2 Inflammation and immune cell response

TBI triggers the activation of inflammatory response and the recruitment of immune cells to the injury areas, fundamental processes of any wound healing pathways. These responses aim to clear the CNS of dead cellular debris and potentially infectious agents. However, the inflammatory reaction in the CNS has a controversial role, as it can promote neuronal cell death when over-activated (Shechter & Schwartz, 2013), depending on the nature of the insult.

Compared to other brain pathologies, in TBI the disruption of BBB integrity is a major contributor to the inflammatory response as it allows a greater infiltration of peripheral immune cells and the extravasation of plasma proteins into the brain. (Karve et al., 2016; Xiong et al., 2018). Additionally, damaged cells from the acute injury release damage-associated molecular patterns (DAMPs), ATP, heat shock proteins (HSPs), and extracellular matrix remodeling enzymes, conveying an activation signal to the immune system and the resident glial cells (Gyoneva & Ransohoff, 2015). Pattern recognition receptors (PRRs) expressed in cells of the peri-lesioned area can sense these signals and contribute to the immune response. Toll-like receptors (TLRs) are members of the PRRs family and are activated by various DAMPs, including dsDNA and RNA, CpG motifs, and chaperone proteins which are released by dying cells (Karve et al., 2016). Signaling through TLRs, in addition to other pathways, can induce the production of cytokines, chemokines, and other small molecules that also contribute to the activation signaling,

resulting in the infiltration of leukocytes to the CNS and activation of the resident glial cells (Gyoneva & Ransohoff, 2015; Shechter & Schwartz, 2013).

The recruitment of peripheral immune cells is observed in phases, and it highly depends on the nature and extent of the injury. Neutrophils are recruited first, followed by monocyte infiltration and delayed lymphocyte entry (Shechter & Schwartz, 2013). In the brain, neutrophil infiltration is minimal and restricted to the lesion site starting already a few hours after the initial insult and decreases substantially over the first week (Alam et al., 2020). Circulating monocytes/macrophages increase their number within 24hrs post-TBI and infiltrate the brain over the first days following chemo-attractants. The chemokine (C-C motif) receptor 2 (CCR2) and its ligand, chemokine (C-C motif) ligand 2 (CCL2), have a critical role in their recruitment, as the inhibition of the pathway reduces the infiltration of monocytes/macrophages into the brain parenchyma and limits neuroinflammation, scar formation, and cognitive decline (Frik et al., 2018; McKee & Lukens, 2016). Depending on the severity of the brain injury, the adaptive immune response can also contribute to the inflammatory response at later time points with the recruitment of T and B cells (Alam et al., 2020).

1.3 Glial cells in health and disease

Glial cells were initially thought of as simply the "glue" of the nervous system (derived from Ancient Greek γλίᾱ /glíā meaning glue). However, decades of research have recognized the critical role of glial cells in the development and function of the CNS, as they are involved in physiological processes including neurogenesis, nutrient and metabolic factors transport, and synaptic transmission (Jakel & Dimou, 2017). Besides they contribute to maintaining the blood-brain barrier (Abbott et al., 2010), and they act as the first line of defense in the central nervous system when it comes to responding to insults such as injury or disease (Fitch & Silver, 2008).

Glial cells constitute roughly half of the CNS cells, subdivided into microglia and macroglia, which include astrocytes and oligodendrocyte lineage cells (Allen & Lyons, 2018; Jakel & Dimou, 2017). They respond rapidly to a CNS insult by developing a reactive phenotype that can lead to functional and morphological changes, resulting in beneficial effects such as the clearance of damaged or dead cells and isolation of the damaged from

the healthy tissue (Batiuk et al., 2020; Robel et al., 2011; Silver & Miller, 2004; Sofroniew, 2009). However, long-term glial activation in combination with neuroinflammation can be detrimental (Mira et al., 2021; R. Z. Zheng et al., 2022). The role of each glial cell type and its contribution to TBI pathology will be discussed in detail in the following sections.

1.3.1 Microglia

Microglial cells, the resident macrophages of the CNS, comprise around 10% of brain cells and are the main immune component and phagocytic cell type of the nervous system, acting as the first line of defense against various types of pathogenic factors (Kettenmann et al., 2011; Kettenmann & Verkhratsky, 2022). Microglial cells have mesodermal/mesenchymal origin and originate from early erythromyeloid progenitors (EMPs) in the extraembryonic yolk sac, with their progenitors migrating into CNS and disseminating throughout the brain parenchyma (Ginhoux et al., 2010). After invading the brain, microglia mature through a stepwise developmental program and acquire a specific ramified morphological phenotype termed "ramified" or "resting microglia", characterized by a small cell body and many thin processes with multiple branches that extend in all directions. Each microglial cell has its territory, constantly randomly scanned by rapid movements and small protrusions (Kettenmann et al., 2011; Kettenmann & Verkhratsky, 2022).

Microglia is a heterogenous population with various densities, morphology, molecular signatures, and metabolism across multiple regions and developmental stages (Hammond et al., 2019; Masuda et al., 2020; Tan et al., 2020). A wide range of receptors on their surface enables them to respond to various pleiotropic stimuli, including neurotransmitters, cytokines, and plasma proteins. Additionally, they contribute to the homeostatic maintenance of the brain, influence cognitive processes, and shape the brain during development by regulating synaptic functions and phagocytosis of dying neurons. Notably, they play a significant role in the healthy adult brain, contributing to synaptic plasticity and adult neurogenesis (Diaz-Aparicio et al., 2020; Kreisel et al., 2019; Pérez-Rodríguez et al., 2021; Szepesi et al., 2018; Wallace et al., 2020; C. Wang et al., 2020; Wu et al., 2015).

Brain-resident microglia are rapidly activated upon CNS insults and change their morphology to a hypertrophic amoeboid morphology (Donat et al., 2017). Additionally, activated microglia start to proliferate, polarize, extend their processes, and migrate to the injury site establishing a barrier between the healthy and injured tissue (Kettenmann et al., 2011; Mira et al., 2021). This rapid chemotactic response is guided by extracellular ATP released from damaged cells (Davalos et al., 2005), which attract microglia to phagocytose damaged cells and debris, promoting brain repair. However, microglia reactivity can also be detrimental and promote further brain damage, hindering brain repair and functional recovery. This is usually linked to excessive activation of microglia and the production of proinflammatory cytokines such as interleukin 1 beta and alpha (IL-1b), IL-6, tumor necrosis factor- α (TNF- α), interferon- γ (IFN- γ) (Xiong et al., 2018). The microglia activation state depends highly on the nature of TBI. It can be observed for weeks to months with varying morphological stages, gene expression patterns, and functions depending on the disease stage and the signals stimulating them, resulting in neuroprotective or neurotoxic phenotypes (Mira et al., 2021). These activation/polarization states are generally classified as M1 (classically activated, proinflammatory) and M2 (alternatively activated anti-inflammatory). The M1 phenotype promotes the production and release of proinflammatory cytokines that can exacerbate brain damage, whereas the M2 is associated with the release of neurotrophic factors that promote repair and have a phagocytic role. However, the unbiased transcriptomic analysis of microglia, using high-throughput transcriptomics such as single-cell RNA-sequencing, revealed a border signature of microglia. Indeed, recent studies revealed a more complex state of microglia than the simple classification in M1 and M2, with a mixed expression of markers associated with both states (Donat et al., 2017; Hammond et al., 2019; Y. Li et al., 2020; Masuda et al., 2020).

1.3.2 Oligodendrocytes progenitor cells

Oligodendrocyte progenitor cells (OPCs) represent 5-10% of the total cellular population in the brain and give rise to oligodendrocytes, the myelin-forming cell type, throughout the lifespan (Dimou et al., 2008; Eugénin-von Bernhardt & Dimou, 2016; Kettenmann & Verkhratsky, 2022). OPCs in the adult brain are often referred to as NG2-

glia due to their specific expression of the proteoglycan neuron-gial antigen 2 (NG2) (also known as CSPG4, Chondroitin Sulfate Proteoglycan 4) on their cell surface, with both terms being interchangeable (Galichet et al., 2021). However, NG2 is also detected in pericytes, cells that enwrap the vasculature of the brain (Ozerdem et al., 2001), thus I will use the term OPCs throughout my thesis

OPCs are the main proliferating cells in the non-neurogenic niches of the healthy adult brain and are organized in distinct domains with specific cell densities all over the brain (Dimou & Götz, 2014; Nishiyama et al., 2009; C. Simon et al., 2011). OPCs numbers and territory are maintained by a self-repulsion mechanism, which regulates these cells' proliferation and short-range migration of neighboring cells after cell death or differentiation (Hughes et al., 2013). One interesting aspect of OPCs function in the adult brain is their ability to form functional synapses with neurons and receive neuronal signals; however, this is not yet well understood (Bergles et al., 2000; Jakel & Dimou, 2017).

Following brain damage associated with BBB disruption, OPCs rapidly respond to the insult with several cellular and molecular changes (Dimou & Götz, 2014; Jakel & Dimou, 2017; Sirko et al., 2013). OPCs respond to injury by increasing the expression of NG2 and increasing in numbers by shortening their cell cycle length and increasing proliferation (C. Simon et al., 2011). Additionally, they become hypertrophic, polarize, and migrate toward the injured area contributing to the glial border formation (Dimou & Götz, 2014; Hughes et al., 2013; C. Simon et al., 2011; von Streitberg et al., 2021). The accumulation of OPCs at the injury site breaks their homeostatic properties where they are organized in non-overlapping domains (Eugenín-von Bernhardt & Dimou, 2016; C. Simon et al., 2011). OPCs show a rapid reactivity in response to stab wound injury, which peaks 2 days post-injury and is resolved after 4 weeks (von Streitberg et al., 2021). Even though the reaction of OPCs to brain injury is not yet well understood, it recently was demonstrated that they have a critical role in wound healing as genetic ablation of proliferating OPCs and a decrease in the cell numbers resulted in a delayed wound healing (von Streitberg et al., 2021).

1.3.3 Astrocytes

Astrocytes, the most abundant glial cell type, are classical neural cells derived from radial glia with neuroepithelial origin (as neurons and oligodendroglial cells) with many important functions for normal development and neural functioning to defense mechanisms (Kettenmann & Verkhratsky, 2022; Verkhratsky & Nedergaard, 2018). Astrocytes are highly heterogeneous in morphological appearance and functions associated with brain regions. For example, grey matter astrocytes have protoplasmic morphology with highly branched fine processes that contact the basement membrane surrounding the blood vessels and enwrap synaptic connections. On the other hand, fibrous astrocytes are present in the white matter and have thicker and less branched processes, which in addition to vascular cells, can also contact axons (Kettenmann & Verkhratsky, 2022; Robel et al., 2011). Furthermore, recent gene expression analysis in the healthy brain has shown that astrocytes are separable between several CNS regions with region-specific gene signatures, which constitute the molecular basis of complex astrocyte morphology (Batiuk et al., 2017; Endo et al., 2022; Ohlig et al., 2021). Many astrocytic functions in the healthy adult brain are well described and span many aspects of brain physiology. In brief, some functional hallmarks which are shared between many astrocytes are to maintain homeostatic control of extracellular ions and neurotransmitters, provide glucose metabolites as neurotrophic support, play an essential role in synapse formation, function, and pruning, as well as maintain the blood-brain barrier (Robel et al., 2011; Sofroniew, 2015).

Astrocytes also have an important role in defense mechanisms with their response including changes in their morphology, gene expression, and function in a process referred to as "reactive astrogliosis" (Dimou & Götz, 2014; Escartin et al., 2021; Robel et al., 2011). Reactive astrogliosis is a widespread reaction of astroglial cells to pathological processes in the brain, ranging from neurodegenerative or inflammatory conditions to acute invasive brain injuries (Sofroniew and Vinters, 2010). Reactive astrocytes are characterized by the upregulation of intermediate filaments, such as glial fibrillary acidic protein (GFAP), nestin, and vimentin (Buffo et al., 2008; Robel et al., 2011; Sirko et al., 2009). In contrast to microglia and OPCs, astrocytes do not migrate to the

injury area after stab-wound injury. Only a tiny proportion of astrocytes (~14%) mainly located around blood vessels (juxtavascular astrocytes) proliferate, and this is the only mechanism contributing to the accumulation of astrocytes around the injury sites (Bardehle et al., 2013). The proliferation of reactive astrocyte proliferation is regulated via various signals, including endothelin-1, sonic hedgehog, and fibroblast growth factor (FGF) signaling pathways (Gadea et al., 2008; Kang et al., 2014; Sirko et al., 2013; Zamanian et al., 2012). The astrocytic proliferation in response to TBI also regulates the monocyte invasion, thus, contributing to immune response (Frik et al., 2018). In addition, reactive astrocytes also express several receptors for DAMPs, including TLRs, allowing them to sense signals from the damaged area and communicate with other innate immune cell types like microglia (Gong et al., 2020).

These initial responses facilitate the formation of a glial border, isolating the area of damage and inflammation from adjacent viable neural tissue (Brenner, 2014; Escartin et al., 2021; Pekny et al., 2014; Sofroniew, 2009). Astrocytes border, besides restricting the damage, is also necessary to promote axonal regeneration and BBB circuit restoration (Anderson et al., 2016; Batiuk et al., 2020; Escartin et al., 2021; Sofroniew, 2009). Indeed, the loss or attenuation of these cells results in more inflammation and increased serum proteins leading to further loss of neural tissue and decreased functional recovery in rodents (Sofroniew, 2015, 2020).

On the contrary, astrocyte reactivity also involves adverse outcomes by contributing to excitotoxicity, spreading the damage to distal sites of the lesion, neuroinflammation, and edema (Karve et al., 2016; Mira et al., 2021). For example, activation of TLR4 leads to the production of proinflammatory cytokines IL-6, IL-1 β , and TNF- α resulting in astrocytes reactivity, brain edema, and neuronal death (Jiang et al., 2018). Additionally, the downregulation of glutamate transporters or excitatory amino acids transporters 1 and 2 (EAAT) in astrocytes after TBI leads to increased accumulation of glutamate in extracellular areas and may contribute to excessive excitotoxicity (Karve et al., 2016; Y. H. Li et al., 2015; Mira et al., 2021). All in all, reactive astrocytes can have a dual role in response to injury, covering important protective aspects which promote recovery. However, the transition from homeostasis to reactivity alters fundamental functions of astrocytes and can be detrimental.

The responses of glial cells to TBI are not isolated but rather a coordinated process that involves an orchestrated interaction of glial and immune cells. Most studies have investigated the interaction of microglia and astrocytes, with very few reports on their interaction with OPCs (Mira et al., 2021; R. Z. Zheng et al., 2022). For example, the extracellular ATP release from astrocytes induces microglial recruitment (Davalos et al., 2005). Microglia and astrocyte crosstalk is also mediated via cytokines and other extracellular mediators, such as exosomes (Laird et al., 2014; Long et al., 2020). The interplay of glial cells and their contribution to neuroinflammation (Mira et al., 2021; R. Z. Zheng et al., 2022) is an important field that will allow us to better understand and characterize TBI pathophysiology.

1.4 Scarless regeneration of the zebrafish CNS and its implication for mammalian research

The restricted regeneration after CNS injury is a feature shared by all mammals, with a prolonged glial border formation as a hallmark. The glial border has a dual effect during the regenerative process. In the early stages, it is essential to isolate the damaged area, however, the long-term consequences of reactive gliosis are less advantageous since it creates an environment with prolonged inflammation and neurotoxicity promoting further neuronal damage. As a great burden of our modern societies, it is essential to explore multiple approaches which can promote new therapeutic targets. In this line better understanding of the great regenerative capacity of anamniotes, such as zebrafish, and comparison to mammalian systems may identify similarities and differences that could be exploited to improve the regenerative outcome in the human CNS.

In contrast to mammals, anamniotes such as zebrafish can fully regenerate their CNS after TBI (Barbosa et al., 2015; Baumgart et al., 2012; Becker & Becker, 2008; Zambusi & Ninkovic, 2020). This enormous regenerative capacity is tightly correlated with the widespread stem cell niches along the zebrafish brain axis, which constitutively produce new neurons (Chapouton et al., 2007; Diotel et al., 2020; Kaslin et al., 2008). Besides that, the transient activation of neuroinflammation is controlled promptly, intervening with glial border formation and promoting neuronal integration and survival (di Giaimo et al., 2018; Kyritsis et al., 2012).

Both the micro- and macroglia reactivity is detected in the zebrafish brain after injury. Invasive injuries in the zebrafish brain, such as the nostril injury paradigm, results in complete tissue regeneration within 1 week (Baumgart et al., 2012). Microglial cells are the first cell type to respond to a CNS injury in zebrafish by becoming hypertrophic, starting to proliferate, and accumulating around the injury site (Baumgart et al., 2012). Furthermore, the accumulation of microglial cells at the injury site correlates with the simultaneous closure of the injury track, suggesting the beneficial effects of microglial cells on wound healing (Baumgart et al., 2012; Kettenmann et al., 2011). The density of microglial cells returns to normal as soon as the injury track closes and the injury site is cleared of cell debris (Baumgart et al., 2012). As a parallel response to microglia recruitment, low numbers of proliferating oligodendrocytes (OPCs) accumulate at the injury site. However, this accumulation is transient as within 1 week, the Olig2+ cell numbers are back to normal, and the tissue is not distinguishable from uninjured control animals (Marz et al., 2011; Sanchez-Gonzalez et al., 2022). One important difference between the zebrafish and mammalian brains is the lack of astrocytes in zebrafish (Baumgart et al., 2012). Instead of astrocytes, zebrafish brains contain ependymoglia cells, which react to injury with cellular hypertrophy. Additionally, it has been shown that TBI in the zebrafish CNS triggers the upregulation of GFAP in ependymoglia cells (Kishimoto et al., 2012; Marz et al., 2011), suggesting that ependymoglia cells in the zebrafish telencephalon may take over the mammalian astrocytic functions in response to injury.

Even though zebrafish CNS can fully regenerate, the type of injury can have different cellular responses. Indeed, when the injury is performed in the dorsal-ventral direction, going through the skull and the meninges (skull injury), it results in prolonged accumulation of Olig2+ cells and microglia (4c4+ cells) replicating the glial border formed observed in mammalian CNS (Marz et al., 2011; Sanchez-Gonzalez et al., 2022). A comparison of two injury types in the adult zebrafish telencephalon identified a couple of pathways involved in the prolonged accumulation of oligodendrocytes and microglia at the injury site (Sanchez-Gonzalez et al., 2022). More specifically, after comparing the transcriptome of regenerating brains between skull and nostril injury, we determined two inflammation-related pathways, the chemokine receptor 3 (Cxcr3) pathway and the toll-

like receptor 2 (Tlr2) triggered pathway, being important for the prolonged glial border formation. Inhibition of these two receptors abolished glial accumulation and improved tissue restoration in zebrafish. These data suggest that Cxcr3 and Tlr2-triggered signaling pathways are involved in the prolonged glial border formation and manipulation of the two pathways might be beneficial for CNS regeneration in mammals as well.

1.5 Innate immune pathways as a target to control glial reactivity

1.5.1 Toll-like receptor overview and Tlr2

As mentioned above, TLRs are part of the PRRs family that plays an essential role in activating innate immunity against various internal and external stimuli. TLRs have been classified as type I transmembrane receptors consisting of an extracellular N-terminal domain with numerous leucine-rich repeats (LRR) and cysteine-rich domains, a transmembrane domain, and intracellular Toll/interleukin-1 receptor (TIR) domain. There are 12 functional members of the TLR family identified in mice, TLR1-9 and TLR11-13 (Kawasaki & Kawai, 2014), and their function is subdivided based on their localization. There are two functional classes of TLRs: the cell membrane receptors expressed on the cell surface and the intracellular ones or nucleic acid sensors localized to the endoplasmic reticulum (ER), endosomes, and lysosomes (El-Zayat et al., 2019).

TLRs are expressed broadly on both immune and non-immune cells. The expression of TLRs is not static but is modulated rapidly in response to pathogens, a variety of cytokines, and environmental stress (Akira et al., 2006). TLRs detect molecular sequences first discovered in bacteria and viruses known as pathogen-associated molecular patterns (PAMPs). However, similar molecular sequences are released from injured or dying cells, which act as DAMPs and can act as endogenous ligands of TLRs. Several components could serve as DAMPs, including extracellular matrix components (for instance, hyaluronan and fibrinogen), nuclear and cytosolic proteins, for example, high-mobility group box protein 1 (HMGB1), and HSPs, plasma membrane constituents, as well as elements of damaged or fragmented organelles (such as mitochondrial DNA) (Gong et al., 2020). Activation of TLRs initiates downstream signaling pathways which induce innate immune responses by producing proinflammatory cytokines, chemokines, type I interferon (IFN-I), and antimicrobial peptides that further orchestrate antigen-

specific adaptive immune responses(El-Zayat et al., 2019; Heidari et al., 2022; Kawasaki & Kawai, 2014).

TLR2 is classified as a cell membrane receptor, usually found in heterodimer forms with TLR1 and TLR6, recognizing triacylated and diacylated lipopeptides, respectively, typically found in bacteria (El-Zayat et al., 2019; Oliveira-Nascimento et al., 2012; Perkins & Vogel, 2015). There are various endogenous ligands binding TLR2, including HSPs, HMGB1, and biglycan, which promote the production of proinflammatory cytokines, chemokines, and IFN-I responses (Gong et al., 2020; Oosenbrug et al., 2020; Y. Wang et al., 2013). It has been shown that TLR2 is expressed in cells of the CNS after pathological conditions, including microglia, astrocytes, oligodendrocytes, and neurons (Bsibsi et al., 2002a, 2002b; Hanke & Kielian, 2011; Kielian et al., 2002; Konat et al., 2006; Mishra et al., 2006). After an injury in the CNS, damaged cells release certain components which can act as DAMPS, including heat-shock proteins (HSP), nucleic acids, and high mobility group protein B1 (HMGB1), which signal principally to Tlr2 and Tlr4 (Gyoneva & Ransohoff, 2015; Y. Wang et al., 2013). In response to these, astrocytes, microglia, and damaged neurons at the injury site start secreting cytokines and chemokines, which further activate microglia and astrocytes and recruit peripheral immune cells (Gyoneva & Ransohoff, 2015).

1.5.2 Chemokine receptor overview and Cxcr3

Chemokines are a large subgroup in the cytokine family, defined as chemotactic cytokines, due to their ability to attract immune system cells to the site of the injury or infection and orchestrate innate and adaptive immune responses. Four major chemokine families are classified based on the number and spacing of the conserved cysteine residues in the N-terminal position, named CXC, C, CC, and CX3C (Cartier et al., 2005; Murphy, 2002; Réaux-Le Goazigo et al., 2013). Chemokine receptors are G protein-coupled receptors (GPCRs), belonging to the superfamily of seven-transmembrane domain receptors that mediate intracellular signals through heterotrimeric GTP-binding proteins. The nomenclature of the receptors follows this of the ligands that activate them, followed by the letter "R" (receptor). The high sequence homology between chemokine receptors of specific classes results in structural similarities. Consequently, these

similarities reflect a degree of redundancy since each chemokine has the capability of activating several different chemokine receptors or vice versa (Cartier et al., 2005; Nomiya et al., 2011).

Besides the structural properties, chemokines can be additionally classified according to function and categorized into inflammatory and homeostatic chemokines (Cartier et al., 2005; Zlotnik & Yoshie, 2012). Inflammatory chemokines are expressed in inflammatory conditions in response to proinflammatory cytokines or contact with pathogens. Consequently, they are primarily associated with the recruitment of leukocytes, such as monocytes, granulocytes, and effector T cells, to inflamed tissue (Cartier et al., 2005; Kiefer & Siekmann, 2011). In contrast, homeostatic chemokines are constitutively expressed under physiological conditions in lymphoid and other organs regulating the migration and homing of cells belonging to the adaptive immune system in physiological conditions. However, some chemokines possess both aspects and are called dual-function chemokines (Nomiya et al., 2011; Zlotnik & Yoshie, 2012). Consistent with the diverse functions of the chemokine system, chemokines, and their receptors are also expressed in the CNS, where they play key functions in the development and homeostatic maintenance (Gyoneva & Ransohoff, 2015).

The C-X-C Motif Chemokine Receptor 3 (CXCR3) can be differentially activated by the inflammatory chemokines CXCL9, CXCL10, and CXCL11 in mice (Colvin et al., 2004; Karin, 2020). The ligands and the receptor itself are mainly induced and regulated by interferon- γ (INF- γ) in response to injury or neuroinflammation (Müller et al., 2010). CXCR3 is expressed in various cell types of the leukocyte lineage, including monocytes, Th1 T cells, CD8 T cells, NKT cells, NK cells, and dendritic cells (Kuo et al., 2018). However, it has been shown that it is also expressed in other cells of the CNS, such as microglia, astrocytes (Biber et al., 2002), and neurons (Qi Xia et al., 2000).

1.6 Single-cell RNA-sequencing for studying glial reactivity

As discussed above, the cellular response to injury is characterized by complex changes in cells of various lineages and complex interplay between many of them during the disease progression. Accordingly, to broaden our understanding of TBI-induced pathology, it is required to enhance our knowledge of this complex system at cellular and

molecular level. In this line, the development of single-cell RNA- sequencing (scRNA-seq) and several closely related technologies like spatial transcriptomics now offer an outstanding chance to interrogate the complex cellular dynamics of the CNS injury at cell-type-specific resolution through the study of their transcriptome. Indeed, an individual cell's RNA transcriptome can readily identify its background while giving a remarkably accurate picture of how it functions and responds to external stimuli. ScRNA-seq, has the ability to identify cellular heterogeneity within seemingly homogeneous cell populations, which may provide explanations for certain complex phenotypes that may be observed (Cardona-Alberich et al., 2021; Hwang et al., 2018).

Single-cell omics was first achieved in 2009, characterizing cells from early developmental stages (Tang et al., 2009), and was advanced rapidly by the development of technologies for profiling the genome, DNA methylome, chromatin accessibility, and histone modifications in an individual cell. In principle, all current scRNA-seq methods involve the dissociation of a sample into single cells, then the barcoding of the individual

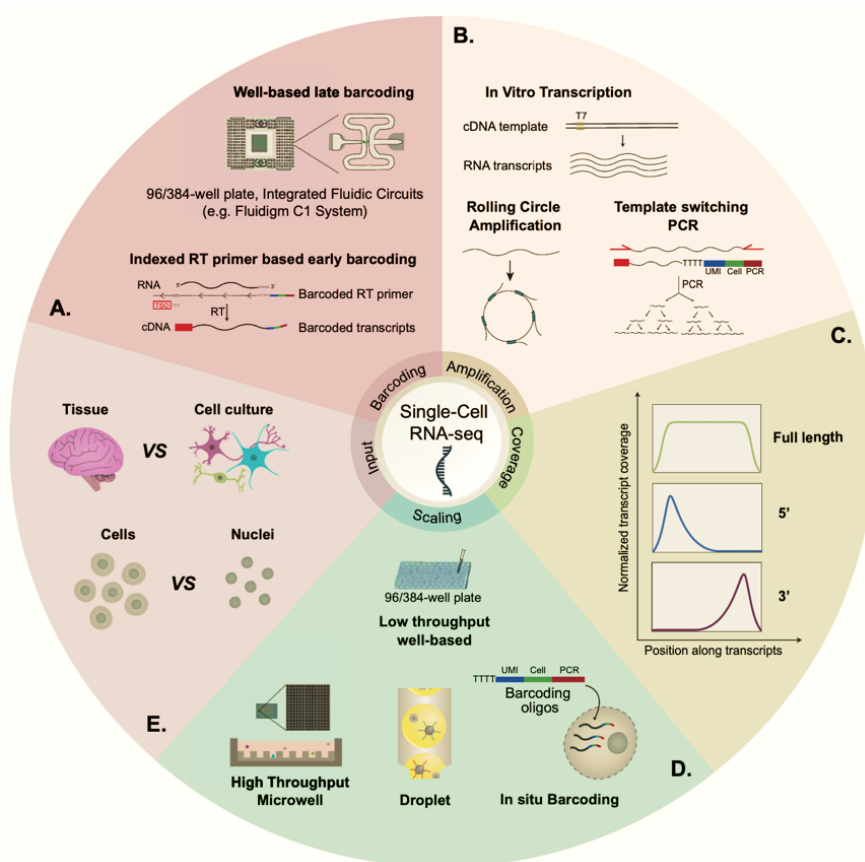


Figure 2. Single-cell isolation and library preparation options: cellular barcoding (A), amplification approach (B) captured RNA transcripts (C) single cell capturing approach (D) starting material (E). (Cardona-Alberich et al., 2021. License CC-BY- NC 4.0)

cells such that all RNA derived from a given cell is labeled with an identical barcode. Consequently, the barcode can be used to identify the cellular origin of each sequenced transcript during downstream bioinformatics analyses. Over the years, the different protocol variants that have emerged differ from one another in various aspects, such as i) their method of barcoding the RNA from individual cells, ii) their method to amplify low abundance cellular RNA, iii) the region of the mRNA transcript that is enriched and sequenced iv) the method used to capture and process the individual cells (e.g., wells and droplets-based methods), and v) the choice of starting material [single cells or single nuclei (sn)] (Figure 2).

Single-cell sequencing technologies, particularly scRNA-seq and snRNA-seq, have been extensively used to profile brain cell type diversity to elucidate the specific function, connectivity, and state of brain cells in physiology and disease (Cardona-Alberich et al., 2021; Zhang et al., 2022). To better understand cellular brain heterogeneity, various approaches have been used, including profiling the whole organ and region-specific analysis, looking holistically at several cell populations, or focusing on specific types of cells, such as microglia and astrocytes (Figure 3). Astrocytes, for example, were characterized in multiple brain regions by performing scRNA-seq analysis of all cell types and then focusing on astrocytes which revealed shared and region-specific astrocytic genes (Endo et al., 2022), whereas other studies enriched for astrocytes prior scRNA-seq (Ohlig et al., 2021). In addition, studying astrocytes in response to inflammation revealed the appearance of distinct inflammatory subpopulations with distinct gene patterns

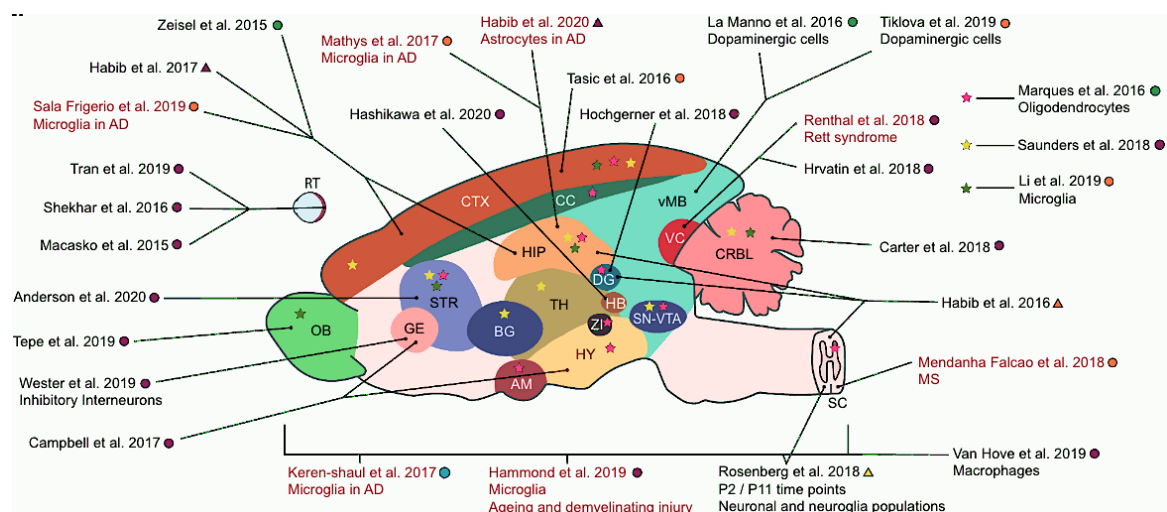


Figure 3. ScRNA-seq and snRNA-seq studies in mouse CNS until 2021. (Cardona-Alberich et al., 2021. License CC-BY- NC 4.0)

(Hasel et al., 2021). With the advent of scRNA-seq in healthy brains, during developmental stages, or in adulthood, as well as specific neurological diseases, new opportunities have been provided to identify novel cell types and disease-specific cell states, to identify molecular changes specific to cells, to study disease progression, and to dissect molecular mechanisms at high resolution.

2 Results

2.1 Aim of study I

The aim of this study was to characterize a zebrafish injury model with prolonged glial activation and investigate the role of innate immunity via Tlr2 and Cxcr3 signaling pathways in the activation and long-term accumulation of OPCs, leading to prolonged neuroinflammation.

Innate Immune Pathways Promote Oligodendrocyte Progenitor Cell Recruitment to the Injury Site in Adult Zebrafish Brain

Rosario Sanchez-Gonzalez, **Christina Koupourtidou**, Tjasa Lepko, Alessandro Zambusi, Klara Tereza Novoselc, Tamara Durovic, Sven Aschenbroich, Veronika Schwarz, Christopher T. Breunig, Hans Straka, Hagen B. Huttner, Martin Irmeler, Johannes Beckers, Wolfgang Wurst, Andreas Zwergal, Tamas Schauer, Tobias Straub, Tim Czopka, Dietrich Trümbach, Magdalena Götz, Stefan H. Stricker, and Jovica Ninkovic.

My contribution to this publication in detail:

For this paper, I was involved in the experiment validating the role of Cxcr3 and Tlr1/2 in OPCs using two *in vitro* approaches. First, with the primary OPC culture and clonal analysis, I assessed the role of the two pathways in the proliferation capacity of OPCs. Furthermore, with the generation of the Oli-neu cell line deficient for Cxcr3 and Tlr2 using the CRISPR/Cas9 approach, I addressed the direct role of the pathways in the proliferation capacity of OPCs and ruled out any pharmacological off-targets. Additionally, I assisted in the preparation of RNA-Seq libraries from FACS-isolated cells. I was also involved in editing and reviewing the paper.

The paper is published in Cells (2022).

<https://doi.org/10.3390/cells11030520>

License: CC-BY- NC 4.0

Article

Innate Immune Pathways Promote Oligodendrocyte Progenitor Cell Recruitment to the Injury Site in Adult Zebrafish Brain

Rosario Sanchez-Gonzalez^{1,2}, Christina Koupourtidou^{1,3,4} , Tjasa Lepko^{1,3,4}, Alessandro Zambusi^{1,3,4}, Klara Tereza Novoselc^{1,3,4}, Tamara Durovic^{1,3,4}, Sven Aschenbroich^{1,3,4}, Veronika Schwarz^{1,3,4}, Christopher T. Breunig^{5,6}, Hans Straka² , Hagen B. Huttner⁷, Martin Irmeler⁸, Johannes Beckers^{8,9,10}, Wolfgang Wurst^{11,12,13,14} , Andreas Zwergal¹⁵, Tamas Schauer¹⁶, Tobias Straub¹⁶, Tim Czopka¹⁷, Dietrich Trümbach^{11,†} , Magdalena Götz^{1,12,18}, Stefan H. Stricker^{5,6} and Jovica Ninkovic^{1,3,12,*}



Citation: Sanchez-Gonzalez, R.; Koupourtidou, C.; Lepko, T.; Zambusi, A.; Novoselc, K.T.; Durovic, T.; Aschenbroich, S.; Schwarz, V.; Breunig, C.T.; Straka, H.; et al. Innate Immune Pathways Promote Oligodendrocyte Progenitor Cell Recruitment to the Injury Site in Adult Zebrafish Brain. *Cells* **2022**, *11*, 520. <https://doi.org/10.3390/cells11030520>

Academic Editors: Sepand Rastegar and Luisa Lübke

Received: 26 December 2021

Accepted: 18 January 2022

Published: 2 February 2022

Publisher's Note: MDPI stays neutral with regard to jurisdictional claims in published maps and institutional affiliations.



Copyright: © 2022 by the authors. Licensee MDPI, Basel, Switzerland. This article is an open access article distributed under the terms and conditions of the Creative Commons Attribution (CC BY) license (<https://creativecommons.org/licenses/by/4.0/>).

- ¹ Institute of Stem Cell Research, Helmholtz Center Munich, 85764 Oberschleißheim, Germany; rosario.sanchez@biologie.uni-muenchen.de (R.S.-G.); koupourtidou@helmholtz-muenchen.de (C.K.); lepko.tjasa@gmail.com (T.L.); alessandro.zambusi@helmholtz-muenchen.de (A.Z.); klara.novoselc@helmholtz-muenchen.de (K.T.N.); durovictamara90@gmail.com (T.D.); sven.aschenbroich@helmholtz-muenchen.de (S.A.); schwarz.veronika@campus.lmu.de (V.S.); magdalena.goetz@helmholtz-muenchen.de (M.G.)
- ² Department Biology II, University of Munich, 80539 München, Germany; straka@biologie.uni-muenchen.de
- ³ Biomedical Center (BMC), Division of Cell Biology and Anatomy, Faculty of Medicine, LMU Munich, 80539 München, Germany
- ⁴ Graduate School Systemic Neurosciences, LMU, 80539 München, Germany
- ⁵ Reprogramming and Regeneration, Biomedical Center (BMC), Physiological Genomics, Faculty of Medicine, LMU Munich, 80539 München, Germany; christopher.breunig@helmholtz-muenchen.de (C.T.B.); stefan.stricker@helmholtz-muenchen.de (S.H.S.)
- ⁶ Epigenetic Engineering, Institute of Stem Cell Research, Helmholtz Center Munich, 85764 Oberschleißheim, Germany
- ⁷ Department of Neurology, Justus-Liebig-University Giessen, Klinikstrasse 33, 35392 Giessen, Germany; hagen.huttner@neuro.med.uni-giessen.de
- ⁸ Institute of Experimental Genetics, Helmholtz Center Munich, 85764 Oberschleißheim, Germany; martin.irmeler@helmholtz-muenchen.de (M.I.); beckers@helmholtz-muenchen.de (J.B.)
- ⁹ German Center for Diabetes Research (DZD e.V.), 85764 Neuherberg, Germany
- ¹⁰ Chair of Experimental Genetics, School of Life Sciences Weihenstephan, Technical University Munich, 80333 München, Germany
- ¹¹ Institute of Developmental Genetics, Helmholtz Center Munich, 85764 Oberschleißheim, Germany; wurst@helmholtz-muenchen.de (W.W.); dietrich.truembach@helmholtz-muenchen.de (D.T.)
- ¹² Munich Cluster for Systems Neurology SYNERGY, LMU, 80539 München, Germany
- ¹³ Chair of Developmental Genetics c/o Helmholtz Zentrum München, School of Life Sciences Weihenstephan, Technical University Munich, 80333 München, Germany
- ¹⁴ German Center for Neurodegenerative Diseases (DZNE), Site Munich, 80539 München, Germany
- ¹⁵ Department of Neurology, Ludwig-Maximilians University, Campus Grosshadern, 81377 München, Germany; andreas.zwergal@med.uni-muenchen.de
- ¹⁶ Biomedical Center (BMC), Bioinformatic Core Facility, Faculty of Medicine, LMU Munich, 80539 München, Germany; tamas.schauer@med.uni-muenchen.de (T.S.); tstraub@bmc.med.lmu.de (T.S.)
- ¹⁷ Centre for Clinical Brain Sciences, University of Edinburgh, Edinburgh EH8 9YL, UK; tim.czopka@tum.de
- ¹⁸ Biomedical Center (BMC), Division of Physiological Genomics, Faculty of Medicine, LMU Munich, 80539 München, Germany
- * Correspondence: ninkovic@helmholtz-muenchen.de
- † Present address: Institute of Metabolism and Cell Death, Helmholtz Center, Munich, 85764 Neuherberg, Germany.

Abstract: The oligodendrocyte progenitors (OPCs) are at the front of the glial reaction to the traumatic brain injury. However, regulatory pathways steering the OPC reaction as well as the role of reactive OPCs remain largely unknown. Here, we compared a long-lasting, exacerbated reaction of OPCs to the adult zebrafish brain injury with a timely restricted OPC activation to identify the specific molecular mechanisms regulating OPC reactivity and their contribution to regeneration. We demonstrated that the influx of the cerebrospinal fluid into the brain parenchyma after injury simultaneously activates the toll-like receptor 2 (Tlr2) and the chemokine receptor 3 (Cxcr3) innate immunity pathways, leading to increased OPC proliferation and thereby exacerbated glial reactivity.

These pathways were critical for long-lasting OPC accumulation even after the ablation of microglia and infiltrating monocytes. Importantly, interference with the Tlr1/2 and Cxcr3 pathways after injury alleviated reactive gliosis, increased new neuron recruitment, and improved tissue restoration.

Keywords: brain regeneration; oligodendrocyte progenitors; reactive gliosis; innate immunity pathways; zebrafish; neurogenesis; brain injury

1. Introduction

Wound healing in the brain is triggered by a temporarily regulated neuroinflammatory response that activates glial cells (reactive gliosis) and induces their recruitment to the injury [1,2]. Despite the many different approaches to model brain injury, there is an emergence of a common pattern in the cellular dynamics of brain resident cells following an insult [3]. Microglia respond to injury within 24 h by changing their morphology, increasing their proliferation rate, and migrating towards the injury site [4]. The activated microglia together with infiltrating monocytes not only phagocytose the cellular debris, but also release several damage-associated molecules (DAMs) to coordinate the subsequential glial reactivity [3,5–8]. In line with the inductive role of microglia released DAMs, the astrocyte reactivity (also termed astrogliosis) typically starts later on (2–3 days after injury) and varies depending on the extent of the damage [9]. Astrogliosis forms the border of GFAP⁺ reactive astrocytes surrounding the injury site by the hypertrophy of astrocytic processes, the upregulation of GFAP, and the increased proliferation of juxtavascular astrocytes [5,10,11]. Ablation experiments have demonstrated that the initial reaction of astrocytes is essential for wound closure and the restoration of the normal brain milieu [12,13]. Moreover, border-forming reactive astrocytes have been described to be necessary for axonal regeneration after spinal cord injury [5,14]. On the other hand, multiple studies have shown that prolonged astrogliosis induced averse extracellular matrix modifications and exacerbated inflammation [15–17] that negatively impact on functional recovery. Recent reports have demonstrated a reciprocal regulatory loop between astrocytes and immune cells. While DAMs released by microglia induce a neurotoxic phenotype in astrocytes [18], astrocytes regulate the extravasation of monocytes and in turn, the long lasting neuroinflammatory response [12,19].

Strikingly, oligodendrocyte progenitor cells (OPCs) react to insults such as demyelination [20,21], traumatic brain injury (TBI) [22], or neurodegenerative disorders [23] as fast as the residential microglial cells. In physiological conditions these slow proliferating progenitors display very limited and short-range migration [24,25] and maintain their non-overlapping cellular domains by balancing cellular proliferation and cell death [22,24–27]. However, a rapid and heterogeneous reaction of OPCs has been documented in response to brain injury [22,24,25,28]. The OPCs polarize shortly after an insult [29] and become fully hypertrophic [24,25] within 48 h after injury. This reaction is followed by migration towards the injury site [24,25] and an increased proliferation rate in the case of a bigger injury [25]. Importantly, during the wound healing process the OPCs do not maintain the non-overlapping domains anymore and they accumulate at the injury site [25]. This accumulation is resolved 4 weeks after the injury and the cellular repulsion mechanisms maintaining the non-overlapping domains are established again. Despite the precise description of the cellular dynamics, our understanding of the OPC reaction to brain injuries and its relevance is still far from being understood. Several reports have suggested that the OPC accumulation at the injury site could promote wound healing [25] and the co-depletion of proliferating microglia and OPCs shown enhanced axonal regeneration [30,31]. In contrast, the accumulation of OPC-derived proteoglycan NG-2 has been associated with the inhibition of axonal growth [32]. These rather opposing observations support the need to identify the pathways regulating the reaction of OPCs to brain injury and to associate them with the observed regenerative outcomes after injury.

The temporal sequence of the glial reaction to injury in the adult zebrafish brain shares some interesting similarities with the injured mammalian brain [1,33,34]. However, in contrast to the exacerbated gliotic wound closure described above for the mammalian brain, the glial response leads to full tissue restoration in zebrafish [1,34–37]. Complete recovery in the zebrafish brain correlates with the capacity to regulate the neuroinflammatory landscape and induce the restorative neurogenesis (neuronal replacement) from endogenous sources [37]. The basis for neuronal replacement resides in the injury-induced activation of neural stem cell-like ependymogial cells [1]. The initial microglial reaction to injury activates developmental and/or injury-specific regulatory pathways in ependymogial cells [1], regulating the timely production of new neurons necessary for tissue recovery. Although several regulatory mechanisms mediating the crosstalk between immune and ependymogial cells have been identified [1], little is known about how OPCs contribute, if at all, to the permissive time window for the integration of new neurons. Zebrafish OPCs exhibit a different reaction to the stab wound injury depending on the injury paradigm [37–39]. While injuries performed rostro-caudally through the nostrils (nostril injury) induced no increased proliferation and no recruitment of OPCs to the damaged area [37], injuries along the dorso-ventral axis (skull injury) induced a long lasting accumulation of OPCs at the injury site [39]. The reaction of the OPCs to the skull injury is indeed very similar to the OPC reaction in the injured mammalian cortex, including the temporal resolution only after 4 weeks [22,34,39]. Nostril and skull injury paradigms offer an ideal comparative model by which to identify specific molecular pathways regulating OPC reactivity and its potential impact on tissue restoration and neuronal replacement as a means for functional recovery. We applied a comparative analysis of “nostril versus skull” zebrafish forebrain tissue to identify novel molecular mechanisms regulating exacerbated and prolonged OPC activation. We identified the toll-like receptor 2 (Tlr2) and the chemokine receptor 3 (Cxcr3) innate immune pathways as key regulators of OPC proliferation. Interference with these signaling pathways after injury not only alleviated the OPC accumulation at the injury site, but it also improved wound healing and restorative neurogenesis. We also showed that prolonged exposure of murine OPCs to human cerebrospinal fluid content activated Tlr2/Cxcr3 signaling and in turn increased OPC proliferation. Taken together, we identified signaling pathways and the source of their ligands regulating exacerbated and prolonged OPC reactivity, opening a new avenue for targeting therapies.

2. Materials and Methods

2.1. Animals

Adult 4–6 month old wild-type zebrafish (*Danio rerio*) of the AB/EK strain, or of the transgenic lines, Tg(olig2:gfp) [40], Tg(olig2:DsRed) [40], Tg(fli1:egfp) [41], Tg(gfap:GFP) [42], Tg(mbp:nsIGFP) [43] and Tg(mpeg1:mCherry) [44] were used for all the experiments. Fish were kept under standard husbandry conditions [45] and experiments were performed according to the handling guidelines and regulation of the EU and the Government of Upper Bavaria (AZ 55.2–1–54–2532–09–16).

2.2. Stab Wound Injuries

We carried out three different stab wound injury paradigms: nostril, skull, and small skull injuries (Figures 1 and 6). Fish were anesthetized with buffered 0.02% MS-222 for 45 s to a minute and then placed in a Tricaine-soaked sponge. With the visual aid of a dissecting microscope, injuries were performed in both telencephalic hemispheres. The nostril injury [37] was performed using a 100 0.9 mm glass capillary needle (KG01, A. Hartenstein). Capillaries were pulled on a Narishige Puller (model PC–10) using a “One-stage” pull setting at a heater level of 63.5 C. The final dimensions of the capillaries were 5 mm in length and 0.1 mm in diameter. For the skull injury, a micro-knife (Fine Science Tools) was inserted vertically through the skull into the medial region of the telencephalon. To perform the small skull injury, the skull was thinned above the telencephalon area using a micro-driller (Foredom) and the glass capillary (identical to that used for the nostril injury)

was inserted vertically through the skull and brain parenchyma. After the injury, fish were placed in fish water with oxygenation to assure complete recovery from the anesthesia.

2.3. Tlr2 Agonist (Zymosan A Bioparticles, Invitrogen) Administration

Fish were anaesthetized in 0.02% MS-222 and a small hole, using a micro-knife (Fine Science Tools), was made into the skull (above the telencephalic ventricle). A glass capillary loaded with 10 mg/mL Zymosan or artificial cerebrospinal fluid with Fast Green dye to visualize the injection site (0.3 mg/mL; Sigma) was inserted into the hole and ~1 L of solution was injected at a pressure of 150 hPa using a microinjector (Eppendorf, Hamburg, Germany). Artificial cerebrospinal fluid was used as a control for the ventricular injections since its composition closely matches the electrolyte concentrations of cerebrospinal fluid (Figure 2).

2.4. Cxcr3 Agonist (VUF 11222, R & D Systems) Administration

Fish were anaesthetized as previously described and the solution was injected intraperitoneally using a 30G needle (Braun). A total of 4 L of VUF 11222 (300 mg/kg) or DMSO vehicle with the Fast Green dye (0.3 mg/mL; Sigma) was intraperitoneally injected (Figure 2). We did not observe any aversive effects by IP injecting up to 4 L of the 80% DMSO solution.

2.5. Inhibitor Administration

Intraperitoneal injections were performed as described above. All inhibitors were dissolved in DMSO with Fast Green dye (0.3 mg/mL; Sigma) for visualization. Cxcr3 inhibitors (NBI 74330 (300 mg/kg, R & D Systems, Minneapolis, MN, USA) and AMG 487 (112 mg/kg, R & D Systems)), and Tlr1/2 inhibitor (CU CPT 22 (150 mg/kg, R & D Systems)) were injected independently (NBI 74330 or CU CPT 22) or in combination (NBI 74330 + CU CPT 22 or AMG 487 + CU CPT 22) (Figure 3 and Figure S5). NBI 74330 and CU CPT 22 were injected daily, while AMG 487 was injected twice per day. The vehicle solution consisted of DMSO and Fast Green dye. A total of 4 L was administered per injection and the maximum number of intraperitoneal injections was 2 injections per day at an interval of 72 h. The mortality rate was less than 5% after any of the treatments.

2.6. BrdU Labelling Experiments

To label proliferating cells and their progeny, we carried out long term bromo-deoxyuridine (BrdU; Sigma Aldrich, St. Louis, MO, USA) incorporation. Fish were kept in BrdU-containing aerated water (10 mM) for 21 h/day or 14 h/day as stated in specific experiments (Figures 4–6).

2.7. Immune Cell Depletion Assay

A two-step approach was used to deplete the immune cells: 2 L of Clodrosome (Encapsula NanoSciences, Brentwood, TN, USA) was injected into the telencephalic ventricle every second day for one week prior to the injury (4 injections in total prior to the injury). Ccr2 inhibitor (MK-0812, 82.5 mg/kg, Cayman Chemical, Ann Arbor, MI, USA) was administered by intraperitoneal injection daily, starting 2 days before the injury (Figures 5 and S6). As a control for the ventricular injection, we used empty liposomes (Encapsome) and DMSO for the intraperitoneal administration.

2.8. Human CSF Sample Collection

Human CSF samples were obtained from two different sources. The first one was Erlangen University Hospital. The patients underwent a lumbar puncture to exclude intracranial hemorrhage or inflammatory diseases of the CNS and they were considered healthy based on normal values for CSF (color, cell count, and total protein). CSF analysis was approved by the institutional review board of Erlangen University Hospital (ethics committee number 3950) and patients gave informed consent. After lumbar puncture, a

protease inhibitor was added to CSF according to the manufacturer's instructions (Roche) and CSF was directly frozen at -80°C . The second source was the University Hospital at LMU Munich (project number 159/03). Human CSF samples were obtained from patients who underwent a lumbar puncture to exclude intracranial hypertension or inflammatory CNS diseases. Routine analysis of CSF (cell count, total protein, glucose) revealed no abnormal values in all samples. All patients gave their informed written consent.

2.9. Human Plasma, Cerebrospinal Fluid, and Heat-Inactivated Cerebrospinal Fluid Administration

A 100 μL 0.9 mm glass capillary needle (KG01, A. Hartenstein, Würzburg, Germany) was loaded with human plasma (Sigma Aldrich), human cerebrospinal fluid, or heat-inactivated human cerebrospinal fluid (single healthy donor). Human cerebrospinal fluid was incubated for 15 min at 90°C to generate heat-inactivated human cerebrospinal fluid. Fish were anesthetized with 0.02% MS-222 (Sigma-Aldrich). The glass capillary was introduced through the nostril and $\sim 1 \mu\text{L}$ of the solution was injected at a pressure of 150 hPa into the injury track in the telencephalic parenchyma (Figure 6).

2.10. Plasmid Electroporation

The plasmid pCS2-tdTomato was diluted in sterile water and Fast green (1 mg/mL), reaching a final concentration of 1 $\mu\text{g}/\mu\text{L}$. $\sim 0.5 \mu\text{L}$ of the solution was injected in the telencephalic ventricle as described previously [46]. Next, the electroporation was carried out by placing the positive electrode at the ventral side of the fish's head and the negative electrode on the dorsal side and giving five pulses at 40 V for 50 ms each at 1-s intervals [47].

2.11. Tissue Preparation and Immunohistochemistry

Animals were sacrificed by an MS-222 overdose. Brains were dissected and fixed for 3 h at 4°C in 4% paraformaldehyde (PFA) in phosphate-buffered saline (PBS), washed three times with PBS, and sectioned. For sectioning, whole brains were embedded in 3% agarose in PBS and cut serially at a 100 μm thickness with a microtome (HM 650V, Microm). Primary antibodies (Table S1) were dissolved in 0.5% Triton X and 10% normal goat serum. Subclass-specific secondary antibodies (1:1000, ThermoFisher, Waltham, MA, USA) were used to detect the primary antibodies. Nuclear staining was performed with 40,6-diamidino-2-phenylindole hydrochloride (DAPI) (Sigma). All sections were mounted using Aqua Polymount (Polyscience, Niles, IL, USA). BrdU immunodetection required 2N HCl pre-treatment for 20 min at room temperature. Pre-treatment of the sections with Dako target retrieval solution (Agilent, Santa Clara, CA, USA) was necessary for the detection of the L-plastin. For whole-mount infarct tissue imaging, 500 μm thick telencephalic sections were cleared using BABB (1 part benzyl alcohol, 2 parts benzyl benzoate method) and stained as previously described [48].

Cryo-sectioning was used for RNA scope (see below). After fixation, whole brains were cryoprotected in a 30% sucrose solution overnight at 4°C . The tissue was embedded in a tissue freezing medium (Leica) and frozen using dry ice. Serial sectioning at 20 μm thickness with a cryostat (Leica) was performed. Sections were stored at -20°C until further processing.

2.12. RNA scope

We used an RNA scope Multiplex Fluorescent Reagent Kit v2 (ACD) to identify and label specific zebrafish RNAs. For tissue processing, pre-treatment, and RNA scope assay we followed the manufacturer's instructions. The RNA scope probes were designed by ACD using the following target sequences: Cxcr3.2 (NM_001007314.1), MYD88 (NM_212814.2), Mxc (NM_001007284.2), Tlr8b (NM_001386709.1), and GFP (Synthetic construct Cox8ND6gfp). For visualization, the TSA Plus Cyanine 3/5 (Perkin Elmer) kit was utilized.

2.13. Image Acquisition and Processing

All immunofluorescence microscopy on sections was performed and analyzed with an Olympus FV1000cLSM system (Olympus, Tokyo, Japan), using the FW10-ASW 4.0 software (Olympus). Bright field images were taken with a Leica DM2500 microscope at the Core Facility Bioimaging at the Biomedical Center (BMC). For whole-mount infarct tissue analysis, images were acquired with a Leica SP8X microscope, using LASX software (Leica) and deconvolved using Huygens Professional deconvolution software (SVI). The injury site was analyzed using Imaris software version 8.4 (Bitplane, Concord, USA). The 3D surface object was generated from manually created contours on 2D slices using the Surface tool to calculate the volume of the Surface object. Animations were made using the Key Frame Animation function (Imaris).

2.14. Quantitative Analysis

For each experiment, animals were randomly distributed into groups and all manual counts were performed blind. For all quantifications 4 to 6 brains were analyzed, coming from at least 2 independent experiments. All the sections belonging to the telencephalon were quantified (sections with the olfactory bulb or optic tectum were excluded), from which we analyzed the entire rostro-caudal extent of the injured tissue. The injured volume was calculated by multiplying the area and the depth of the DAPI dense accumulation for each section. The total injured volume was the sum of all the injured sections. The density of the positive cells in the injured volume was defined by the total number of cells located in the volume occupied by DAPI dense accumulation. Controls for the “injured volume” were measured in uninjured, age matched fish using equivalent volumes for each of the injury paradigms. For 4C4 quantifications, single-channel immunofluorescent images were converted to black and white, thresholded, and the extent of the stained area was measured using NIH ImageJ software. For the analysis of OliNeu proliferation, 25 randomly selected images per coverslip were used for the analysis. The analysis was performed using the automated ImageJ pipeline that is available upon request.

2.15. Statistical Analysis

Data are presented as the mean \pm standard error of the mean (SEM) and each dot represents one animal. Statistical analysis was performed using R (version 3.6.1). Data were investigated to test whether assumptions of parametric tests were satisfied (e.g., t-test or Anova). Residuals (fitted by lm function, stats package, version 3.6.1) were tested for normality by the Shapiro-Wilk normality test (shapiro_test function, rstatix package, version 0.6.0). Further diagnostics of residuals were carried out using the DHARMA package (version 0.3.3.0). The homogeneity of variance assumption was tested using Levene's test (leveneTest function, car package, version 3.0-10). If both normality and equal group variances assumption were met, Student's t-test (t.test function with var.equal = TRUE, stats package, version 3.6.1) for single comparisons and one-way anova (aov function, stats package, version 3.6.1) for multiple group design was used. Anova post-hoc tests, i.e., Tukey or Dunnett tests, were applied either for all pair-wise comparisons (tukeyTest function, PMCMRplus package, version 1.9.0) or Many-to-One comparisons (dunnettTest function, PMCMRplus package, version 1.9.0), respectively. If the normality assumption was satisfied but groups had unequal variances, Welch's t-test (t.test function with var.equal = FALSE, stats package, version 3.6.1) for single comparisons and Welch's one-way Anova (oneway.test function, stats package, version 3.6.1) for multiple group design was used. As a post-hoc test, Dunnett's T3 test for data with unequal variances was applied (dunnettT3Test function, PMCMRplus package, version 1.9.0). For Figure S2E only selected contrasts were tested (i.e., coronal vs. sagittal in each group) using the multcomp package (glht function, version 1.4-15). If the normality assumption was not met, the data were log-transformed to achieve normality of the residuals. In such a case, parametric tests were carried out as described above. If log-transformation did not satisfy the assumption, non-parametric tests were used i.e., Wilcoxon rank sum test (wilcox.test function, stats package,

version 3.6.1) for single comparisons and Kruskal–Wallis test (`kruskal_test` function, `rstatix` package, version 0.6.0) for multiple group design. In the latter case, the post-hoc Dunn test (`kwManyOneDunnTest` function, `PMCMRplus` package, version 1.9.0) was performed for Many-to-One comparisons. Dose–response in Figure 7D was analyzed by linear regression on square–root transformed outcome values. *p*–values were obtained for the regression coefficients: the slope for OliNeu and the difference in slopes (interaction term) for clone1 or clone2 relative to OliNeu. The detailed statistical analysis for all data sets is presented in the Supplementary Materials.

2.16. Analysis of Restorative Neurogenesis

Restorative neurogenesis was defined as the proportion of new neurons that migrated into the parenchyma. Zebrafish were kept in BrdU–containing aerated water (10 mM) overnight during the first 3 days. Simultaneously, vehicle and double inhibitors were injected daily under normal conditions (Figure 4C–H) or after immune cell depletion (Figure 4M–R). Animals were sacrificed at 7 dpi and the expression pattern of HuC/D and BrdU was analyzed. We assessed restorative neurogenesis as completed previously [49] by calculating the proportion of new neurons (HuC/D⁺BrdU⁺) that had migrated from the ventricular zone into the parenchyma as a result of the injury.

2.17. RNA Extraction, cDNA Synthesis, and RT–qPCR

Total RNA was isolated using the Qiagen RNeasy kit for microarray analysis and qPCR experiments. RNA isolation from FACS purified was performed with a PicoPure RNA isolation kit (Thermo Scientific). cDNA synthesis was performed using random primers with the Maxima first strand synthesis kit (Thermo Scientific). The manufacturer's instructions were followed for all the mentioned kits. The real–time qPCR was conducted using SYBR green and Thermo Fisher Quant Studio 6 machine (Table S2).

2.18. Microarray Analysis

Total RNA (20 ng) was amplified using the Ovation Pico WTA System V2 in combination with the Encore Biotin Module (Nugen). Amplified cDNA was hybridized on Affymetrix Zebrafish 1.0ST arrays. Staining and scanning were performed according to the Affymetrix expression protocol including minor modifications as suggested in the Encore Biotin protocol. An expression console (v.1.3.1.187, Affymetrix) was used for quality control and to obtain annotated normalized RMA gene–level data (standard settings including median polish and sketch–quantile normalization). Statistical analyses were performed by utilizing the statistical programming environment R (R Development Core Team implemented in CARMAweb [50]). Genewise testing for differential expression was performed by employing the *limma* *t*–test. Regulated gene sets were defined by *p* < 0.05, fold–change > 1.6x and linear average expression in at least one group > 20. The array data have been submitted to the GEO database at NCBI (GSE98217).

2.19. Assignment of Zebrafish Array Probes to Homologous Mouse Genes

The genomic positions of all probe sets in the presented zebrafish microarray study were extracted from Affymetrix (<http://www.affymetrix.com/analysis/index.affx>; accessed on 24 November 2016) by applying a Batch Query on the GeneChip Array “Zebrafish Gene 1.xST” (genome version Zv9 from 2011). With the help of a custom–written Perl script and the extracted genomic positions of the probe sets, zebrafish gene identifiers were derived from the Ensembl database via the Application Programming Interface (API), version 64, and subsequently passed to the Ensembl Compara database in order to retrieve homologous mouse genes. The Compara database stores pre–calculated comparative genomics data of different species including information on homologous genes, protein family clustering, and whole genome alignments [51]. For the assignment of zebrafish to mouse genes, all kinds of homology (i.e., one–to–one, one–to–many and many–to–many orthologous genes) were taken into account. Gene Ontology enrichment analyses were

performed using the equivalent mouse symbols and DAVID Bioinformatics Resources 6.7 (p-value 0.05, fold change > 2) [52,53].

2.20. FACS Analysis

Animals from the Tg(olig2:DsRed) transgenic lines were sacrificed by an MS-222 overdose and the telencephalon was dissected from each animal. A single cell suspension was prepared according to previously published protocols [54,55] and cells were analyzed using a FACS Aria III (BD) in BD FACS Flow TM medium. Debris and aggregated cells were gated out by forward scatter–sideward scatter; single cells were gated in by FSC–W/FSC–A. Gating for fluorophores was performed using AB/EK animals. Cells were directly sorted into an extraction buffer from PicoPure RNA isolation kit (ThermoFisher) and stored at 80 C until RNA preparation was performed.

2.21. Preparation of Libraries for Deep Sequencing

cDNA was synthesized from 1 ng of total RNA using SMART-Seq v4 Ultra Low Input RNA kit for Sequencing (Clontech), according to the manufacturer's instructions. The quality and concentration of cDNA was assessed on an Agilent 2100 Bioanalyzer before proceeding to the library preparation using a MicroPlex Library Preparation kit v2 (Diagenode). All libraries (minimum of 3 biological replicates per condition) were processed together to minimize batch effects. Final libraries were evaluated and quantified using an Agilent 2100 Bioanalyzer and the concentration was measured additionally with a Quant-iT PicoGreen dsDNA Assay Kit (Thermo Fisher) before sequencing. The uniquely barcoded libraries were multiplexed onto one lane, and 150–bp paired–end deep sequencing was carried out on HiSeq 4000 (Illumina) that generated approximately 20 million reads per sample.

2.22. RNAseq Analysis

The RNA–seq analysis was completed using the kallisto pipeline for the reads mapping and quantification followed with the Sleuth pipeline for the statistical analysis. The cut–off for the differentially regulated genes was based on the expression fold change (> 2 fold) and p–value adjusted for the 10% false discovery rate (q–value < 0.05). FastQ files are deposited at (accession number pending). Gene Ontology enrichment analyses was performed using DAVID Bioinformatics Resources 6.8 (p–value 0.05, fold change > 2) [52,53].

2.23. Primary OPC Culture and Clonal Analysis

Primary cultures of the OPCs were performed as previously published [56]. Cortices of P0 mice were dissected avoiding the inclusion of white matter and grown for 10 days. After the initial culturing, cells were plated in 24–well plates at 727 cells/mm² density. OPC primary cultures were transduced with a GFP–encoding MLV–based virus for clonal analysis as previously described [57]. A total of 12 hrs after the transduction, the cells were treated with 1 M NBI 74330 and 8 M CU CPT 22 and analyzed 5 days later and the clonal analysis was performed as described previously [57].

2.24. Generation of gRNAs for CRISPR/Cas9–Mediated Deletion

Target sequences were chosen within 600 bp after the first ATG of the ORF of Cxcr3 (ENSMUSG00000050232) and Tlr2 (ENSMUSG00000027995). gRNAs were generated using Benchling (www.benchling.com, accessed on 24 September 2019) and chosen according to a high (> 30) specificity score. Multiplexed gRNA vectors were generated using the STAgR protocol [58]. Single gRNA expression units were amplified using overhang primers, employing the N20 targeting sequence as homology for Gibson assembly. gRNAs were assembled into a gRNA expression vector containing a TdTomato reporter, modified after pgRNA1 [59].

2.25. DNA Extraction and PCR

For the DNA extraction from the cells, the DNeasy blood and tissue kit was used (Qiagen, 69504). The region containing the prospective mutation was amplified using the standard PCR condition (denaturation: 20⁰⁰; annealing 20⁰⁰; extension 60⁰⁰; 30 PCR cycles) and locus-specific primer pairs from the positive and negative clones. Tlr2: 5⁰-ggacaaattcaggaagcgca and 5⁰-tgagagatcacggaccaagg; Cxcr3: 5⁰-cctcatagctcgaaaaacgccand 5⁰-ccccggagagaagagtcag. PCR products were cloned using a PCR cloning kit according to the manufacturer's instructions (Stratagene) and were analyzed for the mutation using SANGER sequencing.

2.26. Generation of the Oli-Neu Cell Line Deficient for Cxcr3 and Tlr2

Oli-Neu cells were cultured in a SATO medium containing 1% horse serum. For each transfection, 200,000 cells/well were seeded into 6-well plates and coated with poly-L-lysine (Sigma). A total of 1 μ g of each STAgR (encoding for gRNAs and TdTomato reporter) or control plasmid (encoding for dsRed) in addition to 1 μ g of Cas9 plasmid (with a puromycin resistance cassette) was transfected per sample using Lipofectamin 2000 (Invitrogen, Waltham, MA, USA) according to the manufacturer's instructions. Cells were plated in low density and selected with 0.8 μ g/mL puromycin for Cas9 expression. Five days later, clones transfected with STAgR (TdTomato reporter⁺, positive clones) or only Cas9 (TdTomato reporter⁻, negative clones) were selected and expanded. The proliferation analysis was performed using two independent clones with different deletions in both Tlr2 and Cxcr3 genes. To analyze the clones, 25,000 cells/well were plated in 24-well plates on poly-L-lysine-coated coverslips and analyzed after 48 h. Cells were fixed in 4% paraformaldehyde (PFA) in phosphate-buffered saline (PBS) for 15 min at room temperature and processed for the antibody staining.

2.27. Screen for Cxcr3 Ligands from the CSF

As the screen requires many cells, we decided to conduct it in the oligodendrocyte progenitor line (OliNeu) that also allows for the genetic inactivation of Cxcr3 and Tlr2 as described in Section 2.26. Both WT Oli-Neu and Cxcr3 and Tlr2 deficient clones were expanded onto a SATO medium containing 1% horse serum. After expansion, cells were re-plated on PLL-coated coverslips at an equal density (272 cells/mm²) and cultured for 2 h. After this pre-incubation, cells were treated with different CSF concentrations and vehicles. All cytokine treatments were performed using the WT Oli-Neu cells in quadruplets and at 3 different concentrations (Table S3) that were used as independent replicates for the analysis. Cells were fixed with 4% PFA 24 h after the treatment and assessed for proliferation using the anti-PH3 immunostaining.

2.28. Human Cytokine Antibody Array

Four cerebrospinal fluid samples, derived from healthy patients, were analyzed using a Human Cytokine Antibody Array (abcam, ab133997). All samples induced a scarring reaction upon injection into the nostril injury track. The positive controls were used to normalize signal responses across multiple arrays.

3. Results

3.1. Skull and Nostril Models of Zebrafish Telencephalon Injury Differ in the Kinetics of the Glial Reaction

To identify the molecular and cellular basis for OPC activation during wound healing, we set out to follow the reaction of different cell types to an injury in the zebrafish telencephalon using two paradigms in parallel, one with long-term, exacerbated OPC reactivity (referred to as skull injury, Figure 1A) and the other resulting in time-restricted gliosis and full tissue recovery (referred to as nostril injury, Figure 1B). Injuries were performed in both telencephalic hemispheres and the injury site was defined based on the DAPI accumulation throughout the manuscript (e.g., Figure S11, K). Damage-associated molecules trigger the

early inflammatory response that induces the recruitment of peripheral neutrophils into the injury site in the mammalian brain [60]. In zebrafish, we observed Lys^+ neutrophils 12h after both injuries in the brain parenchyma (Figure S1A,D). Interestingly, Lys^+ cells accumulated at the injury site after the nostril injury (Figure S1B), while they were dispersed throughout the injured parenchyma after the skull injury (Figure S1D). Moreover, Lys^+ neutrophil accumulation resolved 24h after nostril injury and we could not detect any difference 48h after injury (Figure S1C) compared to the intact brain. In contrast, we did not observe the fast clearance of Lys^+ cells after skull injury (Figure S1E).

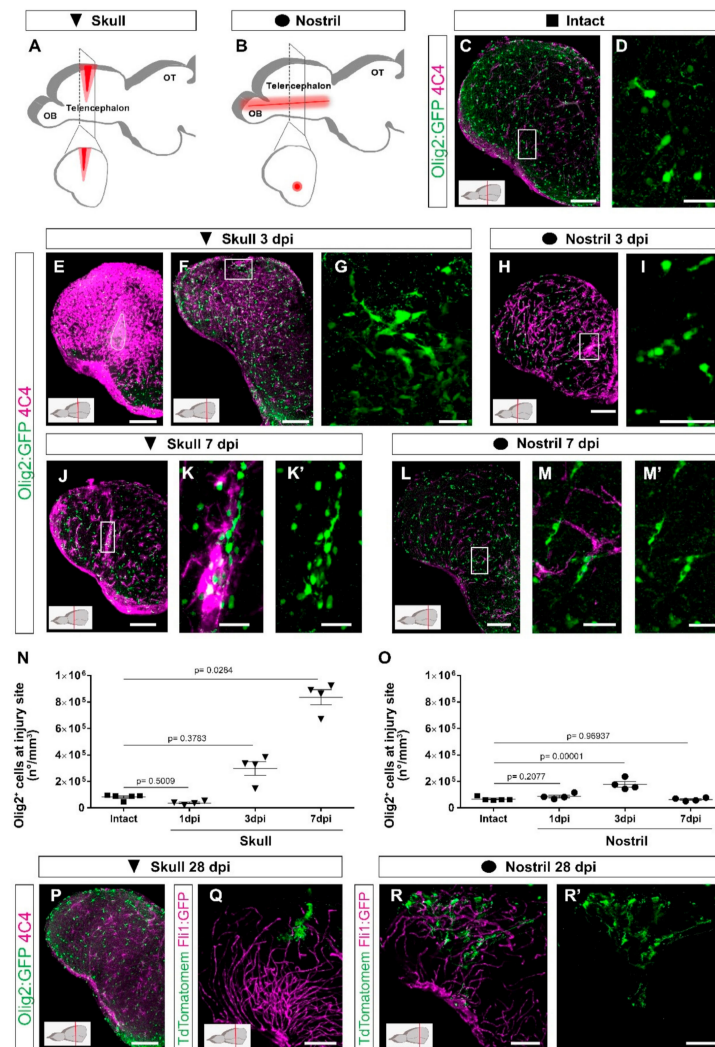


Figure 1. Distinct injury paradigms in the zebrafish telencephalon led to either scarless regeneration or prolonged glial reactivity. (A,B) Schemes depicting skull (A) and nostril (B) injury paradigms. Red triangle (A) and red line (B) illustrate the injury track. (C,D) Micrographs of a telencephalic section showing the distribution of Olig2:GFP⁺ oligodendroglia and 4C4⁺ microglia/monocytes in the intact brain. (E,F) Images of 3 dpi skull-injured sections (4C4⁺ and Olig2:GFP⁺ cells) at the level of the injury core delineated by a white line (E) and lateral to the injury core depicting the first signs of Olig2:GFP⁺ cells to accumulation indicated by the boxed area (F). (H) Image showing the distribution of Olig2:GFP⁺ and 4C4⁺ cells at 3 dpi after a nostril injury. (G,I) are magnifications of the boxed areas in (F) and (H), depicting Olig2:GFP⁺ cell distribution. (J–M) Images showing the reactivity of 4C4⁺

and Olig2:GFP⁺ cells at 7 days after skull (J) and nostril (L) injury. (K,K⁰,M,M⁰) are magnifications of the boxed area in the respective images. (N,O) Graphs depicting the density of Olig2:GFP⁺ cells at the injury site after skull (N) and nostril (O) injury. Data are shown as mean ± SEM; each data point represents one animal. Statistical analysis is based on a non-parametric Kruskal-Wallis Test (p-value = 0.0021) with a post-hoc Dunn test (Many-to-One) in (N) and a one-way ANOVA (p-value = 2.483 × 10⁻⁵) with a post-hoc Dunnett test (many-to-one) in (O). (P) The accumulation of 4C4⁺ and Olig2:GFP⁺ cells resolved at 28 days after skull injury. (Q-R⁰) Images showing the morphology of ependymoglia cells (labelled by electroporation of TdTomato) 28 days after skull (Q) and nostril injury (R,R⁰). While we observed the restoration of the radial morphology of the labelled ependymoglia that contacts the basement membrane after nostril injury (similar to the intact brain), the ependymoglia after skull injury failed to restore radial morphology and built extensive contacts with Fli1-positive blood vessels. All images are full z-projections of a confocal stack; insets indicate the rostro-caudal levels of the sections. Scale bars in (C,E,F,H,J,L,P,Q,R,R⁰) = 100 μm; Scale bars in (D,G,I,K,K⁰,M,M⁰) = 20 μm. Abbreviations: OB: olfactory bulb, OT: optic tectum, dpi: days post-injury; AFOG: acid fuchsin orange G. Symbol description: black triangle: skull injury; black circle: nostril injury.

As neutrophils regulate the activity state of microglia and extravasating monocytes and consequently the regenerative response [60], we analyzed both populations based on the expression of two different immunohistochemical markers (4C4 and L-plastin) as well as the transgenic line Tg(mpeg1:mCherry) [44] labelling both cell types (Figure S1F-H⁰⁰⁰). In the intact condition, the majority of microglia co-expressed all three markers although at the different levels (Figure S1F-F⁰⁰⁰). However, after both nostril and skull injury, we observed an increase in 4C4⁺ cells and only a proportion of them were colocalized with L-plastin and/or with mpeg1:mCherry⁺ cells (Figure S1G-H⁰⁰⁰). Taken together, these data suggest that 4C4 was the broadest marker to identify microglia/monocyte population and, therefore, we used it further in our study. While the initial activation pattern of 4C4⁺ cells was similar in both injury paradigms with the first signs of reactivity detectable already at 24 h after injury (Figure S1J,L), the skull injury induced a stronger reactivity and a long-lasting accumulation of 4C4⁺ cells at the injury site (Figure 1E-M⁰).

The accumulation of cells belonging to the oligodendrocyte lineage (OPCs and mature oligodendrocytes) were labeled using the transgenic line [Tg(Olig2:GFP)] [40] at the injury site was slightly delayed in comparison with the microglia/monocytes (Figure S1I,K). The density of Olig2:GFP⁺ cells was increased at the injury site 3 days after both skull (Figure 1F,G,N) and nostril injury (Figure 1H,I,O), although to different extents. The accumulation of Olig2:GFP⁺ cells was rapidly resolved and returned to pre-injury conditions within 7 days after the nostril injury (Figure 1L-M⁰,O), in agreement with previously published studies [33,37,38]. In contrast, the density of Olig2:GFP⁺ cells further increased and still persisted at 7 days post-injury (dpi) in the skull injury paradigm (Figure 1J-K⁰,N). We analyzed coronal brain sections depicting the skull injury in its full extent, but only part of the nostril injury. Therefore, the accumulation of both 4C4⁺ and Olig2:GFP⁺ cells observed exclusively after skull injury could be a consequence of a bias in the analysis. To exclude any technical bias, the number of Olig2:GFP⁺ cells accumulating at the nostril injury site was also analyzed in sagittal sections depicting the full extent of the nostril injury (Figure S2A-D). No differences were observed at any of the analyzed time points (Figure S2E). Moreover, injury sites were analyzed in BABB-cleared brains. While we could observe a clear accumulation of Sox10⁺ (classical marker for the oligodendrocyte lineage) and 4C4⁺ cells 3 days after nostril injury, 7 days after injury Sox10⁺ and 4C4⁺ cells showed distributions that were indistinguishable from samples of intact brains (Videos S1-S3).

In the zebrafish telencephalon the resident neural stem cell [48,61], the ependymoglia cells, express GFAP. So next, we used the Tg(gfap:GFP) transgenic line [42] to label and characterize the reactivity of ependymoglia cells after both types of injury. Gfap:GFP⁺ cell bodies line up at the ventricular wall of the brain surface with processes reaching

basement membrane (Figure S3A); therefore, after a nostril injury, only some processes of ependymoglia, located in the deep parenchyma, were wounded (Figure S3B,C). Importantly, no sign of damage was observed at 7 days after nostril injury (Figure S3F). On the other hand, upon skull injury, the ependymoglia cell layer was disrupted (Figure S3D,E), but was already restored 7 days after skull injury (Figure S3G). Despite this recovery, we still observed hypertrophic processes and a few misplaced Gfap:GFP⁺ cells at the injury site (Figure S3H).

The accumulation of Olig2:GFP⁺ and immune 4C4⁺ cells was resolved 28 days after the skull injury (Figure 1P), resembling the behavior of OPCs and microglia in the injured mammalian cerebral cortex [19,22]. However, even after the accumulation of Olig2:GFP⁺ and immune 4C4⁺ cells was resolved, the tissue architecture was not fully restored, based on the Gfap:GFP⁺ ependymoglia cell morphology (Figure 1Q–R⁰). To assess the ependymoglia morphology, we labelled them using the electroporation of the TdTomato membrane plasmid both after nostril and skull injury and analyzed their morphology and localization 28 dpi. In line with previous reports [37,47], the nostril injury did not change the morphology or the localization of ependymoglia cells compared to the intact brain. We found ependymoglia cell bodies lining up at the telencephalic ventricular wall with processes mostly spanning the brain parenchyma and anchoring at the basement membrane 28 dpi (Figure 1R,R⁰). However, after skull injury, several of the labelled ependymoglia cells had a bushy morphology and did not reach the basement membrane (Figure 1Q; Video S4).

These data demonstrate the differential reactions of neutrophils, microglia/monocytes, and oligodendrocyte lineage cells in two injury paradigms. The prolonged reaction of these cells correlates with the delay in the tissue restoration.

3.2. Activation of Innate Immunity Pathways Induces Prolonged Glia Reactivity after Injury in the Zebrafish Telencephalon

In view of the above findings, comparing the transcriptome induced by nostril and skull injury offers a unique opportunity to disentangle the specific molecular programs inducing exacerbated gliosis from the beneficial pathways promoting wound healing. We reasoned that some signaling pathways that were activated after a skull injury, but not after a nostril injury, could account for the long-lasting glial accumulation at the injury site and the absence of full tissue restoration. Therefore, we analyzed the gene expression during regeneration (1, 2, 3, and 7 dpi) after a nostril or skull brain injury in the whole telencephalon, using the Affymetrix Zebrafish Gene ST 1.0 array (Figure 2A). Both types of injuries initially induced comparable transcriptome changes, as reflected by a similar number of significantly regulated genes (fold change > 1.6, $p < 0.05$) and a large overlap in significantly overrepresented Gene Ontology (GO) terms (based on DAVID analysis, fold enrichment ≥ 2 ; $p < 0.01$) at 1 and 2 dpi (Figure 2B, Table S4). However, we observed a striking difference in the number of regulated GO terms after nostril and skull injury at 3 dpi (Figure 2B), with 1012 transcripts regulated after a skull but not nostril injury (Figure 2C). Interestingly, this large number of uniquely regulated genes at 3 dpi correlates with differences in the reaction of Olig2:GFP⁺ cells and microglia/monocytes between the two injury paradigms (Figure 1N,O), supporting the idea that understanding these transcriptional differences could identify specific programs inducing long-lasting OPC accumulation and neuroinflammation. To further validate the applicability of this approach, we analyzed the differential expression of genes possibly involved in the ECM modifications, as the specific ECM changes could be associated with exacerbated glial activation [16]. Towards this end, we selected genes related to the GO terms “Extracellular matrix” (GO_0031012) and “Extracellular region” (GO_0005576) and analyzed their expression at 3 days post skull and nostril injury. Among all the regulated ECM-related transcripts (131), 69 of them were exclusively regulated after the skull injury (Figure 2D). These transcripts were overrepresented in GO terms related to the immune response, regulation of immune system process, and proteolysis (Figure 2E, Table S5), processes implicated in the exacerbated glial reaction after wound closure. Moreover, some of these genes encoded for factors reported to regulate

using a Venn diagram illustrating the number of genes exclusively regulated 3 days after skull injury (Skull vs. Intact) and not after nostril 3dpi (Nostril vs. Intact). (D) Venn diagram depicting the overlap between ECM-related genes regulated at 3 days after skull and nostril injury. Regulated genes were defined by a p-value < 0.05, fold-change > 1.6, and a linear average expression > 20. (E) Significantly enriched Gene Ontology (GO) terms of biological processes (color indicates p-values and symbol size number of identified genes within the term) in an ECM-related gene set regulated exclusively 3 days after skull injury (69 genes in panel (D)). (F) Chord diagram depicting selection of regulated ECM-related genes and associated GO terms biological processes. (G) Venn diagram depicting the overlap between genes exclusively regulated at 3 days after skull injury and genes regulated after the nostril injury at any time point. Note that 80% of the genes were exclusively regulated after skull injury at 3 dpi but were never regulated after nostril injury. (H) Plot showing significantly enriched (p-values indicated on bars) GO terms related to biological processes in a gene set regulated exclusively 3 days after skull injury (Skull 3 dpi vs. Nostril at any time point), correlating with glial accumulation. (I) Histogram depicting the regulation of genes related to Cxcr3 and Tlr signatures after nostril and skull injury. The dotted, gray line shows the 1.6-fold change cut off. (J) Scheme of the experimental design analyzing the ability of the Tlr2 agonist to induce glia accumulation after nostril injury. (K,L) Images of 5-day-injured telencephalic sections in the Tg(Olig2:GFP) line after nostril injury and aCSF (K) or zymosan A injections (L). (M,M⁰) Magnifications of the boxed area in L depict the exacerbated accumulation of Olig2:GFP⁺ (M) and 4C4⁺ (M⁰) cells at the injury site. (N) Scheme representing the experimental design to analyze the capacity of the Cxcr3 agonist (VUF 11222) to induce a reactive gliosis. (O) Micrograph illustrating the reactivity of Olig2:DsRed⁺ and 4C4⁺ cells after Cxcr3 activation. (P) Magnification of the injured area in (O). (Q) Graph showing the density of Olig2:GFP⁺ cells in the injured area 5 days after nostril injury with aCSF, Cxcr3 or Tlr2 agonist treatments. Data are shown as mean ± SEM; each data point represents one animal. p-values are based on a one-way ANOVA (p-value = 1.183 × 10⁻⁵) with a post-hoc Dunnett test (Many-to-One). All images are full z-projections of a confocal stack. Insets indicate the rostro-caudal levels of the sections. Scale bars in (K,L,O) = 100 μm; scale bars in (M,M⁰,P) = 20 μm; Abbreviations: dpi: days post-injury, N3d: nostril 3 dpi, S3d: skull 3 dpi; Ctrl: control; aCSF: artificial cerebrospinal fluid. Symbol description: orange square: ventricular injection of aCSF; orange circle: ventricular injection of zymosan A, Tlr2 agonist; green circle: VUF 11222, Cxcr3 agonist; black circle: nostril injury.

In particular, we observed the upregulation of genes indicative of the activation of the Toll-like receptor, Tlr, (mxc, mxe, irf7, irf2) [72–74] and chemokine family 11 (cxcl11.1, cxcl11.5, cxcl11.6 like, and cxcl13) [75] mediated innate immune response, at 3 days after skull injury (Figure 2I). Innate immunity orchestrates the initial events of wound healing after skin [76], heart [77], and CNS [9] injury, and its regulation determines the extent of tissue restoration [78]. Therefore, we set out to address whether the activation of either Tlr- or Cxcl11 family-mediated innate immunity leads to the induction of exacerbated glial reactivity in the zebrafish telencephalon. We first activated the Tlr-mediated innate immune response by injecting zymosan A microparticles [2] 3 days after nostril injury (Figure 2J) to mimic the temporal activation of this pathway observed after skull injury. Zymosan A was injected in the telencephalic ventricle and the glial reactivity was analyzed at 5 dpi, when the Olig2:GFP⁺ cell accumulation was already resolved after nostril and detected only after skull injury (Figure 2J,K,Q). Indeed, the vehicle (artificial cerebrospinal fluid, aCSF) treatment did not alter the reaction of Olig2:GFP⁺ cells and no accumulation was detected at 5 dpi (compare nostril 3 dpi Figure 1O with Figure 2Q for vehicle). In contrast, zymosan A treatment not only prolonged the accumulation of both 4C4⁺ and Olig2:GFP⁺ cells at the injury site (Figure 2K–M⁰,Q), but it also increased 7-fold the number of Olig2:GFP⁺ cells accumulating at the injury site 5 dpi compared with the vehicle treatment (Figure 2Q). Thus, zymosan A treatment turned the initial short-term glial activation into a prolonged and exacerbated accumulation of glial cells at the injury site after nostril injury. The toll-like receptor 2 (Tlr2) mediates the sterile inflammation induced by zymosan A in other systems [72,79], and Tlr2 was expressed in the intact as well as the injured zebrafish telencephalon (Figure S4A). Therefore, we tested whether interfering

with Tlr1/2 pathway activation using a Tlr1/2-specific competitive inhibitor (CU CPT22) would abolish the capacity of zymosan A to induce an exacerbated glial reaction after nostril injury (Figure S4B). Indeed, interference with the activation of the Tlr1/2 pathways prevented the accumulation of Olig2:GFP⁺ cells at the injury site after zymosan A injection (Figure S4C–G), suggesting that activation of Tlr1/2 is sufficient to induce a prolonged accumulation of Olig2:GFP⁺ cells and 4C4⁺ cells at the injury site.

Similar to Tlr2-induced innate immunity, we set out to test whether the Cxcl11 family has a role in prolonged glial activation, in line with the induction of these ligands exclusively after skull injury. As up-regulated Cxcl11-family ligands (Figure 2I) signal through the same chemokine receptor, Cxcr3 [80], we analyzed the ability of a specific Cxcr3 agonist (VUF 11222 [81]) to induce glial accumulation in the nostril injury paradigm (Figure 2N). Similar to the reactivity observed upon Tlr2 pathway activation (Figure 2K–M⁰, Q), treatment with the Cxcr3 agonist was sufficient to trigger exacerbated 4C4⁺ and Olig2:GFP⁺ cell accumulation at the injury site at 5 dpi (Figure 2O–Q).

Taken together, our data suggest that the activation of either Tlr2 or Cxcr3 is sufficient to induce an exacerbated glial reaction after nostril injury.

3.3. Tlr1/2 and Cxcr3 Pathways Cooperatively Control Reactive Gliosis after Injury in the Zebrafish Telencephalon

Because the activation of either Tlr2 or Cxcr3 signaling induced exacerbated glial reactivity in the nostril injury and the transcriptome analysis demonstrated the activation of both pathways exclusively after skull injury, we asked whether interference with these pathways would block the exacerbated gliosis after skull injury. We inhibited the activation of the two signaling pathways by using specific inhibitors: CU CPT22 for the Tlr1/2 [67] pathway and NBI-74330 for the Cxcr3 [68] pathway (Figure 3A). Strikingly, interference with the Tlr1/2 pathway did not change the accumulation of Olig2:GFP⁺ cells after skull injury (Figure 3A–C, F), despite a significant reduction in the area covered by 4C4⁺ immune cells (Figure S5A–C, F). Likewise, the inhibition of the Cxcr3 pathway did not affect the accumulation of either 4C4⁺ or Olig2:GFP⁺ cells (Figure 3D, F and S5D, F). These data suggest that the two signaling pathways might be functionally redundant in controlling the accumulation of Olig2:GFP⁺ cells. To assess their redundancy, we simultaneously inhibited the Tlr1/2 and Cxcr3 pathways with respective inhibitors after skull injury (Figure 3A). Indeed, we observed a significant decrease in the number of Olig2:GFP⁺ cells accumulating at the injury site by 4 dpi in inhibitor-treated animals compared to vehicle (Figure 3E, F). Moreover, Sox10⁺ cells, representing oligodendrocyte lineage cells [69], showed a similar reduction, supporting the idea that the effect of inhibitors on the oligodendrocyte lineage was mainly in regulating their accumulation at the injury site, rather than affecting Olig2-driven expression of GFP (Figure 3B–E). In addition, the area covered by 4C4⁺ microglia/monocytes was also significantly reduced after double-inhibitor treatment (Figure S5E, F). A reduction in the accumulation of Olig2:GFP⁺ cells at the injury site was also observed after Tlr1/2 inhibitor treatment (CU CPT22) combined with a different Cxcr3 inhibitor (AMG-48744) (Figure S5G–J). Thus, the possibility of this phenotype being induced by the off-target effects of our pharmacological treatment is rather low. These effects of the inhibitor cocktail on alleviating Olig2:GFP⁺ glia and microglia/monocytes accumulation persisted also at later time points as no sign of Olig2:GFP⁺ cell accumulation was detectable following the double-inhibitor treatment 7 dpi in the skull injury paradigm (Figure 3G–J).

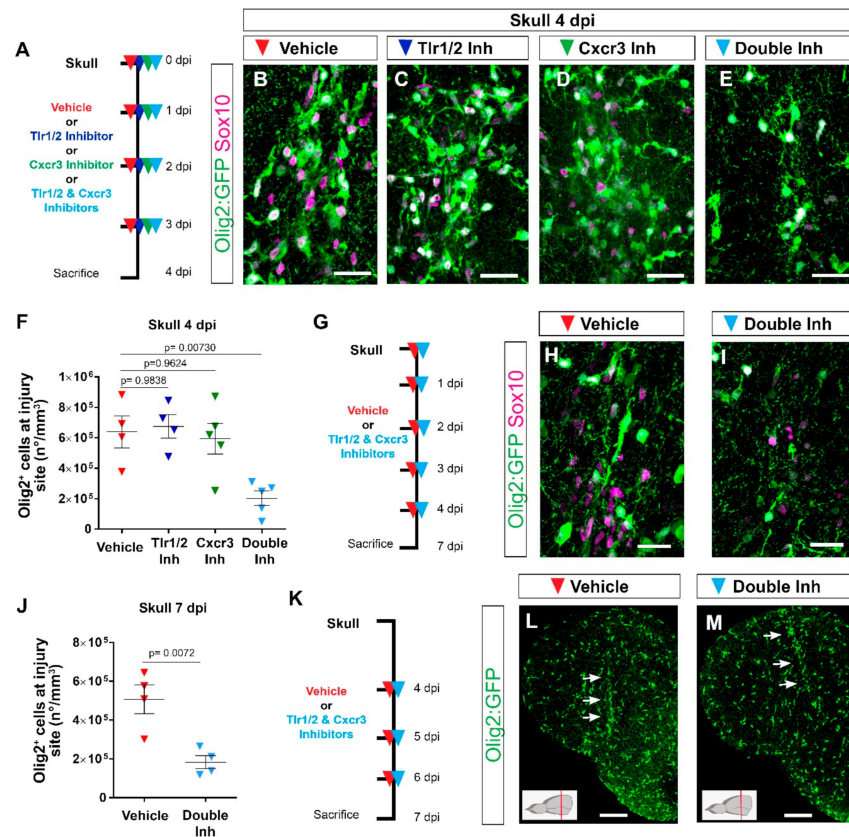


Figure 3. Tlr1/2 and Cxcr3 pathways redundantly control the accumulation of Olig2:GFP⁺ cells but not their maintenance at the injury site in the zebrafish telencephalon. (A) Scheme of the experimental setup to address the role of Cxcr3 and Tlr1/2 in the reactive gliosis 4 days after injury. (B–E) Micrographs of telencephalic sections obtained after 4 dpi depicting Olig2:GFP⁺ and Sox10⁺ oligodendroglia reactivity with vehicle (B), Tlr1/2 inhibitor (C), Cxcr3 inhibitor (D), and double-inhibitor (E) treatments. (F) Graph showing the density of Olig2:GFP⁺ cells located at the injury site after vehicle, Tlr1/2 inhibitor (CU CPT22), Cxcr3 inhibitor (NBI 74330) and double-inhibitor combination (NBI 74330+CU CPT22) treatment. Note that only the double-inhibitor cocktail reduces the number of Olig2:GFP⁺ cells accumulating at the injury site. Data shown as mean ± SEM; each data point represents one animal. *p*-values are based on a one-way ANOVA (*p*-value = 4.074×10^{-3}) with a post-hoc Dunnett test (Many-to-One). (G) Experimental outline to assess the effect of vehicle and double-inhibitor treatment 7 dpi. (H,I) Micrographs of telencephalic sections 7 days after skull injury depicting Olig2:GFP⁺ and Sox10⁺ oligodendroglia after vehicle (H) and inhibitor cocktail (NBI 74330 and CU CPT22) (I) treatment. (J) Graph illustrating the density of Olig2:GFP⁺ cells located within the injured volume after vehicle and double-inhibitor treatment. An equal volume was quantified in both conditions (*p*-values based on Student's *t*-test with equal variances). (K) Scheme depicting the experimental design to assess the capacity of the vehicle and double inhibitors treatment to resolve glial accumulation. (L,M) Micrographs showing telencephalic sections 7 days after skull injury and vehicle (L) or double-inhibitor (M) treatment. White arrows indicate the injury site. Note that both vehicle and inhibitor treatments failed to resolve Olig2:GFP⁺ accumulation. All images are full *z*-projections of confocal stack. The level of the cross-section is indicated in the inset. Scale bars in (L,M) = 100 μm; scale bars in (B–E,H,I) = 20 μm. Abbreviations: dpi: days post-injury, Inh: inhibitor. Symbol description: red triangle: vehicle; dark blue triangle: Tlr1/2 inhibitor, CU CPT22; green triangle: Cxcr3 inhibitor, NBI 74330; light blue triangle: double inhibitors, NBI 74330 and CU CPT22.

The reduction in the number of reactive glial cells accumulating at the injury site after double-inhibitor treatment suggests a role of these pathways in the initial induction of the glial cell reaction, their maintenance at the injury site, or both. To further disentangle the role of Tlr1/2 and Cxcr3 signaling in the maintenance of Olig2:GFP+ cells at the injury site, we pharmacologically blocked both pathways after the initial accumulation of Olig2:GFP+ cells at 4 dpi (Figure 3K). Once the glial cells had accumulated at the injury site (4 dpi), interference with the activation of both pathways failed to resolve the accumulation of Olig2:GFP+ cells 7 dpi (Figure 3L,M), in strong contrast to the improvement observed in the early inhibition protocol (Figure 3G,J). Taken together, these data support the role of Tlr1/2 and Cxcr3 signaling during the initial phase of glial accumulation.

Because immunohistochemical analysis showed a similar initial accumulation of glial cells at the injury site at 3 days following nostril and skull injury (Figure 1N,O), we asked whether interference with Tlr1/2 and Cxcr3 signaling could alter the accumulation of Olig2:GFP+ cells in the nostril injury paradigm. To address this question, we treated nostril-injured animals with Tlr1/2 and Cxcr3 inhibitors and assessed the accumulation of Olig2:GFP+ cells at the injury site (Figure S5K). We observed a similar initial recruitment of Olig2:GFP+ at the injury site in untreated and vehicle-treated animals (Figure S5N). Importantly, double-inhibitor treatment did not interfere with this initial accumulation of Olig2:GFP+ cells (Figure S5L–N), in agreement with the absence of the transcriptional signature indicative of innate immunity activation after the nostril injury.

In conclusion, our data support the hypothesis that the restricted glial response correlating with complete tissue restoration and the long-lasting, reactive gliosis rely largely on different molecular mechanisms. The simultaneous activation of Tlr1/2 and Cxcr3 during the wound healing period is sufficient and necessary to induce a prolonged accumulation of both microglia/monocytes and Olig2:GFP+ cells at the injury site, leading to a long-lasting, exacerbated glial reaction.

3.4. Reduction in Glial Accumulation Correlates with Better Tissue Recovery

The reduction in the exacerbated accumulation of Olig2:GFP+ and microglia/monocytes after double-inhibitor treatment following skull injury prompted us to investigate the effect of prolonged injury-induced gliosis on brain regeneration by measuring the volume of the injured tissue (Figure 4A,B). We observed a significant reduction in the size of the injured tissue 7 dpi after double-inhibitor treatment compared with vehicle treatment (Figure 4B and Video S5). This reduction in the injured volume was not observed in animals treated only with the Tlr1/2 pathway inhibitor (CU CPT22, Figure 4B) that maintains the Olig2:GFP+ cell accumulation but reduces microglial reactivity at 4 dpi (Figure S5C,F). This finding supports the hypothesis that the decrease in the number of reactive Olig2:GFP+ cells at the injury site leads to improved tissue restoration.

We next tested whether the improved tissue recovery induced by the double-inhibitor treatment was accompanied by an addition of new, adult-generated HuC/D+ neurons to the injured brain parenchyma (restorative neurogenesis). As ependymal cells lining the ventricle surface increase their proliferation and generate new neurons in response to an injury [2,33,37], we used BrdU-based birth dating to determine whether the decreased glial reactivity after double-inhibitor treatment also correlated with improved restorative neurogenesis. To assess injury-induced neurogenesis, BrdU was added to the fish water during the first 3 days after injury to label all cells synthesizing DNA; that is, mostly dividing progenitors. The BrdU-incorporation phase was followed by a 4-day chase period, allowing progenitor differentiation, and correlating with the resolution of the glial accumulation upon inhibitor treatment (Figure 4C). We previously showed that the majority of newly generated neurons in the intact brain (BrdU+ and HuC/D+) reside in the ventricular zone (hemisphere periphery, Figure 4G) and display very low migratory potential [47]. Therefore, we analyzed the proportion of HuC/D+ and BrdU+ cells residing outside this neurogenic zone, as we observed the migration of new neurons towards this area only after injury [47]. Both control and inhibitor-treated animals generated

similar total numbers of new neurons (HuC/D⁺ and BrdU⁺) after injury (Figure 4D–F). However, we observed a significantly increased proportion of new neurons located in the brain parenchyma after double-inhibitor treatment (HuC/D⁺ and BrdU⁺ located in the parenchyma in respect to all HuC/D⁺ and BrdU⁺ cells) (Figure 4G,H). As we did not observe any difference in the total number of generated neurons between control and double-inhibitor treated animals, our data exclude an effect of inhibitor treatment on injury-mediated stem cell activation, but rather support the interpretation that the resolution of a long-lasting, exacerbated glial reaction contributed to the better recruitment, survival, or integration of newly generated neurons into the injured brain parenchyma.

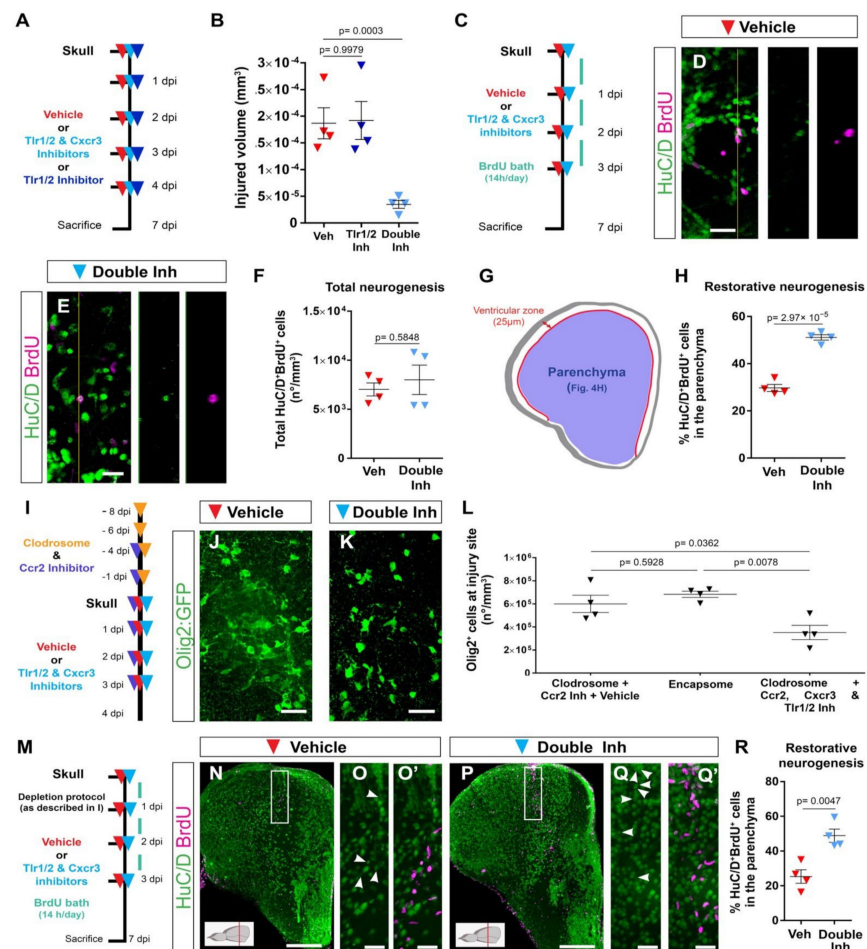


Figure 4. Activation of Tlr1/2 and Cxcr3 creates a detrimental environment by inducing oligodendroglia accumulation in a microglia/monocyte-independent manner. (A) Scheme of the experimental design to analyze the consequences of double-inhibitor treatment (NBI 74330 and CU CPT22). (B) Graph illustrating the size of the injured volume 7 days after skull injury and vehicle, Tlr1/2 inhibitor (CU CPT22), or double Tlr1/2 and Cxcr3 inhibitor (NBI 74330 and CU CPT22) treatment. p -values are based on a one-way ANOVA (p -value = 1.971×10^{-4}) with a post-hoc Dunnett test (Many-to-One). (C) Experimental scheme designed to study restorative neurogenesis upon different treatments. (D,E) Images depicting HuC/D⁺ and BrdU⁺ cells located in the parenchyma following vehicle (D) and double-inhibitor (E) treatment. (F) Dot-plot showing the total density (whole telencephalon) of HuC/D⁺ and BrdU⁺ after vehicle and Tlr1/2 and Cxcr3 inhibitor treatment. p -value is based on Welch's t -test with unequal variances. (G) Diagram illustrating the ventricular zone

(25 μ m from the ventricle surface) and the parenchyma (blue area) in the telencephalic region. Restorative neurogenesis was measured by the proportion of newly generated neurons (HuC/D⁺ and BrdU⁺) that migrated towards the parenchyma with respect to the total number (ventricular zone and parenchyma) of new neurons. (H) Graph depicting the proportion of HuC/D⁺ and BrdU⁺ cells located in the telencephalic parenchyma after vehicle and Tlr1/2 and Cxcr3 inhibitor treatment. p-value is based on Student's t-test with equal variances. (I) Design of the experimental workflow to analyze the effect of Tlr1/2 and Cxcr3 inhibitors on accumulation of Olig2:GFP⁺ cells after microglia/monocytes depletion. (J,K) Micrographs depicting the reactivity of Olig2:GFP⁺ cells after skull injury at 4 dpi with microglia/monocyte depletion and vehicle (J) or Tlr1/2 and Cxcr3 inhibitor treatments (K). (L) Graph illustrating the density of Olig2:GFP⁺ cells at the injury site at 4 dpi following Clodrosome + Ccr2 (MK-0812) inhibitor treatment (microglia/monocyte depletion protocol), Encapsome (empty liposomes, control for Clodrosome; ventricular injection) and Clodrosome + Ccr2 + Tlr1/2 (CU CPT22) + Cxcr3 (NBI 74330) inhibitor treatments. The decrease in Olig2:GFP⁺ cell accumulation after Tlr1/2 and Cxcr3 inhibitor treatment was maintained in microglia/monocyte-depleted brain. p-values are based on a one-way ANOVA (p-value = 7.957×10^{-3}) with a post-hoc Tukey Test (All Pairs). (M) Design of the experimental protocol used to analyze injury-induced neurogenesis (BrdU-based birth dating) in microglia/monocyte-depleted brains treated with vehicle or Tlr1/2 and Cxcr3 inhibitor cocktail. (N,P) Micrographs of injured telencephala at 7 dpi showing the generation of new neurons (HuC/D⁺/BrdU⁺) after vehicle (N) and Tlr1/2 and Cxcr3 inhibitor (P) treatment in microglia/monocyte-depleted brains. (O,O⁰,Q,Q⁰) are magnifications of the areas boxed in (N,P), respectively. White arrowheads depict double HuC/D⁺ and BrdU⁺ cells. The level of the cross-section is indicated in the inset. (R) Graph depicting the proportion of HuC/D⁺ and BrdU⁺ cells located in the telencephalic parenchyma after vehicle and Tlr1/2 and Cxcr3 inhibitor treatment. p-value is based on Student's t-test with equal variances. All images are full z-projections of a confocal stack. Data are shown as mean \pm SEM; each data point represents one animal. Scale bars in (N,P) = 100 μ m; scale bars in (D,E,J,K,O,O⁰,Q,Q⁰) = 20 μ m. Abbreviations: dpi: days post-injury; Veh: vehicle; Inh: inhibitors. Symbol description: red triangle: vehicle; dark blue triangle: Tlr1/2 inhibitor, CU CPT22; light blue triangle: double inhibitors, NBI 74330 and CU CPT22; orange triangle: ventricular Clodrosome injection; purple triangle: intraperitoneal Ccr2 inhibitor injection, MK-0812.

3.5. Microglia/Monocytes Depletion Does Not Alter the Innate Immunity-Regulated Accumulation of Olig2:GFP⁺ Cells at the Injury Site

The simultaneous inhibition of Tlr1/2 and Cxcr3 improved tissue regeneration. However, decreasing only 4C4⁺ cell reactivity with the Tlr1/2 inhibitor without changing Olig2:GFP⁺ cell accumulation showed no beneficial effect on infarct tissue volume (Figure 4B). These data suggest that microglia/monocytes might be unnecessary for the glial response regulated by the Tlr1/2 and Cxcr3 signaling pathways. To directly assess this hypothesis, we analyzed the accumulation of Olig2:GFP⁺ cells at the injury site in brains depleted of microglia/monocytes. A combination of Clodrosome and a Ccr2 inhibitor prior to skull injury depleted 95% of 4C4⁺ cells (microglia and infiltrating monocytes, Figure S6C–F). The 4C4-free condition was then maintained by continuously blocking monocyte extravasation through Ccr2 inhibitor (Figure S6G–I) during the restricted time window when the Tlr1/2 and Cxcr3 pathways induced the long lasting reaction of Olig2:GFP⁺ cells (Figures 2I and 3A–F, K–M). Initial microglia/monocyte depletion did not alter Olig2:GFP⁺ cell accumulation at 4 days after skull injury compared with the control Encapsome treatment (Figures 4I, J, L and S6J, K). Importantly, the inhibition of Tlr1/2 and Cxcr3 successfully blocked the prolonged, exacerbated accumulation of Olig2:GFP⁺ cells in microglia/monocyte-depleted brains (Figure 4K, L) to the same extent these inhibitors prevent the accumulation of Olig2:GFP⁺ cells in brains populated with microglia/monocytes (compare double inhibitor in Figures 3F and 4L). Consistent with this, our expression analysis of FACS-purified Olig2:DsRed⁺ cells (labeling the same oligodendroglia population as Olig2:GFP⁺) showed that they express Cxcr3 (Cxcr3.2 and Cxcr3.3) and Tlr2 (Tlr18) isoforms in both intact and injured brains (Figure S6L). Moreover, the RNAscope analysis

revealed the expression of genes involved in both innate immune pathways (Cxcr3.2, Tlr8b, MYD88 and Mxc) in the Olig2:GFP⁺ population after skull injury (Figure S6M–R). These data support the concept that the activation of microglia and/or invading monocytes is not necessary for Tlr1/2 and Cxcr3 injury-induced oligodendroglial reactivity and their initial accumulation at the injury site in zebrafish.

We next tested the effect of microglia/monocytes depletion on the restorative neurogenesis. To this end, we combined the depletion protocol with the BrdU-based neuronal birth dating used previously (Figure 4M). The initial depletion of injury-activated microglia/monocytes did not alter incorporation of new neurons (Figure 4N–O⁰) compared with untreated control animals (compare Veh in Figure 4H,R), supporting the hypothesis that the activated microglia/monocytes are not the only populations contributing to the adverse environment, restricting new neuron recruitment. Importantly, the inhibition of the Tlr1/2 and Cxcr3 pathways in microglia/monocyte-depleted brains still improved the addition of new neurons (Figure 4M–R), similar to the beneficial effects observed in animals with an intact immune system and further associating the beneficial effects of the double-inhibitor treatment with the resolution of prolonged Olig2:GFP⁺ cell accumulation.

Taken together, our results support the hypothesis that the Tlr1/2 and Cxcr3 pathways promote the accumulation of Olig2:GFP⁺ cells at the injury site and the injury-induced impairment of neuronal recruitment to the injury.

3.6. Olig2:dsRed⁺ Cells Activate Both Innate Immunity Pathways and Transcription Programs Involved in Cell Proliferation in Response to an Injury

In order to understand the regulatory mechanisms of accumulation of Olig2:GFP⁺ cells downstream of innate immunity pathways after skull injury, we analyzed the injury-induced transcriptomic changes in Olig2:dsRed⁺ cells (enriched for OPCs [82]) acutely isolated from the injured zebrafish telencephalon 3 days after either vehicle or inhibitor treatment. We observed 1649 significantly regulated transcripts in dsRed⁺ cells after injury in vehicle-treated brains compared with intact brains (Figure S7A). Interestingly, a minority of transcripts were downregulated (114), suggesting that upon injury OPCs still maintain their oligodendrocyte lineage identity and gain additional features, leading to their reactivity. The distribution of upregulated genes in the biological pathways (Panther-based analysis) revealed the activation of FGF-, EGF-, PDGF-signaling pathways (Figure S6B), which have previously been implicated in the proliferation of OPCs [83–86]. In line with those activated pathways, GO term analysis revealed an enrichment of the processes involved in reactive gliosis, such as cell migration and response to cytokines and chemokines (Figure S7C). Surprisingly, most of the enriched GO terms were related to inflammation (63% of all enriched terms, Figure S7C), including the activation of innate immunity. Importantly, the genes belonging to both cytokine and toll-like receptor signaling were upregulated in response to injury (Figure S7B,C; Table S7). Moreover, 45% of ECM-related genes specifically regulated at 3 days after skull injury in the entire telencephalon were also regulated in the Olig2:dsRed⁺ cell population (Figure S7D). This unbiased transcriptome analysis further corroborated our hypothesis that cells of the oligodendrocyte lineage activate molecular pathways of the innate immune response, including Tlr2 and Cxcr3, which allows their microglia/monocyte-independent reaction and accumulation at the injury site.

The transcriptomic changes after skull injury, supporting the activation of innate immunity pathways directly in Olig2⁺ cells, prompted us to further analyze the effect of the inhibitor cocktail on gene expression in Olig2⁺ cells isolated from injured brains. Interestingly, the inhibitor treatment did not change the overall transcriptome of Olig2⁺ cells. Approximately 80% of regulated transcripts after inhibitor treatment were also regulated in vehicle-treated brains (Figures 5A and S7A,E). This suggests that the inhibitor cocktail treatment did not change the overall transcriptome of Olig2:dsRed⁺ cells, but rather restricted regulatory pathways involved in their long-term reactivity. Importantly, both cytokine receptor signaling and toll-like receptor signaling were no longer regulated in Olig2:dsRed⁺ cells after inhibitor treatment (Figure 5A,B; Table S8). However, the

regulation of number of biological processes linked to the immune response was still present (Table S9). A comparison of injury-regulated genes in Olig2⁺ cells isolated from vehicle- and inhibitor cocktail-treated brains identified a set of 510 genes (597 transcripts) exclusively regulated after brain injury and vehicle treatment (Figure 5A) and, therefore, were likely involved in reactive gliosis downstream of the Tlr1/2 and Cxcr3 pathways. These genes were overrepresented in GO terms related to proliferation and cell migration (Figure 5B, Table S9), both being biological processes at the core of the oligodendroglial reaction to injury and prolonged gliosis in mammals [87,88].

3.7. Regulation of Oligodendrocyte Progenitor Cell Proliferation by Tlr1/2 and Cxcr3 Signaling

Transcriptome data support the role of Tlr1/2 and Cxcr3 signaling pathways in the direct regulation of OPC proliferation leading to persistent accumulation at the injury site. Therefore, we first assessed the proliferation of Olig2:GFP⁺ cells after skull injury in the zebrafish telencephalon. Accordingly, we labeled all cells undergoing S-phase by BrdU within 5 days after the injury to find out if the proliferation contributes to the observed accumulation of oligodendroglia at the injury site (Figure 5C). As expected, we observed an accumulation of Olig2:GFP⁺ cells at the injury site, indicating that the BrdU treatment did not alter the behavior of Olig2:GFP⁺ cells. Importantly, we observed that 45% of all Olig2:GFP⁺ cells at the injury site were BrdU⁺ and hence went through at least one cell cycle during 5 days of labelling (Figure 5D–F), supporting the concept that the Olig2:GFP⁺ accumulation at the skull injury site was, at least in part, achieved by the increased proliferation of progenitor cells labelled by Olig2:GFP transgenic line (OPCs). We next analyzed if these accumulated OPCs further differentiated into mature oligodendrocytes. We made use of the transgenic line Tg(Mbp:nls-GFP) [77] and a BrdU-based birth dating protocol to identify the proportion of the injury-activated OPCs that matured into oligodendrocytes 7 days after the skull injury (Figure S7F). We observed neither a significant increase in the total number of oligodendrocytes nor an increase in the proportion of newly matured, BrdU⁺ oligodendrocytes upon skull injury (Figure S7G–K), supporting the concept that OPCs and not mature oligodendrocytes accumulate at the injury site [25].

Next, we analyzed whether the inhibitor cocktail treatment may alter the proliferation of Olig2:GFP⁺ cells as the cellular basis for reduction in their accumulation at the injury site. As Olig2:GFP⁺ cells display the first signs of exacerbated reactivity 3 days after skull injury, yet without the significant change in total number of Olig2:GFP⁺ cells, we analyzed the proliferation of Olig2:GFP⁺ cells 3 dpi after vehicle and inhibitor treatment (Figure 5G). This experiment revealed a significant reduction in the total number of BrdU⁺ Olig2:GFP⁺ cells after inhibitor cocktail treatment compared with the vehicle treatment (Figure 5H–L). To confirm the activation of Tlr1/2 and Cxcr3 pathways directly in OPCs, we made use of a murine OPC culture system. Moloney murine leukemia virus (MLV)-based clonal analysis was performed in pure primary OPC cultures isolated from P0 mouse cerebral cortex after vehicle or double-inhibitor treatment (Figure 5M). OPCs were permanently labeled with GFP expressing retrovirus and the size of clones produced by transduced progenitors within 5 days was measured (Figure 5N–P). Double-inhibitor treatment reduced the GFP⁺ clone size produced by OPCs, supporting a direct role of Tlr1/2 and Cxcr3 pathways in OPC proliferation (Figure 5P).

Taken together, our data indicate a direct role of Tlr1/2 and Cxcr3 pathways in regulating Olig2⁺ OPC proliferation to achieve long-lasting accumulation at the injury site in the zebrafish telencephalon.

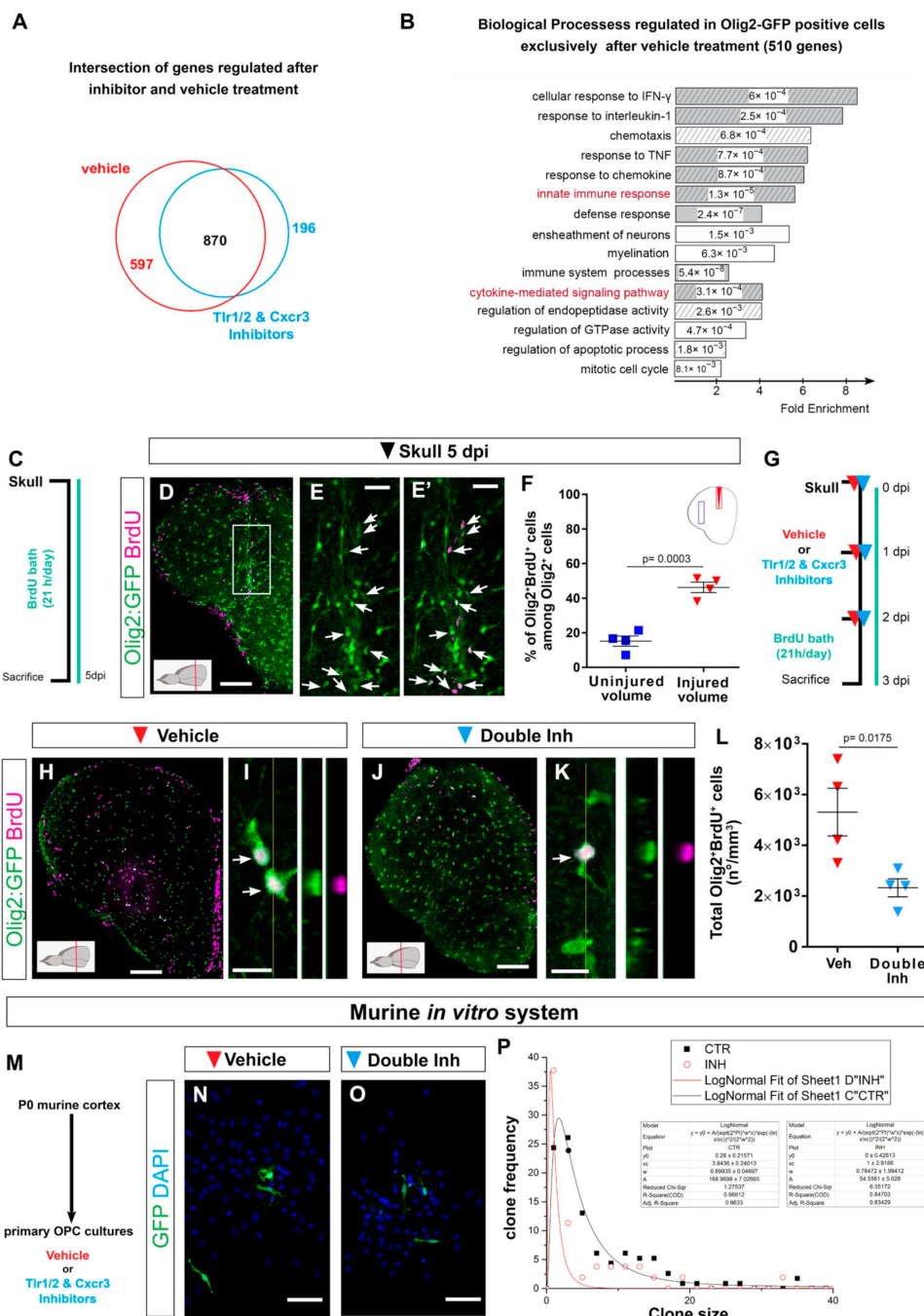


Figure 5. Transcriptome analysis of zebrafish oligodendrocyte lineage reveals the activation of innate immunity and cell cycle pathways after skull injury. (A) Venn diagram of genes regulated at 3 dpi in Olig2-GFP+ cells after vehicle (red) and Tlr1/2 and Cxcr3 inhibitor (cyan) treatment. (B) Histogram depicting GO biological process terms significantly enriched (p-values indicated on bars) in a gene set (510 genes in (A)) normalized after inhibitor treatment and therefore regulated exclusively after vehicle treatment. GO terms related to inflammatory response are shown by gray bars; patterned bars indicate processes previously reported to be activated in response to injury. Note that both innate

immunity and cytokine-mediated signaling pathways are normalized upon inhibitor treatment. (C) Scheme depicting the experimental design to analyze the proliferative capacity of Olig2:GFP⁺ cells during the first 5 days after skull injury. (D) Micrograph of injured section 5 days after skull injury stained for GFP and BrdU. (E, E⁰) Magnification of the oligodendroglial accumulation boxed in (D). Double Olig2:GFP⁺ and BrdU⁺ cells are marked with white arrows. (F) Graph illustrating the proportion of Olig2:GFP⁺ and BrdU⁺ cells located at the injury site and in an equivalent uninjured volume in the same section. Note that 45% of the Olig2:GFP⁺ cells at the injury site proliferated after skull injury. (G) Scheme of the experimental design to assess the proliferation of Olig2-GFP⁺ cells after vehicle and inhibitors treatment. (H, J) Images of telencephalic sections 3 days after skull injury and BrdU bath with vehicle (H) and double inhibitors (J) treatments. (I, K) Micrographs with orthogonal projections of proliferating (BrdU⁺) Olig2:GFP⁺ cells after vehicle (I) and Tlr1/2 and Cxcr3 inhibitor (K) treatment. (L) Graph depicting the density of Olig2:GFP⁺ and BrdU⁺ cells 3 dpi in vehicle and Tlr1/2 and Cxcr3 inhibitor treated animals. (M) Experimental design to measure the clonal growth of murine OPCs primary cultures after vehicle and Tlr1/2 and Cxcr3 inhibitor cocktail treatment. OPCs were permanently labeled with GFP expressing retrovirus. (N, O) Micrographs depicting OPC derived clones 5 days after retroviral infection in vehicle (N) and Tlr1/2 and Cxcr3 inhibitor (NBI 74330 and CU CPT22) cocktail (O) treated primary OPCs culture. (P) Graph depicting the frequency of different clone sizes in the vehicle (CTR) and Tlr1/2 and Cxcr3 inhibitor cocktail (INH) treated primary OPCs culture. Data are shown as mean ± SEM; each data point represents one animal. p-values are based on Student's t-test with equal variances. All images are full z-projection of a confocal stack. The level of the cross-section is indicated in the inset. Scale bars in (D, H, J) = 100 μm; scale bars in (N, O) = 50 μm; scale bars in (E, E⁰) = 20 μm; scale bars in (I, K) = 10 μm. Abbreviations: dpi: days post-injury; Veh: vehicle; Inh: inhibitors; OPC: oligodendrocyte progenitor cell. Symbol description: Triangle: skull injury; blue square: uninjured volume; red triangle: vehicle; light blue triangle: double inhibitors, NBI 74330 and CU CPT22; black square: control primary OPCs; red circle: double inhibitor (NBI 74330 and CU CPT22) treated primary OPCs.

3.8. Cerebrospinal Fluid Induces Exacerbated Glial Reactivity by Increasing OPC Proliferation

To identify the source and nature of the ligands activating the prolonged accumulation of OPCs after brain injury, we first examined the size of the skull versus nostril injury. As the volume of the skull injury was larger than the nostril injury (Figure 6A), we first set out to determine whether this was the cause of the reactive gliosis. We reduced the volume of the skull injury to one-third (small skull injury) using the same glass capillary as for the nostril injury (Figure 6B). The small skull injury still induced a strong reactivity of both 4C4⁺ and Olig2:GFP⁺ cells 7 days after the injury (Figure 6C, D). This reaction was comparable to the outcome of the initial skull injury, allowing us to exclude the size of the injury as a major determinant of differential glial reactivity.

We next hypothesized that an injury-induced ligand that activates the exacerbated reaction must be present only after skull injury. The telencephalic ventricle is located dorsally in the zebrafish brain [78,79] and, therefore, is exclusively damaged during the dorso-ventrally performed skull injury. Cerebrospinal fluid (CSF), which is confined to the ventricles, is rich in cytokines and growth factors that maintain normal homeostasis and nurture the brain; however, direct interaction with the brain parenchyma is restricted and regulated by the CSF-brain barrier [80]. Rupture of the ventricular barrier might allow an influx of CSF-derived molecules into the brain parenchyma, potentially explaining the activation of the Tlr1/2 and Cxcr3 pathways only after skull injury. To validate the potential of CSF to induce OPC reaction, we injected human CSF in the nostril injury site and analyzed glial reactivity (Figure 6E). Notably, we observed an 8-fold increase in the number of Olig2:GFP⁺ cells accumulating at the injury site (Figure 6F, M). As we inject the human CSF, the observed reaction could be a result of xenobiotic response. Therefore, we heat-inactivated the human CSF and probed its capacity to induce the reaction of OPCs in the nostril injury. Importantly, the dramatic CSF effect was not observed upon the administration of heat-inactivated human CSF (Figure S8). Moreover, the administration of the human

plasma containing many of the CSF components failed to induce the response (Figure S8), indicating that the prolonged OPC reactivity was not due to xenobiotic inflammation or misfolded proteins present in the CSF. The extraordinary potential of the CSF to induce exacerbated gliosis prompted us to investigate the cellular basis for the Olig2:GFP⁺ cell accumulation in response to the CSF. As the accumulation of OPCs after a skull injury was achieved, at least in part, by an increased proliferation of OPCs (Figure 6C–F), we assessed whether the proliferation of Sox10⁺ cells was also induced by the CSF injection into the nostril injury site (Figure 6G). Indeed, we observed that the majority of Sox10⁺ cells accumulating around the injury site incorporated BrdU during the initial 3 days after the injury and CSF administration (Sox10⁺ and BrdU⁺ cells in respect to all Sox10⁺ cells) (Figure 6H, H⁰, J). The induced proliferation was not, however, observed after the injection of heat-inactivated CSF (Figure 6I, J), in line with the significantly smaller accumulation of Olig2:GFP⁺ cells at the injury site observed after heat-inactivated CSF treatment (Figure S8C, D). The similarity in OPC reaction induced by CSF injection into the nostril injury and the skull injury motivated us to assess whether CSF-induced accumulation of OPCs involved the activation of the Tlr1/2 and Cxcr3 pathways. Therefore, we inhibited the Tlr1/2 and Cxcr3 pathways together with the administration of human CSF after nostril injury (Figure 6K). Importantly, the accumulation of Olig2:GFP⁺ cells was prevented upon Cxcr3 and Tlr1/2 inhibition, despite the accessibility of the CSF at the injury site (Figure 6L, M). Taken together, these data suggest that the OPC accumulation observed upon skull injury is likely triggered by leakage of CSF into the brain parenchyma and the subsequent activation of the Tlr1/2 and Cxcr3 pathways.

To identify potential ligands activating innate immunity pathways in the CSF, we set up an *in vitro* system that relays on the proliferation of a murine OPC cell line (OliNeu). Importantly, the addition of CSF to the OliNeu culture medium induced a dose-dependent increase in the proportion of proliferating, phospho-histone H3 (pH3) positive cells (Figure 7A–D), in line with our data that human CSF can directly regulate OPC proliferation *in vivo* (Figure 6J). Moreover, this dose-dependent response was completely abolished in the double Tlr2 and Cxcr3 knockout clones generated using CRISPR–Cas9 technology (Figures 7D, Q and S9). These results not only confirmed the pivotal role of Tlr2 and Cxcr3 signaling in the CSF induced proliferation of OPCs, but also additionally validated the specificity of our pharmacological inhibitor treatment *in vivo*.

As cytokines have been reported to activate both Cxcr3 and Tlr2 signaling [61,65,81], we first studied the composition of four healthy donor-derived CSFs using a cytokine antibody array (Figure 7E, F). It is important to mention that all four samples induced increased proliferation *in vivo*. Strikingly, 90% of the analyzed cytokines were present in at least one of the samples and 57% in all four samples (Figure 7E, F).

Out of these cytokines, we pre-selected 30 potential candidates (Figure 7E; Table S3) that were present in at least one CSF sample and available as recombinant protein for further functional screening using OliNeu proliferation as a read-out (Figure 7G). We used three different concentrations of the selected candidates and six of them (Ccl5, EGF, Ccl7, IL-10, Cxcl9 and IL-3) significantly increased the proportion of mitotic pH3⁺ cells (Figure 7G), including a known Cxcr3 ligand (Cxcl9). Interestingly, some candidates such as Cxcl9 were not detected in all CSF samples despite the ability of all four CSF samples to induce the accumulation of Olig2:GFP⁺ cells, suggesting redundancy of ligands in their capacity to activate OPC proliferation. Taken together, our data suggest that the CSF cytokines activate the innate immunity to regulate OPC proliferation in a redundant manner and therefore regulate the reactive gliosis.

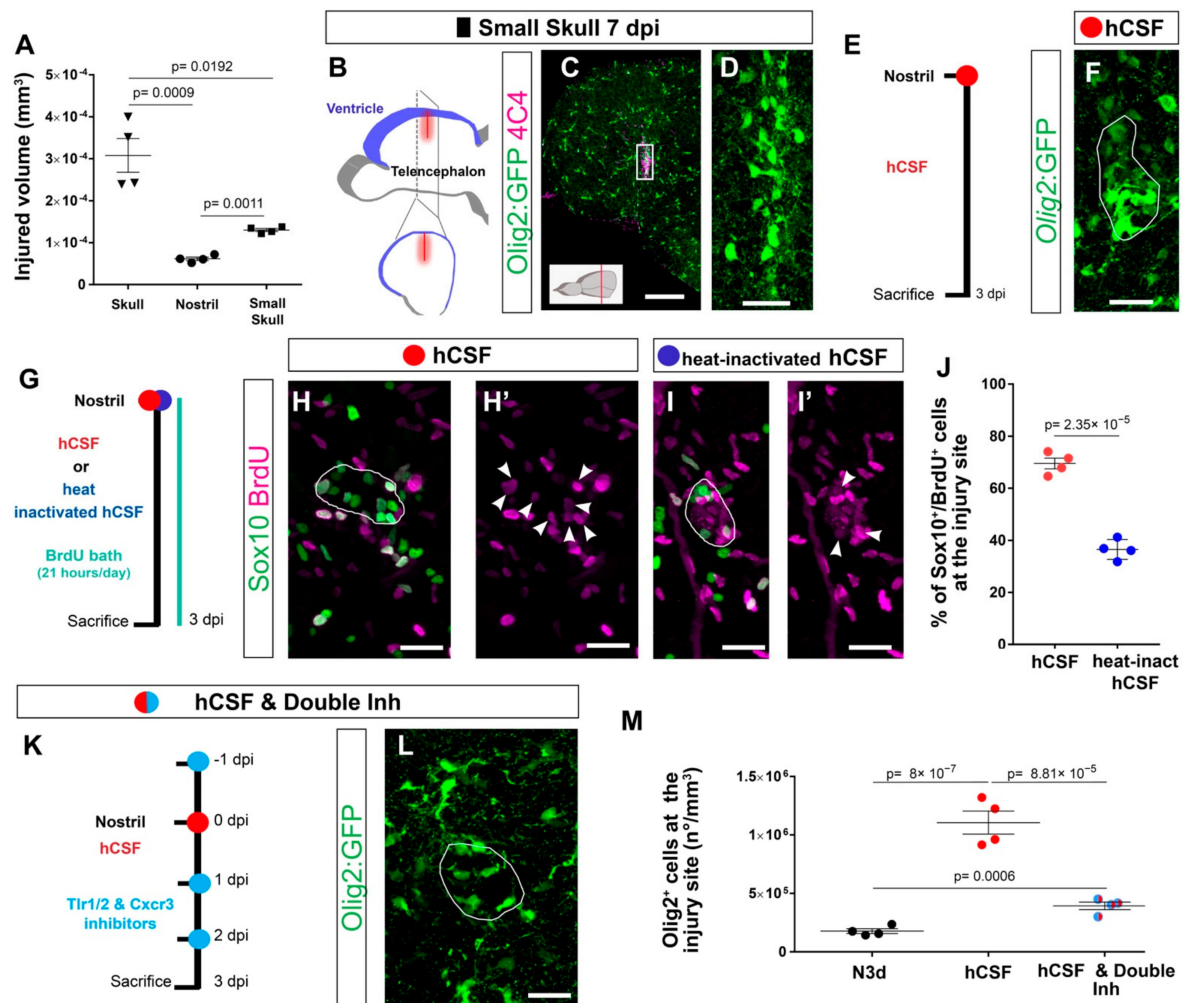


Figure 6. Cerebrospinal fluid–derived molecules induce the proliferation of OPCs and a reactive gliosis–like phenotype. (A) Graph depicting the size of the injured volume after skull, nostril, and small skull injury at 1 dpi. p -values are based on a Welch one–way ANOVA (unequal variances; p -value = 3.034×10^{-4}) with a post–hoc Dunnett T3 test with unequal variances (all pairs). (B) Scheme depicting the small skull injury model. Nostril and small skull injuries were performed with a glass capillary. The red line indicates the dorso–ventral injury through the skull and blue indicates the location of the telencephalic ventricle. (C) Image illustrating the reactivity of Olig2:GFP⁺ and 4C4⁺ cells 7 days after small skull injury. (D) Magnification of the oligodendroglial accumulation boxed in (C). (E) Design of the experimental workflow to analyze the effect of human CSF administration. (F) Image illustrating the reactivity of Olig2:GFP⁺ cells 3 days after nostril injury and hCSF treatment. White line depicts the injury site. (G) Experimental design to analyze the proliferative capacity (BrdU incorporation) of Sox10⁺ cells after nostril injury at 3 dpi and hCSF or heat–inactivated hCSF administration. (H–I) Images showing the accumulation of Sox10⁺ and BrdU⁺ cells at the nostril injury site after hCSF (H, H⁰) or heat–inactivated human CSF (I, I⁰) administration. White lines depict the injury site and white arrowheads the colocalization of BrdU and Sox10. (J) Dot–plot depicting the proportion of Sox10⁺ and BrdU⁺ cells accumulating at the nostril injury site after hCSF or heat–inactivated hCSF administration. p -value is based on Student’s t -test with equal variances. (K) Workflow to study the effect of the Tlr1/2 and Cxcr3 inhibitor treatment after human CSF

injection. (L) Micrograph of a nostril-injured telencephalon at 3 dpi depicting Olig2:GFP⁺ cell reactivity following human CSF and inhibitor treatment. The white line depicts the injury site. (M) Graph showing the density of Olig2:GFP⁺ cells at the injury site at 3 dpi after nostril injury, treatment hCSF, and treatment with hCSF and double-inhibitor. p-values are based on one-way ANOVA (p-value = 1.042 × 10⁻⁶) with post-hoc Tukey Test (all pairs). Data are shown as mean ± SEM; each data point represents one animal. All images are full z-projections of confocal stack. Scale bars in (C) = 100 μm; scale bars in (D,F,H,H⁰,I, I⁰,L) = 20 μm. Abbreviations: dpi: days post-injury; hCSF: human cerebrospinal fluid; Inh: inhibitors; N3d; nostril 3 dpi. Symbol description: black triangle: skull injury; black circle: nostril injury; black rectangle: small skull injury; red circle: human CSF administration; blue circle: heat-inactivated hCSF treatment; light blue circle: double inhibitors, NBI 74330 and CU CPT22.

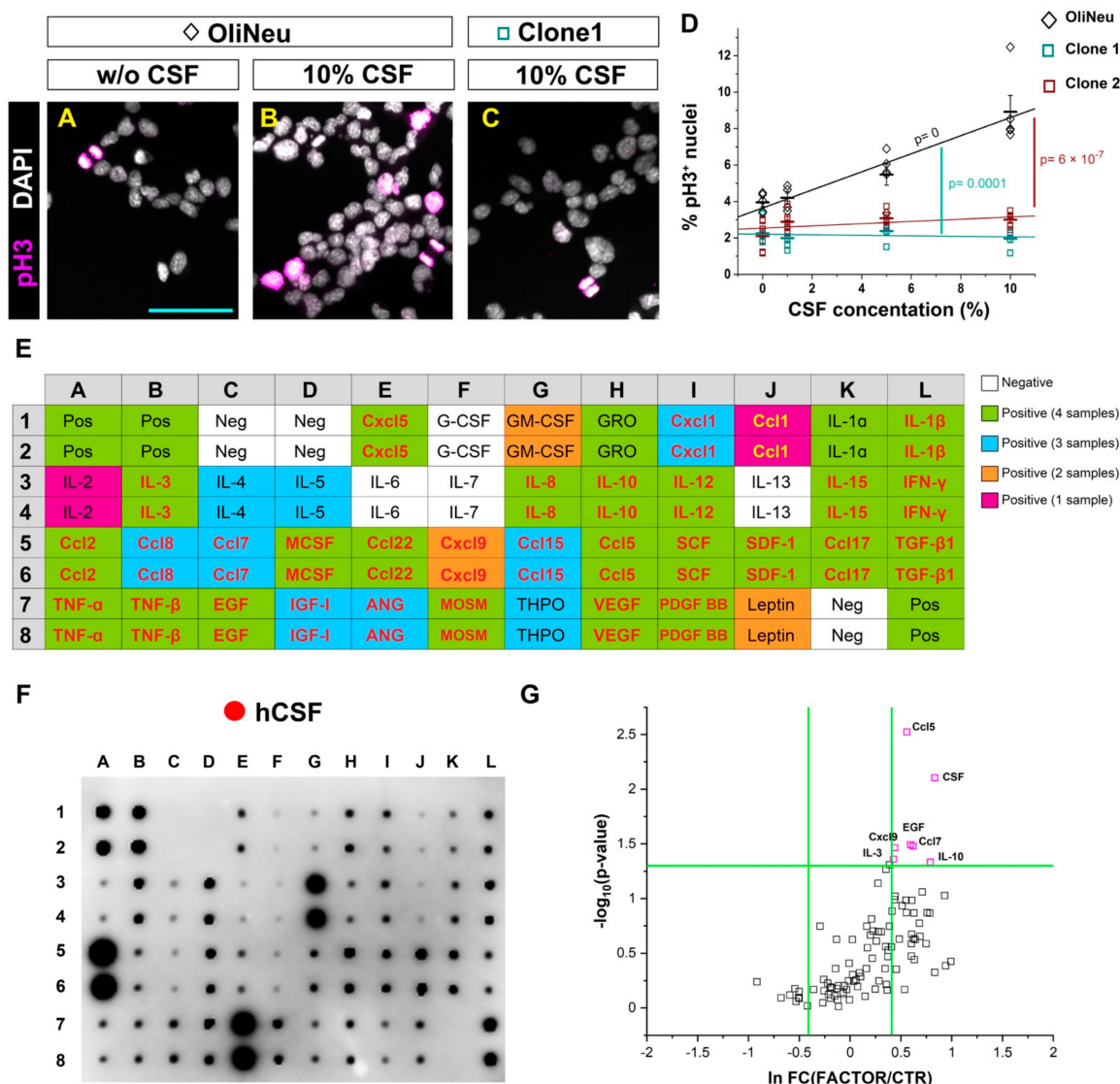


Figure 7. In vitro screening to identify potential candidates from the human cerebrospinal fluid inducing OPC proliferation. (A–C) Micrographs illustrating the proportion of proliferating (pH3 positive) cells in a control wildtype (WT) (A,B) and Tlr2 and Cxcr3-deficient (C) OliNeu oligodendrocyte progenitor cell line in basal conditions (A) and in response to the CSF treatment (B,C). (D) Dot-plot

depicting the proportion of proliferating WT and Tlr2 and Cxcr3-deficient Oli-Neu cells after CSF treatment. The line indicates the corresponding linear data-fit. Data are shown as mean \pm SEM; each data point represents one independent experiment. Adjusted p -values assess the quality of the linear fit for the WT clone (black) and difference in the slopes of the linear fits (color-coded) using the linear regression model. (E) Table showing the map of the array in (F). Color-code illustrates the presence of each cytokine in CSF samples (White: negative in all samples; Green: positive in all samples; Blue: positive in 3 out of 4 samples; Orange: positive in 2 out of 4 samples; Magenta: Positive in 1 out of 4 samples). Cytokines names colored in red or yellow were selected for the screening in (G). (F) Representative image of a cytokine antibody array depicting the cytokine composition of a healthy donor-derived CSF. (G) Dot plot depicting proliferation of Oli-Neu cells after treatment with different cytokines and CSF. Scale bars in (A-C) = 50 μ m. Abbreviations: hCSF: human cerebrospinal fluid. Symbol description: Black diamond: control Oli-Neu cells; green square: Tlr2 and Cxcr3-deficient clone 1; red square Tlr2 and Cxcr3-deficient clone 2; red circle: human CSF administration.

4. Discussion

Despite the general agreement that mammals exhibit a limited regenerative capacity after CNS trauma, it remains controversial which specific cellular and molecular mechanisms trigger the long-lasting glial reaction that in turn, negatively impact the endogenous regeneration. Comparative studies analyzing the regeneration of competent and incompetent species have failed to identify the specific mechanisms involved in the pathogenesis of traumatic injuries [89–94], even after comparing evolutionarily close species [95–97]. This is due to the complexity of the wound healing response that involves a number of molecular pathways and different cell types [9,34]. There has been a long-held belief that microglia and astrocytes are at the core of the poor regenerative outcome [98,99]. However, recent studies have challenged this concept [5,14]. Ablation of microglia upon CNS injury failed to improve neuronal survival and functional recovery and in some cases, even worsened the regenerative outcome [100,101]. Astrocytic activation after trauma appeared to be more complex than originally expected. Microglia-induced inflammation regulates the activation of different types of reactive astrocytes named “A1” and “A2” [18]. While A1 displayed a neurotoxic phenotype, A2 astrocytes appeared to exert neuroprotective functions [64]. The differential activation of A1 and/or A2 astrocytes might explain the controversy about the functional consequences of astrogliosis and whether reactive astrocytes promote endogenous regeneration or contribute to the detrimental reactive gliosis. Surprisingly, and despite their rapid and robust reaction to injury, it is largely unknown how the oligodendrocyte progenitors (OPCs) fit in this inflammatory cascade. To study the role of OPCs during the wound healing process, we performed a comparative analysis of two injury paradigms displaying differential OPC reactivity in the same organ and model organism. In contrast to the previously described nostril injury of brain parenchyma [33,37,38], skull injury showed more similarities to the glial response reported in mammals, such as prolonged OPC accumulation, lack of tissue restoration, extracellular matrix modifications, and exacerbated inflammatory response [34,102].

Comparative analysis (nostril vs. skull) revealed a shared cellular reaction and large overlap in gene regulation shortly after injury, highlighting the common features of the initial wound healing processes regardless if it is associated with prolonged, exacerbated, or restricted glial reactivity [9]. Importantly, a unique molecular signature, including specific innate immunity pathways, was expressed 3 days after the skull injury, correlating with the first signs of the exacerbated glial reaction. These pathways were never regulated during the nostril wound healing, validating the theory that the prolonged, reactive gliosis is induced by a specific molecular program independent of the initial wound healing response [19]. Our study does not support the concept that the regenerative capacity of the CNS is an evolutionarily fixed feature of a given species [103,104]; rather, it is a highly regulated, adaptive response to a specific type of injury. This concept is shared with skin regeneration, in which the depth of the injury determines the scar response [105].

We identified two receptors, Tlr1/2 and Cxcr3, as main regulators of the exacerbated glial reactivity. Interestingly, the inhibition of either of the two pathways separately showed no beneficial effect, whereas the activation of either Tlr2 or Cxcr3 in the nostril paradigm was sufficient to induce gliosis. Hence, both signaling pathways control reactive gliosis in a redundant and synergistic manner. As previously discussed, the complex cross-regulation of immune cells (monocytes and microglia) and astrocytes after brain injury is crucial for the regenerative outcome [19,106–108]. The classical inflammatory cascade is initiated by activation and polarization of microglia and invading monocytes. Consequently, these cells regulate the reactivity of astrocytes that, in turn, limits the inflammatory response [17,19,109,110]. However, our data demonstrate, for the first time, that microglia/monocytes are not essential for the initial activation of OPCs and that the Tlr1/2 and Cxcr3 pathways can be directly regulated in this population. Our study, therefore, brings forth a new concept that OPCs can sense and react to injury-induced signals independent of microglia and invading monocytes. However, we cannot exclude any involvement of microglia/monocytes in other aspects of the wound healing. As we did not perform cell-specific interference and because both receptors are expressed in several cell types (microglia/monocytes [111,112]; astrocytes [113,114]; oligodendroglia [114]; neurons [113,115]), we cannot exclude the possibility that other cell types contribute to the induction of the wound closure via the Tlr1/2 and Cxcr3 signaling pathways. However, our knockout in vitro model validated the role of the Tlr2 and Cxcr3 pathways in directly activating OPC proliferation and hence, demonstrated that they are clearly involved in a crucial manner in the reactive gliosis. Moreover, the improvement in tissue recovery (reduced injured volume and enhanced restorative neurogenesis) observed after double-inhibitor treatment correlates nicely with a reduction in the number of accumulating Olig2⁺ cells. Our data support the hypothesis that the detrimental environment classically associated with the reactive gliosis might be driven specifically by reactive OPCs.

The central role of the Tlr1/2 and Cxcr3 pathways in regulating gliosis and tissue restoration motivated us to investigate injury-induced mechanisms. Our study suggests that the ligand(s) activating the Tlr1/2 and Cxcr3 pathways are part of the CSF that leaks into the CNS parenchyma upon traumatic injury [116]. The capability of the CSF to directly induce OPC proliferation in a Tlr2 and Cxcr3-dependent manner, further corroborates the pivotal role of OPCs in initiating the long-lasting glial response and generating a harmful environment. Although the specific CSF-derived molecule/s driving the reactive gliosis in vivo remain unidentified, our in vitro screening suggests that some of the cytokines present in the CSF could be responsible for the OPC activation induced by the traumatic brain injury. These data support a central regulatory role of CSF in controlling not only the activation of neural stem cells in the intact brain, but also the activation state of CNS glia after injury [117,118]. Overall, our work highlights novel pathways in exacerbated OPC activation as potential targets for developing efficient therapies improving regeneration in the mammalian brain.

Supplementary Materials: The following supporting information can be downloaded at: <https://www.mdpi.com/article/10.3390/cells11030520/s1>, Figure S1. Immune cell reactivity after nostril and skull injury. (A,C) Images of Lys⁺ neutrophils and 4C4⁺ cells accumulating at the injury site 12h (A) and 2 days (C) after the nostril injury. (B) Magnification of the boxed area in A. The number of neutrophils located in the telencephalic parenchyma already decreased at 2 dpi. (D,E) Images of Lys⁺ neutrophils and 4C4⁺ cells 12h (D) and 2 days (E) after the skull injury. Note that already 12h after the skull injury neutrophils were distributed throughout the whole parenchyma and they maintained such distribution even after 2 days. (F–H⁰⁰⁰) Micrographs illustrating the distribution and morphology of 4C4⁺, L-plastin⁺ and Mpeg1:mCherry⁺ cells in intact condition (F–F⁰⁰⁰), 3 days after nostril (G–G⁰⁰⁰) and 3 days after skull (H–H⁰⁰⁰) injury. Note that most of the microglia in the intact brain co-expressed all three markers, although 4C4⁺ single-expressing cells can be often observed (yellow arrows). Both nostril (G–G⁰⁰⁰) and skull injury (H–H⁰⁰⁰) changed the morphology and expression pattern of microglia/monocytes. (I–L) Micrographs illustrating the Olig2:GFP (I,K) and 4C4 (J,L) reactivity 1 day after skull (I,J) and nostril (K,L) injury. White lines outline the injured area. All images are full

z-projections of a confocal stack. Scale bars in A, C, D, E, I, J, K and L = 100 μ m; Scale bars in B, F, F⁰, F⁰⁰, F⁰⁰⁰, G, G⁰, G⁰⁰, G⁰⁰⁰, H, H⁰, H⁰⁰, H⁰⁰⁰ = 20 μ m. Abbreviations: dpi: days post-injury; hpi: hours post-injury. Symbol description: black rectangle: intact; black triangle: skull injury; black circle: nostril injury. Figure S2. Nostril injury does not induce long-lasting accumulation of Olig2:GFP⁺ cells in the zebrafish telencephalon. (A) Experimental design to analyze the kinetics and reactivity of the Olig2:GFP⁺ cell population after sagittal sectioning. (B–D) Micrographs of sagittal telencephalic sections at 1 day (B), 3 days (C) and 7 days (D) after nostril injury illustrating the 4C4 and Olig2:GFP reactivity. (E) Dot plot comparing the density of Olig2:GFP⁺ cells located at the injury site after coronal (data presented in Figure 1N) and sagittal sectioning. Data are shown as mean \pm SEM; each data point represents one animal. p-values are based on one-way ANOVA (p-value = 2.419×10^{-6}) and Multiple Comparisons of Means (adjusted p-values reported, single-step method) was performed. All images are full z-projections of confocal stack. Scale bars in B, C, D, = 100 μ m. Abbreviation: dpi: days post-injury. Figure S3. Reactivity of Gfap⁺ ependymoglia after nostril and skull injury in the zebrafish telencephalon. (A) Image of an uninjured telencephalic section from the Tg(gfap:GFP) line. White arrow indicates the basement membrane. (B,D) Micrographs of nostril (B) and skull (D) injured sections at 3 dpi illustrating the reactivity of 4C4⁺ and Gfap:GFP⁺ cells. C and E are magnifications from the boxed areas in (B,D). (F,G) Images depicting the reactivity of Gfap:GFP⁺ cells at 7 days after nostril (F) and skull (G) injury. Note that 7 days after skull injury, the ependymoglia cell layer is restored. (H) Magnification of the injured area boxed in (G); white arrows illustrate misplaced Gfap:GFP⁺ cells and arrowheads depict hyperreactive Gfap:GFP⁺ processes. All images are full z-projections of confocal stack. Insets indicate the rostro-caudal levels of the sections. Scale bars in A, B, D, F and G = 100 μ m; scale bars in C, E and H = 20 μ m. Abbreviation: dpi: days post-injury. Symbol description: black rectangle: intact; black triangle: skull injury; black circle: nostril injury. Figure S4. Activation of Tlr1/2 innate immunity pathways induces prolonged accumulation of Olig2:GFP⁺ cells after nostril injury. (A) Histogram illustrating the expression level of Tlr2 in the intact and injured adult zebrafish telencephalon measured by qPCR. Data are shown as mean \pm SEM (n = 3 animals). (B) Scheme of the experimental design to identify receptor mediating zymosan A effect. (C,E) Micrographs of zymosan A-treated telencephalic sections of the Tg(Olig2:GFP) line 5 days after nostril injury and vehicle (C) or Tlr1/2 inhibitor (E) treatment. (D,F) are magnifications of the boxed areas in (C,E), respectively. (G) Graph depicting the density of Olig2:GFP⁺ cells located at the injured area after aCSF, zymosan A, and zymosan A and Tlr1/2 inhibitor treatment. Data are shown as mean \pm SEM, each data point represents one animal. p-values are based on a one-way ANOVA (p-value = 1.312×10^{-5}) with a post-hoc Tukey Test. All images are full z-projections of confocal stack. Insets indicate the rostro-caudal levels of the sections. Scale bars in C and D = 100 μ m; scale bars in D and F = 20 μ m. Abbreviations: N3d: nostril 3 days post-injury; S3d: skull 3 days post-injury; aCSF: artificial cerebrospinal fluid; Inh: inhibitor. Symbol description: black circle: nostril injury; red circle: intraperitoneal injection of vehicle; dark blue circle: intraperitoneal injection of Tlr1/2 inhibitor, CU CPT22; orange circle: ventricular zymosan A injection; orange rectangle: aCSF. Figure S5. Innate immunity pathways and glial reactivity 4 days after skull and nostril injury. (A) Experimental outline to assess the reaction of 4C4⁺ cells after skull injury with vehicle, Tlr1/2 inhibitor (CU CPT22), Cxcr3 inhibitor (NBI 74330) and Cxcr3 and Tlr1/2 inhibitor (NBI 74330 and CU CPT22) treatment. (B–E) Micrographs depicting telencephalic sections 4 days after skull injury stained for 4C4 after vehicle (B), Tlr1/2 inhibitor (C), Cxcr3 inhibitor (D) and double Tlr1/2 and Cxcr3 inhibitor treatment. Cyan line delineates telencephalic hemisphere. (F) Graph illustrating the proportion of area covered by 4C4 signal after different treatments. p-values are based on One-way ANOVA (p-value = 7.021×10^{-5}) with post-hoc Dunnett Test (Many-to-One). (G) Scheme of the experimental workflow to analyze the effect of the second inhibitor combination (CU CPT22 + AMG-487) on reactive gliosis. (H,I) Images of injured Tg(Olig2:GFP) section at 4 dpi stained for GFP and Sox10 after vehicle (H) and CU CPT22 + AMG-487 inhibitor (I) treatment. (J) Dot-plot showing the accumulation of Olig2:GFP⁺ cells at the injury site after vehicle, first combination of double inhibitors, and second combination of double inhibitors treatment. Note that both double-inhibitor combinations reduced oligodendroglia accumulation to the same extent. p-values are based on a one-way ANOVA (p-value = 1.221×10^{-3}) with a post-hoc Dunnett Test (Many-to-One). (K) Scheme depicting the experimental design to analyze oligodendroglial reaction after nostril injury and vehicle or double Tlr1/2 and Cxcr3 inhibitor (NBI 74330 and CU CPT22) treatment. (L–M⁰) Micrographs illustrating accumulation of oligodendroglia (Olig2:GFP⁺ cells) at the injury site 3 days after nostril injury and vehicle (L,L⁰) or double inhibitor treatment (M,M⁰). White lines delineate the injury site. (N) Graph depicting the density of

Olig2:GFP⁺ cells located at the injury area as a function of Tlr1/2 and Cxcr3 pathways. *p*-values are based on a one-way ANOVA (p -value = 3.674×10^{-1}) with a post-hoc Dunnett Test (Many-to-One). All images are full *z*-projections of a confocal stack. Insets indicate the rostro-caudal levels of the sections. Data are shown as mean \pm SEM; each data point represents one animal. Scale bars in B, C, D, and E = 100 μ m; scale bars in H, I, L, L⁰, M and M⁰ = 20 μ m. Abbreviations: dpi: days post-injury; N3d: nostril 3 days post-injury; Inh: inhibitor. Symbol description: red triangle: vehicle; dark blue triangle: Tlr1/2 inhibitor, CU CPT22; green triangle: Cxcr3 inhibitor, NBI 74330; light blue triangle: double inhibitors, NBI 74330 and CU CPT22; orange triangle: CU CPT22 + AMG-487 injection; black circle: nostril injury; red circle: vehicle; light blue circle: double inhibitors, NBI 74330 and CU CPT22. Figure S6. Tlr1/2 and Cxcr3 pathways regulate exacerbated oligodendroglia activation independently from microglial and monocyte activation. (A) Scheme of the experimental setting to address the role of Cxcr3 and Tlr1/2 in tissue restoration. (B) Graph showing the volume of the injured tissue after different treatments. *p*-value is based on one-way ANOVA (p -value = 1.801×10^{-1}) with post-hoc Dunnett test. (C) Image of an uninjured section stained for two microglia/monocyte markers (L-plastin and 4C4). (D) Scheme of the experimental setting to eliminate microglia and infiltrating monocytes using Clodrosome to deplete resident microglia and Ccr2 inhibitor to block the extravasation of monocytes. (E) Micrograph illustrating the depletion of L-plastin⁺ and 4C4⁺ cells in intact brain. (F) Graph depicting the proportion of the section covered with a 4C4 signal in untreated and treated brains; 95% of the 4C4⁺ signal was depleted after combined Clodrosome and Ccr2 inhibitor treatment. *p*-value is based on Welch's *t*-test with unequal variances. (G) Scheme of the experimental setting to analyze 4C4 reactivity upon skull injury and microglia/monocyte depletion. (H,I) Micrographs illustrating 4C4 depletion 1 (H) and 2 (I) days after skull injury. White lines depict the injury site and section profiles are delimited by yellow and blue lines. (J) Scheme of the experimental design to analyze reactive gliosis after injecting empty control liposomes used as vehicle for Clodrosome (Encapsome). (K) Image depicting the Olig2:GFP⁺ cell accumulation at the injury site in Encapsome-treated brains. Note that repetitive ventricular injections did not alter oligodendroglial accumulation. (L) Graph illustrating the expression levels of Cxcr3 (Cxcr3.1, Cxcr3.2, Cxcr3.3) and Tlr2 (Tlr2, Tlr18) zebrafish orthologs in Olig2:dsRed⁺ cells analyzed by RNA sequencing. (M–P) Micrographs with orthogonal projections illustrating the expression of Cxcr3.2 (M), Tlr8b (N), MYD88 (O) and Mxc (P) genes in the Olig2:GFP⁺ cells 3 days after skull injury. (Q,R) Images showing the RNAscope negative controls for the Cy3 (Q) and Cy5 (R) channels. All images are full *z*-projections of confocal stack. The level of the cross-section is indicated in the inset. Data are shown as mean \pm SEM and each data point represents one animal. Scale bars in C, E, H, and I = 100 μ m; scale bar in K = 20 μ m; scale bar in M, N, O, P, Q, R = 10 μ m. Abbreviations: TPM: transcripts per million reads; dpi: days post-injury; Inh: inhibitor. Symbol description: red triangle: vehicle; dark blue triangle: Tlr1/2 inhibitor, CU CPT22; green triangle: Cxcr3 inhibitor, NBI 74330; light blue triangle: double inhibitors, NBI 74330 and CU CPT22; black rectangle: intact; orange square: ventricular injection of clodrosome; purple square: intraperitoneal injection of Ccr2 inhibitor; black triangle: skull injury; gray triangle: encapsome; Orange triangle: ventricular injection of clodrosome; purple triangle: intraperitoneal injection of Ccr2 inhibitor. Figure S7. Oligodendrocyte lineage cells respond to injury by activation of innate immunity, cell proliferation and cell migration pathways. (A) Dot plot depicting up- and down-regulated genes in FACS-purified Olig2:dsRed⁺ cells isolated from the injured zebrafish telencephalon after vehicle treatment. Lines indicate cut-off borders (p -value < 0.05 and FC > 2). (B) Pie chart showing the proportion of injury-regulated genes in zebrafish Olig2⁺ cells belonging to different pathways based on a Panther analysis. (C) Histogram depicting GO terms related to biological process significantly enriched (*p*-values indicated on bars) in a gene set up-regulated after brain injury in zebrafish Olig2⁺ cells. GO terms related to inflammatory response are shown by gray bars; patterned bars indicate processes previously reported to be activated in response to injury. Note that both toll-like receptor signaling and the response to the cytokine are induced by the injury. (D) Dot plot depicting the coregulation of ECM-related genes in the entire telencephalon and Olig2⁺ cells after 3 days after skull injury. Lines indicate cut-off borders (p -value < 0.05 and FC > 2). (E) Dot plot depicting up- and down-regulated genes in FACS-purified Olig2:dsRed⁺ positive cells isolated from the injured zebrafish telencephalon after Tlr1/2 and Cxcr3 inhibitor treatment. (F) Experimental design to analyze the density and maturation rate of oligodendrocytes after skull injury. (G–I⁰) Images depicting the distribution of Mbp:nls-GFP⁺ cells and BrdU⁺ cells in intact condition (G–H⁰) and 7 days after skull injury (I, I⁰). Double positive Mbp:nls-GFP and BrdU cells (White arrow) represent oligodendrocyte progenitor cells that differentiated into mature oligodendrocyte

after the injury. (J,K) Dot plots showing the total density of Mbp:nls-GFP⁺ cells (J) and the proportion of newly matured oligodendrocytes (K) in intact brains and 7 days after skull injury. Data are shown as mean SEM; each data point represents one animal. p-values are based on Student's t-test with equal variances. All images are full z-projections of a confocal stack. Scale bars in G, I, I⁰ = 100 μm; scale bars in H, H⁰ = 20 μm. Abbreviations: dpi: days post-injury; VEH: vehicle; INT: intact; INH: inhibitor. Symbol description: black rectangle: intact; black triangle: skull injury. Figure S8. Human plasma and heat-inactivated human CSF do not induce accumulation of Olig2:GFP⁺ cells. (A–C⁰) Micrographs showing the Olig2:GFP and 4C4 reactivity after nostril injury and the administration of either human plasma (A–B⁰) or heat-inactivated hCSF (C–C⁰). White lines delineate the injury site. (D) Dot plot illustrating the density of Olig2:GFP⁺ cells at the injury site after different treatments. Data are shown as mean SEM; each data point represents one animal. p-values are based on a one-way ANOVA (p-value = 2.091 × 10^{−4} with a post-hoc Dunnett test (Many-to-One)). All images are full z-projections of a confocal Z-stack. Scale bars: 20 μm. Abbreviations: dpi: days post-injury; hPlasma: human plasma; hCSF: human cerebrospinal fluid. Symbol description: red circle: hCSF; green circle: human plasma; blue circle: heat-inactivated hCSF. Figure S9. Generation of the Tlr2 and Cxcr3 OliNeu knockout line. (A,B) Sequence alignment of the Cxcr3 (A) and Tlr2 (B) locus depicting the Cas9-mediated bi-allelic deletions (green blocks) leading to the premature STOP codon generation (red asterisk) in oligodendrocyte progenitor OliNeu cell line. The position of gRNAs is indicated with grey boxes. (C,D) Micrographs depicting Ki67-positive cells in WT OliNeu cell clone (only transfected with Cas9) (C) and Cxcr3/Tlr2 mutant clone 1 (D). (E) Dot plot depicting the proportion of pH3 positive cells in WT OliNeu cells and two mutant cell clones (Clone 1, Clone 2). Data are shown as mean SEM; each data point represents single coverslip. p-value is based on one-way ANOVA (p-value = 2.473 × 10^{−3}) and Dunnett Test (Many-to-One). Scale bars in C, D = 50 μm. Symbol description: Black diamond: control OliNeu cells; green square: Tlr2 and Cxcr3-deficient clone 1; red square: Tlr2 and Cxcr3-deficient clone 2. Table S1. List of all the primary antibodies used in this study, and the correspondent information about each antibody. Table S2. List of primers used in this study for RT-qPCR. Table S3. List of recombinant proteins used for the screening in Figure 7G (www.rndsystems.com accessed on 24 September 2019). Table S4. Microarray data illustrating the GO Terms Biological Processes enriched in genes commonly or exclusively regulated in skull and nostril injury at different time points (related to Figure 2B). Table S5. RNAseq data depicting the gene ontology terms related to the biological processes significantly enriched in an ECM-related gene set (69 genes) regulated exclusively 3 days after skull injury (Related to Figure 2E). Table S6. Microarray data illustrating the GO terms related to the biological processes enriched in genes exclusively regulated 3 days after skull injury (related to Figure 2H). Table S7. RNAseq data showing the GO Terms related to the biological processes (PANTHER) upregulated after brain injury in zebrafish Olig2⁺ cells (Related to Figure S7C, GO Terms marked in red are shown in the graph S7C). Table S8. RNAseq data depicting the Gene Ontology terms related to biological processes (PANTHER) significantly enriched in a gene set (597 genes) with normalized expression after Tlr1/2 and Cxcr3 inhibitor treatment in zebrafish. (Related to Figure 5B). Table S9. RNAseq data depicting the gene ontology terms related to biological processes (PANTHER) significantly enriched in a gene set still regulated after inhibitor treatment. (Related to Figure 5). Video S1. Three-dimensional reconstruction of cleared intact telencephalic tissue stained for Sox10 (magenta), 4C4 (cyan) and DAPI (blue). Video S2. Three-dimensional reconstruction of cleared telencephalic tissue stained for Sox10 (magenta), 4C4 (cyan) and DAPI (blue) 3 days after nostril injury. Video S3. Three-dimensional reconstruction of cleared telencephalic tissue stained for Sox10 (magenta), 4C4 (cyan) and DAPI (blue) 7 days after nostril injury. Video S4. Three-dimensional reconstruction of Tg(fli1:eGFP) transgenic line 28 days after nostril and skull injury. Ependymoglia cells were labeled by electroporation of a plasmid encoding for membrane localized tdTomato 21 days after injury. Video S5. Three-dimensional reconstruction of cleared infarct tissue stained for Sox10 and DAPI 7 days after skull injury and vehicle or double inhibitor treatment.

Author Contributions: Conceptualization, R.S.–G., J.N. and M.G.; methodology, R.S.–G., J.N., C.K., T.L., A.Z. (Alessandro Zambusi), K.T.N., T.D., M.I., S.A., V.S., C.T.B. and S.H.S.; software, D.T. and W.W.; formal analysis, T.S. (Tamas Schauer), R.S.–G., T.S. (Tobias Straub), M.I., J.B. and J.N.; resources, H.S., H.B.H., A.Z. (Andreas Zwergal) and T.C.; writing—original draft preparation, R.S.–G. and J.N.; writing—review and editing, all authors. All authors have read and agreed to the published version of the manuscript.

Funding: We gratefully acknowledge funding to JN from the German Research Foundation (DFG) by the SFB 870, SPP1757, TRR274; to MG the German Research Foundation (DFG) by the SFB 870, and the ERC grant ChroNeuroRepair: GA No. 340793; Workin W. W. lab is by the German Science Foundation Collaborative Research Centre (CRC) 870; funds from the Bayerisches Staatsministerium für Bildung und Kultus, Wissenschaft und Kunst within Bavarian Research Network “Human Induced Pluripotent Stem Cells” (ForIPS) and (in part) by the Helmholtz Portfolio Theme ‘Supercomputing and Modelling for the Human Brain’ (SMHB). H.S. is supported by the DFG (CRC 870). Dr. Huttner was supported by a research grant from the German Research Foundation (DFG–HU1961/2–1).

Institutional Review Board Statement: The animal study protocol was approved by the Government of Upper Bavaria (AZ 55.2–1–54–2532–09–16).

Informed Consent Statement: Patient consent was waived as CSF from different patients was pooled and individual patients can not be identified.

Data Availability Statement: All data are available upon request.

Acknowledgments: We want to thank Pamela Raymonds for sharing the Tg(gfap:GFP)mi2001 fish line and Bruce Apple for sharing Tg(Olig2:GFP) and Tg(Olig2:DsRed) fish lines. We are thankful to Andrea Steiner–Mazzardi, Sarah Hübinger and Beate Stiening for excellent technical help, and to Sofia Grade and Clayton Gordy for critical reading of the manuscript.

Conflicts of Interest: The authors declare no conflict of interest. The funders had no role in the design of the study; in the collection, analyses, or interpretation of data; in the writing of the manuscript, or in the decision to publish the results.

References

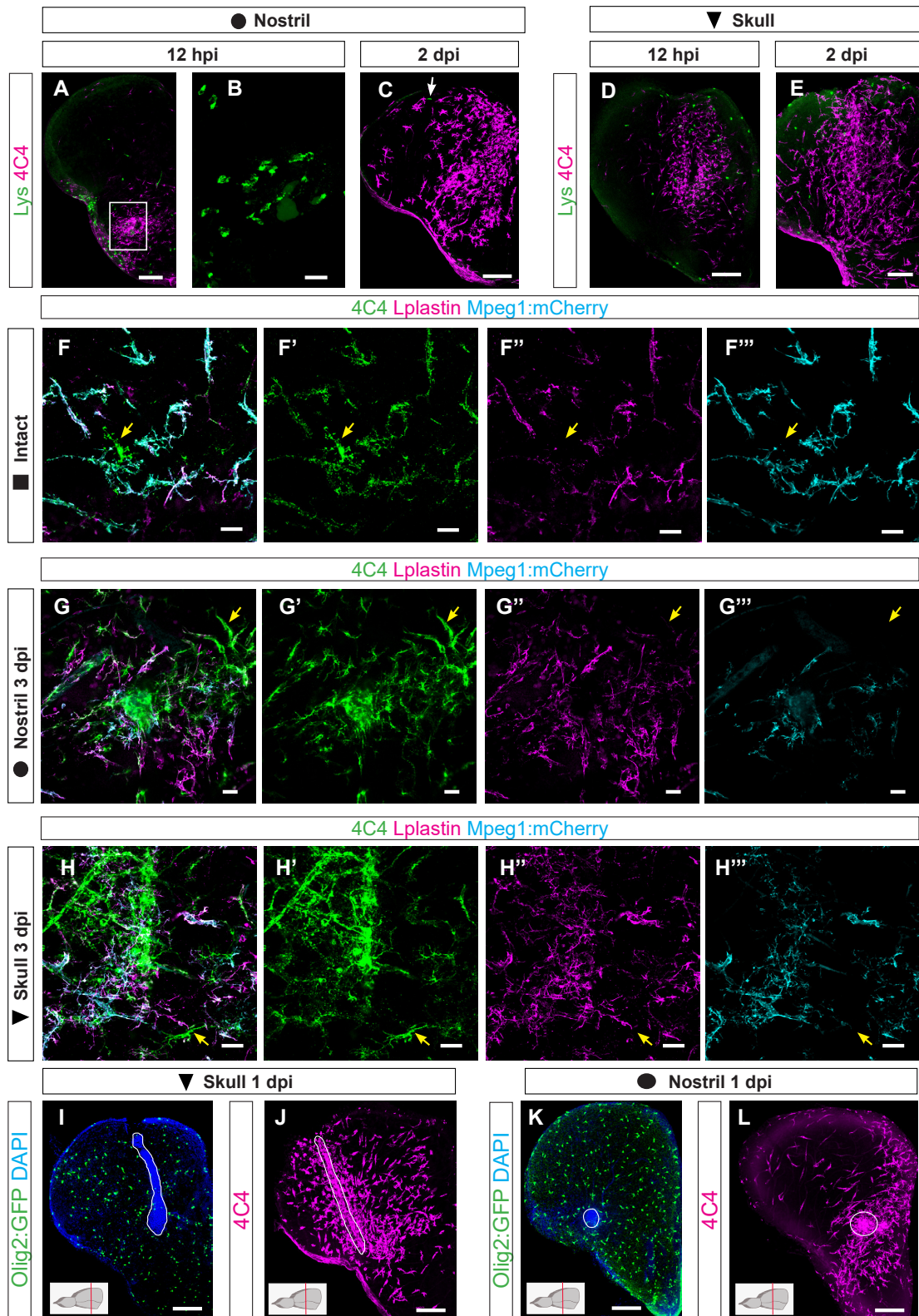
- Zambusi, A.; Ninkovic, J. Regeneration of the central nervous system—principles from brain regeneration in adult zebrafish. *World J. Stem Cells* **2020**, *12*, 8–24. [[CrossRef](#)] [[PubMed](#)]
- Kyritsis, N.; Kizil, C.; Zocher, S.; Kroehne, V.; Kaslin, J.; Freudenreich, D.; Iltzsche, A.; Brand, M. Acute inflammation initiates the regenerative response in the adult zebrafish brain. *Science* **2012**, *338*, 1353–1356. [[CrossRef](#)] [[PubMed](#)]
- Sofroniew, M.V. Astrocyte Reactivity: Subtypes, States, and Functions in CNS Innate Immunity. *Trends Immunol.* **2020**, *41*. [[CrossRef](#)] [[PubMed](#)]
- Donat, C.K.; Scott, G.; Gentleman, S.M.; Sastre, M. Microglial activation in traumatic brain injury. *Front. Aging Neurosci.* **2017**, *9*, 208. [[CrossRef](#)]
- Anderson, M.A.; Burda, J.E.; Ren, Y.; Ao, Y.; O’Shea, T.M.; Kawaguchi, R.; Coppola, G.; Khakh, B.S.; Deming, T.J.; Sofroniew, M.V. Astrocyte scar formation hinders central nervous system axon regeneration. *Nature* **2016**, *532*, 195–200. [[CrossRef](#)]
- Dias, D.O.; Kim, H.; Holl, D.; Solnestam, B.W.; Lundeberg, J.; Carlen, M.; Goritz, C.; Frisen, J. Reducing Pericyte-Derived Scarring Promotes Recovery after Spinal Cord Injury. *Cell* **2018**, *173*, 153–165.e22. [[CrossRef](#)]
- Goritz, C.; Dias, D.O.; Tomilin, N.; Barbacid, M.; Shupliakov, O.; Frisen, J. A pericyte origin of spinal cord scar tissue. *Science* **2011**, *333*, 238–242. [[CrossRef](#)]
- O’Shea, T.M.; Burda, J.E.; Sofroniew, M.V. Cell biology of spinal cord injury and repair. *J. Clin. Investig.* **2017**, *127*, 3259–3270. [[CrossRef](#)] [[PubMed](#)]
- Burda, J.E.; Sofroniew, M.V. Reactive gliosis and the multicellular response to CNS damage and disease. *Neuron* **2014**, *81*, 229–248. [[CrossRef](#)]
- Bardehle, S.; Kruger, M.; Buggenthin, F.; Schwausch, J.; Ninkovic, J.; Clevers, H.; Snippert, H.J.J.; Theis, F.J.J.; Meyer-Luehmann, M.; Bechmann, I.; et al. Live imaging of astrocyte responses to acute injury reveals selective juxtavascular proliferation. *Nat. Neurosci.* **2013**, *16*, 580–586. [[CrossRef](#)]
- Shandra, O.; Winemiller, A.R.; Heithoff, B.P.; Munoz-Ballester, C.; George, K.K.; Benko, M.J.; Zuidhoek, I.A.; Besser, M.N.; Curley, D.E.; Edwards, G.F.; et al. Repetitive diffuse mild traumatic brain injury causes an atypical astrocyte response and spontaneous recurrent seizures. *J. Neurosci.* **2019**, *39*, 1944–1963. [[CrossRef](#)] [[PubMed](#)]
- Bush, T.G.; Puvanachandra, N.; Horner, C.H.; Polito, A.; Ostenfeld, T.; Svendsen, C.N.; Mucke, L.; Johnson, M.H.; Sofroniew, M.V. Leukocyte infiltration, neuronal degeneration, and neurite outgrowth after ablation of scar-forming, reactive astrocytes in adult transgenic mice. *Neuron* **1999**, *23*, 297–308. [[CrossRef](#)]
- Hol, E.M.; Pekny, M. Glial fibrillary acidic protein (GFAP) and the astrocyte intermediate filament system in diseases of the central nervous system. *Curr. Opin. Cell Biol.* **2015**, *32*, 121–130. [[CrossRef](#)] [[PubMed](#)]
- Willis, E.F.; MacDonald, K.P.A.; Nguyen, Q.H.; Garrido, A.L.; Gillespie, E.R.; Harley, S.B.R.; Bartlett, P.F.; Schroder, W.A.; Yates, A.G.; Anthony, D.C.; et al. Repopulating Microglia Promote Brain Repair in an IL-6-Dependent Manner. *Cell* **2020**, *180*, 833–846. [[CrossRef](#)]
- Silver, J.; Miller, J.H. Regeneration beyond the glial scar. *Nat. Rev. Neurosci.* **2004**, *5*, 146–156. [[CrossRef](#)] [[PubMed](#)]

16. Busch, S.A.; Silver, J. The role of extracellular matrix in CNS regeneration. *Curr. Opin. Neurobiol.* **2007**, *17*, 120–127. [[CrossRef](#)] [[PubMed](#)]
17. Fitch, M.T.; Silver, J. CNS injury, glial scars, and inflammation: Inhibitory extracellular matrices and regeneration failure. *Exp. Neurol.* **2008**, *209*, 294–301. [[CrossRef](#)]
18. Liddelow, S.A.; Guttenplan, K.A.; Clarke, L.E.; Bennett, F.C.; Bohlen, C.J.; Schirmer, L.; Bennett, M.L.; Münch, A.E.; Chung, W.S.; Peterson, T.C.; et al. Neurotoxic reactive astrocytes are induced by activated microglia. *Nature* **2017**, *541*, 481–487. [[CrossRef](#)]
19. Frik, J.; Merl-Pham, J.; Plesnila, N.; Mattugini, N.; Kjell, J.; Kraska, J.; Gomez, R.M.; Hauck, S.M.; Sirko, S.; Gotz, M. Cross-talk between monocyte invasion and astrocyte proliferation regulates scarring in brain injury. *EMBO Rep.* **2018**, *19*, e45294. [[CrossRef](#)]
20. Di Bello, I.C.; Dawson, M.R.L.; Levine, J.M.; Reynolds, R. Generation of oligodendroglial progenitors in acute inflammatory demyelinating lesions of the rat brain stem is associated with demyelination rather than inflammation. *J. Neurocytol.* **1999**, *28*, 365–381. [[CrossRef](#)]
21. Domingues, H.S.; Portugal, C.C.; Socodato, R.; Relvas, J.B. Oligodendrocyte, astrocyte, and microglia crosstalk in myelin development, damage, and repair. *Front. Cell Dev. Biol.* **2016**, *4*, 71. [[PubMed](#)]
22. Simon, C.; Dimou, L.; Gotz, M. Progenitors in the adult cerebral cortex—Cell cycle properties and regulation by physiological stimuli and injury. *Glia* **2011**, *59*, 869–881. [[CrossRef](#)] [[PubMed](#)]
23. Kang, S.H.; Li, Y.; Fukaya, M.; Lorenzini, I.; Cleveland, D.W.; Ostrow, L.W.; Rothstein, J.D.; Bergles, D.E. Degeneration and impaired regeneration of gray matter oligodendrocytes in amyotrophic lateral sclerosis. *Nat. Neurosci.* **2013**, *16*, 571–579. [[CrossRef](#)] [[PubMed](#)]
24. Hughes, E.G.; Kang, S.H.; Fukaya, M.; Bergles, D.E. Oligodendrocyte progenitors balance growth with self-repulsion to achieve homeostasis in the adult brain. *Nat. Neurosci.* **2013**, *16*, 668–676. [[CrossRef](#)]
25. Von Streitberg, A.; Jäkel, S.; Eugenin von Bernhardt, J.; Straube, C.; Buggenthin, F.; Marr, C.; Dimou, L. NG2-Glia Transiently Overcome Their Homeostatic Network and Contribute to Wound Closure After Brain Injury. *Front. Cell Dev. Biol.* **2021**, *9*, 762. [[CrossRef](#)]
26. Komitova, M.; Zhu, X.; Serwanski, D.R.; Nishiyama, A. NG2 cells are distinct from neurogenic cells in the postnatal mouse subventricular zone. *J. Comp. Neurol.* **2009**, *512*, 702–716. [[CrossRef](#)]
27. Nishiyama, A.; Komitova, M.; Suzuki, R.; Zhu, X. Polydendrocytes (NG2 cells): Multifunctional cells with lineage plasticity. *Nat. Rev. Neurosci.* **2009**, *10*, 9–22. [[CrossRef](#)]
28. Buffo, A.; Vosko, M.R.; Erturk, D.; Hamann, G.F.; Jucker, M.; Rowitch, D.; Gotz, M. Expression pattern of the transcription factor Olig2 in response to brain injuries: Implications for neuronal repair. *Proc. Natl. Acad. Sci. USA* **2005**, *102*, 18183–18188. [[CrossRef](#)]
29. Wellman, S.M.; Kozai, T.D.Y. In vivo spatiotemporal dynamics of NG2 glia activity caused by neural electrode implantation. *Biomaterials* **2018**, *164*, 121–133. [[CrossRef](#)]
30. Rhodes, K.E.; Moon, L.D.F.; Fawcett, J.W. Inhibiting cell proliferation during formation of the glial scar: Effects on axon regeneration in the CNS. *Neuroscience* **2003**, *120*, 41–56. [[CrossRef](#)]
31. Busch, S.A.; Horn, K.P.; Cuascut, F.X.; Hawthorne, A.L.; Bai, L.; Miller, R.H.; Silver, J. Adult NG2+ cells are permissive to neurite outgrowth and stabilize sensory axons during macrophage-induced axonal dieback after spinal cord injury. *J. Neurosci.* **2010**, *30*, 255–265. [[CrossRef](#)]
32. Chen, Z.J.; Ughrin, Y.; Levine, J.M. Inhibition of axon growth by oligodendrocyte precursor cells. *Mol. Cell. Neurosci.* **2002**, *20*, 125–139. [[CrossRef](#)]
33. Kroehne, V.; Freudenreich, D.; Hans, S.; Kaslin, J.; Brand, M. Regeneration of the adult zebrafish brain from neurogenic radial glia-type progenitors. *Development* **2011**, *138*, 4831–4841. [[CrossRef](#)]
34. Dimou, L.; Gotz, M. Glial cells as progenitors and stem cells: New roles in the healthy and diseased brain. *Physiol. Rev.* **2014**, *94*, 709–737. [[CrossRef](#)]
35. Reimer, M.M.; Kuscha, V.; Wyatt, C.; Sorensen, I.; Frank, R.E.; Knuwer, M.; Becker, T.; Becker, C.G. Sonic hedgehog is a polarized signal for motor neuron regeneration in adult zebrafish. *J. Neurosci.* **2009**, *29*, 15073–15082. [[CrossRef](#)]
36. Reimer, M.M.; Sorensen, I.; Kuscha, V.; Frank, R.E.; Liu, C.; Becker, C.G.; Becker, T. Motor neuron regeneration in adult zebrafish. *J. Neurosci.* **2008**, *28*, 8510–8516. [[CrossRef](#)]
37. Baumgart, E.V.V.; Barbosa, J.S.S.; Bally-Cuif, L.; Gotz, M.; Ninkovic, J.; Götz, M.; Ninkovic, J. Stab wound injury of the zebrafish telencephalon: A model for comparative analysis of reactive gliosis. *Glia* **2012**, *60*, 343–357. [[CrossRef](#)]
38. Ayari, B.; Elhachimi, K.H.; Yanicostas, C.; Landoulsi, A.; Soussi-Yanicostas, N. Prokineticin 2 expression is associated with neural repair of injured adult zebrafish telencephalon. *J. Neurotrauma* **2010**, *27*, 959–972. [[CrossRef](#)] [[PubMed](#)]
39. Marz, M.; Schmidt, R.; Rastegar, S.; Strahle, U. Regenerative response following stab injury in the adult zebrafish telencephalon. *Dev. Dyn.* **2011**, *240*, 2221–2231. [[CrossRef](#)] [[PubMed](#)]
40. Shin, J.; Park, H.C.; Topczewska, J.M.; Mawdsley, D.J.; Appel, B. Neural cell fate analysis in zebrafish using olig2 BAC transgenics. *Methods Cell Sci* **2003**, *25*, 7–14. [[CrossRef](#)] [[PubMed](#)]
41. Lawson, N.D.; Weinstein, B.M. In vivo imaging of embryonic vascular development using transgenic zebrafish. *Dev. Biol.* **2002**, *248*, 307–318. [[CrossRef](#)] [[PubMed](#)]
42. Bernardos, R.L.; Raymond, P.A. GFAP transgenic zebrafish. *Gene Expr. Patterns* **2006**, *6*, 1007–1013. [[CrossRef](#)] [[PubMed](#)]
43. Jung, S.H.; Kim, S.; Chung, A.Y.; Kim, H.T.; So, J.H.; Ryu, J.; Park, H.C.; Kim, C.H. Visualization of myelination in GFP-transgenic zebrafish. *Dev. Dyn.* **2010**, *239*, 592–597. [[CrossRef](#)]

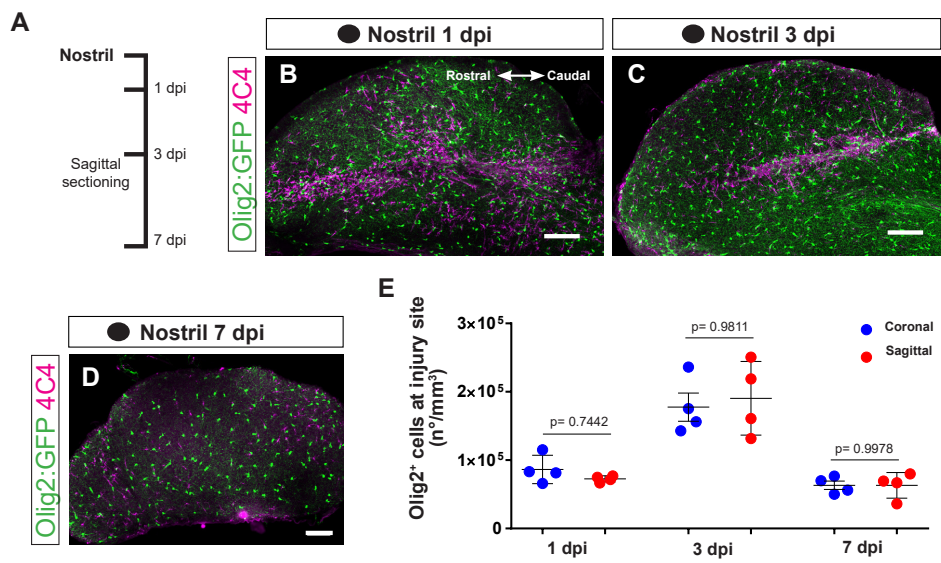
44. Bernut, A.; Herrmann, J.L.; Kissa, K.; Dubremetz, J.F.; Gaillard, J.L.; Lutfalla, G.; Kremer, L. Mycobacterium abscessus cording prevents phagocytosis and promotes abscess formation. *Proc. Natl. Acad. Sci. USA* **2014**, *111*, E943–E952. [\[CrossRef\]](#) [\[PubMed\]](#)
45. Westerfield, M. *The Zebrafish Book. A Guide for the Laboratory Use of Zebrafish (Danio Rerio)*, 4th ed.; Univ. of Oregon Press: Eugene, OR, USA, 2000.
46. Durovic, T.; Ninkovic, J. Electroporation method for in vivo delivery of plasmid dna in the adult zebrafish telencephalon. *J. Vis. Exp.* **2019**, *13*, e60066. [\[CrossRef\]](#)
47. Barbosa, J.S.S.; Sanchez-Gonzalez, R.; Di Giaimo, R.; Baumgart, E.V.V.; Theis, F.J.J.; Götz, M.; Ninkovic, J.; Gotz, M.; Ninkovic, J.; Gonzalez-Sanchez, R.; et al. Live imaging of adult neural stem cell behavior in the intact and injured zebrafish brain. *Science* **2015**, *348*, 789–793. [\[CrossRef\]](#)
48. Barbosa, J.S.S.; Di Giaimo, R.; Götz, M.; Ninkovic, J.; Gotz, M.; Ninkovic, J. Single-cell in vivo imaging of adult neural stem cells in the zebrafish telencephalon. *Nat. Protoc.* **2016**, *11*, 1360–1370. [\[CrossRef\]](#)
49. Di Giaimo, R.; Durovic, T.; Barquin, P.; Kocijaj, A.; Lepko, T.; Aschenbroich, S.; Breunig, C.T.T.; Irmeler, M.; Cernilogar, F.M.M.; Schotta, G.; et al. The Aryl Hydrocarbon Receptor Pathway Defines the Time Frame for Restorative Neurogenesis. *Cell Rep.* **2018**, *25*, 3241–3251. [\[CrossRef\]](#)
50. Rainer, J.; Sanchez-Cabo, F.; Stocker, G.; Sturn, A.; Trajanoski, Z. CARMAweb: Comprehensive R- and bioconductor-based web service for microarray data analysis. *Nucleic Acids Res.* **2006**, *34*, W498–W503. [\[CrossRef\]](#)
51. Herrero, J.; Muffato, M.; Beal, K.; Fitzgerald, S.; Gordon, L.; Pignatelli, M.; Vilella, A.J.; Searle, S.M.J.; Amode, R.; Brent, S.; et al. Ensembl comparative genomics resources. *Database* **2016**, *2016*, baw053. [\[CrossRef\]](#)
52. Huang, D.W.; Sherman, B.T.; Lempicki, R.A. Systematic and integrative analysis of large gene lists using DAVID bioinformatics resources. *Nat. Protoc.* **2009**, *4*, 44–57. [\[CrossRef\]](#) [\[PubMed\]](#)
53. Huang, D.W.; Sherman, B.T.; Lempicki, R.A. Bioinformatics enrichment tools: Paths toward the comprehensive functional analysis of large gene lists. *Nucleic Acids Res.* **2009**, *37*, 1–13. [\[CrossRef\]](#) [\[PubMed\]](#)
54. Fischer, J.; Beckervordersandforth, R.; Tripathi, P.; Steiner-Mezzadri, A.; Ninkovic, J.; Gotz, M.; Götz, M. Prospective isolation of adult neural stem cells from the mouse subependymal zone. *Nat. Protoc.* **2011**, *6*, 1981–1989. [\[CrossRef\]](#) [\[PubMed\]](#)
55. Di Giaimo, R.; Aschenbroich, S.; Ninkovic, J. Fluorescence-Activated Cell Sorting-Based Isolation and Characterization of Neural Stem Cells from the Adult Zebrafish Telencephalon. *Adv. Struct. Saf. Stud.* **2019**, *1938*, 49–66.
56. He, D.; Meyer, B.; Lu, R. *Isolation and Culture of Oligodendrocyte Precursor Cells from Prenatal and Postnatal Rodent Brain*. In *Stem Cell Technologies in Neuroscience*; Humana Press: New York, NY, USA, 2017.
57. Walcher, T.; Xie, Q.; Sun, J.; Irmeler, M.; Beckers, J.; Öztürk, T.; Niessing, D.; Stoykova, A.; Cvekl, A.; Ninkovic, J.; et al. Functional dissection of the paired domain of Pax6 reveals molecular mechanisms of coordinating neurogenesis and proliferation. *Development* **2013**, *140*, 1123–1136. [\[CrossRef\]](#) [\[PubMed\]](#)
58. Breunig, C.T.; Durovic, T.; Neuner, A.M.; Baumann, V.; Wiesbeck, M.F.; Köferle, A.; Götz, M.; Ninkovic, J.; Stricker, S.H. One step generation of customizable gRNA vectors for multiplex CRISPR approaches through string assembly gRNA cloning (STAgR). *PLoS ONE* **2018**, *13*, e0196015. [\[CrossRef\]](#)
59. Köferle, A.; Worf, K.; Breunig, C.; Baumann, V.; Herrero, J.; Wiesbeck, M.; Hutter, L.H.; Gotz, M.; Fuchs, C.; Beck, S.; et al. CORALINA: A universal method for the generation of gRNA libraries for CRISPR-based screening. *BMC Genomics* **2016**, *17*, 917. [\[CrossRef\]](#) [\[PubMed\]](#)
60. Soehnlein, O.; Lindbom, L. Phagocyte partnership during the onset and resolution of inflammation. *Nat. Rev. Immunol.* **2010**, *10*, 427–439. [\[CrossRef\]](#)
61. Adolf, B.; Chapouton, P.; Lam, C.S.; Topp, S.; Tannhauser, B.; Strahle, U.; Gotz, M.; Bally-Cuif, L. Conserved and acquired features of adult neurogenesis in the zebrafish telencephalon. *Dev. Biol.* **2006**, *295*, 278–293. [\[CrossRef\]](#)
62. Horvat, A.; Schwaiger, F.W.; Hager, G.; Bröcker, F.; Streif, R.; Knyazev, P.G.; Ullrich, A.; Kreutzberg, G.W. A novel role for protein tyrosine phosphatase SHP1 in controlling glial activation in the normal and injured nervous system. *J. Neurosci.* **2001**, *21*, 865–874. [\[CrossRef\]](#)
63. Zhu, Y.M.; Gao, X.; Ni, Y.; Li, W.; Kent, T.A.; Qiao, S.G.; Wang, C.; Xu, X.X.; Zhang, H.L. Sevoflurane postconditioning attenuates reactive astrogliosis and glial scar formation after ischemia-reperfusion brain injury. *Neuroscience* **2017**, *356*, 125–141. [\[CrossRef\]](#) [\[PubMed\]](#)
64. Liddelow, S.A.; Barres, B.A. Reactive Astrocytes: Production, Function, and Therapeutic Potential. *Immunity* **2017**, *46*, 957–967. [\[CrossRef\]](#)
65. Hsu, J.Y.C.; Bourguignon, L.Y.W.; Adams, C.M.; Peyrollier, K.; Zhang, H.; Fandel, T.; Cun, C.L.; Werb, Z.; Noble-Haeusslein, L.J. Matrix metalloproteinase-9 facilitates glial scar formation in the injured spinal cord. *J. Neurosci.* **2008**, *28*, 13467–13477. [\[CrossRef\]](#) [\[PubMed\]](#)
66. Schachtrup, C.; Ryu, J.K.; Helmrick, M.J.; Vagena, E.; Galanakis, D.K.; Degen, J.L.; Margolis, R.U.; Akassoglou, K. Fibrinogen triggers astrocyte scar formation by promoting the availability of active TGF- β after vascular damage. *J. Neurosci.* **2010**, *30*, 5843–5854. [\[CrossRef\]](#) [\[PubMed\]](#)
67. Rüniger, T.M.; Quintanilla-Dieck, M.J.; Bhawan, J. Role of cathepsin K in the turnover of the dermal extracellular matrix during scar formation. *J. Investig. Dermatol.* **2007**, *127*, 293–297. [\[CrossRef\]](#)
68. Li, X.; Wu, Z.; Ni, J.; Liu, Y.; Meng, J.; Yu, W.; Nakanishi, H.; Zhou, Y. Cathepsin B Regulates Collagen Expression by Fibroblasts via Prolonging TLR2/NF- κ B Activation. *Oxid. Med. Cell. Longev.* **2016**, *2016*, 7894247. [\[CrossRef\]](#) [\[PubMed\]](#)

69. Lalmanach, G.; Saidi, A.; Marchand-Adam, S.; Lecaille, F.; Kasabova, M. Cysteine cathepsins and cystatins: From ancillary tasks to prominent status in lung diseases. *Biol. Chem.* **2015**, *396*, 111–130. [\[CrossRef\]](#)
70. Pan, Z.; Yang, K.; Wang, H.; Xiao, Y.; Zhang, M.; Yu, X.; Xu, T.; Bai, T.; Zhu, H. MFAP4 deficiency alleviates renal fibrosis through inhibition of NF- κ B and TGF- β /Smad signaling pathways. *FASEB J.* **2020**, *34*, 14250–14263. [\[CrossRef\]](#)
71. Sulimai, N.; Lominadze, D. Fibrinogen and Neuroinflammation During Traumatic Brain Injury. *Mol. Neurobiol.* **2020**, *57*, 4692–4703. [\[CrossRef\]](#)
72. Dietrich, N.; Lienenklaus, S.; Weiss, S.; Gekara, N.O. Murine Toll-Like Receptor 2 Activation Induces Type I Interferon Responses from Endolysosomal Compartments. *PLoS ONE* **2010**, *5*, e10250. [\[CrossRef\]](#)
73. Owens, B.M.J.; Moore, J.W.J.; Kaye, P.M. IRF7 regulates TLR2-mediated activation of splenic CD11c^{hi} dendritic cells. *PLoS ONE* **2012**, *7*, e41050. [\[CrossRef\]](#)
74. Liljeroos, M.; Vuolteenaho, R.; Rounioja, S.; Henriques-Normark, B.; Hallman, M.; Ojaniemi, M. Bacterial ligand of TLR2 signals Stat activation via induction of IRF1/2 and interferon-production. *Cell. Signal.* **2008**, *20*, 1873–1881. [\[CrossRef\]](#)
75. Nomiyama, H.; Osada, N.; Yoshie, O. The evolution of mammalian chemokine genes. *Cytokine Growth Factor Rev.* **2010**, *21*, 253–262. [\[CrossRef\]](#)
76. Portou, M.J.; Baker, D.; Abraham, D.; Tsui, J. The innate immune system, toll-like receptors and dermal wound healing: A review. *Vasc. Pharmacol.* **2015**, *71*, 31–36. [\[CrossRef\]](#)
77. Mann, D.L.; Topkara, V.K.; Evans, S.; Barger, P.M. Innate immunity in the adult mammalian heart: For whom the cell tolls. *Trans. Am. Clin. Clim. Assoc.* **2010**, *121*, 31–34.
78. Griffiths, M.R.; Gasque, P.; Neal, J.W. The regulation of the CNS innate immune response is vital for the restoration of tissue homeostasis (repair) after acute brain injury: A brief review. *Int. J. Inflamm.* **2010**, *2010*, 151097. [\[CrossRef\]](#) [\[PubMed\]](#)
79. Sato, M.; Sano, H.; Iwaki, D.; Kudo, K.; Konishi, M.; Takahashi, H.; Takahashi, T.; Imaizumi, H.; Asai, Y.; Kuroki, Y. Direct Binding of Toll-Like Receptor 2 to Zymosan, and Zymosan-Induced NF- κ B Activation and TNF-Secretion Are Down-Regulated by Lung Collectin Surfactant Protein A. *J. Immunol.* **2003**, *171*, 417–425. [\[CrossRef\]](#) [\[PubMed\]](#)
80. Marcel, L.; Pius, L.; Nicole, B.; Eckart, M.; Bernhard, M. Lymphocyte-specific chemokine receptor CXCR3: Regulation, chemokine binding and gene localization. *Eur. J. Immunol.* **1998**, *28*, 3696–3705.
81. Wijtman, M.; Scholten, D.J.; Roumen, L.; Canals, M.; Custers, H.; Glas, M.; Vreeker, M.C.A.; de Kanter, F.J.J.; de Graaf, C.; Smit, M.J.; et al. Chemical subtleties in small-molecule modulation of peptide receptor function: The case of CXCR3 biaryl-type ligands. *J. Med. Chem.* **2012**, *55*, 10572–10583. [\[CrossRef\]](#)
82. Zambusi, A.; Pelin Burhan, Ö.; Di Giaimo, R.; Schmid, B.; Ninkovic, J. Granulins Regulate Aging Kinetics in the Adult Zebrafish Telencephalon. *Cells* **2020**, *9*, 350. [\[CrossRef\]](#) [\[PubMed\]](#)
83. Kuroda, M.; Muramatsu, R.; Maedera, N.; Koyama, Y.; Hamaguchi, M.; Fujimura, H.; Yoshida, M.; Konishi, M.; Itoh, N.; Mochizuki, H.; et al. Peripherally derived FGF21 promotes remyelination in the central nervous system. *J. Clin. Investig.* **2017**, *127*, 3496–3509. [\[CrossRef\]](#)
84. Yang, J.; Cheng, X.; Qi, J.; Xie, B.; Zhao, X.; Zheng, K.; Zhang, Z.; Qiu, M. EGF enhances oligodendrogenesis from glial progenitor cells. *Front. Mol. Neurosci.* **2017**, *10*, 106. [\[CrossRef\]](#) [\[PubMed\]](#)
85. Vinukonda, G.; Hu, F.; Mehdizadeh, R.; Dohare, P.; Kidwai, A.; Juneja, A.; Naran, V.; Kierstead, M.; Chawla, R.; Kayton, R.; et al. Epidermal growth factor preserves myelin and promotes astrogliosis after intraventricular hemorrhage. *Glia* **2016**, *64*, 1987–2004. [\[CrossRef\]](#) [\[PubMed\]](#)
86. Pei, D.; Liu, N.; Li, D.; Yan, H.; Wang, Q.B.; Fang, Y.; Xie, L.; Li, H.P. Inhibition of platelet-derived growth factor receptor reduces reactive glia and scar formation after traumatic brain injury in mice. *Brain Res. Bull.* **2017**, *134*, 121–127. [\[CrossRef\]](#) [\[PubMed\]](#)
87. Robel, S.; Berninger, B.; Götz, M.; Gotz, M. The stem cell potential of glia: Lessons from reactive gliosis. *Nat. Rev. Neurosci.* **2011**, *12*, 88–104. [\[CrossRef\]](#)
88. Eugenin-von Bernhardt, J.; Dimou, L. NG2-glia, more than progenitor cells. In *Glial Cells in Health and Disease of the CNS; Advances in Experimental Medicine and Biology*; Springer: Cham, Switzerland, 2016; pp. 27–45. [\[CrossRef\]](#)
89. Zupanc, G.K. Adult neurogenesis and neuronal regeneration in the brain of teleost fish. *J. Physiol.* **2008**, *102*, 357–373. [\[CrossRef\]](#)
90. Zupanc, G.K. Towards brain repair: Insights from teleost fish. *Semin Cell Dev. Biol.* **2009**, *20*, 683–690. [\[CrossRef\]](#)
91. Zupanc, G.K. Neurogenesis and neuronal regeneration in the adult fish brain. *J. Comp. Physiol. A Neuroethol. Sens Neural Behav. Physiol.* **2006**, *192*, 649–670. [\[CrossRef\]](#) [\[PubMed\]](#)
92. Alunni, A.; Bally-Cuif, L. A comparative view of regenerative neurogenesis in vertebrates. *Development* **2016**, *143*, 741–753. [\[CrossRef\]](#)
93. Kizil, C.; Dudczig, S.; Kyritsis, N.; Machate, A.; Blaesche, J.; Kroehne, V.; Brand, M. The chemokine receptor cxcr5 regulates the regenerative neurogenesis response in the adult zebrafish brain. *Neural Dev.* **2012**, *7*, 27. [\[CrossRef\]](#) [\[PubMed\]](#)
94. Labbe, R.M.; Irimia, M.; Currie, K.W.; Lin, A.; Zhu, S.J.; Brown, D.D.; Ross, E.J.; Voisin, V.; Bader, G.D.; Blencowe, B.J.; et al. A comparative transcriptomic analysis reveals conserved features of stem cell pluripotency in planarians and mammals. *Stem Cells* **2012**, *30*, 1734–1745. [\[CrossRef\]](#)
95. Simkin, J.; Gawriluk, T.R.; Gensel, J.C.; Seifert, A.W. Macrophages are necessary for epimorphic regeneration in African spiny mice. *eLife* **2017**, *6*, e24623. [\[CrossRef\]](#) [\[PubMed\]](#)
96. Seifert, A.W.; Kiama, S.G.; Seifert, M.G.; Goheen, J.R.; Palmer, T.M.; Maden, M. Skin shedding and tissue regeneration in African spiny mice (*Acomys*). *Nature* **2012**, *489*, 561–565. [\[CrossRef\]](#) [\[PubMed\]](#)

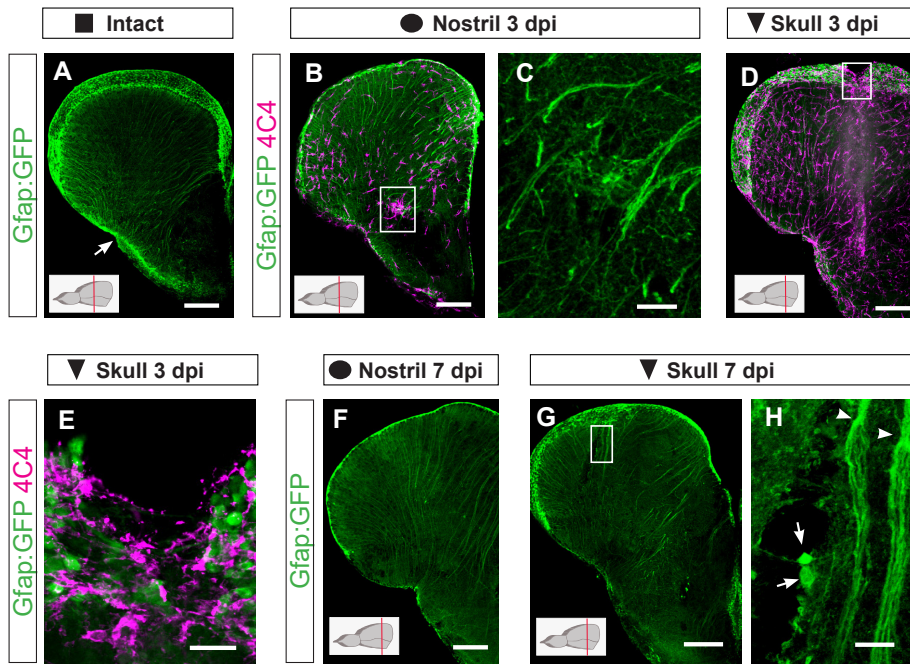
97. Brant, J.O.; Yoon, J.H.; Polvadore, T.; Barbazuk, W.B.; Maden, M. Cellular events during scar-free skin regeneration in the spiny mouse, *Acomys*. *Wound Repair Regen.* **2016**, *24*, 75–88. [[CrossRef](#)]
98. Sofroniew, M.V. Molecular dissection of reactive astrogliosis and glial scar formation. *Trends Neurosci.* **2009**, *32*, 638–647. [[CrossRef](#)] [[PubMed](#)]
99. Pekny, M.; Nilsson, M. Astrocyte activation and reactive gliosis. *Glia* **2005**, *50*, 427–434. [[CrossRef](#)] [[PubMed](#)]
100. Jin, W.N.; Shi, S.X.Y.; Li, Z.; Li, M.; Wood, K.; Gonzales, R.J.; Liu, Q. Depletion of microglia exacerbates postischemic inflammation and brain injury. *J. Cereb. Blood Flow Metab.* **2017**, *37*, 2224–2236. [[CrossRef](#)] [[PubMed](#)]
101. Fu, H.; Zhao, Y.; Hu, D.; Wang, S.; Yu, T.; Zhang, L. Depletion of microglia exacerbates injury and impairs function recovery after spinal cord injury in mice. *Cell Death Dis.* **2020**, *11*, 528. [[CrossRef](#)]
102. Grade, S.; Götz, M. Neuronal replacement therapy: Previous achievements and challenges ahead. *npj Regen. Med.* **2017**, *2*, 29. [[CrossRef](#)]
103. Grandel, H.; Brand, M. Comparative aspects of adult neural stem cell activity in vertebrates. *Dev. Genes Evol.* **2013**, *223*, 131–147. [[CrossRef](#)]
104. Kizil, C.; Kaslin, J.; Kroehne, V.; Brand, M. Adult neurogenesis and brain regeneration in zebrafish. *Dev. Neurobiol.* **2012**, *72*, 429–461. [[CrossRef](#)] [[PubMed](#)]
105. Dunkin, C.S.; Pleat, J.M.; Gillespie, P.H.; Tyler, M.P.; Roberts, A.H.; McGrouther, D.A. Scarring occurs at a critical depth of skin injury: Precise measurement in a graduated dermal scratch in human volunteers. *Plast. Reconstr. Surg.* **2007**, *119*, 1722–1724. [[CrossRef](#)] [[PubMed](#)]
106. Bouabe, H.; Liu, Y.; Moser, M.; Bosl, M.R.; Heesemann, J. Novel highly sensitive IL-10-β-lactamase reporter mouse reveals cells of the innate immune system as a substantial source of IL-10 in vivo. *J. Immunol.* **2011**, *187*, 3165–3176. [[CrossRef](#)] [[PubMed](#)]
107. Hsieh, C.L.; Niemi, E.C.; Wang, S.H.; Lee, C.C.; Bingham, D.; Zhang, J.; Cozen, M.L.; Charo, I.; Huang, E.J.; Liu, J.; et al. CCR2 deficiency impairs macrophage infiltration and improves cognitive function after traumatic brain injury. *J. Neurotrauma* **2014**, *31*, 1677–1688. [[CrossRef](#)] [[PubMed](#)]
108. Wattananit, S.; Tornero, D.; Graubardt, N.; Memanishvili, T.; Monni, E.; Tatarishvili, J.; Miskinyte, G.; Ge, R.; Ahlenius, H.; Lindvall, O.; et al. Monocyte-Derived Macrophages Contribute to Spontaneous Long-Term Functional Recovery after Stroke in Mice. *J. Neurosci.* **2016**, *36*, 4182–4195. [[CrossRef](#)]
109. Rothhammer, V.; Maccanfroni, I.D.; Bunse, L.; Takenaka, M.C.; Kenison, J.E.; Mayo, L.; Chao, C.C.; Patel, B.; Yan, R.; Blain, M.; et al. Type I interferons and microbial metabolites of tryptophan modulate astrocyte activity and central nervous system inflammation via the aryl hydrocarbon receptor. *Nat. Med.* **2016**, *22*, 586–597. [[CrossRef](#)]
110. Rothhammer, V.; Borucki, D.M.; Tjon, E.C.; Takenaka, M.C.; Chao, C.C.; Ardura-Fabregat, A.; de Lima, K.A.; Gutierrez-Vazquez, C.; Hewson, P.; Staszewski, O.; et al. Microglial control of astrocytes in response to microbial metabolites. *Nature* **2018**, *557*, 724–728. [[CrossRef](#)]
111. Kielian, T. Toll-like receptors in central nervous system glial inflammation and homeostasis. *J. Neurosci. Res.* **2006**, *83*, 711–730. [[CrossRef](#)]
112. Krauthausen, M.; Saxe, S.; Zimmermann, J.; Emrich, M.; Heneka, M.T.; Müller, M. CXCR3 modulates glial accumulation and activation in cuprizone-induced demyelination of the central nervous system. *J. Neuroinflammation* **2014**, *11*, 109. [[CrossRef](#)]
113. Goldberg, S.H.; van der Meer, P.; Hesselgesser, J.; Jaffer, S.; Kolson, D.L.; Albright, A.V.; Gonzalez-Scarano, F.; Lavi, E. CXCR3 expression in human central nervous system diseases. *Neuropathol. Appl. Neurobiol.* **2001**, *27*, 127–138. [[CrossRef](#)]
114. Bsibsi, M.; Ravid, R.; Gveric, D.; van Noort, J.M. Broad expression of Toll-like receptors in the human central nervous system. *J. Neuropathol. Exp. Neurol.* **2002**, *61*, 1013–1021. [[CrossRef](#)]
115. Dzamko, N.; Gysbers, A.; Perera, G.; Bahar, A.; Shankar, A.; Gao, J.; Fu, Y.; Halliday, G.M. Toll-like receptor 2 is increased in neurons in Parkinson's disease brain and may contribute to alpha-synuclein pathology. *Acta Neuropathol.* **2017**, *133*, 303–319. [[CrossRef](#)] [[PubMed](#)]
116. Mestre, H.; Du, T.; Sweeney, A.M.; Liu, G.; Samson, A.J.; Peng, W.; Mortensen, K.N.; Stæger, F.F.; Bork, P.A.R.; Bashford, L.; et al. Cerebrospinal fluid influx drives acute ischemic tissue swelling. *Science* **2020**, *367*, eaax7171. [[CrossRef](#)] [[PubMed](#)]
117. Lepko, T.; Pusch, M.; Müller, T.; Schulte, D.; Ehses, J.; Kiebler, M.; Hasler, J.; Huttner, H.B.; Vandenbroucke, R.E.; Vandendriessche, C.; et al. Choroid plexus-derived miR-204 regulates the number of quiescent neural stem cells in the adult brain. *EMBO J.* **2019**, *38*, e100481. [[CrossRef](#)] [[PubMed](#)]
118. Sirko, S.; Behrendt, G.; Johansson, P.A.; Tripathi, P.; Costa, M.; Bek, S.; Heinrich, C.; Tiedt, S.; Colak, D.; Dichgans, M.; et al. Reactive glia in the injured brain acquire stem cell properties in response to sonic hedgehog. [corrected]. *Cell Stem Cell* **2013**, *12*, 426–439. [[CrossRef](#)] [[PubMed](#)]



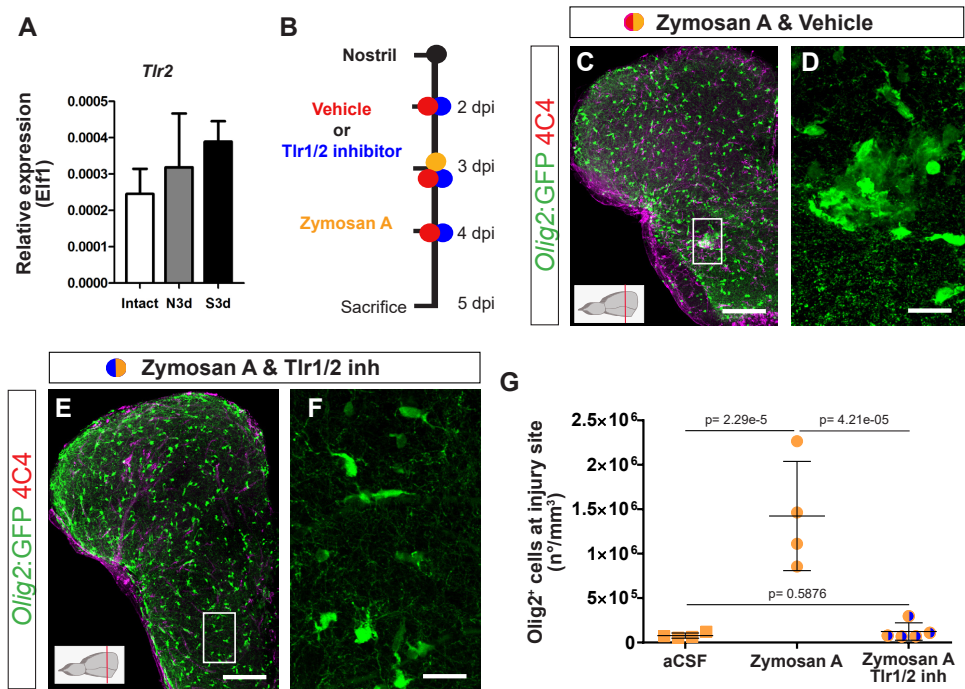
Supplementary Figure S1



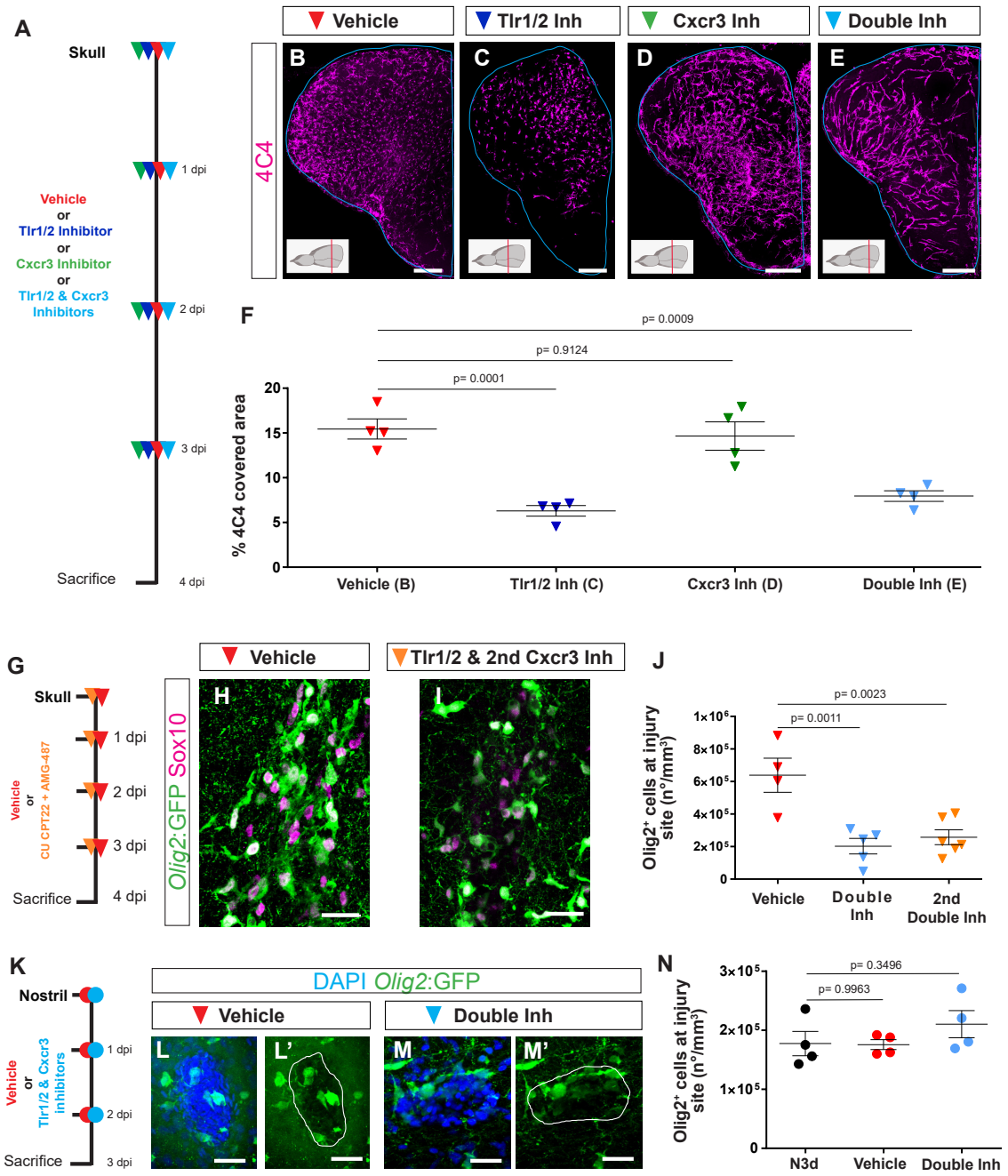
Sanchez-Gonzalez et al., 2021 Supplementary Figure S2



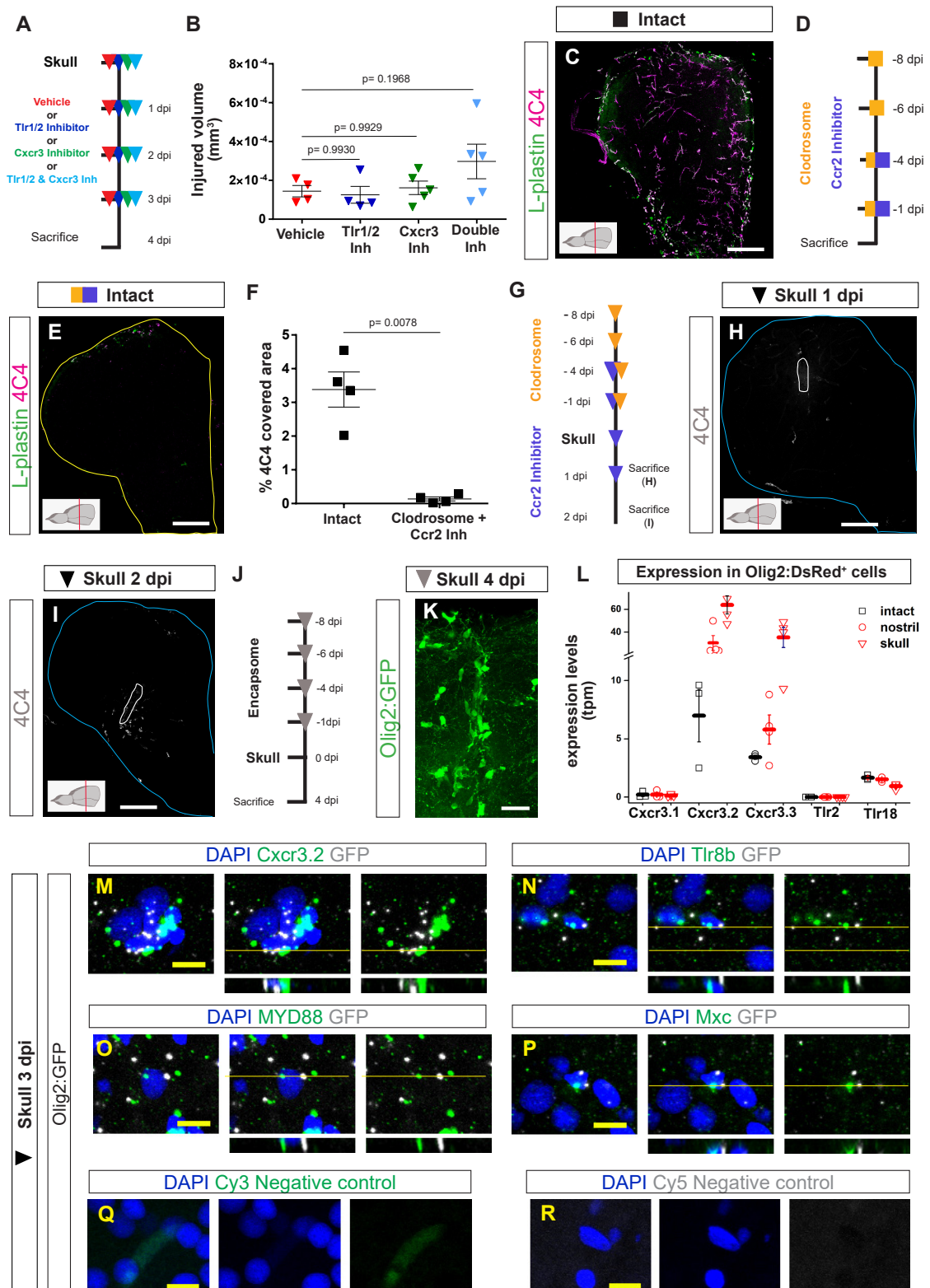
Sanchez-Gonzalez et al., 2021 Supplementary Figure S3



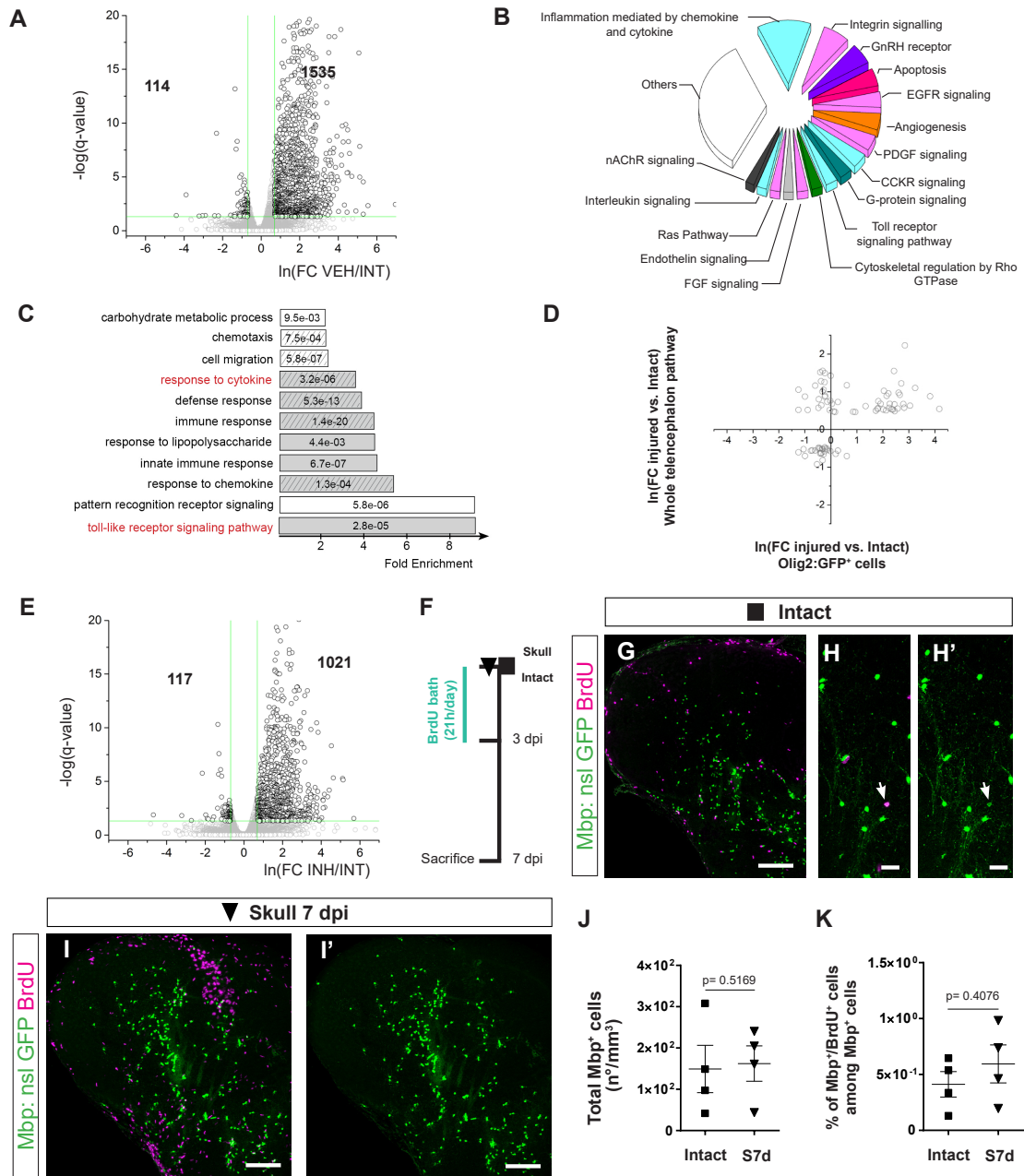
Sanchez-Gonzalez et al., 2021 Supplementary Figure S4



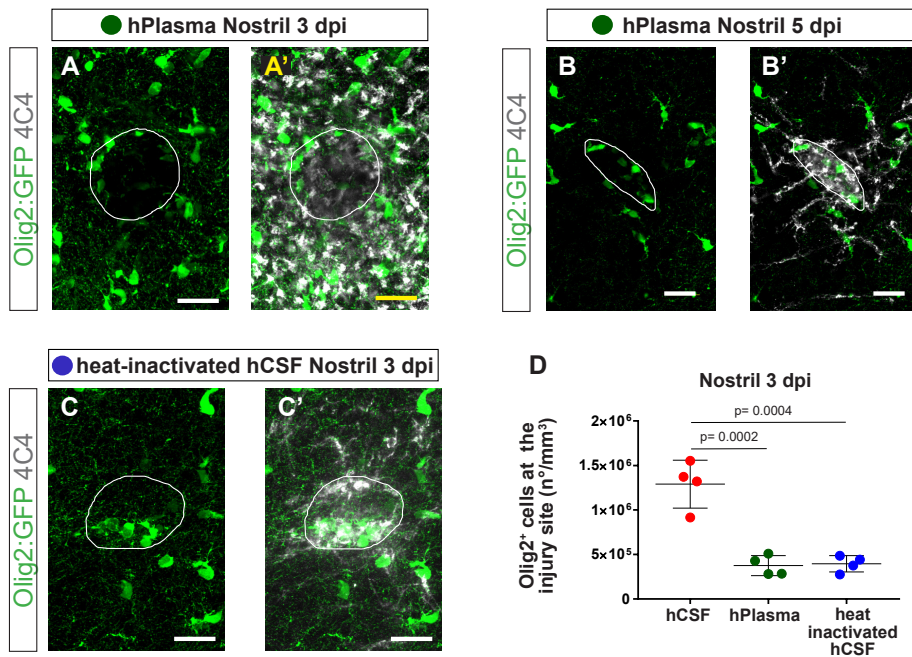
Sanchez-Gonzalez et al., 2021 Supplementary Figure S5



Sanchez-Gonzalez et al., 2021 Supplementary Figure S6



Sanchez-Gonzalez et al., 2021 Supplementary Figure S7



Sanchez-Gonzalez et al., 2021 Supplementary Figure S8

A mutation in Cxcr3

```

35 D F S D S P P C P Q D F S L N F D R T F L P A P Y S L L F L L G L L G N
WT allele gacttctctgactcccgcccctgcccaaagattttagcctgaaactttgacagaaaccttctgcccagccctacagcctctcttcttctgtgggctgtaggcaat
35 D F S D S P P A H R I S A T L T E P S C Q P S T A S S S C W G C A A M
MUT allele 1 gacttctctgactcccgcctgcccacaggatttcagcctgaaactttgacagaaaccttctgcccagccctacagcctctcttcttctgtgggctgtaggcaat
35 D F S D S P P A H R I S A T L T E P S C Q P S T A S S S C W G C A A M
MUT allele 2 gacttctctgactcccgcctgcccacaggatttcagcctgaaactttgacagaaaccttctgcccagccctacagcctctcttcttctgtgggctgtaggcaat

71 G A V A A V L L S Q R T A L S S T D T F L L H L A V A D V L L V L T L P
WT allele gggggcgtggctgctgtgctactgagtcagcgcactgcctgagcagcagggacaccttctgctccactggtgtagccgatttctgctgtgttactcttcca
71 G R W L L C Y V S A L P A A R T P S C S T W L V L T L P
MUT allele 1 gggggcgtggctgctgtgctactgagtcagcgcactgcctgagcagcagggacaccttctgctccactggtgtagcgtgtgtgtagcttcttca
71 G R W L L C Y V S A L P A A R T P S C S T W L L L T L P
MUT allele 2 gggggcgtggctgctgtgctactgagtcagcgcactgcctgagcagcagggacaccttctgctccactggtgtagcgtgtgtgtgtgtagcttcttca
    
```

B mutation in Tlr2

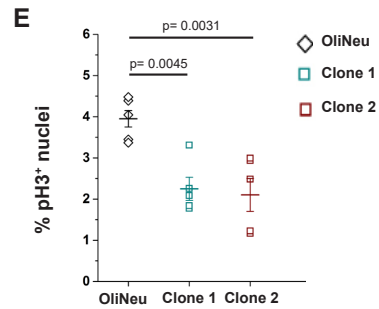
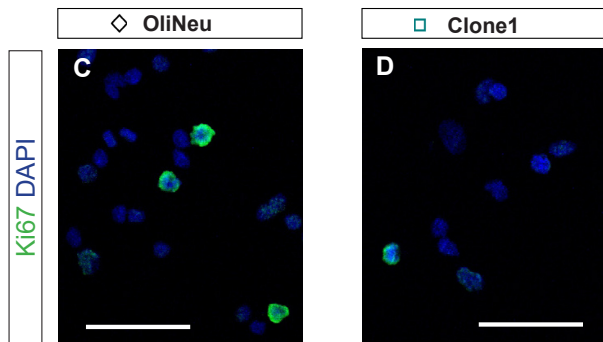
```

57 L D L S F N K I T Y I G H G D L R A C A N L Q V L M L K S S R I N T I E G D A
WT allele cttgacctgtcttcaacaaatacactacattggccatggtagacctccagcgtgtgccaacctccaggttctgatgttgaagtcacagcaatacaatacaatagaggagagcct
57 L D L S F N K M V T S E R V R T S R F C S P A E S I Q R E F P
MUT allele 1 cttgacctgtcttcaacaagatggtagacctccagcgtgtgccaacctccaggttctgatgttgaagtcacagcaatacaatacaatagaggagagcct
57 L D L S F N K I T Y I G
MUT allele 2 cttgacctgtcttcaacaagatcactacattggc

96 F Y S L G S L E H L D L S D N H L S S L S S W F G P L S S L K Y L N L M G N
WT allele ttttattctctggcagctcttgaacatttggatttctgataatccactatctagtttatctctcctgggtcgggcccttctctcttgaataactaaacttaagggaaat
96 F I L W A V L N I W I C L I I T Y L V Y L P P G S G P F P L N T T W E I
MUT allele 1 ttttattctctggcagctcttgaacatttggatttctgataatccactatctagtttatctctcctgggtcgggcccttctctcttgaataactaaacttaagggaaat
MUT allele 2

135 P Y Q T L G V T S L F P N L T N L Q T L R I G N V E T F S E I R R I D F A G L
WT allele cttaccagacactgggggtaacatcgcttttcccaatctcaaaatttcaaaacctcaggataggaatgtagagacttccagtgagataaggaagatagatttctggcctg
135 L T R H W G * H R F F P I S Q I Y K P S G E M R R L S V R G E I L L G
MUT allele 1 cttaccagacactgggggtaacatcgcttttcccaatctcaaaatttcaaaacctcaggataggaatgtagagacttccagtgagataaggaagatagatttctggcctg
MUT allele 2

174 T S L N E L E I K A L S L R N Y Q S Q S L K S I R D I H H L T L H L S E S
WT allele acttctctcaatgaacttgaattaaggcattaagtctccggaattatcagtcocaaagctaaagtcgatccgacatcgaacactttcaacttaagcagctct
174 L L S M N L K L R H V S G I I S P K V S R S A T S I T L P T A S
MUT allele 1 acttctctcaatgaacttgaattaaggcattaagtctccggaattatcagtcocaaagctaaagtcgatccgacatccatcactgactcttcaacttaagcagctct
69 I H H L T L H L S E S
MUT allele 2 atccatcactgactcttcaacttaagcagctct
    
```



Sanchez-Gonzalez et al., 2021 Supplementary Figure S9

2.2 Aim of study II

In this study, we aimed to address the activation states of microglia upon injury in adult zebrafish telencephalons, the necessity of regulating clearance of phase-separated TDP-43 condensates for deactivating immune responses, as well as the role of granulins in regulating these processes.

TDP-43 condensates and lipid droplets regulate the reactivity of microglia and regeneration after traumatic brain injury

Alessandro Zambusi*, Klara Tereza Novoselc*, Saskia Hutten, Sofia Kalpazidou, **Christina Koupourtidou**, Rico Schieweck, Sven Aschenbroich, Lara Silva, Ayse Seda Yazgili, Bettina Schmid, Claire Delbridge, Swetlana Sirko, Zeynep Irem Günes, Sabine Liebscher, Jürgen Schlegel, Hananeh Aliee, Fabian Theis, Silke Meiners, Michael Kiebler, Dorothee Dormann and Jovica Ninkovic

* These authors contributed equally to the manuscript

My contribution to this publication in detail:

For this paper, I was involved in the scRNA-seq and snRNA-seq experiments and bioinformatic analysis. More specifically, I assisted from the step of cell/nuclei preparation until the library preparation, aligned the data, established the bioinformatic analysis pipeline, and supported the downstream bioinformatic analysis. I was also involved in editing and reviewing the paper.

The preprint below has not undergone peer review or any post-submission improvements or corrections. The Version of Record of this article is published in Nature Neuroscience (2022) with title ***“TDP-43 condensates and lipid droplets regulate the reactivity of microglia and regeneration after traumatic brain injury”***, and is available online at <https://doi.org/10.1038/s41593-022-01199-y>

1 **Phase-separated TDP-43 regulates the activation states of microglia**
2 **after traumatic brain injury**

3 Alessandro Zambusi^{1,2*}, Klara Tereza Novoselc^{1,2*}, Christina Koupourtidou^{1,2}, Sofia
4 Kalpazidou¹, Saskia Hutten¹, Lara Silva¹, Bettina Schmid³, Claire Delbridge⁴, Jürgen
5 Schlegel⁴, Hananeh Aliee⁵, Fabian Theis⁵, Dorothee Dormann^{1,7} and Jovica
6 Ninkovic^{1,6,7,8#}

7

8 ¹ Biomedical Center Munich (BMC), Department of Cell Biology and Anatomy, LMU,
9 Munich, Germany

10 ² Graduate School of Systemic Neurosciences, LMU, Munich, Germany.

11 ³ German Center for Neurodegenerative Diseases (DZNE), Munich, Germany

12 ⁴ Institute of Pathology, Faculty of Medicine, TUM, Munich, Germany

13 ⁵ Institute of Computational Biology, Helmholtz Zentrum Munich, Munich, Germany

14 ⁶ Biomedical Center Munich (BMC), Faculty of Medicine, LMU, Munich, Germany

15 ⁷ Munich Cluster for Systems Neurology SYNERGY, LMU, Munich, Germany

16 ⁸ Institute of Stem Cell Research, Helmholtz Zentrum Munich, Munich, Germany

17

18 * these authors equally contributed to the work

19 #Correspondence to: ninkovic@helmholtz-muenchen.de

20

21 **Abstract**

22

23 Inactivation of pathology-activated microglia is crucial to prevent chronic
24 neuroinflammation and tissue scarring. We identified an injury-induced microglial state
25 at the transition between activation and homeostasis in injured zebrafish brains, which
26 was characterized by accumulation of lipid droplets and phase-separated TDP-43
27 condensates. Granulin-mediated clearance of both lipid droplets and TDP-43
28 condensates was necessary and sufficient to promote this microglial transition and the
29 return to homeostatic function. Clearance of phase-separated TDP-43 condensates
30 promoted both the return of activated microglia back to homeostasis and scarless
31 regeneration. Importantly, the activated state of microglia also correlated with the
32 accumulation of lipid droplets, TDP-43 condensates and stress granules in patients
33 with ischemic stroke, thus supporting the existence of a similar regulatory mechanism
34 in humans. Together, our results identified a drug-targetable mechanism required for
35 the inactivation of microglia, which is necessary to avoid chronic neuroinflammation
36 and has high potential for new therapeutic applications in humans.

1 Main

2
3 Regeneration of the damaged adult mammalian central nervous system (CNS),
4 including that in humans, is largely limited^{1,2}. Despite the injury-induced enhancement
5 of adult neurogenesis and neuronal migration to injury sites, young neurons fail to
6 integrate into pre-existing neural circuits and to survive³⁻⁷. Similarly, the numbers of
7 transplanted neurons decrease over time, and their functional benefits decline in
8 different models of neurodegenerative diseases^{8,9}. This response is largely due to an
9 adverse environment generated by prolonged neuroinflammation and glial scar
10 formation^{10,11}. Both neuroinflammation and the glial scarring are initially beneficial in
11 limiting the expansion of the damage, but they later hinder functional recovery by
12 tissue remodeling and result in the generation of an inflamed environment^{2,12-14}.

13 Under physiological conditions, microglia, the brain-resident immune cells, are
14 dynamically activated by environmental and microglia-intrinsic pathways and
15 subsequently surveil the local environment and shape the organization and
16 functionality of neural circuits¹⁵⁻²¹. Microglial activation is, however, tightly controlled
17 by the balance between activating “ON” and inactivating “OFF” signals. Indeed, the
18 loss of “OFF” signals, such as TREM2, leads to the development of disease-
19 associated microglia, which can enhance the progression of neurodegenerative
20 phenotypes²²⁻²⁷. Importantly, the injury-induced inflammatory response activated in
21 the mammalian brain lacks “OFF” signals, thus leading to persistent
22 neuroinflammation and cellular stress.

23 In contrast to that in mammals, the injured CNS in adult zebrafish displays
24 exceptional regenerative capacity, including the generation of long-lasting neurons
25 from endogenous neural stem cell pools (restorative neurogenesis) in different areas
26 of the brain and the spinal cord^{28,29,38,30-37}. Injury in the zebrafish CNS induces only
27 transient neuroinflammation, which is terminated in a timely manner, promoting
28 neuronal integration and the resolution of scar tissue^{29-31,39-43}. Therefore,
29 understanding of the cellular dynamics and signaling cues underlying the resolution of
30 the inflammatory cascade in the zebrafish CNS is crucial to ameliorate the
31 regenerative outcomes in the mammalian CNS in response to traumatic brain injury
32 and neurodegenerative diseases.

33 Here, we sought to investigate the microglial dynamics in the injured adult
34 zebrafish telencephalon. We identified the transient state of activated pro-regenerative
35 microglia that spontaneously return to homeostasis in a granulin-dependent manner.
36 Furthermore, we demonstrated that granulin-mediated clearance of phase-separated
37 TDP-43 condensates in microglial cells is fundamental for the activation of “OFF”
38 signals in activated microglia and the scarless regeneration in the adult zebrafish CNS.
39 These results highlight liquid-liquid phase separation (LLPS) of TDP-43 as valuable
40 target for new approaches to improve CNS regeneration in response to traumatic brain
41 injury and neurodegenerative diseases. The translational value of our research is
42 strengthened by the observation of high microglial reactivity correlating with the
43 presence of TDP-43 condensates and lipid droplets in human patients with stroke.

44 **Stab wound injury induces a pro-regenerative signature in a *granulin a*-** 45 **expressing microglial subpopulation**

46
47
48 The activation state of microglia is a key regulator of neuroinflammation during aging,
49 neurodegeneration and CNS injuries⁴⁴⁻⁵⁰. Moreover, injury-induced activation of
50 immune cells is necessary to initiate restorative programs in regeneration-competent

1 species such as zebrafish³⁰. However, little is known about the mechanisms
2 promoting the transition of activated microglia back to homeostasis, and the avoidance
3 of long-lasting and chronic neuroinflammation. Therefore, we first analyzed the
4 dynamics of the microglial response to injury in the adult zebrafish telencephalon (Fig.
5 1A), on the basis of the expression of 4C4, an established marker for labeling immune
6 cells in the zebrafish telencephalon²⁹. Indeed, we observed ramified, homeostatic
7 microglia throughout the intact telencephalic parenchyma (Fig. 1A). Stab wound injury
8 through the zebrafish nostrils induced an immediate microglial response that reached
9 a maximum intensity 3 days post-injury (dpi), as evidenced by the accumulation of
10 activated 4C4⁺ microglial cells at injury sites (red square in Fig. 1A). However, the
11 4C4⁺ microglial cell accumulation was only transient and resolved by 7 dpi, in
12 agreement with the observation of complete scarless tissue regeneration at the same
13 time point (Fig. 1A, Extended Data Fig. 1A, B). Microglial activation was restricted to
14 the site of the injury, because reactive microglia were not detected far from it (blue
15 square in Fig. 1A). This finding is consistent with recent observations that different
16 microglial populations emerge after brain injury and neurodegenerative diseases, and
17 have distinct dynamics and roles in regulating neuroinflammation, including the
18 modulation of other scar-forming cells^{51,52}.

19 To assess the composition of microglia and identify the molecular pathways
20 controlling their dynamics during scarless regeneration, we followed the transcriptional
21 changes at the single-cell level in the whole zebrafish telencephalon in response to
22 brain injury. We isolated cells from intact and injured wildtype (Wt) telencephali (3 and
23 7 dpi) and compared their transcriptomes with a droplet-based single cell RNA-
24 sequencing (scRNA-seq) platform (10x Genomics Chromium) (Fig. 1B, Extended Data
25 Fig. 1A). After applying quality control filters, we identified 29603 single cells uniformly
26 distributed over different conditions (Extended Data Fig. 1C). Unsupervised clustering
27 of single cells according to their transcriptomes revealed 30 distinct clusters (Fig. 1B,
28 Extended Data Fig. 1A). We identified neuronal clusters as well as distinct glial
29 populations, including microglia, oligodendrocyte lineage cells and radial glial cells
30 (RGCs), on the basis of the expression of established markers characterizing these
31 populations (Fig. 1B, Extended Data Fig. 1A, D). We first analyzed changes in the
32 abundance of cellular populations (Extended Data Fig. 1B). We detected an increase
33 in microglial and oligodendroglial cell abundance at 3 dpi (Extended Data Fig. 1B) and
34 a concomitant decrease in RGCs, findings that may be explained by direct damage to
35 RGC processes spanning the parenchyma and subsequent RGC death. The
36 abundance of oligodendroglial and microglial cells decreased at 7 dpi and almost
37 reached the levels detected in intact brains (Extended Data Fig. 1B). The observed
38 kinetics of microglial cells was compatible with the hypothesis that regeneration-
39 competent species have mechanisms that prevent the prolonged activation and
40 amplification of immune cells, and subsequent chronic neuroinflammation. Therefore,
41 we focused our analysis on the transcriptional changes in microglial cells (cluster 17
42 in Fig. 1B) during the course of regeneration. We identified 420 differentially expressed
43 genes (DEGs) ($\log_2\text{FC} \geq 1$; $\text{FDR} \leq 0.05$) at 3 dpi compared with other conditions (intact
44 and 7 dpi) (Extended Data Fig. 1E; Supplementary Table 1). GO term analysis (DAVID
45 6.8) of enriched DEGs identified innate immunity (Toll-like receptor (TLR) signaling
46 pathway), inflammation (cytokine-cytokine receptor interaction), lipid metabolism,
47 extracellular matrix remodeling (collagen trimer) and phospholipase inhibitor activity
48 as enriched processes (Fig. 1C; Supplementary Table 1). These processes have been
49 associated with pro-regenerative microglia emerging after spinal cord injury in mice⁵¹.
50 Interestingly, the comparison between microglial cells isolated from intact and injured

1 telencephali at 7 dpi revealed only a limited number of DEGs without any GO term
2 enrichment (Extended Data Fig. 1E), in line with the transient activation and timely
3 transition of microglia to the homeostatic state observed in our previous
4 immunohistochemical analysis (Fig. 1A).

5 To further gain insights into the transient microglial activation and its importance
6 in scarless tissue restoration, we isolated cells belonging to microglial cluster 17,
7 performed unsupervised subclustering and identified six distinct states with specific
8 transcriptional signatures (Fig. 1D, E; Supplementary Table 2). RNA velocity-based
9 analysis of cellular dynamics^{53,54} revealed three parallel, non-overlapping trajectories
10 (Wt-MG4 \Rightarrow Wt-MG1 \Rightarrow Wt-MG2; Wt-MG3 \Rightarrow Wt-MG2; Wt-MG5 \Rightarrow Wt-MG0 \Rightarrow Wt-
11 MG2) (Fig. 1F). Numerous pro-inflammatory programs associated with immune cell
12 activation, including tumor necrosis factor (TNF), TLR, NOD-like receptor and IL1-
13 dependent signaling pathways, were detected with different patterns in distinct
14 subclusters (Supplementary Table 2). The IL1-dependent signaling pathway was
15 enriched in Wt-MG3, whereas the TNF- and TLR-dependent signaling pathways were
16 enriched exclusively in Wt-MG0. Interestingly, the TNF-, TLR- and NOD-signaling
17 pathways were downregulated in Wt-MG4 (Supplementary Table 2), thus suggesting
18 that microglial cells belonging to this trajectory might have anti-inflammatory
19 properties. These observations are consistent with distinct activated microglia
20 emerging after injury in the adult zebrafish telencephalon and suggest that specific
21 regulatory mechanisms may be involved in their return to a homeostatic state.

22 Interestingly, all three trajectories converged on the Wt-MG2 state, the most abundant
23 state in the intact brain (Fig. 1E, F). Functional analysis of genes enriched in Wt-MG2
24 microglia revealed over-representation of glycolysis, vacuolar acidification and
25 lysosome composition, and under-representation of pro-inflammatory cytokines
26 (Supplementary Table 2), findings indicative of *in vivo* homeostatic microglia involved
27 in tissue surveillance⁵⁵⁻⁵⁸. Therefore, we further analyzed injury-induced microglial
28 states transitioning back to Wt-MG2 (homeostatic microglia) to reveal the mechanisms
29 promoting the inactivation of microglial cells in the zebrafish CNS at 3 dpi. We
30 particularly focused on the Wt-MG0 state, because it displayed a significant increase
31 in proportion at 3 dpi, coinciding with the peak of microglial accumulation at injury sites,
32 followed by a significant decrease and return to normal levels at 7 dpi, thus faithfully
33 reproducing the dynamics of 4C4⁺ microglial cells at injury sites observed by
34 immunohistochemistry (Fig. 1A, E). Wt-MG0 cells displayed enriched expression of
35 genes identified in pro-regenerative microglia induced after spinal cord injury in
36 neonatal mice⁵¹, including *ctsba*, *anxa1*, *anxa2* and *anxa5* (Fig. 1G). Moreover, the
37 Wt-MG0 state was characterized by high expression of *granulin a* (*grna*) (Fig. 1H),
38 encoding a secreted factor that regulates inflammation, promotes wound healing and
39 modulates the formation of lipid droplets, first-line intracellular defenses that activate
40 innate immunity and sequester cytotoxic compounds detrimental to other cells
41^{46,59,68,60-67}. Indeed, Wt-MG0 cells were also enriched in genes associated with lipid
42 droplet-accumulating microglia (Fig. 1I, Extended Data Fig. 1F). On the basis of these
43 results, we propose that Wt-MG0 cells are the population of microglial cells that
44 accumulate at injury sites and activate specific programs promoting regeneration.
45 When regeneration is terminated, activated Wt-MG0 cells require the initiation of anti-
46 inflammatory programs, including granulins (Grns), to transition back to the
47 homeostatic Wt-MG2 state. In line with this hypothesis, we detected significant
48 upregulation of different members of the granulin family (*grna*, *grnb* and *grn1-2*) at 3
49 dpi and their return to basal levels at 7 dpi (Fig. 1J, Extended Data Fig. 1G).

1 Granulins are necessary and sufficient to limit prolonged microglial activation 2 at injury sites

3
4 To address the hypothesis that granulins are required for the transition from a pro-
5 inflammatory to a homeostatic microglial state, we assessed the microglial reactivity
6 to stab wound injury in granulin-deficient zebrafish^{69,70}. Because Wt-MG0 microglia
7 express both *grna* and *grnb* (gene duplication of mammalian progranulin (PGRN)), we
8 used a composite mutant (Grn-deficient) to avoid possible compensatory
9 mechanisms. As expected, 4C4⁺ microglial cells accumulated at injury sites in Wt
10 animals at 3 dpi and we did not detect any 4C4⁺ microglial cell accumulation at the
11 injury site at 7 dpi (Fig. 2A). Interestingly, Grn-deficient microglia accumulated at injury
12 sites in a manner indistinguishable from that of Wt microglia at 3 dpi, thus supporting
13 that the injury-induced activation of microglial cells is Grn independent (Fig. 2A).
14 However, Grn-deficient microglial cell accumulation, in contrast to that of Wt cells, was
15 still detected at injury sites at 7 dpi (Fig. 2A). Because scRNA-seq analysis revealed
16 numerous genes associated with high lipid droplet content in Wt-MG0 microglia (Fig.
17 1I), thus indicating their activated state⁴⁶, we assessed the lipid droplet formation in
18 Wt and Grn-deficient brains in response to injury by using an antibody against the lipid
19 droplet surface protein perilipin 3 (Plin3) (Fig. 2A-C, Extended Data Fig. 2A, B) or
20 BODIPY (Extended Data Fig. 2C). Plin3⁺ lipid droplets were nearly absent from both
21 Wt and Grn-deficient intact brains (Fig. 2A). Plin3⁺ lipid droplets were detected after
22 injury, almost exclusively in the 4C4⁺ microglial cells accumulating at injury sites at 3
23 dpi in both Wt and Grn-deficient animals (Fig. 2A-C, Extended Data Fig. 2B). In line
24 with their prolonged retention at injury sites, Grn-deficient 4C4⁺ microglia maintained
25 elevated numbers of Plin3⁺ and BODIPY⁺ lipid droplets at 7 dpi, whereas lipid droplets
26 were completely cleared in Wt animals (Fig. 2A-C, Extended Data Fig. 2C). To further
27 substantiate these observations, we isolated microglial cells identified by scRNA-seq
28 from Wt (Fig. 1B, D) and Grn-deficient telencephali (Extended Data Fig. 4A-D), and
29 analyzed the expression of genes enriched in lipid droplet-accumulating microglia⁴⁶.
30 The expression of these genes was comparable in microglia isolated from the intact
31 brains of both genotypes (Fig. 2D). Similarly, this set of genes was comparably
32 induced in Wt and Grn-deficient microglia at 3 dpi. However, whereas the expression
33 of most lipid droplet-related genes returned to normal levels in Wt microglia at 7 dpi, it
34 persisted at high levels in Grn-deficient microglia (Fig. 2D), in agreement with the
35 immunohistochemistry results for Plin3⁺ and BODIPY⁺ lipid droplets in the injured
36 brains of Wt and Grn-deficient animals (Fig. 2A, Extended Data Fig. 2C). Quantitative
37 lipid content analysis of intact and injured (7 dpi) Wt and Grn-deficient telencephali
38 revealed an increase in the relative abundance of triacylglycerols (TAGs) and
39 diacylglycerols (DAGs), major components of lipid droplets, in the injured brains of
40 Grn-deficient animals compared with Wt brains at 7 dpi (Fig. 2E, Extended Data Fig.
41 2D). These results were similar to the changes reported in lipidomic analysis of
42 progranulin (PGRN)-deficient mouse brains⁷¹.

43 To verify the direct roles of granulins in regulating lipid droplet clearance and
44 transition to a homeostatic state of microglial cells at injury sites, we injected
45 recombinant progranulin (PGRN) while performing injury in Grn-deficient animals (Fig.
46 2F). Intraparenchymal injection of recombinant PGRN was sufficient to resolve the
47 microglial cell accumulation at injury sites and to promote the clearance of lipid
48 droplets in Grn-deficient microglia at 7 dpi (Fig. 2G-I), with similar kinetics to that in Wt
49 animals.

1 Collectively, our data support the roles of granulins in clearing injury-induced
2 lipid droplets in microglial cells and promoting their transition back to a homeostatic
3 state.

4
5 **Granulin deficiency-induced neuroinflammation prolongs glial reactivity at**
6 **injury sites and impairs restorative neurogenesis**

7
8 The interaction of immune cells with resident parenchymal glia is the key determinant
9 of scar formation in the mammalian brain after stroke or traumatic brain injury². The
10 prolonged accumulation of 4C4⁺ microglial cells at injury sites and the excessive lipid
11 droplet formation in Grn-deficient animals prompted us to investigate whether this
12 prolonged neuroinflammation changed glial reactivity in response to injury, possibly
13 through causing the scarless regeneration in zebrafish to transition to a scarring model
14 typical of the mammalian CNS. To examine the reaction of parenchymal cells
15 belonging to the oligodendrocyte lineage, we used the pan-oligodendrocyte marker
16 Sox10⁷² and followed the reaction of Sox10⁺ cells to injury in Wt and Grn-deficient
17 animals (Fig. 3A, B, Extended Data Fig. 3A-C; Supplementary Videos 1-3). Wt Sox10⁺
18 oligodendroglial cells responded to the injury with similar kinetics to that in 4C4⁺
19 microglial cells (Fig. 1A, 3A). Despite the transient accumulation of Sox10⁺ cells at
20 injury sites at 3 dpi, we observed no glial cell accumulation at 7 or 21 dpi in Wt brains
21 (Fig. 3A, B; Supplementary Video 1). Grn-deficient Sox10⁺ oligodendroglial cells
22 accumulated similarly to Wt cells at injury sites at 3 dpi, thus further supporting a Grn-
23 independent initial glial response to injury (Fig. 3A, B). However, Sox10⁺ cell
24 accumulation still occurred at injury sites in Grn-deficient animals, in contrast to Wt
25 animals, at 7 dpi and 31 dpi (Fig. 3A, B; Supplementary Videos 2, 3). The phenotype
26 observed in the Grn-deficient CNS resembled the neuroinflammation-driven prolonged
27 reactivity of glial cells observed in the mammalian brain in response to injury. These
28 data support the hypothesis that a failure to promote the transition of microglial cells
29 back to the homeostatic state accounts for the prolonged glial cell reactivity at injury
30 sites. To further test this hypothesis, we prevented the exacerbated inflammatory
31 response and long-lasting inflammation in Grn-deficient animals through treatment
32 with dexamethasone, an anti-inflammatory drug known to block microglial activation
33 in the adult zebrafish telencephalon after injury³⁰. We pretreated Grn-deficient animals
34 for 10 days with either dexamethasone or methanol (MeOH, as solvent control),
35 injured them, and analyzed 4C4 and Sox10 immunoreactivity at 3 dpi and 7 dpi (Fig.
36 3C-E, Extended Data Fig. 3D-F). Importantly, MeOH treatment did not alter the
37 reactivity of glial cells (microglia and oligodendroglia), because we observed
38 prolonged accumulation of glial cells at injury sites in MeOH-treated Grn-deficient
39 animals at 7 dpi (Fig. 3D, E). Strikingly, dexamethasone treatment rescued the
40 prolonged accumulation of 4C4⁺ microglial and Sox10⁺ oligodendroglial cells at injury
41 sites in Grn-deficient animals (Fig. 3D, E). Cell densities of 4C4⁺ microglia and Sox10⁺
42 oligodendroglia at injury sites in dexamethasone-treated Grn-deficient animals were
43 comparable to those detected in Wt animals at 7 dpi (Fig. 3B, E). Together, these
44 results demonstrate that prolonged activation of microglia, caused by Grn-deficiency,
45 is sufficient to prevent the resolution of the glial cell accumulation at injury sites, thus
46 transforming the scarless regeneration in the zebrafish CNS into a scarring model.

47 Because glial scarring in the mammalian CNS hinders functional regeneration
48 ^{2,73}, we set out to address whether prolonged accumulation of glial cells (microglia and
49 oligodendroglia) at injury sites might impair the injury-induced generation and/or the
50 survival of new neurons, a key feature in regeneration in the adult zebrafish CNS⁴³.

1 We kept Wt and Grn-deficient injured animals for 3 days in 5-bromo-2'-deoxyuridine
2 (BrdU) water to label the injury-activated stem cell population and the newly formed
3 neurons migrating to the brain parenchyma generated by the injury-activated stem cell
4 population (Fig. 3F, G). On the basis of the immunoreactivity of neural HUC and HUD
5 proteins (HuC/D), we observed significantly fewer newly formed BrdU⁺/HuC/D⁺
6 neurons in Grn-deficient animals than in Wt animals at 31 dpi (Fig. 3H, I). Together,
7 these results demonstrate that the prolonged neuroinflammation and glial cell
8 accumulation in Grn-deficient animals generate an environment not permissive to
9 restorative neurogenesis in the zebrafish brain, similarly to the observed reaction to
10 injury in the mammalian brain.

11

12 **Activated microglia fail to transition back to the homeostatic state in the Grn-** 13 **deficient injured CNS**

14

15 On the basis of previous results, we reasoned that excessive neuroinflammation
16 leading to prolonged glial cell accumulation at injury sites and impaired regeneration
17 might be caused by specific microglial states present in the Grn-deficient brain. To
18 address this question, we isolated and re-clustered all microglial cells identified by
19 scRNA-seq from Wt and Grn-deficient telencephali (Fig. 4A, Extended Data Fig. 4D,
20 E). We identified eight subclusters representing distinct microglial states (Fig. 4A),
21 which we were able to directly relate to those identified in Wt brains through cluster
22 similarity matrix analysis (Extended Data Fig. 4F, G). Importantly, six of these clusters
23 were previously identified in Wt brains, whereas two clusters appeared only after the
24 analysis that included Grn-deficient microglia (Fig. 4A, B, Extended Data Fig. 4D-F).
25 The identified states contained different numbers of cells derived from Wt and Grn-
26 deficient brains (Fig. 4B, Extended Data Fig. 4E). The MG4 state, corresponding to
27 the pro-regenerative Wt-MG0 state, and the MG3 state, corresponding to the
28 homeostatic Wt-MG2 state (Fig. 4A, Extended Data Fig. 4F, G), were largely under-
29 represented in Grn-deficient brains at both 3 dpi and 7 dpi (Fig. 4B, Extended Data
30 Fig. 4E). We identified activated microglia of both genotypes within the MG1 state,
31 which had a high similarity score with respect to the Wt-MG4 cluster (Fig. 1D, 4A, B,
32 Extended Data Fig. 4D-G). As expected, in the velocity analysis, activated Wt
33 microglial cells from the MG4 and MG1 clusters projected toward the MG3 cluster,
34 which was mainly composed of homeostatic microglia at 7 dpi (Fig. 4B, C, Extended
35 Data Fig. 4E-G). In contrast, Grn-deficient activated microglia projected towards
36 clusters MG5 and MG0, which contained almost exclusively Grn-deficient cells (Fig.
37 4B, C, Extended Data Fig. 4E). Interestingly, the MG0 and MG5 microglial states
38 displayed enrichment in numerous genes associated with innate immunity, lysosomes,
39 phagosomes and apoptosis (Supplementary Table 3), thus contributing to the
40 activated signature detected at 7 dpi in Grn-deficient microglial cells, as compared with
41 the homeostatic signature of Wt microglial cells at the same time point (Fig. 4D, E;
42 Supplementary Table 3). Additionally, microglia from the MG0 and MG5 clusters were
43 enriched in numerous genes associated with lipid droplet formation, and cellular and
44 mechanical stress, including several members of the Hsp70 family (Fig. 4F, G). Our
45 findings thus support that Grn-deficient microglia fail to transition back to homeostasis
46 and remain activated at 7 dpi.

47 Together, these results suggest that dysregulated injury-induced cellular stress
48 in Grn-deficient brains promotes long-lasting pro-inflammatory microglial cell
49 accumulation at injury sites. Grn-deficient pro-inflammatory microglia do not fully

1 transition back to homeostasis and induce long-lasting glial cell accumulation, thus
2 causing detrimental consequences in neuronal regeneration.

3
4 **Clearance of extranuclear TDP-43 condensates formed through LLPS is**
5 **required for termination of microglia-driven neuroinflammation**

6
7 Analysis of microglial populations revealed that MG0 and MG5 microglial cells in Grn-
8 deficient brains displayed dysregulated lipid metabolism, were unable to dissolve lipid
9 droplets and underwent cellular stress. Therefore, we aimed at identifying signals
10 leading to lipid droplet formation and cellular stress after brain injury. The RNA-binding
11 protein TAR DNA binding protein of 43 kDa (TDP-43) is a pathological marker protein
12 associated with neurodegeneration and brain injury⁷⁴⁻⁷⁷. In several
13 neurodegenerative diseases, including amyotrophic lateral sclerosis (ALS) and
14 frontotemporal dementia (FTD), and after traumatic brain injury, TDP-43 relocalizes
15 from the nucleus to the cytoplasm, forms cytoplasmic condensates or aggregates
16 through LLPS, and colocalizes with stress granules (SGs). Granulins have been
17 demonstrated to alter the solubility of TDP-43, modulating its LLPS and aggregation
18 behavior⁷⁸⁻⁸⁰. Therefore, we analyzed TDP-43 immunoreactivity in response to injury
19 in Wt and Grn-deficient brains (Fig. 5A, Extended Data Fig. 5A, B). In intact brains, we
20 observed TDP-43 signal exclusively in cell nuclei, mostly in HuC/D⁺ neuronal cells
21 (Extended Data Fig. 5A). Interestingly, the nuclear TDP-43 signal was complemented
22 by extranuclear TDP-43⁺ condensates in both Wt and Grn-deficient brains at injury
23 sites at 3 dpi (Fig. 5A, B, Extended Data Fig. 5B). Importantly, a proportion of TDP-
24 43⁺ condensates colocalized with 4C4⁺ microglia (Extended Data Fig. 5B).
25 Unexpectedly, whereas extranuclear TDP-43⁺ condensates were cleared at 7 dpi in
26 Wt animals, they were detected at injury sites in Grn-deficient animals at the same
27 time point (Fig. 5A, B), in a manner following Plin3⁺ lipid droplet kinetics (Fig. 2A, B).
28 Therefore, we hypothesized that Wt microglia upregulate granulins to clear potentially
29 cytotoxic TDP-43 condensates. Indeed, intraparenchymal injection of recombinant
30 PGRN in Grn-deficient brains was sufficient to clear extranuclear TDP-43⁺
31 condensates at 7 dpi (Extended Data Fig. 5C-E).

32 Because granulins regulate the LLPS behavior of TDP-43⁸⁰, we hypothesized that the
33 balance between granulins and LLPS-driven TDP-43⁺ condensates might define the
34 activation state of microglial cells in response to injury. In the absence of granulins,
35 TDP-43 was expected to form long-lasting condensates via LLPS, thus causing
36 cellular stress, and prolonged microglial activation and accumulation at injury sites. To
37 test this hypothesis, we made use of the finding that TDP-43 fused to maltose binding
38 protein (MBP) via a TEV proteolytic site does not undergo LLPS (Extended Data Fig.
39 6B, C). The proteolytic removal of MBP is sufficient to induce LLPS of TDP-43⁸¹⁻⁸⁴.
40 We injected TDP-43 (containing the maltose binding protein (MBP) tag preventing
41 LLPS) and phase-separated TDP-43 (MBP tag cleaved off) proteins while performing
42 injury in Wt brains (Fig. 5C-E, Extended Data Fig. 6A-D), aiming to oversaturate the
43 system with phase-separated TDP-43 and bypass available granulins. Injection of
44 both versions of TDP-43 prolonged microglial accumulation at injury sites at 7 dpi in
45 Wt animals, although a stronger reaction was observed when we injected phase-
46 separated TDP-43 (Fig. 5E, Extended Data Fig. 6D). In line with our hypothesis, only
47 the injection of phase-separated TDP-43 induced excessive formation of Plin3⁺ lipid
48 droplets and extranuclear TDP-43⁺ condensates, which colocalized primarily with 4C4⁺
49 microglial cells at injury sites (Fig. 5E-G, Extended Data Fig. 6D, E), thus mimicking
50 the phenotype of the reaction observed in Grn-deficient brains in response to injury.

1 Because we detected numerous cytosolic TDP-43 condensates in 4C4⁺ cells after
2 injection of phase-separated TDP-43 in Wt animals, and we did not observe any
3 upregulation of TDP-43 mRNA in microglial cells during the course of regeneration
4 (Extended Data Fig. 6F), we speculate that microglial cells accumulate at injury sites,
5 phagocytose TDP-43 released by dying neurons and do not dissolve LLPS-driven
6 TDP-43⁺ condensates when the amount of phase-separated TDP-43 is in excess or
7 when granulin levels are low.

8 To determine whether the phenotype detected in Grn-deficient animals was
9 specifically associated with the dysregulation of LLPS of TDP-43, we injected the
10 neurodegeneration-linked RNA-binding protein Fused in Sarcoma (FUS) or phase-
11 separated FUS while performing injury in Wt brains (Extended Data Fig. 6A, G, H). In
12 contrast to TDP-43, injections of FUS and phase-separated FUS promoted only mild
13 reactivity of microglial cells at injury sites and did not affect the number of Plin3⁺ lipid
14 droplets in Wt microglia at 7 dpi (Extended Data Fig. 6H-J). Therefore, we propose
15 that the phenotype observed in Grn-deficient animals is not caused by general
16 dysregulation of LLPS but instead may be caused by dysregulation of LLPS of specific
17 proteins, including TDP-43, thus leading to an excess of cytotoxic extranuclear TDP-
18 43⁺ condensates.

19 20 **Prevention of excessive LLPS-mediated formation of SGs is sufficient to** 21 **terminate prolonged neuroinflammation in Grn-deficient animals**

22
23 We hypothesized that Grn-controlled LLPS of TDP-43 must be tightly regulated to
24 successfully clear the TDP-43⁺ condensates formed in response to brain injury in
25 microglial cells and enable their return to the homeostatic state. To directly test this
26 hypothesis, we interfered with the formation of SGs, phase-separated cytosolic
27 condensates, in injured Grn-deficient brains through the administration of lipoamide
28 (Fig. 6A, B), a newly identified agent that decreases SG formation⁸⁵. We kept Grn-
29 deficient animals in either DMSO- or lipoamide-containing water for 7 days after injury
30 and assessed the formation of TDP-43⁺ condensates and the accumulation of 4C4⁺
31 microglial cells and Plin3⁺ lipid droplets at injury sites at that time point (Fig. 6C, D).
32 As expected, injured Grn-deficient animals kept in the DMSO-containing water
33 displayed prolonged accumulation of extranuclear TDP-43⁺ condensates and lipid
34 droplet-accumulating 4C4⁺ microglial cells at injury sites at 7 dpi (Fig. 6B-D). In
35 contrast, treatment of Grn-deficient animals with lipoamide resolved the accumulation
36 of lipid droplet-accumulating 4C4⁺ microglial cells at injury sites (Fig. 6B-D). Moreover,
37 we did not observe extranuclear TDP-43⁺ condensates at injury sites in lipoamide-
38 treated Grn-deficient animals (Fig. 6B-D), thus suggesting that lipoamide treatment
39 rescues the phenotype generated by Grn deficiency and promotes the return of
40 microglial cells to the homeostatic state. To verify this, we compared the reaction of
41 Grn-deficient microglia to injury after lipoamide treatment (*LipoGrn*-deficient cells) to
42 the reaction of microglia isolated from untreated Wt and Grn-deficient animals at 7 dpi
43 by using scRNA-seq analysis (Fig. 6E). *LipoGrn*-deficient microglia were identified
44 within the cluster of activated microglia (MG1 and MG5), and, in a lower proportion,
45 within the cluster composed of homeostatic microglia (MG3) (Fig. 6F, G). Interestingly,
46 lipoamide treatment significantly decreased the number of Grn-deficient microglia
47 within the pro-inflammatory MG0 cluster, which contained almost exclusively Grn-
48 deficient cells that did not fully transition back to the homeostatic state (Fig. 6F, G,
49 Extended Data Fig. 4E). Moreover, the relative number of *LipoGrn*-deficient microglial
50 cells returned to normal after lipoamide treatment at 7 dpi and was comparable to the

1 microglial abundance detected in Wt brains at the same time point. In line with this
2 analysis, *LipoGrn*-deficient microglia did not show upregulation of the inflammatory
3 pathways enriched in *Grn*-deficient microglia (Fig. 4D; Supplementary Table 3), as
4 compared with Wt microglia at 7 dpi. However, we detected 1349 significantly
5 downregulated genes in *LipoGrn*-deficient microglia compared with untreated *Grn*-
6 deficient microglia at the same time point. This regulated gene set was enriched in GO
7 processes associated with microglial functions, microglial activation and lipid
8 metabolism (Fig. 6H). Lastly, we observed lower expression of numerous genes
9 associated with lipid droplet-accumulating microglia (Fig. 6I) and cellular-stress (Fig.
10 6J) in *LipoGrn*-deficient microglia than in untreated *Grn*-deficient microglia at 7 dpi,
11 thus suggesting that the *LipoGrn*-deficient microglial cell reactivity and transcriptome
12 are more similar to those of Wt microglia.

13 Collectively, these results demonstrate that in Wt microglia, LLPS-mediated
14 TDP-43⁺ condensates form only transiently and are cleared in a timely manner, thus
15 leading to scarless regeneration in the zebrafish brain. Granulin deficiency impairs the
16 ability of microglia to clear the LLPS-mediated extranuclear TDP-43⁺ condensates
17 accumulating in SGs, thus leading to a cascade that locks microglial cells in their pro-
18 inflammatory state and prevents them from transitioning back to homeostasis.

19 20 **Stroke induces lipid droplet and SG formation in the human brain**

21
22 The gene signature conservation previously reported between zebrafish pro-
23 regenerative, lipid droplet-forming microglia and pro-regenerative microglia detected
24 in response to spinal cord injury in neonatal mice (Fig. 1G)⁵¹ prompted us to assess
25 whether CNS damage might induce similar formation of lipid droplets, TDP-43⁺
26 condensates and SGs in the human brain. Therefore, we assessed the reactivity of
27 IBA1⁺ microglial cells, PLIN3⁺ lipid droplets, TDP-43⁺ and G3BP⁺ SGs in post-mortem
28 brain tissues obtained from patients several weeks after ischemic stroke (Fig. 7A, B).
29 Notably, we detected neuroinflammation in the penumbra, as characterized by the
30 high expression of the microglial marker IBA1 (Fig. 7B). High IBA1 immunoreactivity
31 of microglial cells located in the penumbra was accompanied by morphological
32 changes indicative of their activated state (Fig. 7A, B). Importantly, the penumbra
33 containing highly activated microglia was also enriched in TDP-43⁺, PLIN3⁺ and
34 G3BP⁺ signals (Fig. 7B), in line with our data implicating their roles in maintaining long-
35 lasting neuroinflammation.

36 37 **Discussion**

38
39 Our data support a model of CNS regeneration wherein injury causes the release of
40 intracellular proteins able to undergo LLPS (including TDP-43) into the extracellular
41 space. These proteins are subsequently phagocytosed by pro-regenerative activated
42 microglia at injury sites. Granulins regulate the clearance of phagocytosed proteins
43 and condensates, which is necessary to allow activated microglia to transition back to
44 the homeostatic state. A failure to clear TDP-43⁺ condensates locks pro-regenerative
45 microglia in a pro-inflammatory, disease-associated state. Pro-inflammatory microglia
46 further enhance the transition of the remaining microglial cells to an activated state
47 (positive feedback loop) and prolong the accumulation of oligodendrocyte lineage cells
48 at injury sites, thus leading to long-term neuroinflammation and glial scar formation.
49 According to this model, microglial cells have several partially overlapping roles
50 defined by their activation state. In line with their known physiological roles in the intact

1 brain, microglia are dynamically activated by “ON” signals and inactivated by “OFF”
2 signals in an array of functions, such as phagocytosis of cellular debris, trophic support
3 of neurons, synaptic organization and the regulation of neuronal excitability^{15,61,86–88}.
4 The tight balance between activating “ON” and inactivating “OFF” signals, such as
5 cytokines and chemokines, ATP, PAMPs and TREM2^{23,25,27,89–91}, allows microglia to
6 perform their scavenging functions without generating chronic neuroinflammation. In
7 regeneration-competent species, such as zebrafish, CNS injuries induce the activation
8 of homeostatic microglial cells. However, immune cell activation is only transient and
9 is terminated in a timely manner, thereby enabling long-term integration and survival
10 of new neurons necessary for full tissue restoration and neuronal replacement at injury
11 sites^{30,43}. Interestingly, we identified different subpopulations of activated microglia
12 that returned to the homeostatic state through parallel, possibly independent,
13 trajectories, thus suggesting that distinct microglial cells may have different functions
14 in the injured CNS, and specific regulatory mechanisms may ensure the timely
15 termination of their activated state. Indeed, different activation states were also
16 characterized by the enrichment and downregulation of specific neuroinflammatory
17 programs. TNF-, TLR-, NOD- and IL1-dependent pro-inflammatory cascades are
18 major drivers of long-term neuroinflammation and scar formation in the mammalian
19 brain^{92,93}. Their separation and unique combinations in different microglial
20 subpopulations might possibly determine the overall activation state of single
21 microglial cells, thus facilitating their return to the homeostatic state after regeneration
22 is completed. The return of all activated microglial subpopulations to the homeostatic
23 state, however, involves a tight regulation of lysosomal functions and lytic vacuoles as
24 well as a return to glycolysis as a major energy supply source. These features have
25 recently been associated with the homeostatic scavenger function of microglia
26 detected in the mammalian brain^{56,94}. Because the trajectories describing microglial
27 dynamics do not overlap, these processes appear to be independently regulated along
28 each trajectory, in line with their specific roles in defining the activation state of
29 microglia. Interestingly, one population of transiently activated microglia in the
30 zebrafish telencephalon (Wt-MG0, mostly enriched at 3 dpi) expressed genes that
31 have recently been associated with pro-regenerative microglia emerging after spinal
32 cord injury in a neonatal mouse model⁵¹. These observations suggest the intriguing
33 possibility that both mammals and zebrafish may share several programs underlying
34 the transition of microglia to the activated state necessary for early beneficial effects
35^{10,45}. Furthermore, these results suggest that the regulatory mechanisms required for
36 the inactivation and the return of pro-regenerative microglia to the homeostatic state,
37 as observed in regeneration-competent species, were lost not during evolution but
38 during mammalian development and aging. Accordingly, long-term neuroinflammation
39 after CNS injury, aging and neurodegenerative diseases may be considered a
40 consequence of the aging-associated loss of “OFF” signals in microglial cells, whose
41 chronic activation hinders glial scar resolution and the functionality of neuronal circuits
42^{2,11,27,12–14,22–26}.

43 Interestingly, the subpopulation of Wt-MG0 pro-regenerative microglial cells, which
44 partially shares a signature with mammalian neonatal pro-regenerative microglia,
45 displayed elevated expression of genes associated with lipid droplet-accumulating
46 microglia⁴⁶, thus supporting the possibility that the timely inactivation of this specific
47 subpopulation is the key regulatory mechanism preventing chronic neuroinflammation.
48 Lipid droplets are among the first-line intracellular defenses that activate innate
49 immunity and sequester cytotoxic compounds detrimental to other cells^{46,68}. However,
50 the excessive production of lipid droplets in microglial cells during aging and

1 degenerative diseases, such as atherosclerosis, has been demonstrated to be
2 detrimental to cell functionality^{46,95}. Indeed, our findings that granulins regulate lipid
3 droplet resolution and microglial transition back to the homeostatic state, together with
4 previously demonstrated roles of granulins in the regulation of the inflammatory
5 response and microglial lipid metabolism^{46,59–61,63,65–67}, further support the importance
6 of the granulin-mediated return of Wt-MG0 microglial cells to homeostasis in limiting
7 long-lasting neuroinflammation. In fact, unbiased single-cell transcriptomic analysis
8 focusing on microglial subpopulations in Wt and Grn-deficient animals showed a
9 significant underrepresentation of homeostatic and pro-regenerative microglia in Grn-
10 deficient brains in response to injury. A large proportion of Grn-deficient microglial cells
11 are “locked” in an activated state after injury and do not fully transition back to the
12 homeostatic state. Because lipid droplets are composed of acyl-glycerols that are
13 synthesized by diacylglycerol transferases, converting DAGs to TAGs, which fill the
14 lipid droplet core⁹⁶, an increase in DAGs after injury in Grn-deficient animals suggests
15 an even more severe impairment of lipid metabolism than that in other
16 neuropathological states⁹⁶.

17 We showed that the prolonged neuroinflammation in Grn-deficient animals was
18 accompanied by prolonged accumulation of oligodendroglial cells at injury sites,
19 thereby mimicking the common features of the glial scar generated in response to
20 injury in the mammalian CNS^{2,11,97}. This data set further strengthens the key
21 regulatory role of the Wt-MG0 microglial state and underscores the need for deeper
22 understanding of Wt-MG0 microglial dynamics and regulation.

23 We propose that Grn-regulated LLPS of TDP-43 defines the activation state of
24 Wt-MG0 microglia. We showed that extranuclear TDP-43⁺ condensates (possibly
25 derived from TDP-43 released by dying neurons) were also present during the course
26 of normal regeneration in the adult zebrafish telencephalon. However, in the absence
27 of granulins, extranuclear TDP-43⁺ condensates persisted at injury sites along with
28 activated lipid droplet-accumulating microglia. This cascade of detrimental events was
29 prevented by inhibition of LLPS-mediated SG formation through administration of
30 lipoamide⁸⁵ or exogenous PGRN. Indeed, inflammation has recently been associated
31 with SG-mediated cellular stress⁹⁸, a process that may contribute to long-term
32 neuroinflammation and the persistence of glial scars. In line with that possibility,
33 traumatic brain injury has been reported to induce SG formation^{67,76,77}. In a survival
34 mechanism, after stress, cells inhibit global protein translation by sequestering RNA-
35 protein complexes involved in the pre-initiation of protein synthesis into SGs^{99,100}. SGs
36 are dynamic membrane-less cytoplasmic condensates that form through a process of
37 LLPS, a reversible unmixing of molecules into two separate phases, a dilute and
38 condensed phase, that are in constant exchange with each other^{101,102}. LLPS is
39 important in a variety of cellular functions, such as metabolism, transcriptional and
40 translational regulation, signal transduction and cellular motility^{101,103}. Moreover, LLPS
41 has been suggested to be involved in the development of various neurodegenerative
42 diseases, including ALS and FTD¹⁰⁴. ALS-causing mutations in RNA-binding proteins
43 have been shown to alter LLPS *in vitro* and to result in the localization of RNA-binding
44 proteins, including TDP-43, to SGs^{105–113}. Furthermore, cells exposed to chronic
45 stress form SGs and persistent TDP-43 condensates, thus suggesting that chronic
46 stress and SG localization leads to disease-like aggregation of TDP-43^{113–116}. Finally,
47 TDP-43 solubility, aggregation and LLPS properties, as well as its levels and toxicity,
48 have been shown to be influenced by granulins^{78–80}. Together, these results support
49 our model of development of chronic neuroinflammation. However, how LLPS-
50 mediated TDP-43⁺ condensate formation in activated microglia regulates and

1 coordinates glial reactivity during scar formation remains unclear. A growing body of
2 evidence suggests that lipid droplet composition changes depending on the
3 physiological state of the cell and that lipid droplets could serve as signaling mediators
4 in cellular communication ¹¹⁷, including non-cell autonomous glial scar cellular
5 interactions. In addition, SG-related proteins have been associated with the regulation
6 of translation and cell motility via mTORC signaling ¹¹⁸. Finally, SG proteins are
7 associated with microtubules and centrosomes, crucial structures for cellular migration
8 ^{119,120}. Therefore, SG-mediated alterations in microglial cell motility may account for
9 the persistence of these cells at injury sites and the induction of chronic
10 neuroinflammation.

11 Overall, our model provides new insights into basic regulatory mechanisms that
12 may prevent long-term neuroinflammation and promote CNS regeneration. Our new
13 findings on the crosstalk between granulins and the LLPS of TDP-43 could potentially
14 be targeted to develop new approaches to improve CNS regeneration in response to
15 traumatic brain injury and neurodegenerative diseases in mammalian species,
16 including humans.

17

18 **Methods**

19

20 **Human post-mortem brain tissues**

21

22 Brain tissue was collected several weeks after infarction of the right arteria cerebri
23 media with hemiparesis. Tissue was fixed in 4% PFA and embedded in paraffin.
24 Sample collection was performed according to the legal guidelines of Government of
25 Upper Bavaria (BayKrG Art. 27 Abs. 4).

26

27 **Zebrafish lines**

28

29 *Zebrafish from the $grna^{+/+};grnb^{+/+}$, $grna^{-/-};grnb^{-/-}$ and AB/EK strains and from the*
30 *transgenic strains Tg(olig2:DsRed), Tg(mpeg1:mCherry),*
31 *Tg(olig2:DsRed; $grna^{-/-};grnb^{-/-}$) and Tg(mpeg1:mCherry; $grna^{-/-};grnb^{-/-}$) were used in*
32 *all experiments. All experiments were performed in 3-5-month-old animals, as in this*
33 *range we do not observe any age-associated differences. Wildtype and Granulin-*
34 *deficient intact, injured and treated animals were sex-mixed littermates in individual*
35 *experiments. 4-5 independent biological replicates were used in every experiment (the*
36 *exact number of analyzed animals is specified in each dot plot) and analysis was*
37 *performed blindly. All animals were kept under standard husbandry conditions and*
38 *experiments were performed according to the handling guidelines and regulations of*
39 *EU and the Government of Upper Bavaria (AZ 55.2-1-54-2532-0916).*

40

41 **Treatment with dexamethasone**

42

43 3-5-month-old, mixed-sex zebrafish from specific genotypes were immersed for 10
44 days in dexamethasone-containing (15 mg/L) or MeOH-containing (0.0001%) aerated
45 water. Animals were immersed in dexamethasone- or MeOH-containing water for the
46 whole duration of the experiment until sacrifice (time point indicated in the
47 experimental paradigm). Water was changed daily and animals were fed every second
48 day, 4 hours prior the water change.

1 Treatment with lipoamide

2
3 3-5-month-old, mixed-sex zebrafish from specific genotypes were immersed for the
4 whole duration of the experiment in lipoamide-containing (20 μ M) or DMSO-containing
5 aerated water until sacrifice (time point indicated in the experimental paradigm). Water
6 was changed daily and animals were fed 4 hours prior the water change.

7 8 Genotype identification

9
10 Genotyping was performed by cutting a small part of the zebrafish tail fin. REExtract-
11 N-Amp Tissue Kit (Sigma-Aldrich) was used to extract genomic DNA according to
12 manufacturer's instructions. Isolated genomic DNA was amplified by PCR and Sanger
13 sequencing was performed to compare the nucleotide sequences and identify the
14 selected mutations for *grna* and *grnb*. Mutations selected are the following: mde54a
15 and mde360 for *grna* and *grnb* respectively, as indicated in ZFIN database
16 (<https://zfin.org/action/publication/ZDB-PUB-200208-2/feature-list>).

17 18 Stab wound injury

19
20 Stab wound injury from zebrafish nostrils was performed in both telencephalic
21 hemispheres according to previous publication²⁹. 100 x 0.9 mm glass capillary needle
22 (KG01, A. Hartenstein) was used. The needle was pulled on a Narishige Puller (model
23 PC-10) with "one-stage" pull setting at 63.5°C. The needle used to perform the stab
24 wound injury resulted in 5 mm length and 0.1 mm diameter.

25 26 Tissue preparation and immunohistochemistry

27
28 Animals were sacrificed by MS222 overdose of tricaine methane sulfonate (MS222,
29 0,2%) by prolonged immersion. Tissue processing was performed as described
30 previously²⁹. Immunodetection of BrdU required a pretreatment with 4 N HCl followed
31 by washes with borate buffer and PBS before placing sections in anti-BrdU antibody.

32 33 BrdU labeling experiment

34
35 To assess the number of newly formed neurons in response to injury (restorative
36 neurogenesis), zebrafish from specific genotypes were immersed, immediately after
37 stab wound injury, in BrdU-containing aerated water (10 mM) for 16 h/day during 3
38 consecutive days. During the 8 hours outside BrdU-containing water, fish were kept in
39 fresh water and fed. Animals were sacrificed 28 days after BrdU treatment (3 days
40 BrdU water + 28 days chase) to allow the incorporation of BrdU in activated stem cells
41 that would generate neurons in response to injury and the migration of newly formed
42 BrdU⁺ neurons at injury sites in the brain parenchyma.

43 44 Lipidomic analysis

45
46 Single telencephali were isolated and completely dissolved with mechanical
47 homogenization procedures in D-PBS without Mg, Ca to reach the final concentration
48 of 4-5 mg/mL (tissue wet weight per volume). Mass spectrometry-based analysis was
49 performed by Lipotype GmbH.

50

1 Injection of recombinant Progranulin (mPGRN)

2

3 Intraparenchymal injection of recombinant mPGRN was performed while we executed
4 stab wound injury. 5 μ L of recombinant mPGRN (dilution of 1:250 from stock solution
5 of 250 ng/ μ L, reconstituted in sterile PBS) were injected in both hemispheres of the
6 zebrafish telencephalon.

7

8 Protein expression

9

10 TDP-43-MBP-His6 was purified according to ⁸¹ with slight adaptations. Expression
11 was performed in *E. coli* BL21-DE3 Rosetta 2 using 0.5 mM IPTG overnight at 16°C.
12 Cells were lysed in purification buffer (20 mM Tris pH 8, 1 M NaCl, 10 mM imidazole,
13 10 % (v/v) glycerol, 4 mM β -mercaptoethanol and 1 μ g/ml each of aprotinin, leupeptin
14 hemisulfate and pepstatin A) supplemented with 0.1 mg/ml RNase A using lysozyme
15 and sonication. Afterwards, the protein was purified by Ni-NTA agarose (Qiagen) and
16 eluted using 300 mM imidazole. Finally, eluates were further purified using size
17 exclusion chromatography (Hiload 16/600 Superdex 200 pg, GE Healthcare) in
18 storage buffer (20 mM Tris pH 8, 300 mM NaCl, 10% (v/v) glycerol supplemented with
19 2 mM TCEP) in order to obtain monomeric TDP-43-MBP-His₆.

20 For MBP-FUS-His6 ¹²¹, protein expression was induced in *E. coli* Rosetta-LysS after
21 cold shock using 100 nM IPTG overnight at 12°C. Protein was purified as described
22 above for TDP-43-MBP. SEC eluates were additionally purified using amylose HS
23 (NEB) in amylose binding buffer (20 mM Tris pH6, 150 mM NaCl, 5% (v/v) glycerol
24 supplemented with 2 mM DTT and 1 μ g/ml each of aprotinin, leupeptin hemisulfate
25 and pepstatin A and eluted using 10 mM maltose in storage buffer.

26 Purified protein was concentrated using Amicon ultra centrifugal filters, flash frozen
27 and stored at -80°C. Protein concentration was determined by measuring absorbance
28 at 280 nm using the respective extinction coefficient (ϵ) predicted by the ProtParam
29 tool. A260/280 ratio of purified protein was between 0.5-0.7, showing deprivation of
30 nucleic acids.

31 Purified TDP-43-TEV-MBP-His6 was exchanged to Hepes buffer (20 mM Hepes, pH
32 7.5, 150 mM NaCl, 1 mM DTT). For visualization of condensates the reaction was
33 setup directly in a Uncoated μ -Slide 18 Well - Flat chambers (Cat.No: 81821, Ibbidi),
34 where protein was diluted to a concentration of 5 μ M and phase separation was
35 induced by addition of 100 μ g/ml His6-TEV protease at RT. After ~20 min, imaging
36 was performed by bright field microscopy using a widefield microscope.

37

38 Injection of TDP-43 and FUS proteins

39

40 TDP-43-MBP and MBP-FUS proteins were independently incubated for 30 min at RT
41 with TEV and TEV buffer (Tris 20 mM pH 8.0, 300mM NaCl, 2mM dTT in H₂O) to
42 cleave the MBP tag. 5 μ L of uncleaved and cleaved TDP-43 (20 μ M) and FUS (20 μ M)
43 proteins were independently injected in both hemispheres of the zebrafish
44 telencephalon while performing the injury. 5 μ L of TEV+TEV buffer were also injected
45 in control animals to account for possible changes in reactivity due to the injection.

46

47 Tissue dissociation

48

1 Cells were isolated from zebrafish telencephali (n=4) and dissociated into single cell
2 suspension using the papain kit (Worthington) according to manufacturer's
3 instructions. Incubation in dissociating enzyme was performed for 30 min.

4 5 **Library preparation and sequencing**

6
7 Single cell suspensions were loaded into 10x Genomics Single Cell 3' Chips according
8 to manufacturer's instruction for Chromium Single Cell 3' Reagent Kits v3 (10x
9 Genomics) to generate single cell bead emulsion (GEMs). cDNA synthesis was
10 carried out according to 10x Genomics guidelines. Libraries were pooled and
11 sequenced on NovaSeq6000 (Illumina) with the recommended number of cycles (28-
12 8-91) according to Chromium Single Cell 3' Reagent Kits v3. Sequencing was
13 performed by the Core Sequencing Facility at the Helmholtz Zentrum München.

14 15 **Alignment and data analysis**

16
17 Transcriptome alignment of single cell data was performed using Cell Ranger 4.0.0
18 against the *Danio rerio* reference genome assembly GRCz11 (Ensembl Release 100).
19 Quality Control (QC) of mapped cells was performed adjusting the recommendations
20 from previous publication (gene counts ≥ 350 ; $40000 \leq$ reads per cell ≥ 800 ;
21 mitochondrial fraction ≤ 0.2)¹²². Batch-correction and integration of different scRNA-
22 seq datasets was performed using Scanorama¹²³. Unsupervised clustering of cells
23 was performed using the Louvain algorithm (<https://doi.org/10.5281/zenodo.595481>),
24 implemented in SCANPY with resolution parameter of 1 and 0.8 when the
25 unsupervised cell clustering was applied to all cells or to microglia-only cells,
26 respectively. Marker genes specific for each cluster were identified using t-test
27 between the counts of each gene in a cell cluster against all other clusters with the
28 function *rank_genes_groups* in SCANPY. Visualization of cell clusters was performed
29 with Uniform Manifold Approximation and Projection (UMAP)¹²⁴ in SCANPY. Velocity
30 analysis⁵⁴ to identify differences in the dynamics of microglial cells reactivity to injury
31 was performed following the instructions from previous publication using *scvelo*
32 package in SCANPY⁵³.

33 34 **Tissue preparation and immunohistochemistry of human brain tissues with 3,3'-** 35 **diaminobenzidine (DAB) development**

36
37 Sections were deparaffinized in xylene and rehydrated in 96% and 70% EtOH. Antigen
38 retrieval was then performed for 30 min with the use of citrate buffer (10 mM, pH: 6,0)
39 and washing steps with bidistilled water followed. Tissue was incubated in 4%
40 hydrogen peroxidase solution for 10 min at RT, washed with bidistilled water and
41 subsequently blocked for 30 min in RT in Blocking Buffer (1X PBS, 2.5% normal horse
42 serum, 1% BSA, 0.1% Triton x-100, 0.2% Gold Fish Gelatine and 0.02% sodium azide
43 solution (10%) and Avidin). Primaries were diluted in Blocking buffer with biotin and
44 an overnight incubation at 4°C was carried out. On the following day, the primaries
45 were washed with PBS and biotinylated secondary antibodies (1:400 in blocking
46 buffer) were applied and incubated for 30 min at RT. Washing steps with PBS followed
47 and incubation with the Avidin-Biotin Complex (ABC) for 30 min at RT was carried out.
48 After extensive washing with PBS, DAB solution was applied to the samples
49 (ImmPACT DAB, SK4104 Vector). Stainings were checked under the microscope and
50 the reaction was stopped in bidistilled water. 3 min in haematoxylin allowed the

1 counterstaining of samples. Dehydration in 70% and 96% EtOH and incubation in
2 xylene were performed and the samples were then coverslipped.

3 4 **Quantification and statistical analysis**

5
6 Statistical analyses were performed with Prism 8 software (GraphPad Software).
7 Individual animal experiments were performed with 4 or 5 zebrafish per group
8 (identified by genotype and by condition, i.e. intact/injured). The specific number of
9 animals analyzed is specified in each dot plot and quantifications were performed
10 blindly. Data of same experimental groups derived from multiple experiments with
11 identical conditions were combined and analyzed statistically to determine normality
12 ($n \geq 8$). All data analyzed passed normality test and for this reason unpaired t test,
13 ordinary one-way ANOVA and two-way ANOVA were used when 2 groups, more than
14 2 groups from different genotypes or conditions (i.e. intact, injured, drug-treated) or
15 more than 2 groups from different genotypes and conditions were statistically
16 analyzed, respectively. Statistical tests and post-hoc tests for multiple comparisons
17 are indicated in the figure legends. Each data point is obtained by quantifying multiple
18 sections (from zebrafish telencephalon) per biological replicate. Data are presented
19 as the mean \pm standard error of the mean (SEM).

20 21 **Data and software availability**

22
23 The scRNA-seq data has been deposited in GEO under accession code GEO:
24 pending.

25 The analysis was performed by following the guidelines obtained from previously
26 released as open source codes on GitHub at the following
27 links: [https://github.com/theislab/single-cell-](https://github.com/theislab/single-cell-tutorial/blob/master/latest_notebook/Case-study_Mouse-intestinal-epithelium_1906.ipynb)
28 [tutorial/blob/master/latest_notebook/Case-study_Mouse-intestinal-](https://github.com/theislab/single-cell-tutorial/blob/master/latest_notebook/Case-study_Mouse-intestinal-epithelium_1906.ipynb)
29 [epithelium_1906.ipynb](https://github.com/brianhie/scanorama), <https://github.com/brianhie/scanorama>,
30 https://github.com/theislab/scvelo_notebooks/blob/master/VelocityBasics.ipynb.

31 32 **Contact for reagent and resource sharing**

33
34 Further information and requests for resources and reagents should be directed to and
35 will be fulfilled by the Lead Contact, Prof. Jovica Ninkovic ([ninkovic@helmholtz-](mailto:ninkovic@helmholtz-muenchen.de)
36 [muenchen.de](mailto:ninkovic@helmholtz-muenchen.de)).

37 38 **References**

- 39
40 1. Dimou, L. & Gotz, M. Glial cells as progenitors and stem cells: new roles in the
41 healthy and diseased brain. *Physiol Rev* **94**, 709–737 (2014).
42 2. O’Shea, T. M., Burda, J. E. & Sofroniew, M. V. Cell biology of spinal cord injury
43 and repair. *J Clin Invest* **127**, 3259–3270 (2017).
44 3. Arvidsson, A., Collin, T., Kirik, D., Kokaia, Z. & Lindvall, O. Neuronal
45 replacement from endogenous precursors in the adult brain after stroke. *Nat*
46 *Med* **8**, 963–970 (2002).
47 4. Thored, P. *et al.* Long-term neuroblast migration along blood vessels in an
48 area with transient angiogenesis and increased vascularization after stroke.
49 *Stroke* **38**, 3032–3039 (2007).

- 1 5. Thored, P. *et al.* Persistent production of neurons from adult brain stem cells
2 during recovery after stroke. *Stem Cells* **24**, 739–747 (2006).
- 3 6. Ernst, A. *et al.* Neurogenesis in the striatum of the adult human brain. *Cell* **156**,
4 1072–1083 (2014).
- 5 7. Winpenny, E. *et al.* Sequential generation of olfactory bulb glutamatergic
6 neurons by Neurog2-expressing precursor cells. *Neural Dev* **6**, 12 (2011).
- 7 8. Henriques, D., Moreira, R., Schwamborn, J., Pereira de Almeida, L. &
8 Mendonça, L. S. Successes and Hurdles in Stem Cells Application and
9 Production for Brain Transplantation. *Frontiers in Neuroscience* (2019)
10 doi:10.3389/fnins.2019.01194.
- 11 9. Grade, S. & Götz, M. Neuronal replacement therapy: previous achievements
12 and challenges ahead. *Regen Med* (2017).
- 13 10. Adams, K. L. & Gallo, V. The diversity and disparity of the glial scar. *Nature*
14 *Neuroscience* vol. 21 9–15 (2018).
- 15 11. Frik, J. *et al.* Cross-talk between monocyte invasion and astrocyte proliferation
16 regulates scarring in brain injury. *EMBO Rep* **19**, (2018).
- 17 12. Anderson, M. A. *et al.* Astrocyte scar formation AIDS central nervous system
18 axon regeneration. *Nature* (2016) doi:10.1038/nature17623.
- 19 13. Goritz, C. *et al.* A pericyte origin of spinal cord scar tissue. *Science* (80-.).
20 **333**, 238–242 (2011).
- 21 14. Dias, D. O. *et al.* Reducing Pericyte-Derived Scarring Promotes Recovery after
22 Spinal Cord Injury. *Cell* **173**, 153-165 e22 (2018).
- 23 15. Badimon, A. *et al.* Negative feedback control of neuronal activity by microglia.
24 *Nature* (2020) doi:10.1038/s41586-020-2777-8.
- 25 16. Helmut, K., Hanisch, U. K., Noda, M. & Verkhratsky, A. Physiology of
26 microglia. *Physiol. Rev.* (2011) doi:10.1152/physrev.00011.2010.
- 27 17. Hanisch, U. K. Microglia as a source and target of cytokines. *GLIA* (2002)
28 doi:10.1002/glia.10161.
- 29 18. Koizumi, S., Ohsawa, K., Inoue, K. & Kohsaka, S. Purinergic receptors in
30 microglia: Functional modal shifts of microglia mediated by P2 and P1
31 receptors. *Glia* (2013) doi:10.1002/glia.22358.
- 32 19. Fontainhas, A. M. *et al.* Microglial morphology and dynamic behavior is
33 regulated by ionotropic glutamatergic and GABAergic neurotransmission.
34 *PLoS One* (2011) doi:10.1371/journal.pone.0015973.
- 35 20. Pocock, J. M. & Kettenmann, H. Neurotransmitter receptors on microglia.
36 *Trends in Neurosciences* (2007) doi:10.1016/j.tins.2007.07.007.
- 37 21. Michell-Robinson, M. A. *et al.* Roles of microglia in brain development, tissue
38 maintenance and repair. *Brain* (2015) doi:10.1093/brain/awv066.
- 39 22. Colonna, M. & Butovsky, O. Microglia function in the central nervous system
40 during health and neurodegeneration. *Annual Review of Immunology* (2017)
41 doi:10.1146/annurev-immunol-051116-052358.
- 42 23. Song, W. M. & Colonna, M. The identity and function of microglia in
43 neurodegeneration. *Nature Immunology* (2018) doi:10.1038/s41590-018-0212-
44 1.
- 45 24. Krasemann, S. *et al.* The TREM2-APOE Pathway Drives the Transcriptional
46 Phenotype of Dysfunctional Microglia in Neurodegenerative Diseases.
47 *Immunity* (2017) doi:10.1016/j.immuni.2017.08.008.
- 48 25. Deczkowska, A. *et al.* Disease-Associated Microglia: A Universal Immune
49 Sensor of Neurodegeneration. *Cell* (2018) doi:10.1016/j.cell.2018.05.003.
- 50 26. Fetler, L. & Amigorena, S. Brain under surveillance: The microglia patrol.

- 1 *Science* (2005) doi:10.1126/science.1114852.
- 2 27. Casano, A. M., Albert, M. & Peri, F. Developmental Apoptosis Mediates Entry
3 and Positioning of Microglia in the Zebrafish Brain. *Cell Rep.* (2016)
4 doi:10.1016/j.celrep.2016.06.033.
- 5 28. Barbosa, J. S. S. *et al.* Single-cell in vivo imaging of adult neural stem cells in
6 the zebrafish telencephalon. *Nat Protoc* **11**, 1360–1370 (2016).
- 7 29. Baumgart, E. V. V *et al.* Stab wound injury of the zebrafish telencephalon: a
8 model for comparative analysis of reactive gliosis. *Glia* **60**, 343–357 (2012).
- 9 30. Kyritsis, N. *et al.* Acute inflammation initiates the regenerative response in the
10 adult zebrafish brain. *Science (80-.)*. **338**, 1353–1356 (2012).
- 11 31. Kroehne, V., Freudenreich, D., Hans, S., Kaslin, J. & Brand, M. Regeneration
12 of the adult zebrafish brain from neurogenic radial glia-type progenitors.
13 *Development* **138**, 4831–4841 (2011).
- 14 32. Kishimoto, N., Shimizu, K. & Sawamoto, K. Neuronal regeneration in a
15 zebrafish model of adult brain injury. *Dis Model Mech* **5**, 200–209 (2012).
- 16 33. Becker, C. G. & Becker, T. Growth and pathfinding of regenerating axons in
17 the optic projection of adult fish. *J. Neurosci. Res.* **85**, 2793–2799 (2007).
- 18 34. Becker, T. & Becker, C. G. Regenerating descending axons preferentially
19 reroute to the gray matter in the presence of a general macrophage/microglial
20 reaction caudal to a spinal transection in adult zebrafish. *J Comp Neurol* **433**,
21 131–147 (2001).
- 22 35. Becker, C. G. & Becker, T. Neuronal Regeneration from Ependymo-Radial
23 Glial Cells: Cook, Little Pot, Cook! *Dev. Cell* **32**, 516–527 (2015).
- 24 36. Reimer, M. M. *et al.* Motor neuron regeneration in adult zebrafish. *J Neurosci*
25 **28**, 8510–8516 (2008).
- 26 37. Lindsey, B. W. *et al.* Midbrain tectal stem cells display diverse regenerative
27 capacities in zebrafish. *Sci. Rep.* (2019) doi:10.1038/s41598-019-40734-z.
- 28 38. Fleisch, V. C., Fraser, B. & Allison, W. T. Investigating regeneration and
29 functional integration of CNS neurons: Lessons from zebrafish genetics and
30 other fish species. *Biochimica et Biophysica Acta - Molecular Basis of Disease*
31 (2011) doi:10.1016/j.bbadis.2010.10.012.
- 32 39. Guarino, A. M. *et al.* YB-1 recruitment to stress granules in zebrafish cells
33 reveals a differential adaptive response to stress. *Sci. Rep.* (2019)
34 doi:10.1038/s41598-019-45468-6.
- 35 40. Acosta, J. R. *et al.* Mutant human FUS is ubiquitously mislocalized and
36 generates persistent stress granules in primary cultured transgenic zebrafish
37 cells. *PLoS One* (2014) doi:10.1371/journal.pone.0090572.
- 38 41. Zampedri, C. *et al.* Zebrafish P54 RNA helicases are cytoplasmic granule
39 residents that are required for development and stress resilience. *Biol. Open*
40 (2016) doi:10.1242/bio.015826.
- 41 42. R., W., H., Z., J., D. & J., X. Heat resilience in embryonic zebrafish revealed
42 using an in vivo stress granule reporter. *J. Cell Sci.* (2019).
- 43 43. Di Giaimo, R. *et al.* The Aryl Hydrocarbon Receptor Pathway Defines the Time
44 Frame for Restorative Neurogenesis. *Cell Rep* **25**, 3241–3251 e5 (2018).
- 45 44. Zambusi, A. & Ninkovic, J. Regeneration of the central nervous system-
46 principles from brain regeneration in adult zebrafish. *World Journal of Stem*
47 *Cells* (2020) doi:10.4252/wjsc.v12.i1.8.
- 48 45. Burda, J. E. & Sofroniew, M. V. Reactive gliosis and the multicellular response
49 to CNS damage and disease. *Neuron* **81**, 229–248 (2014).
- 50 46. Marschallinger, J. *et al.* Lipid-droplet-accumulating microglia represent a

- 1 dysfunctional and proinflammatory state in the aging brain. *Nat. Neurosci.*
2 (2020) doi:10.1038/s41593-019-0566-1.
- 3 47. Mazaheri, F. *et al.* TREM2 deficiency impairs chemotaxis and microglial
4 responses to neuronal injury. *EMBO Rep* **18**, 1186–1198 (2017).
- 5 48. Schlepckow, K. *et al.* Enhancing protective microglial activities with a dual
6 function TREM 2 antibody to the stalk region. *EMBO Mol. Med.* (2020)
7 doi:10.15252/emmm.201911227.
- 8 49. Zhou, X. *et al.* Loss of Tmem106b exacerbates FTLD pathologies and causes
9 motor deficits in progranulin-deficient mice. *EMBO Rep.* **21**, (2020).
- 10 50. Werner, G. *et al.* Loss of TMEM 106B potentiates lysosomal and FTLD-like
11 pathology in progranulin-deficient mice. *EMBO Rep.* **21**, (2020).
- 12 51. Li, Y. *et al.* Microglia-organized scar-free spinal cord repair in neonatal mice.
13 *Nature* **587**, 613–618 (2020).
- 14 52. Masuda, T. *et al.* Spatial and temporal heterogeneity of mouse and human
15 microglia at single-cell resolution. *Nature* **566**, 388–392 (2019).
- 16 53. Bergen, V., Lange, M., Peidli, S., Wolf, F. A. & Theis, F. J. Generalizing RNA
17 velocity to transient cell states through dynamical modeling. *Nat. Biotechnol.*
18 (2020) doi:10.1038/s41587-020-0591-3.
- 19 54. La Manno, G. *et al.* RNA velocity of single cells. *Nature* (2018)
20 doi:10.1038/s41586-018-0414-6.
- 21 55. Lauro, C. & Limatola, C. Metabolic Reprograming of Microglia in the
22 Regulation of the Innate Inflammatory Response. *Frontiers in Immunology*
23 (2020) doi:10.3389/fimmu.2020.00493.
- 24 56. Bernier, L. P. *et al.* Microglial metabolic flexibility supports immune surveillance
25 of the brain parenchyma. *Nat. Commun.* (2020) doi:10.1038/s41467-020-
26 15267-z.
- 27 57. Majumdar, A. *et al.* Activation of microglia acidifies lysosomes and leads to
28 degradation of Alzheimer amyloid fibrils. *Mol. Biol. Cell* (2007)
29 doi:10.1091/mbc.E06-10-0975.
- 30 58. Dou, Y. *et al.* Microglial migration mediated by ATP-induced ATP release from
31 lysosomes. *Cell Res.* (2012) doi:10.1038/cr.2012.10.
- 32 59. Altmann, C. *et al.* Progranulin promotes peripheral nerve regeneration and
33 reinnervation: Role of notch signaling. *Mol. Neurodegener.* **11**, 69 (2016).
- 34 60. He, Z., Ong, C. H. P., Halper, J. & Bateman, A. Progranulin is a mediator of
35 the wound response. *Nat. Med.* **9**, 225–229 (2003).
- 36 61. Lui, H. *et al.* Progranulin Deficiency Promotes Circuit-Specific Synaptic
37 Pruning by Microglia via Complement Activation. *Cell* **165**, 921–935 (2016).
- 38 62. Rhinn, H. & Abeliovich, A. Differential Aging Analysis in Human Cerebral
39 Cortex Identifies Variants in TMEM106B and GRN that Regulate Aging
40 Phenotypes. *Cell Syst.* **4**, 404–415.e5 (2017).
- 41 63. Tanaka, Y., Matsuwaki, T., Yamanouchi, K. & Nishihara, M. Exacerbated
42 inflammatory responses related to activated microglia after traumatic brain
43 injury in progranulin-deficient mice. *Neuroscience* **231**, 49–60 (2013).
- 44 64. Valenzano, D. R. *et al.* The African Turquoise Killifish Genome Provides
45 Insights into Evolution and Genetic Architecture of Lifespan. *Cell* **163**, 1539–
46 1554 (2015).
- 47 65. Wils, H. *et al.* Cellular ageing, increased mortality and FTLD-TDP-associated
48 neuropathology in progranulin knockout mice. *J. Pathol.* **228**, 67–76 (2012).
- 49 66. Yin, F. *et al.* Exaggerated inflammation, impaired host defense, and
50 neuropathology in progranulin-deficient mice. *J. Exp. Med.* **207**, 117–128

- 1 (2010).
- 2 67. Zhang, J. *et al.* Neurotoxic microglia promote TDP-43 proteinopathy in
3 progranulin deficiency. *Nature* **588**, (2020).
- 4 68. Bosch, M. *et al.* Mammalian lipid droplets are innate immune hubs integrating
5 cell metabolism and host defense. *Science* (80-.). **370**, (2020).
- 6 69. Solchenberger, B., Russell, C., Kremmer, E., Haass, C. & Schmid, B. Granulin
7 Knock Out Zebrafish Lack Frontotemporal Lobar Degeneration and Neuronal
8 Ceroid Lipofuscinosis Pathology. *PLoS One* **10**, e0118956 (2015).
- 9 70. Zambusi, A., Pelin Burhan, Ö., Di Giaimo, R., Schmid, B. & Ninkovic, J.
10 Granulins Regulate Aging Kinetics in the Adult Zebrafish Telencephalon. *Cells*
11 (2020) doi:10.3390/cells9020350.
- 12 71. Evers, B. M. *et al.* Lipidomic and Transcriptomic Basis of Lysosomal
13 Dysfunction in Progranulin Deficiency. *Cell Rep.* **20**, 2565–2574 (2017).
- 14 72. Simon, C., Lickert, H., Gotz, M. & Dimou, L. Sox10-iCreERT2 : a mouse line to
15 inducibly trace the neural crest and oligodendrocyte lineage. *Genesis* **50**, 506–
16 515 (2012).
- 17 73. Buffo, A. *et al.* Expression pattern of the transcription factor Olig2 in response
18 to brain injuries: implications for neuronal repair. *Proc Natl Acad Sci U S A*
19 **102**, 18183–18188 (2005).
- 20 74. Thammisetty, S. S. *et al.* Age-related deregulation of TDP-43 after stroke
21 enhances NF-κB-mediated inflammation and neuronal damage 11 Medical and
22 Health Sciences 1109 Neurosciences. *J. Neuroinflammation* **15**, (2018).
- 23 75. Heyburn, L., Sajja, V. S. S. S. & Long, J. B. The role of TDP-43 in military-
24 relevant TBI and chronic neurodegeneration. *Frontiers in Neurology* vol. 10
25 (2019).
- 26 76. Anderson, E. N. *et al.* Traumatic injury induces stress granule formation and
27 enhances motor dysfunctions in ALS/FTD models. *Hum. Mol. Genet.* **27**,
28 1366–1381 (2018).
- 29 77. Wiesner, D. *et al.* Reversible induction of TDP-43 granules in cortical neurons
30 after traumatic injury. *Exp. Neurol.* **299**, 15–25 (2018).
- 31 78. Salazar, D. A. *et al.* The progranulin cleavage products, granulins, exacerbate
32 TDP-43 toxicity and increase TDP-43 levels. *J. Neurosci.* **35**, 9315–9328
33 (2015).
- 34 79. Beel, S. *et al.* Progranulin reduces insoluble TDP-43 levels, slows down axonal
35 degeneration and prolongs survival in mutant TDP-43 mice 11 Medical and
36 Health Sciences 1109 Neurosciences. *Mol. Neurodegener.* **13**, (2018).
- 37 80. Bhopatkar, A. A., Uversky, V. N. & Rangachari, V. Granulins modulate liquid–
38 liquid phase separation and aggregation of the prion-like C-terminal domain of
39 the neurodegeneration-associated protein TDP-43. *J. Biol. Chem.* **295**, 2506–
40 2519 (2020).
- 41 81. Wang, A. *et al.* A single N-terminal phosphomimic disrupts TDP-43
42 polymerization, phase separation, and RNA splicing. *EMBO J.* **37**, (2018).
- 43 82. Fox, J. D. & Waugh, D. S. Maltose-binding protein as a solubility enhancer.
44 *Methods Mol. Biol.* **205**, 99–117 (2003).
- 45 83. Nallamsetty, S. & Waugh, D. S. Solubility-enhancing proteins MBP and NusA
46 play a passive role in the folding of their fusion partners. *Protein Expr. Purif.*
47 **45**, 175–182 (2006).
- 48 84. Nallamsetty, S., Austin, B. P., Penrose, K. J. & Waugh, D. S. Gateway vectors
49 for the production of combinatorially-tagged His₆-MBP fusion proteins in the
50 cytoplasm and periplasm of *Escherichia coli*. *Protein Sci.* **14**, 2964–2971

- 1 (2005).
- 2 85. Wheeler, R. J. *et al.* Small molecules for modulating protein driven liquid-liquid
3 phase separation in treating neurodegenerative disease. *bioRxiv* (2019)
4 doi:10.1101/721001.
- 5 86. Lalancette-Hébert, M., Gowing, G., Simard, A., Yuan, C. W. & Kriz, J.
6 Selective ablation of proliferating microglial cells exacerbates ischemic injury in
7 the brain. *J. Neurosci.* **27**, 2596–2605 (2007).
- 8 87. Paolicelli, R. C. *et al.* Synaptic pruning by microglia is necessary for normal
9 brain development. *Science* (80-.). **333**, 1456–1458 (2011).
- 10 88. Brown, G. C. & Neher, J. J. Microglial phagocytosis of live neurons. *Nat. Rev.*
11 *Neurosci.* **15**, 209–216 (2014).
- 12 89. Hanisch, U.-K. & Kettenmann, H. Microglia: active sensor and versatile effector
13 cells in the normal and pathologic brain. *Nat Neurosci* **10**, 1387–1394 (2007).
- 14 90. Davalos, D. *et al.* ATP mediates rapid microglial response to local brain injury
15 in vivo. *Nat. Neurosci.* (2005) doi:10.1038/nn1472.
- 16 91. Nimmerjahn, A., Kirchhoff, F. & Helmchen, F. Resting microglial cells are
17 highly dynamic surveillants of brain parenchyma in vivo. *Neuroforum* (2005)
18 doi:10.1515/nf-2005-0304.
- 19 92. Dinarello, C. A. Overview of the IL-1 family in innate inflammation and acquired
20 immunity. *Immunological Reviews* vol. 281 (2018).
- 21 93. Lucas, K. & Maes, M. Role of the toll like receptor (TLR) radical cycle in
22 chronic inflammation: Possible treatments targeting the TLR4 pathway.
23 *Molecular Neurobiology* vol. 48 (2013).
- 24 94. Song, Q., Meng, B., Xu, H. & Mao, Z. The emerging roles of vacuolar-type
25 ATPase-dependent Lysosomal acidification in neurodegenerative diseases.
26 *Translational Neurodegeneration* vol. 9 (2020).
- 27 95. Childs, B. G. *et al.* Senescent intimal foam cells are deleterious at all stages of
28 atherosclerosis. *Science* (80-.). **354**, 472–477 (2016).
- 29 96. Harris, C. A. *et al.* DGAT enzymes are required for triacylglycerol synthesis
30 and lipid droplets in adipocytes. *J. Lipid Res.* **52**, 657–667 (2011).
- 31 97. Mori, T., Buffo, A. & Gotz, M. The novel roles of glial cells revisited: the
32 contribution of radial glia and astrocytes to neurogenesis. *Curr Top Dev Biol*
33 **69**, 67–99 (2005).
- 34 98. Herman, A. B. *et al.* Regulation of stress granule formation by inflammation,
35 vascular injury, and atherosclerosis. *Arterioscler. Thromb. Vasc. Biol.* (2019)
36 doi:10.1161/ATVBAHA.119.313034.
- 37 99. Ivanov, P., Kedersha, N. & Anderson, P. Stress granules and processing
38 bodies in translational control. *Cold Spring Harb. Perspect. Biol.* **11**, (2019).
- 39 100. Jaud, M. *et al.* Translational Regulations in Response to Endoplasmic
40 Reticulum Stress in Cancers. *Cells* **9**, 540 (2020).
- 41 101. Alberti, S., Gladfelter, A. & Mittag, T. Considerations and Challenges in
42 Studying Liquid-Liquid Phase Separation and Biomolecular Condensates. *Cell*
43 vol. 176 419–434 (2019).
- 44 102. Boeynaems, S. *et al.* Protein Phase Separation: A New Phase in Cell Biology.
45 *Trends in Cell Biology* vol. 28 420–435 (2018).
- 46 103. Shin, Y. & Brangwynne, C. P. Liquid phase condensation in cell physiology
47 and disease. *Science* vol. 357 (2017).
- 48 104. Alberti, S. & Dormann, D. Liquid–Liquid Phase Separation in Disease. *Annu.*
49 *Rev. Genet.* **53**, 171–194 (2019).
- 50 105. Protter, D. S. W. & Parker, R. Principles and Properties of Stress Granules.

- 1 *Trends in Cell Biology* vol. 26 668–679 (2016).
- 2 106. Molliex, A. *et al.* Phase Separation by Low Complexity Domains Promotes
3 Stress Granule Assembly and Drives Pathological Fibrillization. *Cell* **163**, 123–
4 133 (2015).
- 5 107. Lin, Y., Protter, D. S. W., Rosen, M. K. & Parker, R. Formation and Maturation
6 of Phase-Separated Liquid Droplets by RNA-Binding Proteins. *Mol. Cell* **60**,
7 208–219 (2015).
- 8 108. Murakami, T. *et al.* ALS/FTD Mutation-Induced Phase Transition of FUS Liquid
9 Droplets and Reversible Hydrogels into Irreversible Hydrogels Impairs RNP
10 Granule Function. *Neuron* **88**, 678–690 (2015).
- 11 109. Patel, A. *et al.* A Liquid-to-Solid Phase Transition of the ALS Protein FUS
12 Accelerated by Disease Mutation. *Cell* **162**, 1066–1077 (2015).
- 13 110. Conicella, A. E., Zerze, G. H., Mittal, J. & Fawzi, N. L. ALS Mutations Disrupt
14 Phase Separation Mediated by α -Helical Structure in the TDP-43 Low-
15 Complexity C-Terminal Domain. *Structure* **24**, 1537–1549 (2016).
- 16 111. Lee, K. H. *et al.* C9orf72 Dipeptide Repeats Impair the Assembly, Dynamics,
17 and Function of Membrane-Less Organelles. *Cell* **167**, 774-788.e17 (2016).
- 18 112. Wang, J. *et al.* A Molecular Grammar Governing the Driving Forces for Phase
19 Separation of Prion-like RNA Binding Proteins. *Cell* **174**, 688-699.e16 (2018).
- 20 113. McGurk, L. *et al.* Poly(ADP-Ribose) Prevents Pathological Phase Separation
21 of TDP-43 by Promoting Liquid Demixing and Stress Granule Localization.
22 *Mol. Cell* **71**, 703-717.e9 (2018).
- 23 114. Gasset-Rosa, F. *et al.* Cytoplasmic TDP-43 De-mixing Independent of Stress
24 Granules Drives Inhibition of Nuclear Import, Loss of Nuclear TDP-43, and Cell
25 Death. *Neuron* **102**, 339-357.e7 (2019).
- 26 115. Fernandes, N. *et al.* Stress granule assembly can facilitate but is not required
27 for TDP-43 cytoplasmic aggregation. *Biomolecules* **10**, 1–19 (2020).
- 28 116. Hayashi, Y., Ford, L. K., Fioriti, L., McGurk, L. & Zhang, M. Liquid-Liquid
29 Phase Separation in Physiology and Pathophysiology of the Nervous System.
30 *J. Neurosci.* **41**, JN-SY-1656-20 (2021).
- 31 117. Cruz, A. L. S., Barreto, E. de A., Fazolini, N. P. B., Viola, J. P. B. & Bozza, P.
32 T. Lipid droplets: platforms with multiple functions in cancer hallmarks. *Cell*
33 *Death and Disease* vol. 11 (2020).
- 34 118. Prentzell, M. T. *et al.* G3BPs tether the TSC complex to lysosomes and
35 suppress mTORC1 signaling. *Cell* **184**, (2021).
- 36 119. Kolobova, E. *et al.* Microtubule-dependent association of AKAP350A and
37 CCAR1 with RNA stress granules. *Exp. Cell Res.* **315**, (2009).
- 38 120. Youn, J. Y. *et al.* High-Density Proximity Mapping Reveals the Subcellular
39 Organization of mRNA-Associated Granules and Bodies. *Mol. Cell* **69**, (2018).
- 40 121. Hofweber, M. *et al.* Phase Separation of FUS Is Suppressed by Its Nuclear
41 Import Receptor and Arginine Methylation. *Cell* **173**, 706-719.e13 (2018).
- 42 122. Luecken, M. D. & Theis, F. J. Current best practices in single-cell RNA-seq
43 analysis: a tutorial. *Mol. Syst. Biol.* **15**, e8746 (2019).
- 44 123. Hie, B., Bryson, B. & Berger, B. Efficient integration of heterogeneous single-
45 cell transcriptomes using Scanorama. *Nat. Biotechnol.* **37**, 685–691 (2019).
- 46 124. McInnes, L., Healy, J., Saul, N. & Großberger, L. UMAP: Uniform Manifold
47 Approximation and Projection. *J. Open Source Softw.* **3**, 861 (2018).
- 48 125. Deka, K. & Saha, S. Regulation of Mammalian HSP70 Expression and Stress
49 Response. in 3–25 (Springer, Cham, 2018). doi:10.1007/978-3-319-74715-
50 6_1.

1 Acknowledgments

2
3 We are particularly grateful to Dr. Magdalena Götz and Dr. Stefan Stricker (Ludwig-
4 Maximilians-University, Munich) for the valuable support toward this study,
5 experimental suggestions and critical reading of the manuscript. We would also like to
6 thank Dr. Michael Kiebler (Ludwig-Maximilians-University, Munich) for the critical
7 reading of the manuscript. Lastly, we thank all the members of the Neurogenesis and
8 Regeneration group for experimental inputs, discussions and critical reading of the
9 manuscript. We acknowledge the support of the following core facilities: the
10 Bioimaging Core Facility at the BioMedical Center of LMU Munich and the Sequencing
11 Facility at the Helmholtz Zentrum München.

12 This work was supported by the German research foundation (DFG) by the SFB 870;
13 TRR274; SPP 1738 “Emerging roles of non-coding RNAs in nervous system
14 development, plasticity & disease”, SPP1757 “Glial heterogeneity”; SPP2191
15 “Molecular mechanisms of functional phase separation” (ID 402723784) and the
16 Excellence Strategy within the framework of the Munich Cluster for Systems
17 Neurology (EXC 2145/1010 SyNergy – ID 390857198) and Ampro Helmholtz Alliance.

18 19 Author contributions

20
21 A.Z., K.T.N. and J.N. conceived the project and experiments. A.Z., K.T.N., S.K., S.H.,
22 L.S., C.D. performed the experiments and analyzed the data; A.Z., K.T.N., C.K., H.A.
23 and F.T. performed the bioinformatic analyses. A.Z., K.T.N., and J.N. wrote the
24 manuscript with inputs from B.S., J.S., and D.D. J.N. and D.D. supervised research
25 and acquired funding.

26 27 Declaration of Interests

28
29 The authors declare no competing interests.

30 31 Supplementary information

32
33 **Supplementary Table 1:** GO Terms (p-value < 0.05 and fold enrichment > 1.5) from
34 enriched genes in Wt microglia at 3 dpi. Related to Fig. 1.

35
36 **Supplementary Table 2:** GO Terms (p-value < 0.05 and fold enrichment > 1.5) from
37 upregulated and downregulated genes identified comparing each Wt microglia cluster
38 with all the others. Related to Fig. 1.

39
40 **Supplementary Table 3:** GO Terms (p-value < 0.05 and fold enrichment > 1.5) from
41 enriched genes in Grn-deficient vs Wt microglia at 7 dpi and in MG0 vs MG3 microglial
42 clusters. Related to Fig. 4.

43
44 **Supplementary Video 1:** Microglial and oligodendroglial cell reactivity in Wt
45 telencephalon at 7 dpi. Related to Fig. 3.

46
47 **Supplementary Video 2:** Microglial and oligodendroglial cell reactivity in Grn-deficient
48 telencephalon at 7 dpi. Related to Fig. 3.

1 **Supplementary Video 3:** Microglial and oligodendroglial cell reactivity in Grn-deficient
2 telencephalon at 31 dpi. Related to Fig. 3.

3

4 **Figures**

5

6 **Fig. 1: Stab wound injury induces a pro-regenerative signature in a *granulin a*- 7 expressing microglial subpopulation**

8 **(A)** Representative images of 4C4⁺ microglia (white) at different time points after injury
9 in the adult zebrafish telencephalon. Red and blue framed images are magnifications
10 of brain parenchyma near (red) and far from (blue) from injury sites. Scale bars, 100
11 μm or 20 μm (magnifications).

12 **(B)** UMAP plot depicting color-coded cellular clusters identified through single-cell
13 transcriptome analysis of Wt cells, isolated from intact and injured (3 and 7 dpi)
14 zebrafish telencephali. Cells are colored according to their cell type identity; each point
15 represents a single cell.

16 **(C)** Dot plot depicting representative GO terms enriched in the gene set identifying
17 microglial cells (cluster 17, Fig. 1B) at 3 dpi. GO Terms include Kyoto Encyclopedia of
18 Genes and Genomes (KEGG) pathways, Molecular Function (MF)- and Cellular
19 Component (CC)-related terms. Dot color, p-value; dot size, number of genes.

20 **(D)** Subclustering of Wt microglial cells (cluster 17, Fig. 1B) isolated from intact and
21 injured telencephali and combined. Cells are colored according to their microglial
22 subcluster identity; each point represents a single cell.

23 **(E)** Abundance of Wt microglial subclusters (from Fig. 1E) in different conditions: intact
24 (top), 3 dpi (middle), 7 dpi (bottom).

25 **(F)** Velocity analysis depicting Wt microglial dynamics in response to injury. Each dot
26 represents a single cell.

27 **(G-J)** Dot plots depicting the expression of genes associated with pro-regenerative
28 mouse microglia⁵¹ **(G)**, identified as significantly enriched in MG0 activated microglia
29 **(H)**, associated with lipid droplet formation⁴⁶ **(I)**, and depicting the expression of
30 granulin genes in different conditions **(J)**. Dot color, mean expression; dot size, fraction
31 of cells.

32

33 **Fig. 2: Granulins are necessary and sufficient to limit prolonged microglial 34 activation at injury sites**

35 **(A)** Representative images of 4C4 (red) and Plin3 (cyan) immunoreactivity in intact
36 parenchyma and at injury sites in Wt and Grn-deficient brains. Scale bars, 20 μm .

37 **(B, C)** Dot plots depicting the total number of Plin3⁺ droplets **(B)** and number of Plin3⁺
38 droplets within 4C4⁺ microglia **(C)** at injury sites in Wt and Grn-deficient brains. Data
39 are shown as mean \pm SEM. Each point represents one animal. Significance was
40 calculated with ordinary two-way ANOVA, and post-hoc Tukey test was used for
41 multiple comparison. *p < 0.05, **p < 0.01.

42 **(D)** Dot plot depicting the expression of genes associated with lipid droplet formation⁴⁶
43 in Wt and Grn-deficient microglia. Dot color, mean expression; dot size, fraction of
44 cells.

45 **(E)** Heatmaps depicting triacylglycerols (TAGs) and diacylglycerols (DAGs) content in
46 intact and injured Wt and Grn-deficient telencephali (7 dpi). Scale bar, z-score.

47 **(F)** Experimental paradigm of intraparenchymal recombinant progranulin (PGRN)
48 injections in the adult Grn-deficient zebrafish.

1 (G) Representative images of 4C4 (red) and Plin3 (cyan) immunoreactivity at injury
 2 sites in vehicle- and PGRN-injected Grn-deficient animals. Scale bars, 100 μ m or 20
 3 μ m (magnifications).
 4 (H, I) Dot plots showing the number of total Plin3⁺ droplets (H) and Plin3⁺ droplets
 5 within 4C4⁺ microglia (I) at injury sites of Wt, Grn-deficient and mPGRN-injected Grn-
 6 deficient animals at 7 dpi. Data are shown as mean \pm SEM. Each point represents
 7 one animal. Significance was calculated with ordinary one-way ANOVA, and post-hoc
 8 Tukey test was used for multiple comparison. *p < 0.05, **p < 0.01, ***p < 0.001.

9
 10 **Fig. 3: Granulin deficiency-induced neuroinflammation prolongs glial reactivity**
 11 **at injury sites and impairs restorative neurogenesis**

12 (A) Representative images of 4C4 (red) and Sox10 (cyan) immunoreactivity of injured
 13 Wt and Grn-deficient telencephalic hemispheres at different time points (3, 7 and 21
 14 dpi). Boxed areas representing injury site are magnified. Scale bars, 100 μ m or 20 μ m
 15 (magnifications).

16 (B) Dot plot depicting the number of Sox10⁺ cells at injury sites in Wt and Grn-deficient
 17 animals. Data are shown as mean \pm SEM. Each point represents one animal.
 18 Significance was calculated with ordinary two-way ANOVA, and post-hoc Tukey test
 19 was used for multiple comparison. *p < 0.05, **p < 0.01.

20 (C) Scheme depicting the experimental timeline of methanol/dexamethasone
 21 manipulations in the adult Grn-deficient brain.

22 (D) Representative images of 4C4 (red) and Sox10 (cyan) of
 23 methanol/dexamethasone-treated Grn-deficient animals at 7 dpi. Scale bars, 100 μ m
 24 or 20 μ m (magnifications).

25 (E) Dot plot depicting the number of Sox10⁺ cells injury sites in
 26 methanol/dexamethasone-treated Grn-deficient animals at 7 dpi. Data are shown as
 27 mean \pm SEM. Each point represents one animal. Significance was calculated with
 28 unpaired Student's t-test. *p < 0.05, **p < 0.01.

29 (F, G) Schemes depicting the experimental paradigm (F) and brain areas analyzed
 30 (G) to assess restorative neurogenesis in Wt and Grn-deficient animals.

31 (H) Representative images and orthogonal projections of HuC/D (green) and BrdU
 32 (magenta) immunoreactivity in the telencephalic parenchyma of Wt and Grn-deficient
 33 animals. Boxed areas are magnified. Scale bars, 100 μ m or 20 μ m (magnifications).

34 (I) Dot plot depicting the number of HuC/D⁺BrdU⁺ cells in the telencephalic
 35 parenchyma of Wt and Grn-deficient animals. Data are shown as mean \pm SEM. Each
 36 point represents one animal. Significance was calculated with unpaired Student's T-
 37 test. *p < 0.05, **p < 0.01.

38
 39 **Fig. 4: Activated microglia fail to transition back to the homeostatic state in the**
 40 **Grn-deficient injured CNS**

41 (A) UMAP plot depicting subclustering of merged Wt and Grn-deficient microglial cells
 42 isolated from intact and injured (3 dpi and 7 dpi) telencephali on the basis of their
 43 transcriptomes. Cells are colored according to their microglial subcluster identity; each
 44 point represents a single cell.

45 (B) UMAP plots depicting color-coded microglia from Wt or Grn-deficient zebrafish
 46 telencephali (intact and injured conditions were merged). Cells are colored according
 47 to which genotype they are isolated from; each point represents a single cell.

48 (C) Velocity analysis depicting microglial dynamics in response to injury in Wt and Grn-
 49 deficient microglia. Each dot represents a single cell. Dot color, p-value; dot size,
 50 number of genes.

1 (D, E) Dot plots depicting representative GO terms enriched in the upregulated gene
2 set in Grn-deficient microglia compared with Wt microglia at 7 dpi (D) and enriched in
3 MGO cells vs MG3 cells (E). Dot color, p-value; dot size, number of genes.
4 (F, G) Dot plots depicting the expression of genes associated with lipid droplet
5 formation⁴⁶ (F) and stress related genes¹²⁵ (G). Dot color, mean expression; dot size,
6 fraction of cells.

7

8 **Fig. 5: Clearance of extranuclear TDP-43 condensates formed through LLPS is**
9 **required for termination of microglia-driven neuroinflammation**

10 (A) Representative images of 4C4 (magenta), Plin3 (green) and TDP-43 (cyan) Wt
11 and Grn-deficient injured telencephali at 3 dpi and 7 dpi. Scale bar, 20 μ m.

12 Yellow arrowheads indicate examples of extranuclear TDP-43⁺ condensates; white
13 arrowheads indicate examples of nuclear TDP-43⁺ signal.

14 (B) Dot plot depicting numbers of TDP-43⁺ condensates at injury sites in Wt and Grn-
15 deficient animals. Data are shown as mean \pm SEM. Each point represents one animal.
16 Significance was calculated with ordinary two-way ANOVA, and post-hoc Tukey test
17 was used for multiple comparison. *p < 0.05, **p < 0.01, ***p < 0.001, ****p < 0.0001.

18 (C) Scheme of experimental paradigm of intraparenchymal injections of vehicle/TDP-
19 43 (uncleaved)/phase-separated TDP-43 (cleaved) in Wt zebrafish.

20 (D) Schematic representation of TDP-43 (containing MBP tag) and phase-separated
21 TDP-43 (MBP tag cleaved off).

22 (E) Representative images of 4C4 (magenta) and Plin3 (green) in Wt injured (7 dpi)
23 telencephali injected with vehicle, TDP-43 or phase-separated TDP-43 proteins. Scale
24 bar, 20 μ m.

25 (F, G) Dot plots depicting total numbers of Plin3⁺ droplets (F) and numbers of Plin3⁺
26 droplets within 4C4⁺ microglia (G) at injury sites in vehicle/TDP-43-injected Wt
27 animals. Data are shown as mean \pm SEM. Each point represents one animal.
28 Significance was calculated with ordinary one-way ANOVA, and post-hoc Tukey test
29 was used for multiple comparison. *p < 0.05, **p < 0.01.

30

31 **Fig. 6: Prevention of excessive LLPS-mediated formation of SGs is sufficient to**
32 **terminate prolonged neuroinflammation in Grn-deficient animals**

33 (A) Scheme of experimental timeline of lipoamide/DMSO administration in injured Grn-
34 deficient animals.

35 (B) Representative images of 4C4 (magenta), TDP-43 (cyan) and Plin3 (green) in
36 injured (7 dpi) Grn-deficient animals treated with DMSO/lipoamide. Scale bar, 20 μ m.

37 (C, D) Dot plots depicting the total number of TDP-43⁺ condensates (C) and the
38 number of Plin3⁺ droplets within 4C4⁺ microglia (D) at injury sites at 7 dpi in Wt, Grn-
39 deficient and lipoamide-treated Grn-deficient animals. Data are shown as mean
40 \pm SEM. Each point represents one animal. Significance was calculated with ordinary
41 one-way ANOVA, and post-hoc Tukey test was used for multiple comparison. *p <
42 0.05, **p < 0.01, ***p < 0.001, ****p < 0.0001.

43 (E) UMAP plot depicting subclustering of merged Wt and Grn-deficient (including
44 lipoamide-treated cells) microglial cells isolated from intact and injured (3 dpi and 7
45 dpi) telencephali on the basis of their transcriptomes. Cells are colored according to
46 their microglial subcluster identity; each point represents a single cell.

47 (F) UMAP plot depicting color coded microglia from lipoamide-treated Grn-deficient
48 zebrafish telencephali (for lipoamide-treated microglia, only 7 dpi was included). Cells
49 are colored according to which condition and genotype they are isolated from; each
50 point represents a single cell.

1 (G) Abundance of microglial subclusters (from Fig. 6E) in different conditions:
 2 untreated Grn-deficient (top) and lipoamide-treated Grn-deficient microglia (bottom) at
 3 7 dpi.

4 (H) Dot plot depicting representative GO terms enriched in the downregulated gene
 5 set of lipoamide-treated Grn-deficient microglia at 7 dpi (compared with untreated Grn-
 6 deficient microglia at the same time point). GO Terms include Kyoto Encyclopedia of
 7 Genes and Genomes (KEGG) pathways, Molecular Function (MF)- and Cellular
 8 Component (CC)-related terms. Dot color, p-value; dot size, number of genes.

9 (I, J) Dot plots depicting the expression of genes associated with lipid droplet formation
 10 ⁴⁶ (I) and stress-related genes ¹²⁵ (J) in untreated Grn-deficient and lipoamide-treated
 11 Grn-deficient microglia at 7 dpi. Dot color, mean expression; dot size, fraction of cells.
 12

13 Fig. 7: Stroke induces lipid droplet and SG formation in the human brain

14 (A, B) Representative images of IBA1, PLIN3, TDP-43 and G3BP immunoreactivity in
 15 healthy area distant from stroke area (A) and penumbra area (B) from post-mortem
 16 human brain tissues obtained from patients with ischemic stroke. Scale bar, 200 μ m
 17 or 20 μ m (magnifications).
 18

19 Extended Data Figures

20 Extended Data Fig. 1: Extended scRNA-seq analysis of Wt cells

21 (A) UMAP plot depicting color-coded cellular clusters identified on the basis of the
 22 single-cell transcriptome analysis of cells isolated from intact and injured (3 and 7 dpi)
 23 Wt zebrafish telencephali. Cells are colored according to their cell type identity; each
 24 point represents a single cell.
 25

26 (B) Injury response kinetics of indicated cell types relative to intact condition.

27 (C) UMAP plots depicting color-coded Wt conditions (intact, 3 dpi, 7 dpi). Cells are
 28 colored according to the condition they are isolated from; each point represents a
 29 single cell.

30 (D) UMAP plots depicting characteristic cell-type marker gene expression (identifying
 31 microglial, radial glial, oligodendroglial and neuronal clusters) in single cells isolated
 32 from intact and injured (3 and 7 dpi) Wt telencephali. Scale, normalized expression
 33 level; each point represents a single cell.

34 (E) Table depicting the number of differentially upregulated genes in specific condition
 35 in microglia isolated from Wt telencephali.

36 (F-G) Dot plots depicting the expression of genes associated with lipid droplet
 37 formation in different conditions (Marschallinger et al., 2020) (F) and expression of
 38 granulin genes in different microglial subclusters (G). Dot color, mean expression; dot
 39 size, fraction of cells.
 40

41 Extended Data Fig. 2: Lipid composition of Wt and Grn-deficient telencephali

42 (A) Representative images of 4C4 (red) and Plin3 (cyan) immunoreactivity with
 43 orthogonal projections at injury sites in Wt and Grn-deficient brains displaying
 44 colocalization of Plin3⁺ lipid droplets with 4C4⁺ microglial cells. Scale bars, 20 μ m.

45 (B) Dot plot showing the proportion of Plin3⁺4C4⁺ double-positive lipid droplets among
 46 total Plin3⁺ droplets at injury sites in Wt and Grn-deficient brains. Data are shown as
 47 mean \pm SEM. Each point represents one animal. Significance was calculated with
 48 ordinary two-way ANOVA, and post-hoc Tukey test was used for multiple comparison.

49 (C) Representative images of 4C4 (red) and BODIPY (cyan) reactivity at injury sites
 50 in Wt and Grn-deficient brains. Scale bars, 20 μ m.

1 (D) Heatmaps depicting phosphatidylcholine (PC), cholesteryl ester (CE) and
2 phosphatidylethanolamine (PE) content in intact and injured (7 dpi) Wt and Grn-
3 deficient telencephali. Scale bar, z-score.

4

5 **Extended Data Fig. 3: Extended characterization of wound healing progression**
6 **in Wt and Grn-deficient CNS**

7 (A) Representative images of 4C4 (red) and Sox10 (cyan) immunoreactivity in intact
8 Wt and Grn-deficient telencephalic hemispheres. Boxed areas are magnified. Scale
9 bars, 100 μm or 20 μm (magnifications).

10 (B) Dot plot depicting the number of Sox10⁺ cells in intact Wt and Grn-deficient brains.
11 Data are shown as mean \pm SEM. Each point represents one animal. Significance was
12 calculated using Student's t-test.

13 (C) Representative images of DAPI (white) labelling in intact and injured (3 and 7 dpi)
14 Wt and Grn-deficient telencephali. Scale bars, 100 μm .

15 (D) Scheme depicting the experimental timeline of dexamethasone/methanol
16 manipulations in the adult Grn-deficient brain at 3 dpi.

17 (E) Representative images of 4C4 (red) and Sox10 (cyan) of
18 methanol/dexamethasone-treated Grn-deficient animals at 3 dpi. Scale bars, 100 μm
19 or 20 μm (magnifications).

20 (F) Dot plot depicting the number of Sox10⁺ cells at injury sites in
21 methanol/dexamethasone-treated Grn-deficient animals at 3 dpi. Data are shown as
22 mean \pm SEM. Each point represents one animal. Significance was calculated using
23 Student's t-test.

24

25 **Extended Data Fig. 4: Extended scRNA-seq analysis of Wt and Grn-deficient**
26 **cells**

27 (A) UMAP plot depicting color-coded cellular clusters identified on the basis of the
28 single-cell transcriptome analysis of cells, isolated from intact and injured (3 and 7 dpi)
29 Wt and Grn-deficient zebrafish telencephali. Cells are colored according to their cell
30 type identity; each point represents a single cell.

31 (B) UMAP plots depicting color-coded intact and injured (3 and 7 dpi) conditions from
32 Wt and Grn-deficient zebrafish telencephali. Cells are colored according to the
33 condition they are isolated from; each point represents a single cell.

34 (C) UMAP plots depicting characteristic cell-type marker gene expression (identifying
35 microglial, radial glial, oligodendroglial and neuronal clusters) in single cells isolated
36 from intact and injured (3 and 7 dpi) Wt and Grn-deficient zebrafish telencephali.
37 Scale, normalized expression level; each point represents a single cell.

38 (D) UMAP plot depicting subclustering of Wt and Grn-deficient microglial cells in intact
39 an injured telencephali based on their transcriptome. Cells are colored according to
40 their microglial subcluster identity; each point represents a single cell. (Same as Fig.
41 4A).

42 (E) Abundance of microglial subclusters (from Fig. S4D) from different Wt and Grn-
43 deficient conditions: intact (left), 3 dpi (middle) and 7 dpi (right).

44 (F) Similarity matrix depicting correlation between Wt-only microglial subclusters (from
45 Fig. 1) and merged (Wt and Grn-deficient) microglial subclusters (from Fig. 4). Scale
46 bar, similarity index.

47 (G) UMAP plots depicting the cell identity of Wt microglia to correlate Wt-only
48 microglial subclusters (from Fig. 1) and merged (Wt and Grn-deficient) microglial
49 subclusters (from Fig. 4).

50

1 **Extended Data Fig. 5: Characterization of TDP-43⁺ condensate formation and**
 2 **clearance in response to brain injury**

3 (A) Representative images of HuC/D (magenta) and TDP-43 (cyan) immunoreactivity
 4 in intact zebrafish telencephalon. Scale bar, 100 μ m or 20 μ m (magnifications).

5 (B) Representative images of 4C4 (magenta) and TDP-43 (cyan) immunoreactivity
 6 with orthogonal projections at injury sites of Wt and Grn-deficient brains displaying
 7 colocalization of TDP-43⁺ condensates with 4C4⁺ microglial cells. Scale bar, 20 μ m.

8 (C) Experimental paradigm of the intraparenchymal recombinant progranulin (PGRN)
 9 injections in the adult Grn-deficient zebrafish.

10 (D) Representative images of 4C4 (magenta) and TDP-43 (cyan) immunoreactivity at
 11 injury sites of vehicle- and PGRN-injected Grn-deficient animals. Scale bars, 100 μ m
 12 or 20 μ m (magnifications).

13 (E) Dot plot depicting the numbers of TDP-43⁺ condensates at injury sites of Wt, Grn-
 14 deficient and PGRN-injected Grn-deficient animals at 7 dpi. Data are shown as mean
 15 \pm SEM. Each point represents one animal. Significance was calculated with ordinary
 16 one-way ANOVA, and post-hoc Tukey test was used for multiple comparison. *p <
 17 0.05, **p < 0.01, ***p < 0.001, ****p < 0.0001.

18
 19 **Extended Data Fig. 6: Specificity of phase-separated TDP-43 overload in**
 20 **promoting persistent neuroinflammation**

21 (A) Scheme depicting the experimental paradigm of intraparenchymal injections of
 22 vehicle/uncleaved/cleaved TDP-43 and FUS in Wt zebrafish.

23 (B) Coomassie blue-stained SDS-PAGE gel of different intraparenchymal injection
 24 solutions: vehicle (buffer + TEV), TDP-43 (uncleaved) and phase-separated TDP-43
 25 (cleaved).

26 (C) Representative bright field microscopy images of phase-separated TDP-43
 27 (cleaved) and unseparated TDP-43 (uncleaved). Scale bar, 50 μ m or 25 μ m
 28 (magnifications).

29 (D) Representative images of 4C4 (magenta) and TDP-43 (cyan) in injured (7 dpi) Wt
 30 telencephali injected with TDP-43 (uncleaved) or phase-separated (cleaved) TDP-43.
 31 Scale bar, 20 μ m.

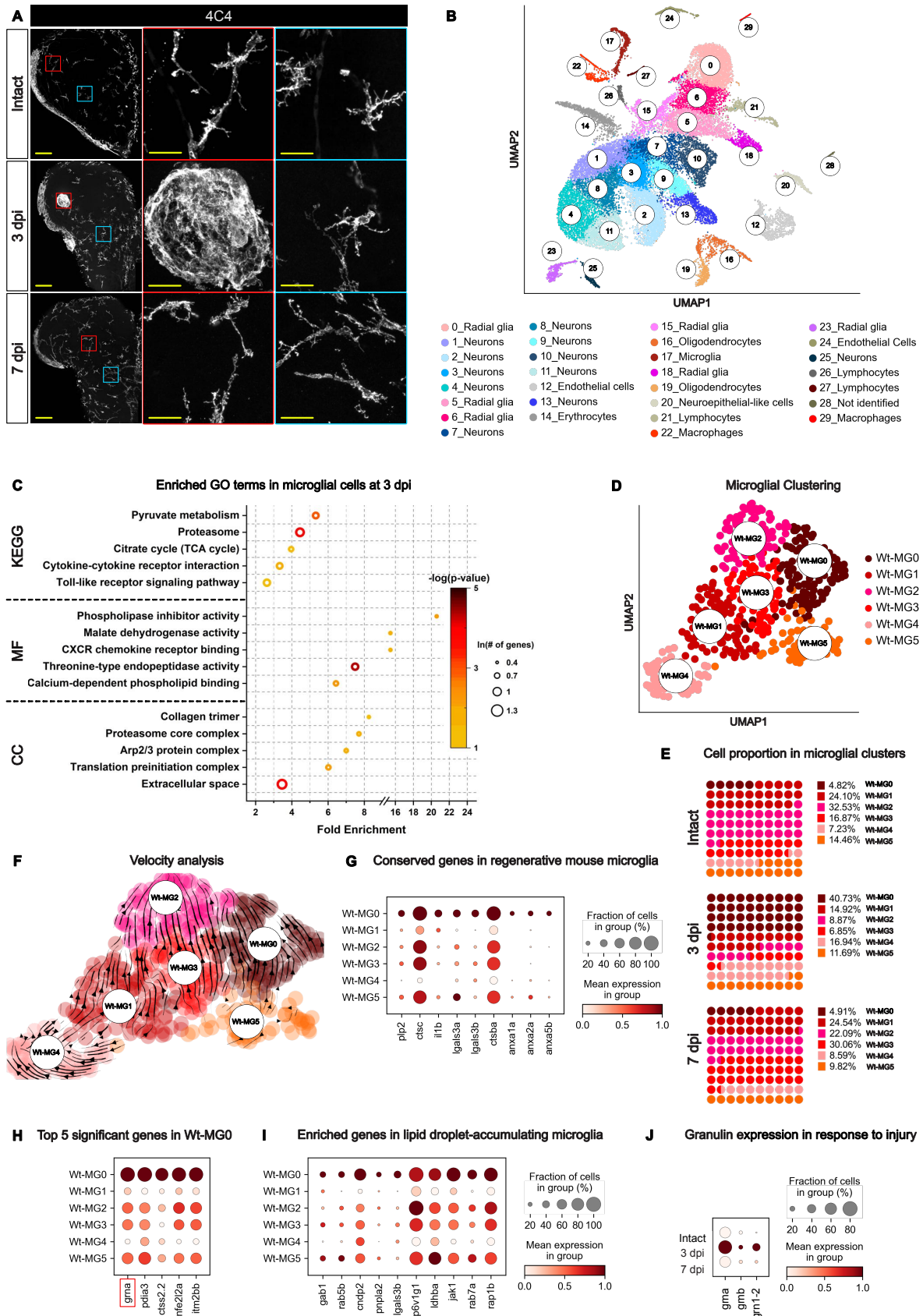
32 (E) Dot plot depicting the total number of TDP-43⁺ condensates at injury sites in
 33 vehicle-, TDP-43- and phase-separated TDP-43-injected Wt animals at 7 dpi. Data are
 34 shown as mean \pm SEM. Each point represents one animal. Significance was
 35 calculated with ordinary one-way ANOVA, and post-hoc Tukey test was used for
 36 multiple comparison. *p < 0.05, **p < 0.01.

37 (F) Dot plot depicting the expression of *tardbp* and *tardbpl* genes in microglia in
 38 different Wt conditions. Dot color, mean expression; dot size, fraction of cells.

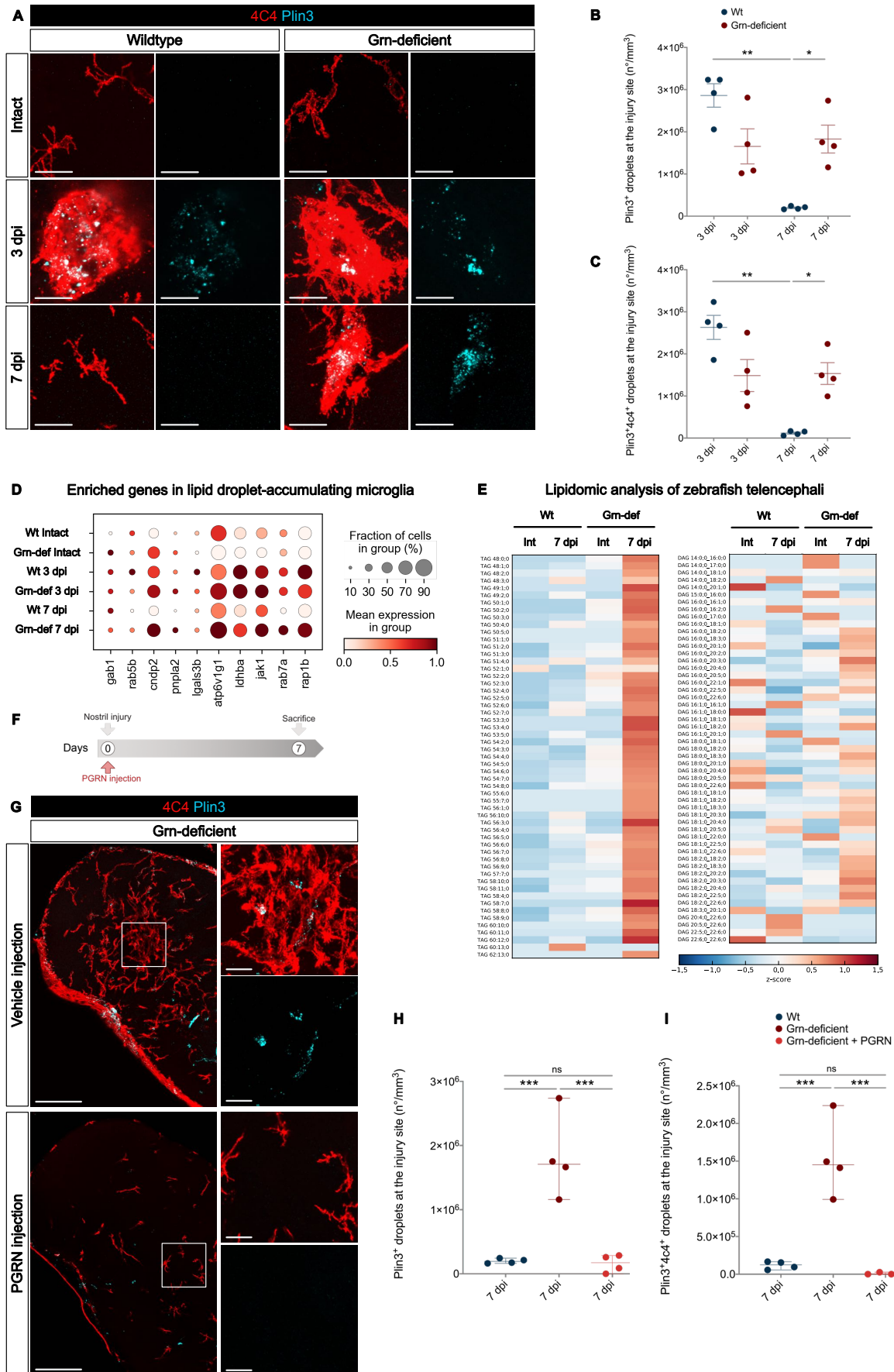
39 (G) Schematic representation of FUS (containing MBP tag) and phase-separated
 40 (MBP tag cleaved off) FUS proteins.

41 (H) Representative images of 4C4 (magenta) and Plin3 (green) in Wt injured (7 dpi)
 42 telencephali injected with FUS (uncleaved) or phase-separated (cleaved) FUS. Scale
 43 bar, 20 μ m.

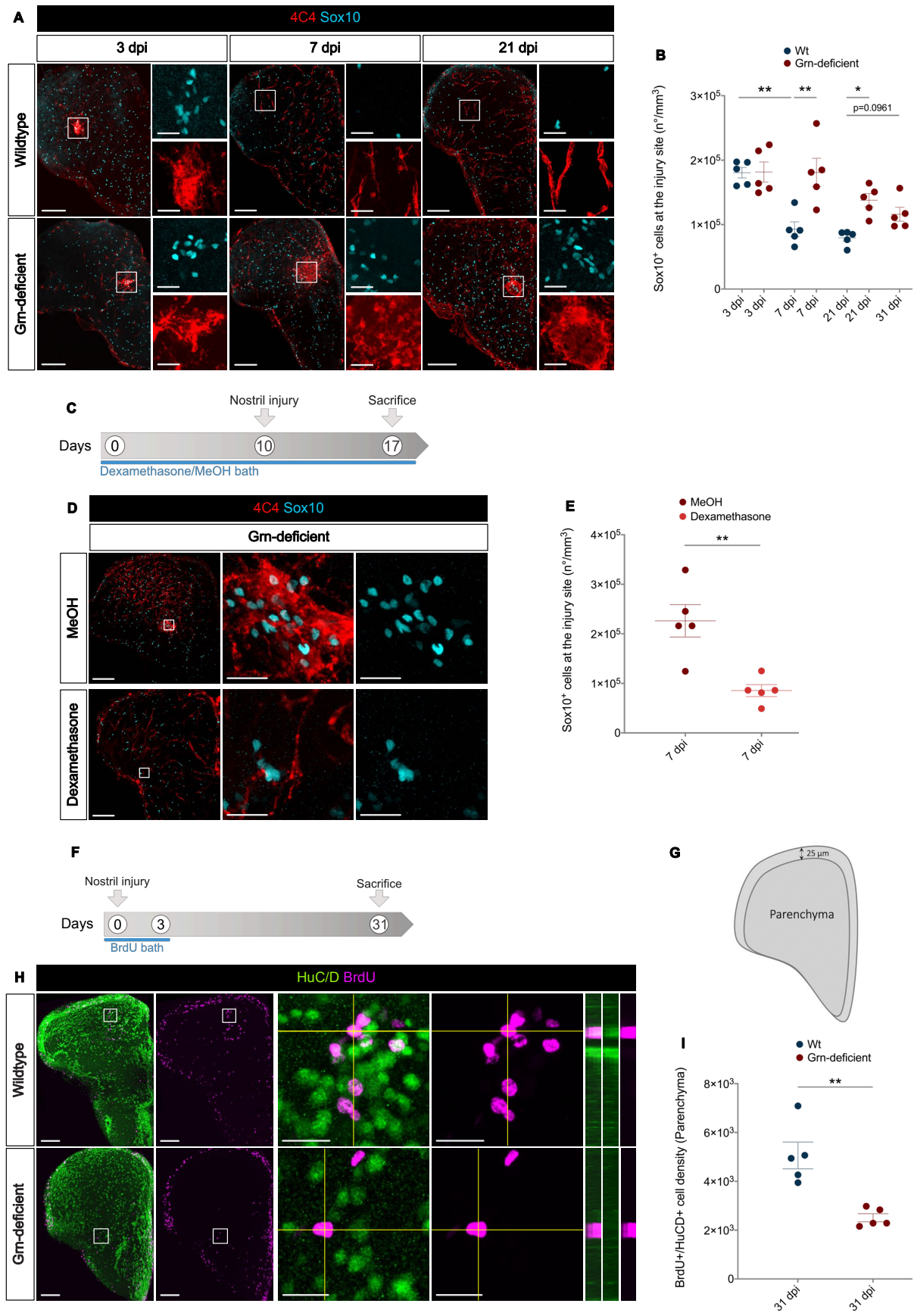
44 (I-J) Dot plots depicting the total numbers of Plin3⁺ lipid droplets (I) and numbers of
 45 Plin3⁺ lipid droplets within 4C4⁺ microglia (J) at injury sites in vehicle/FUS-injected
 46 Wt animals. Data are shown as mean \pm SEM. Each point represents one animal.
 47 Significance was calculated with ordinary one-way ANOVA, and post-hoc Tukey test
 48 was used for multiple comparison.



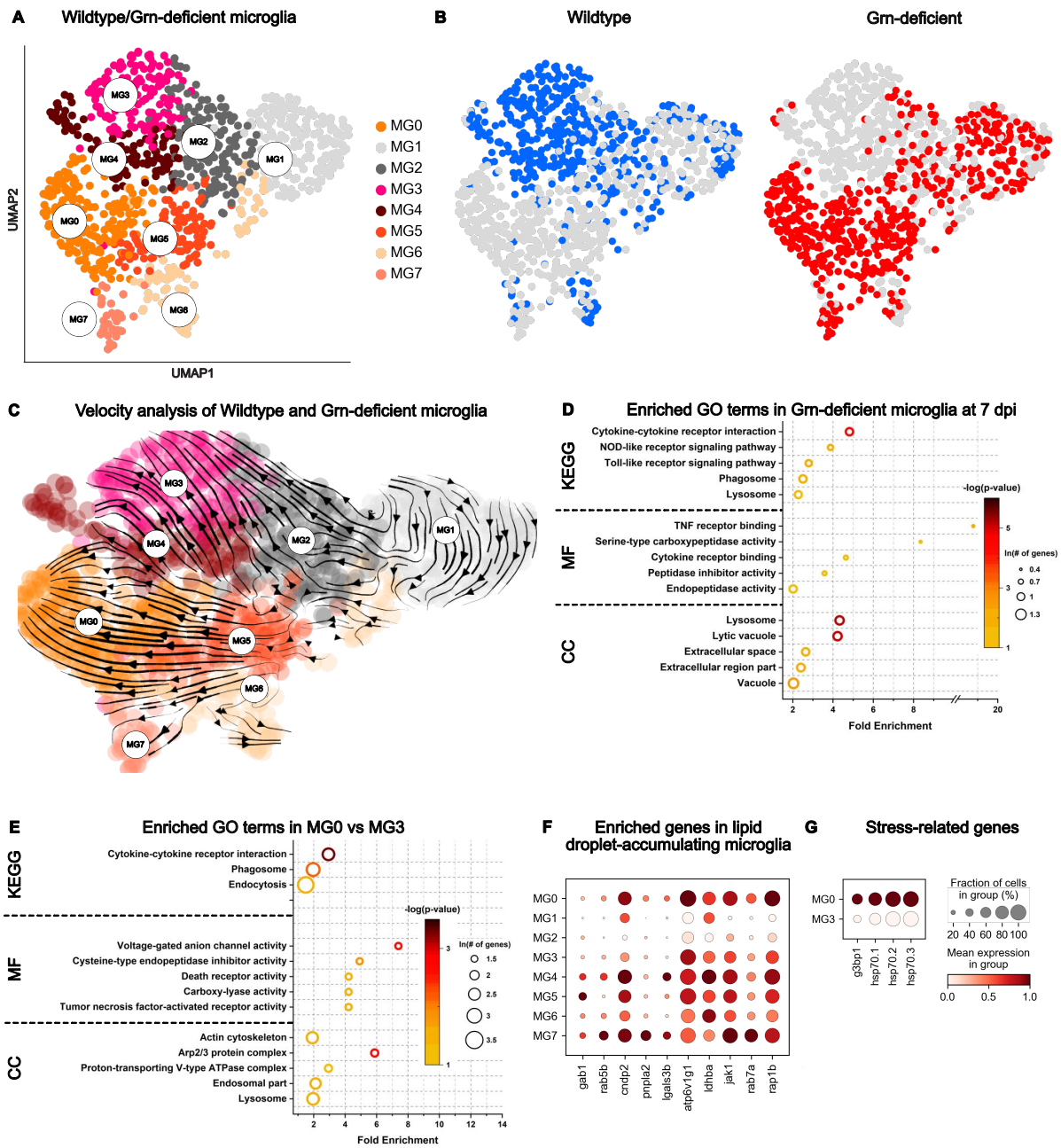
Zambusi, Novoselc et al., Fig. 1



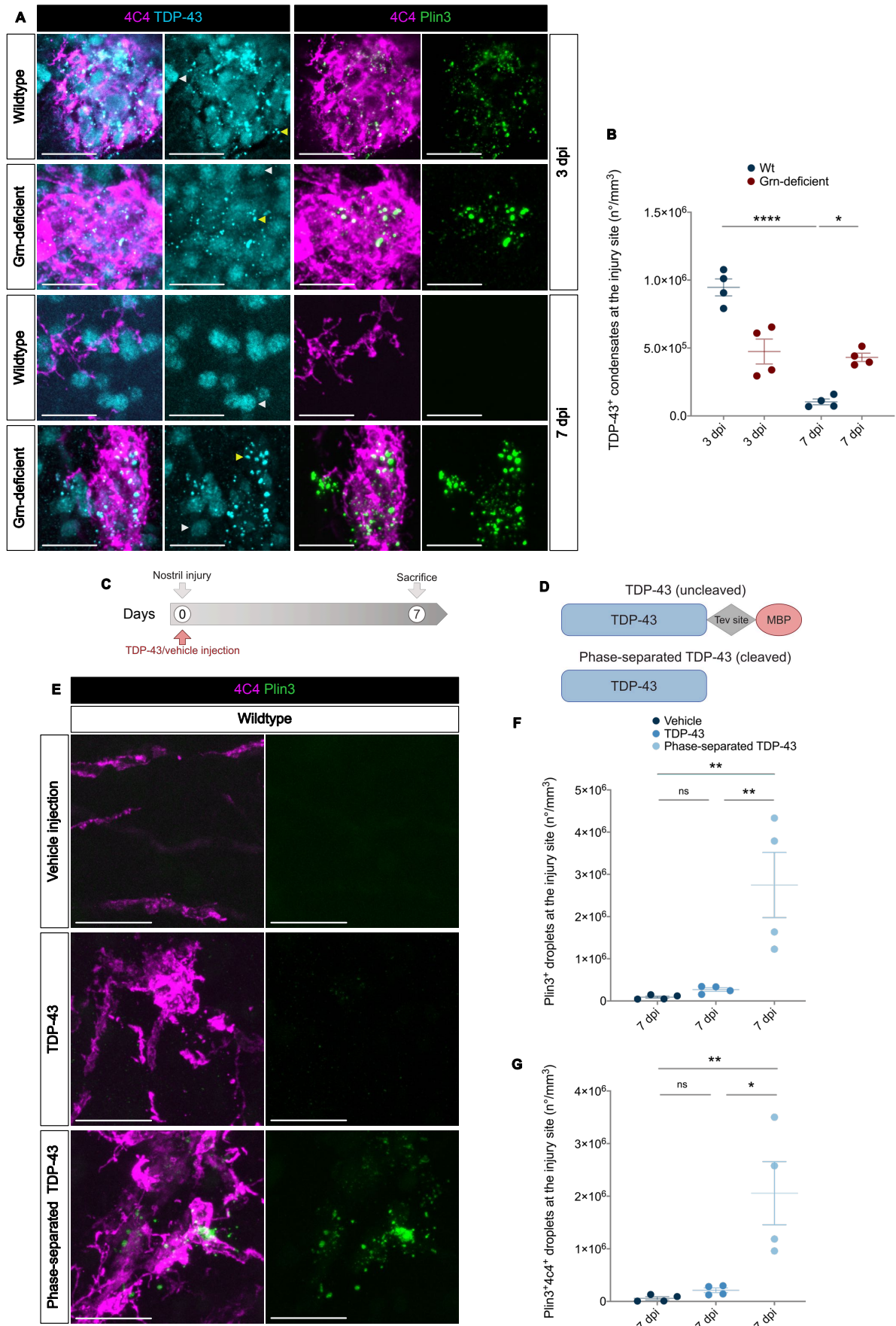
Zambusi, Novoselc et al., Fig. 2



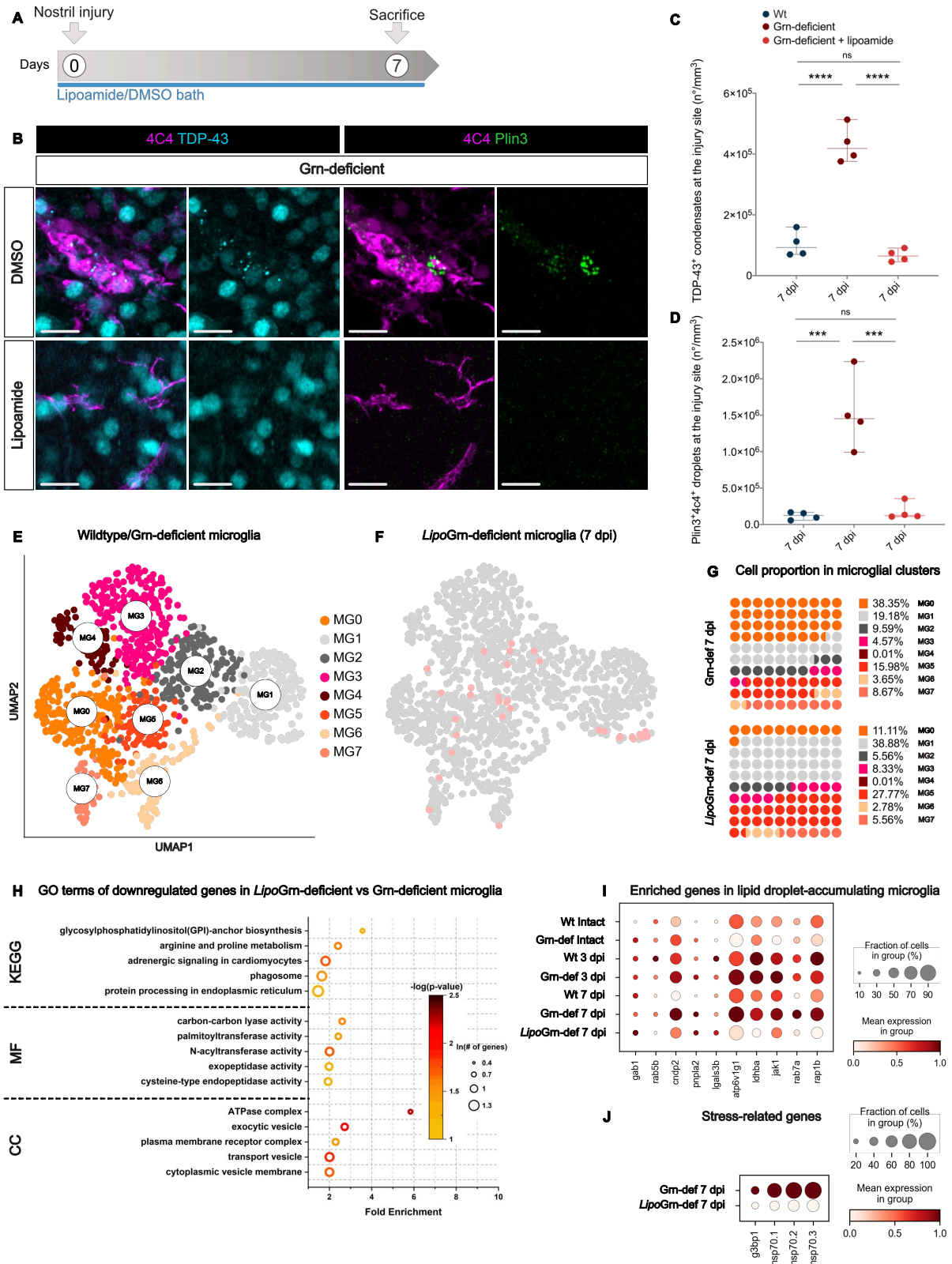
Zambusi, Novoselc et al., Fig. 3



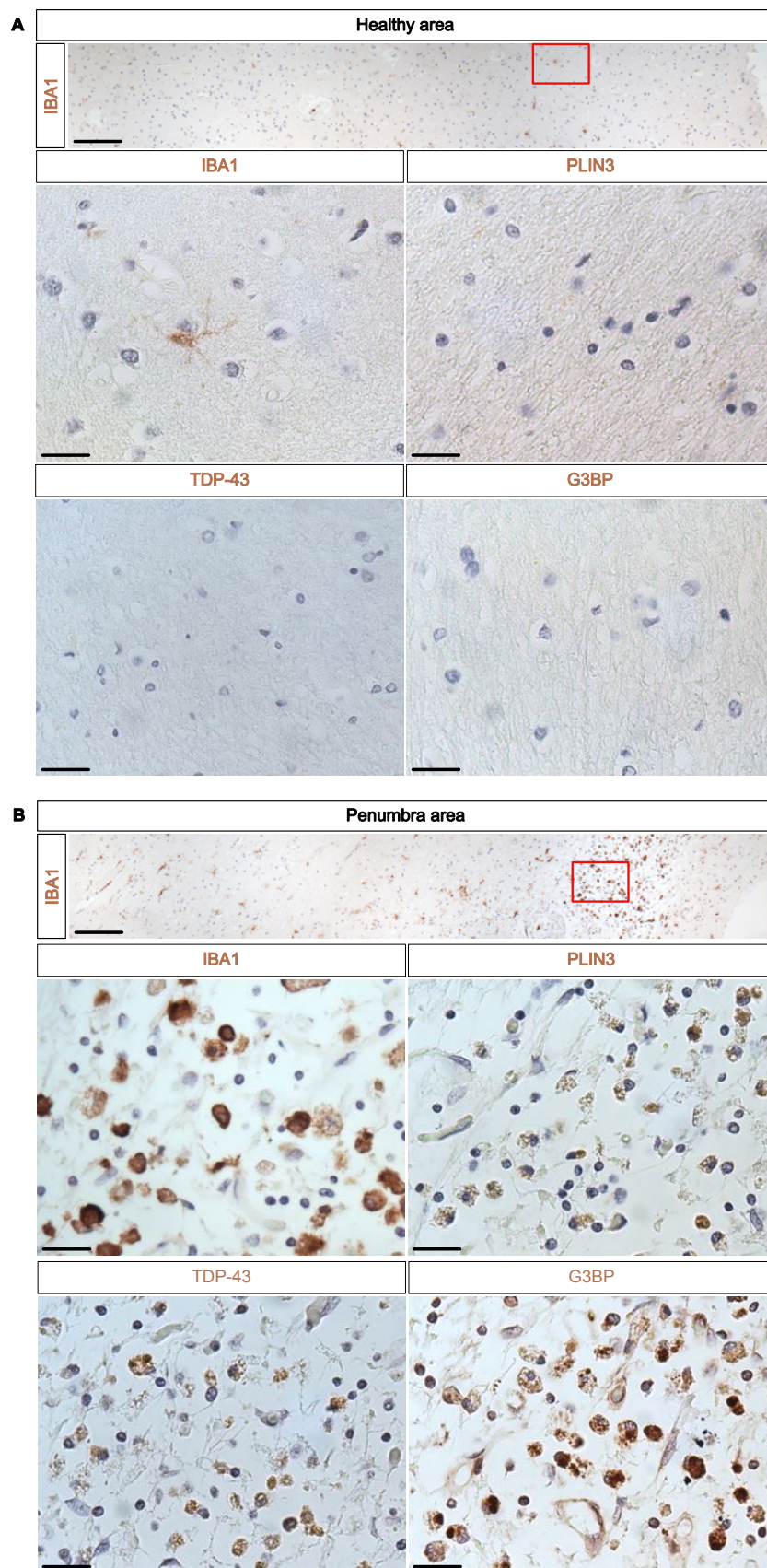
Zambusi, Novoselc et al., Fig. 4



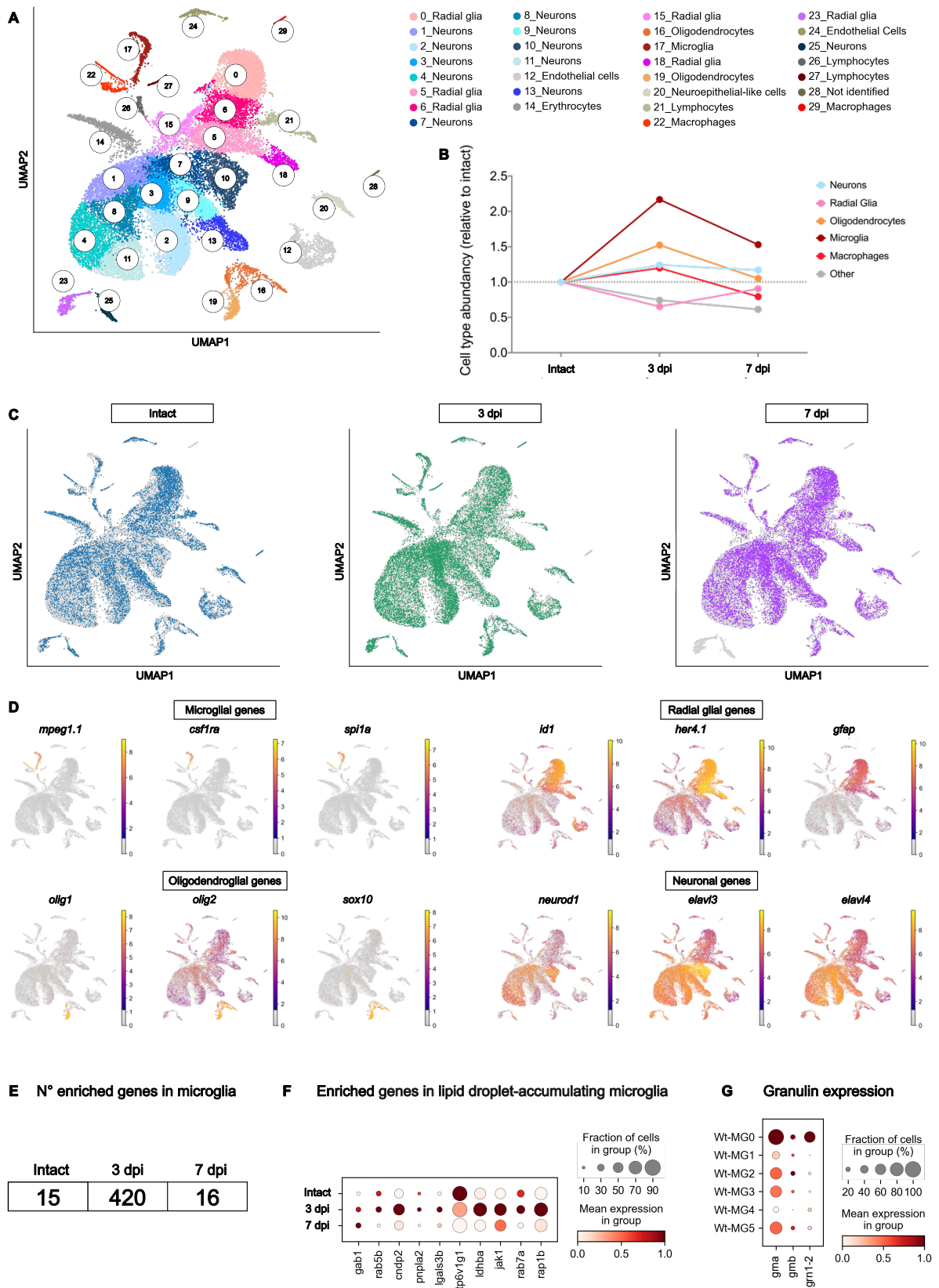
Zambusi, Novoselc et al., Fig. 5



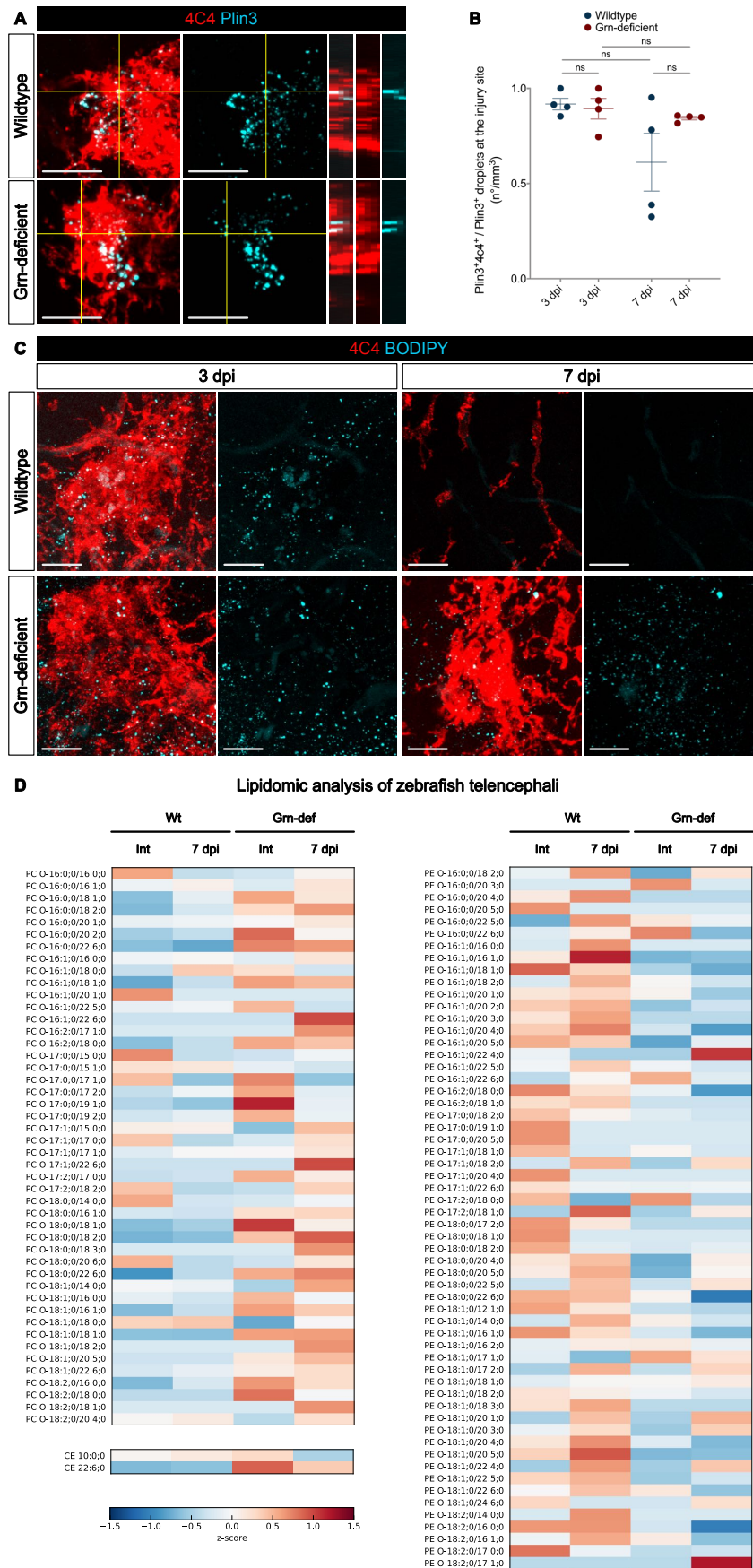
Zambusi, Novoselc et al., Fig. 6



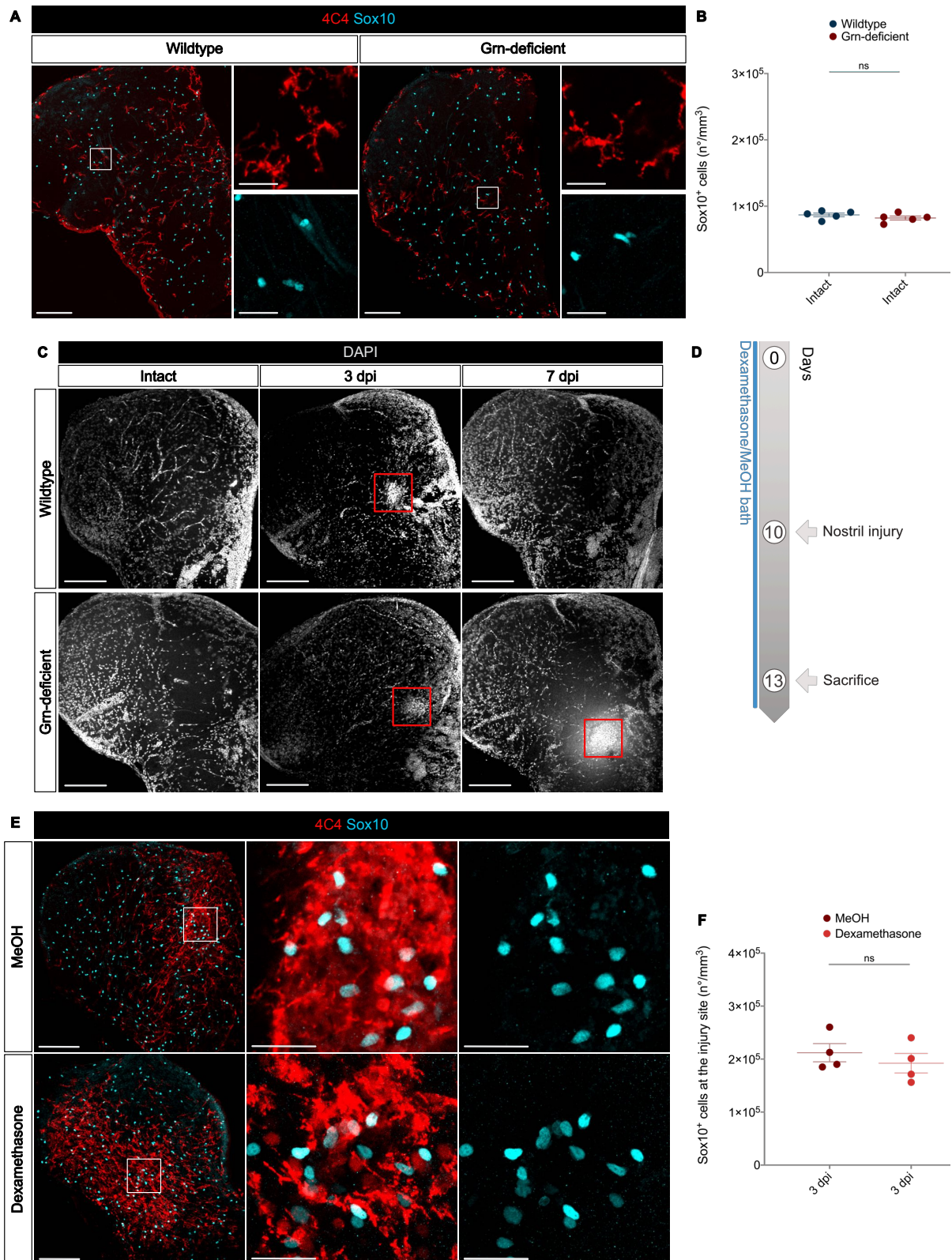
Zambusi, Novoselc et al., Fig. 7



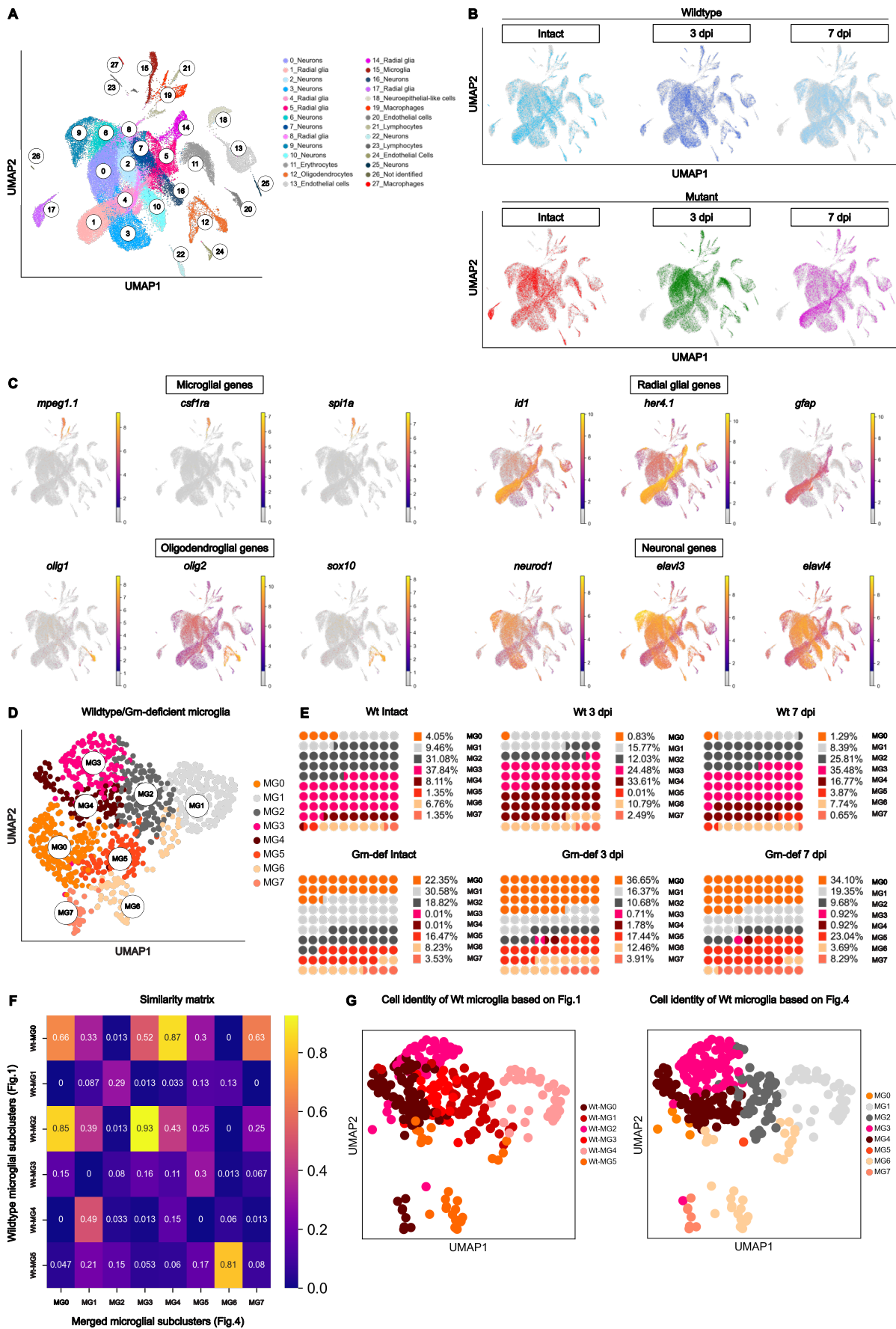
Zambusi, Novoselc et al., Extended Data Fig. 1



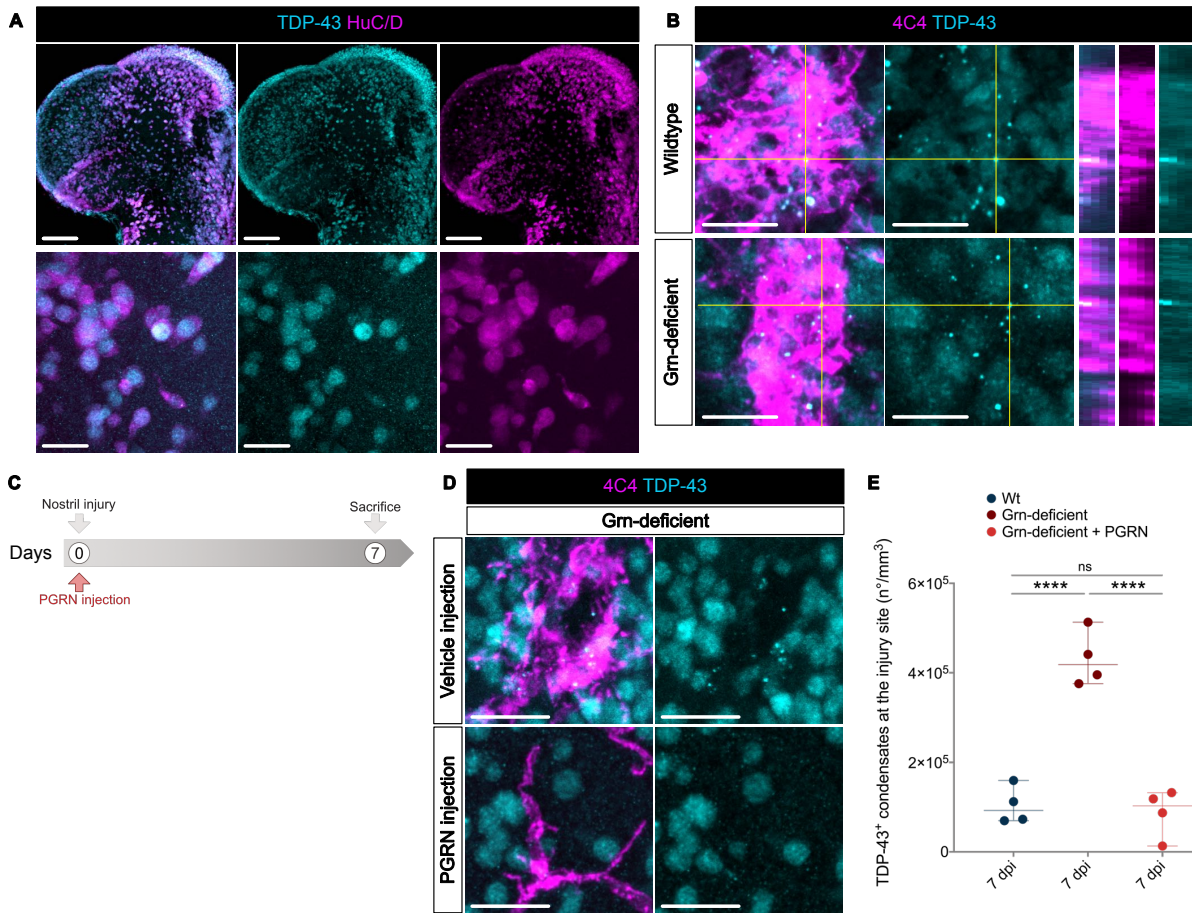
Zambusi, Novoselc et al., Extended Data Fig. 2

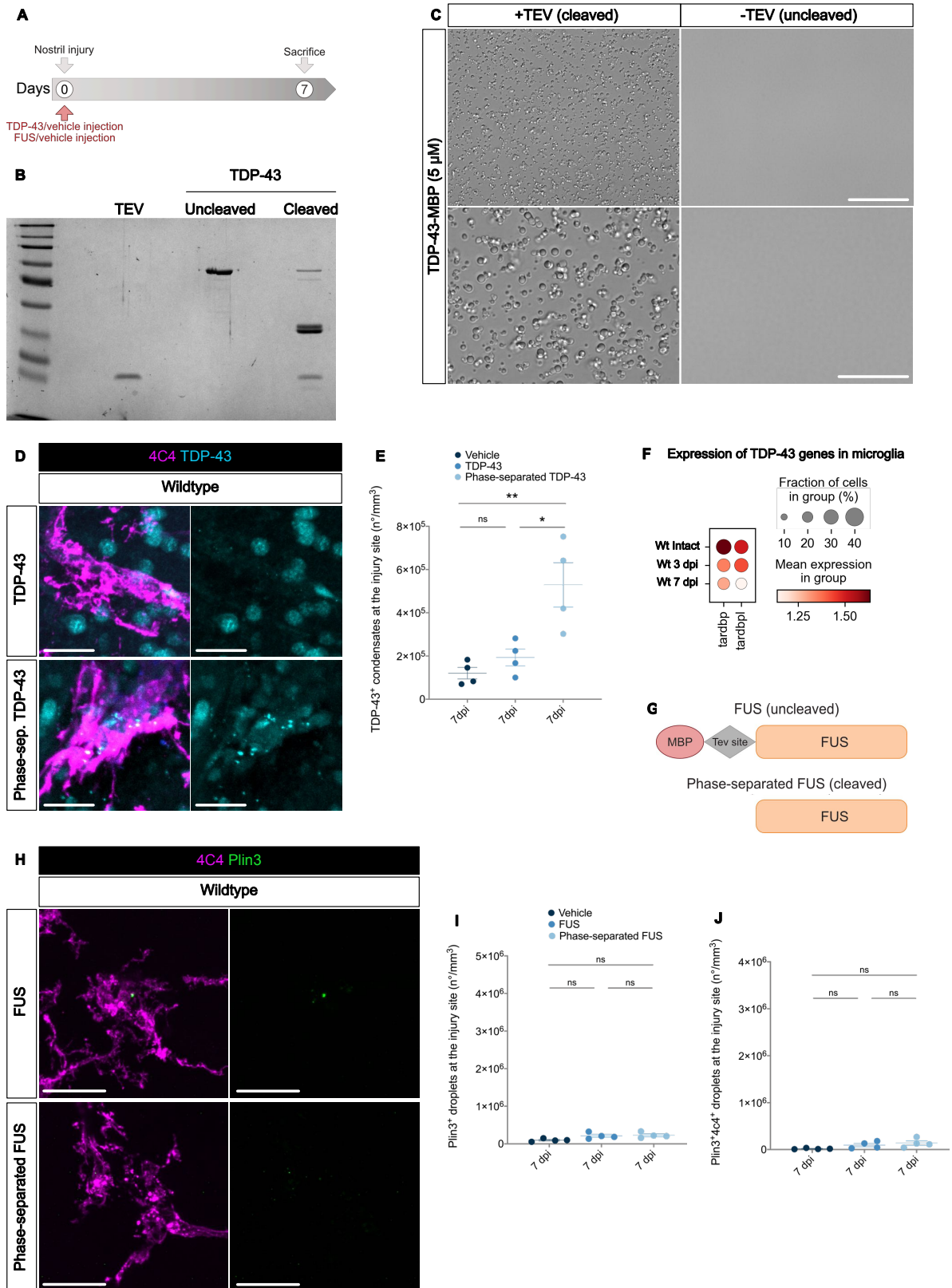


Zambusi, Novoselc et al., Extended Data Fig. 3



Zambusi, Novoselc et al., Extended Data Fig. 4





Zambusi, Novoselc et al., Extended Data Fig. 6

2.3 Aim of study III

The study aims to generate a transcriptomic toolbox of the injured murine brain, which can be used to understand cellular reactivity in response to injury and identify therapeutical targets to improve regeneration. As a target, I assessed the role of two innate immunity pathways, namely Tlr1/2 and Cxcr3, in glial reactivity upon injury in the murine cerebral cortex.

Spatial, temporal and cell-type-specific profiling of the injured brain

Christina Koupourtidou*, Veronika Schwarz*, Hananeh Aliee, Simon Frerich, Judith Fischer-Sternjak, Tatiana Simon-Ebert, Riccardo Bocchi, Magdalena Götz, Fabian J. Theis, Jovica Ninkovic

* These authors contributed equally to the manuscript

My contribution to this manuscript in detail:

For this manuscript, I performed all animal experiments for the experiments mentioned below. I performed the scRNA-seq and spatial transcriptomics, including wet-bench and bioinformatic analysis of the data. I also was responsible for the validations with RNA scope. Furthermore, I contributed to the writing and editing of the manuscript.

The current manuscript will be submitted to Nature Neuroscience next month following its review by the co-authors.

Note that due to an elevated number of pages, Extended Tables are not included in the PDF version of the dissertation but are available as separate excel files via the following link <https://syncandshare.lrz.de/getlink/fi15N6AGbSvM3yJL6Yxqho/Ext.Tables>

Spatial, temporal and cell-type-specific profiling of the injured brain

Christina Koupourtidou^{1,2*}, Veronika Schwarz^{1,2*}, Hananeh Aliee³, Simon Frerich^{2,7}, Judith Fischer-Sternjak^{4,5}, Tatiana Simon-Ebert^{4,5}, Riccardo Bocchi^{4,5}, Magdalena Götz^{4,5,6}, Fabian J. Theis³, Jovica Ninkovic^{1,5,6#}

¹ Department for Cell Biology and Anatomy, Biomedical Center (BMC), Ludwig-Maximilians-Universität (LMU), Planegg-Martinsried, Germany

² Graduate School Systemic Neurosciences, LMU, Munich, Germany.

³ Institute of Computational Biology, Helmholtz Zentrum Munich, Munich, Germany

⁴ Department of Physiological Genomics, BMC, LMU, Planegg-Martinsried, Germany

⁵ Institute of Stem Cell Research, Helmholtz Zentrum Munich, Munich, Germany

⁶ Munich Cluster for Systems Neurology SYNERGY, LMU, Munich, Germany

⁷ Institute for Stroke and Dementia Research, University Hospital of Munich, LMU Munich

* these authors equally contributed to the manuscript

#Correspondence to: ninkovic@helmholtz-muenchen.de

Abstract

Traumatic brain injury (TBI) is a major contributor to death and disability and is a risk factor for the development of neurodegenerative diseases. The initial trauma disrupts brain homeostasis leading to a highly orchestrated immune- and glial cell response. A holistic understanding of mechanisms involved in the injury-induced activation of specific cell types is indispensable for manipulating their response. Thus, we developed a toolbox profiling the transcriptional changes across various cell types in spatial and temporal context. By combining spatial- and single-cell transcriptomics, we revealed the transcriptomic signature of the injured murine cerebral cortex, which is shaped by distinct subpopulations of astrocytes, microglia, and oligodendrocyte precursor cells (OPCs) accumulating around the injury site. Interestingly, these cellular subpopulations displayed a shared inflammatory signature involving the innate immune-related pathways Tlr1/2 and Cxcr3. Systemic manipulation of these pathways altered the transcriptional profile of glial cells associated with selective changes of their reactive states.

Introduction

Traumatic brain injuries (TBIs) are important health and societal problem as TBIs affect people of all ages and is one of the major causes of death and disability. In the European Union alone around 1.5 million incidences are annually reported^{1,2}. TBIs are defined as acute brain insults due to an external force, such as direct impact of the penetrating object on the brain or acceleration/deceleration force-induced concussions². TBI-induced damages are characterized by complex and progressive pathophysiology, triggering structural and functional changes and can be classified into primary and secondary damage³. The primary damage is triggered at the time of injury by the external force itself leading to neuronal and glial cell death, axonal damage, edema and disruption of the BBB⁴. The initial insult is followed by progressive secondary damage phase, which develops over hours and days, including metabolic, neurochemical, cellular and molecular changes^{4,5}. Additionally, secondary damages further induce neuronal circuit dysfunction, neuroinflammation, oxidative stress and protein aggregation. These cellular changes have been linked to prolonged symptom persistence and increased vulnerability to additional pathologies, including neurodegenerative disorders^{4,5}.

The TBI-induced pathophysiology evolves through a highly orchestrated response of glial cells with peripherally derived infiltrating immune cell populations³. Upon CNS insults, brain-resident microglia are rapidly activated and change their morphology to a hypertrophic, ameboid morphology⁶. Additionally, activated microglia proliferate, polarize and extend their processes and migrate to the injury site^{3,7}. Similar to microglia, the oligodendrocyte progenitor cells (OPCs), known as NG2-glia, display rapid cellular changes in response to damage, including hypertrophy, increase in cell number, polarisation and migration towards the injury site⁸⁻¹¹. Although, astrocytes also react to injury with changes in their morphology, gene expression and function in a process referred to "reactive astrogliosis", cell number enlarges only slightly and astrocyte proliferation occurs later in the time course of the injury^{8,12,13}. Reactive astrocytes are characterised by upregulation of intermediate filaments, such as glial fibrillary acidic protein (GFAP), nestin and vimentin¹³⁻¹⁵. In contrast to microglia and OPCs, astrocytes do not migrate to the injury area after stab-wound injury and only a small proportion of astrocytes, located around blood vessels (juxtavascular astrocytes), proliferate¹⁶. These initial responses facilitate the formation of a glial border between intact and damaged tissue^{12,17,18}, which is not only necessary to restrict the damage^{12,17-19} but also to promote axonal regeneration and circuit restoration^{12,19-21}. However, an adequate border establishment requires distinct reactions of glial cells in relative distance to the injury site. Indeed, for astrocytes and OPCs it has already been demonstrated that the distance from the injury site is shaping their reactive state^{10,16,22}. Despite recent advances on deciphering molecular signals essential for driving cells in distinct reactive states^{20,23,24}, the molecular pathways and cellular interactions underlying glial border formation are largely unknown. Essential cross-regulations of different cell types have been reported in several pathological conditions²⁵⁻²⁷, including the TBI^{23,28}. For example, under neuroinflammatory conditions, reactive microglia instruct astrocytes to be neurotoxicity²⁹. Furthermore, proliferating astrocytes regulate monocyte invasion²³, while BBB dysfunction alters astrocyte homeostasis and contributes to epileptic episodes^{30,31} following TBI.

One major limitation preventing a comprehensive understanding of cellular interactions and mediating signals essential for glial border formation is the restricted

view of most studies on a single cellular population. Addressing the injury-induced changes holistically requires a broad investigation of multiple cell types in the injury milieu and would hence provide a thorough insight in the cellular reactivity following brain injury. To unbiasedly identify regulatory pathways inducing distinct spatial glial reaction and to understand how each cell type contributes to glial border formation following TBI, we generated a cellular profile at spatial and single-cell resolution, using the 10x Genomics platforms Visium and Chromium, respectively. This data provided insights into the spatial, temporal and single-cell responses of multiple cell types and revealed a novel, so far overlooked common injury-induced innate immunity-shared glia signature.

Results

Brain injury elicits localised, injury-specific transcriptomic profile in the murine cerebral cortex

Traumatic brain injury (TBI) induces coordinated cellular reactions leading to glial border formation and isolation of the injury site from adjacent healthy tissue¹². Importantly, the TBI-induced cellular response is dependent on the distance of the cell to the injury site^{9,16}. To unbiasedly identify regulatory pathways leading to individual, spatially defined reaction of glial cells associated with glial border formation after stab-wound injury, we made use of the 10x Genomics Visium Spatial Gene Expression platform (Visium). This gave us the advantage not only to investigate the expression of a multitude of genes at the injury site but also to examine their dynamic expression as a function of the distance to the injury. The primary impact initiates a cascade of processes, which involve reaction of both: glial- and infiltrating or resident immune cells^{22,32}. To capture the response of both, infiltrating immune cells (peak at 3 days post-injury (dpi)²³) and different glial cells (reactivity peak range 2-5dpi^{13,23,33}), we performed spatial transcriptomics at 3dpi. Injury-induced alterations were determined by comparing stab-wounded brain sections to corresponding intact sections (Fig. 1a, Ext. Fig. 1a). Stab wound injuries were performed at the border between the motor and somatosensory cortex of both hemispheres by inserting a V-lance surgical knife into the cortical parenchyma without injuring the white matter as previously described³⁴. Since our main focus lies on examining the injury-induced changes in the cerebral cortex, we manually resected the mouse brain (Fig. 1a, Ext. Fig. 1a) to generate smaller sample sizes. This allowed us to position two parenchymal sections on a single capture area (Ext. Fig. 1b). Each section contained the following brain areas: cortex (CTX), white matter (WM) and hippocampal formation (HPF), as identified by using the Allen brain atlas as a reference (Fig. 1b). The selected sections covered 1991 and 1740 spots of the Visium capture area, of intact and injured condition, respectively. Libraries were prepared using the 10x Visium approach and were subsequently sequenced on the Illumina NextSeq 2000 platform. The quality of both data sets was examined utilizing the scanpy³⁵ and squidpy pipelines^{35,36}.

To identify changes induced by the injury, we integrated the two datasets and analyzed in total 3710 spots with 4804 median genes per spot. We identified 16 transcriptomic signatures (clusters) based on transcriptional similarities using the highly variable genes and dimensionality reduction using 17 principal components (Fig. 1c, Ext. Fig. 1c, d, Ext. Table 1). Notably, we were able to identify clusters corresponding to specific anatomical structures such as cluster II expressing genes characteristic of cortical layer 2/3 neurons, cluster VIII genes representing layer 4

neurons, cluster I genes identifying layer 5- and cluster IV genes characterizing layer 6 neurons³⁷ (Ext. Fig. 1c-e, Ext. Table 2). Importantly, this global cortical layer patterning was not affected by the injury as we could observe similar clusters identifying neuronal layers also in the injured brain section (Fig. 1c, Ext. Fig. 1c, e). However, in addition to clusters characterizing individual anatomical structures, we were also able to identify an injury-specific cluster, cluster VI that was localized around the injury core (Fig. 1b, c, Ext. Fig. 1c). Interestingly, cluster VI spread throughout cortical layers 1-5 and was absent in the intact brain sections (Fig. 1c, Ext. Fig. 1c). Cluster VI was characterised by a specific transcriptomic signature and showed enrichment of genes related to reactive astrocytes³⁸⁻⁴¹ (*Gfap*, *Lcn2*, *Serpina3n*, *Vim*, *Lgals1*, *Fabp7* and *Tspo*) and microglia⁴² (*Aif1*, *Csf1r*, *Cd68*, *Tspo*), which have been reported before to be hallmarks of CNS damage⁴⁰ (Fig. 1d, Ext. Fig. 1d, Ext. Table 1).

To understand the spatial distribution of these reactivity hallmarks, we conducted spatial trajectory analysis using the SPATA2 analysis pipeline⁴³. This allowed us to visualise individual gene expression patterns as a function of the distance from the injury core (Fig. 1e). Along the mediolateral trajectory we compared gene expression patterning to a variety of mathematical models (using the function `assessTrajectoryTrends`). We mainly focused on the 'peaking genes', which displayed enriched expression at the injury core (Fig. 1f, Ext. Fig. 1f). Among the top genes, which peaked in the injured area (Ext. Fig. 1f), we validated the expression of *Serpina3n* and *Lcn2* on RNA and protein level, as both genes exhibited strong specificity to the injury area, both by clustering (Fig. 1g) and the trajectory analysis (Fig. 1h). In line with the spatial gene expression analysis, *Serpina3n* and *Lcn2* displayed an enriched expression profile in the injured area, overall reminiscent of cluster VI patterning (Fig. 1c). Although, both genes are particularly enriched at the injury site, *Serpina3n* expression, in comparison to *Lcn2*, is not exclusively restricted to the injury, but can also be observed in subcortical areas such as the HPF (Fig. 1i, j). Additionally, we investigated the expression of *Cd68* as one of the genes being specific for cluster VI (Fig. 1g). However, since *Cd68* expression is solely restricted to the injury core and the expression in the injury vicinity is negligible, a fit to mathematic models was not attainable (Fig. 1g, h, Ext. Fig. 1f). A pronounced expression of *Cd68* around the injury core was further confirmed with RNA scope as well as by immunohistochemistry (Fig. 1i, j).

Furthermore, to get a closer insight into the regulated processes within cluster VI, we performed Gene Ontology (GO) term analysis using the 718 significantly enriched genes ($pval < 0.05$, \log_2 fold change > 1) of this cluster in comparison to all other clusters. The main regulated biological processes (BP) were related to immune response and angiogenesis, whereby the molecular functions (MF) and the cellular components (CC) exhibited changes in genes related to the extracellular matrix (Fig. 1k). All these processes have been reported to drive glial reaction in response to brain injury and to facilitate glial border formation¹⁹. Moreover, processes associated with phagocytosis (lysosome, lytic vacuole, phagocytotic vesicle) were enriched in cluster VI (Fig. 1k), in line with the described importance of phagocytotic processes in the context of brain insults⁴⁴. Taken together, our spatial gene expression analysis identified an injury-specific cluster, characterized by angiogenesis and immune system-related processes, including phagocytosis.

Multiple cellular states contribute to injury-induced local transcriptome

Even though the Visium platform offers the possibility to profile transcriptomic changes by preserving spatial information, the profile itself arises from multiple cells, which are captured in each spot (1-10 cell resolution). To assess the cellular composition of the injured area and to identify which cell population(s) define the transcriptomic profile of cluster VI, we performed single-cell RNA-sequencing (scRNA-seq) analysis from intact and stab wound-injured (3dpi) cortices by utilizing the droplet-based approach offered by the 10x Genomics Chromium platform (Fig. 2a). After applying quality control filters, we identified in total 6322 single cells (Fig. 2b) emerging from both conditions (Intact: 2676 cells, 3dpi: 3646 cells, Fig. 2c) with overall 19290 detected genes. Cells were distributed in 30 distinct clusters based on the expression of highly variable genes and subsequent unsupervised clustering (Fig. 2b, Ext. Fig. 2a, b). To annotate these clusters, we selected the 50 most enriched genes of each cluster and used online available databases for the mouse brain (<http://mousebrain.org>) and immune cells (http://rstats.immgen.org/MyGeneSet_New/index.html) to reveal their identity. By this approach, we identified neuronal as well as glial clusters including astrocytes, microglia and oligodendrocyte lineage cells besides vascular cells, pericytes and multiple types of immune cells (Fig. 2b, Ext. Fig. 2a, b). Additionally, we generated gene expression scores based on established marker genes of well-characterized cell populations in the adult mouse brain (Ext. Table 3). Indeed, these gene scores exhibited enrichment in the corresponding cellular populations, further cross-validating the cluster annotation (Fig. 2d).

Interestingly, by comparing the cell distribution between both conditions (intact and injured), we observed that several clusters of immune and glial cells were highly abundant only in the injured paradigm (Fig. 2c, Ext. Fig. 2a). Clusters '8_NKT/T cells', '13_Macrophages/Monocytes', '17_DCs', '18_Monocytes' and '22_DCs', for example, mainly appeared after injury and in addition to their distinct cell identity markers (Ext. Fig. 2b, Ext. Table 4) were also expressing *Ccr2*^{6,22} (Ext. Fig. 1c). Microglia clusters, which appeared after injury ('11_Microglia', '16_Microglia'), exhibited high expression of *Aif1* and low expression of the homeostatic microglia markers *Tmem119* and *P2ry12*⁴⁵ (Ext. Fig. 2c). Similarly, the astrocytic clusters '12_Astrocytes' and '23_Astrocytes' were mainly displayed in the injured condition and were characterized by high expression of classical reactive astrocyte markers such as *Gfap* and *Lcn2*^{38,46} (Ext. Fig. 2d). In addition to microglia and astrocytes, also OPC cluster '15_OPCs' was mainly present after injury (Ext. Fig. 2a). The cells of cluster '15_OPCs' expressed a combination of several genes related to cell cycle (G2M phase, Ext. Table 5^{47,48}) and *Cspg4* (Ext. Fig. 2e), both hallmarks of NG2-glia which rapidly proliferate upon brain injury⁹.

To elucidate, which of these cellular clusters form the injury-specific transcriptome of cluster VI, we mapped the single cell expression data onto the spatial gene expression data set (Fig. 2e-f, Ext. Fig. 3 + 4) using Tangram⁴⁹. To implement Tangram, we restricted the data set to the cortical clusters of the Visium data set (Clusters: I, II, IV, VI, VII, VIII, IX) in order to include the same anatomical region as for the acquisition of the scRNA-seq data. We trained Tangram by using 439 training genes. This gene set constituted the union of top marker genes for each cluster in the scRNA-seq data set, which were also detectable in the Visium. The training genes were selected using the AutoGeneS⁵⁰ pipeline (for more details see the methods section). The probabilistic mapping predicted cluster '11_Microglia', '16_Microglia',

'12_Astrocytes', '23_Astrocytes', '13_Macrophages/Monocytes', '18_Monocytes' and '15_OPCs' to be localized in proximity to the injury core (Fig. 2e, Ext. Fig. 3a). In contrast, neuronal clusters '1_Neurons', '2_Neurons', '24_Neurons' as well as astrocytic clusters '3_Astrocytes', '5_Astrocytes', '7_Astrocytes' and '9_Astrocytes' displayed decreased representation around the injury site (Ext. Fig. 3a). Additionally, we used the H&E image of the Visium data set to estimate the cell number within each spot of the Visium capture area, which in combination with the probabilistic mapping can be used for deconvolution. To some extent, this analysis further associated the above-mentioned clusters with the injury milieu (Fig. 2f, Ext. Fig. 4a, b). Importantly, not all glial cells contributed to the injury environment (Ext. Fig. 3b, 4b). The vast majority of astrocytic clusters, with the only exception of clusters '12_Astrocytes' and '23_Astrocytes', did not show an enriched mapping at the injury site and this was also true for the oligodendrocyte clusters "20_MOL" and "27_COPs" (Ext. Fig. 3b). Furthermore, also with the deconvolution analysis these populations displayed no enrichment to the injury vicinity (Ext. Fig. 4c). In summary, by combining spatial transcriptomics with corresponding scRNA-sequencing data sets, we identified an injury-specific transcriptional profile, which exhibits an enrichment of individual glial subpopulations and subsequent depletion of distinct astrocytic and neuronal clusters.

Injury induces common transcriptomic changes in glia cells

Glia cell reactivity exhibits various temporal dynamics in response to injury^{13,23,33}, thus we decided to add an additional timepoint, 5dpi, to our scRNA-seq analysis (Fig. 3a). After the quality check, datasets of intact and injured samples, from both timepoints (3 and 5dpi), were integrated and batch corrected using the scVI tool^{51,52}. In total, we retrieved 35240 cells (Intact: 16567, 3dpi: 3637, 5dpi: 13658) with overall 19290 detected genes. Using unsupervised clustering, these cells were distributed among 35 clusters (Fig. 3b, Ext. Fig. 5a-c, Ext. Table 6). By comparing all three conditions (Intact, 3dpi and 5dpi) we observed several clusters being mainly formed by cells originating from injured samples (Ext. Fig. 5b). Additionally, we did not observe any of these injury-induced clusters being specific to one timepoint (Ext. Fig. 5b).

To unravel how each population transitioned from a resting, homeostatic to an activated, reactive state we focused on each individual population separately. Hence, we further subclustered astrocytes, microglia and oligodendrocytes (Fig. 3c-e, Ext. Fig. 6). As expected, we identified distinct clusters in each of the investigated cell populations consisting mainly of cells from the injured samples (Ext. Fig. 6c, h, m). In line with their origin, these cells also expressed typical markers of glial reactivity. We identified clusters 'AG5', 'AG6' and 'AG8' as the main population of reactive astrocytes (Fig. 3c, Ext. Fig. 6a-e), which expressed high levels of *Gfap*, *Vim* and *Lcn2*^{38,46} (Ext. Fig. 6e). Microglial clusters 'MG4' and 'MG6' displayed high expression of *Aif1* and low expression of the homeostatic markers *Tmem119* and *P2ry12*⁴⁵ (Fig. 3d, Ext. Fig. 6f-j). By subclustering cells belonging to the oligodendrocytic lineage, we were able to identify two populations of OPCs ('OPCs1' and 'OPCs2') (Fig. 3e, Ext. Fig. 6k-o), with cluster 'OPCs2' containing mainly cells from the injured samples (Fig. 3e). Of note, we were not able to identify a unique marker within the 'OPCs2' cluster, which could henceforth be used as a reactive OPC marker (Ext. Fig. 6o). Importantly, cells from the injury-responding clusters, as identified by the single cell deconvolution analysis ('11_Microglia', '12_Astrocytes', '15_OPCs' (Fig. 2f, Ext. Fig. 4)), also predominantly mapped to the glial subclusters that are evoked by injury (Ext. Fig. 6d, i, n). This

ensures, together with the above highlighted marker expression, the reactive state of these glial subclusters (therefore from now on referred to as reactive clusters).

By subclustering glial cells and investigating those at higher resolution, we did not discover any cluster(s) being unique for either the 3 or 5 dpi timepoint. Hence, this finding hints towards a gradual activation of glial cells in response to injury rather than distinct, timepoint-dependent activation states. To shed light on this hypothesis, we examined the cell distributions of all subclustered glial cells among all timepoints (Intact, 3dpi and 5dpi, Fig. 3c-e). Interestingly, we observed prominent changes in the distribution of reactive clusters between the two timepoints after injury. More specifically, many of the astrocytes at 3dpi were still present in the homeostatic clusters and partially in the reactive clusters 'AG6' and 'AG8', whereas at 5dpi most cells were residing in cluster AG5 (Fig. 3c). Microglia on the other hand displayed a faster transition to reactivity compared to astrocytes, as at 3dpi the vast majority of cells were already localized in the reactive clusters 'MG4' and 'MG6'. At 5dpi, however, most of the cells started to transition back to the homeostatic clusters with a high proportion of cells being present in cluster 'MG3' (Fig. 3d). Furthermore, also OPCs reacted promptly after injury as at 3dpi the majority of cells resided in the reactive cluster 'OPCs2', whereas only a few cells were present in this cluster at 5dpi (Fig. 3e). All these findings are in line with the literature, where it has been described that microglia and OPCs rapidly respond to injury with their reactivity peak ranging from 2-3dpi, whereas, based on immunohistochemical analysis^{13,23,33}, astrocyte reactivity peaks at 5dpi.

The enriched immune system-related processes around the injury site, as depicted by the spatial transcriptomic, and the identification of specific reactive subtypes of glial cells, which populate the injury environment, raised the question of whether the inflammatory gene expression is a unique signature of one specific cell type or whether it is a common feature of reactive glia. Therefore, within each glial population (Fig. 3 c-e), we extracted the differentially expressed genes (DEGs) of each glial subcluster ($p\text{val} < 0.05$, \log_2 fold change > 1.6 or \log_2 fold change < -1.6) and compared those among the entity of all glial subclusters (Ext. Fig. 7a, b). Interestingly, we could observe that among all clusters the highest similarity of upregulated genes was evident between the reactive glial clusters ('MG4', 'AG5' and 'OPCs2') with 66 enriched genes commonly shared (Ext. Fig. 7b). This data therefore implies that in response to injury individual reactive glial clusters might share some cellular programs. Hence, we performed GO term analysis using the 192 commonly upregulated genes, that arose from the comparison of clusters 'MG4', 'AG5' and 'OPCs2', independent of other glial subclusters (Fig. 4a). Most of the commonly regulated processes were related to cell proliferation (Fig. 4b), which has been reported to be a shared hallmark of glial cell reactivity^{13,38}. Furthermore, we could also identify processes related to innate immunity (Fig. 4b) with many genes being associated to the type I interferon signaling pathway (*Ifitm3*, *Ifit3*, *Bst2*, *Isg15*, *Ifit3b*, *Irf7*, *Ifit1*, *Ifi2712a*, *Oasl2*, *Oasl1a*) (Fig. 4c) as well as *Cxcl10*, a ligand activating the *Cxcr3* pathway⁵³. Additionally, we observed common expression of Galectin1 (*Lgals1*) by a subset of microglia, astrocytes and OPCs which was also validated on protein level (Ext. Fig. 8b-d). Noteworthy, the expression of these innate immunity-related genes is clearly restricted to distinct glia subpopulations, as not all glial cells co-express these markers (Fig. 4g, Ext. Fig. 8b-d). Taken together, our data proposes a common inflammatory regulation in a subset of glial cells in response to injury.

Regulation of injury-induced innate immune response via Cxcr3 and Tlr1/2 pathways

Shared regulation of the innate immunity pathways, including components of Tlr2 and Cxcr3 pathways (Ext. Fig. 8e), and our recent findings that Cxcr3 and Tlr1/2 regulate OPC accumulation at the injury site in the zebrafish brain⁵⁴, prompted us to investigate the role of Cxcr3 and Tlr1/2 pathways in response to mammalian stab-wound injury. We performed scRNA-seq analysis at 3dpi and 5dpi following treatment with a specific antagonist for the Cxcr3⁵⁵ (NBI-74330) and a Tlr1/2 pathway inhibitor (CU CPT 22)⁵⁶ (from now on referred to as SW INH or if distinct timepoints are addressed 3/5dpi_INH) (Fig. 5a). The specificity of these chemical compounds was validated using a murine knock-out OPC cell lines⁵⁴. Following quality control steps, the data was integrated with our previously acquired datasets (Fig. 3b) from intact (INT) and injured animals (from now on referred to SW CTRL or if distinct timepoints are addressed 3/5dpi_CTRL). The datasets were batch corrected using the scVI tool^{51,52}. In total, we retrieved 53813 cells (Fig. 5a, Ext. Fig. 9a) (Intact: 16649 cells, 3dpi_CTRL: 3643 cells, 3dpi_INH: 4613 cells, 5dpi_CTRL: 13766 cells, 5dpi_INH: 15142), with overall 19290 detected genes. By using unsupervised clustering, these cells distributed among 36 clusters (Fig. 5b). Of note, with the integration of additional conditions (SW INH 3 and 5dpi), which subsequently enlarged the total cell number, we did not observe new clusters emerging. Furthermore, even with the integration of SW INH datasets the overall cluster identity is unaffected, as depicted by high similarity scores between each of the clusters (Ext. Fig. 9b). As microglia, astrocytes and OPCs displayed common innate immune-related genes after stab-wound injury (Fig. 4), we set out to investigate the possible influence of Cxcr3 and Tlr1/2 pathway inhibition on microglia, astrocytes and OPCs by further subclustering. In each investigated cell population, we again identified distinct clusters containing primarily cells from injured samples (Fig. 5c-e, Ext. Fig. 9c-e). Of note, these clusters are composed of cells originating from both, SW CTRL and SW INH samples, suggesting that the inhibition of Cxcr3 and Tlr1/2 pathways following stab-wound injury does not induce new transcriptional states. However, the inhibitor treatment resulted in a partial downregulation of the previously identified common inflammatory genes (see Fig. 4f) shared between the reactive clusters 'AG7', 'MG3' and 'OPCs2' (Fig. 5f, Ext. Table. 7).

To address transcriptional changes induced by the inhibitor treatment, we performed differential gene expression analysis of each subcluster between SW CTRL and SW INH condition at each timepoint (p val < 0.05, \log_2 fold change > 0.7 or \log_2 fold change < -0.7). Interestingly, most of the inhibitor-induced changes at 3 and 5dpi were subcluster-specific, as only few DEGs overlapped (Ext. Fig. 10a-d). To reveal the biological processes regulated in each glial subcluster (Fig. 5c-e), we utilized the function compareCluster⁵⁷ (clusterProfile R package) and calculated the enriched GO over-representation score for the genes of each cluster. This function summarized the results into a single object and allowed us to compare the enriched biological processes of all glial subclusters at once. Indeed, by comparing the processes of all significantly downregulated genes after treatment at 3dpi, we found many processes linked to innate immune response, which were shared among several glial populations, including the reactive astrocytes (clusters: 'AG5', 'AG6', 'AG7' & 'AG9'), microglia (clusters: 'MG3' & 'MG6') and OPCs (cluster: 'OPCs2') (Fig. 5g). Interestingly, although immune response-related processes were still downregulated at 5 dpi, these processes were not anymore shared between the different glial

populations (Fig. 5h). Conversely, biological processes induced by the inhibitor treatment are cluster-specific, independent of the analysis timepoint (Ext. Fig. 10e, f). Taken together, our scRNAseq analysis implies that *Cxcr3* and *Tlr1/2* signaling pathways regulate similar processes to initially activate (3dpi) different glial cells. This activation, however, is followed by cell type-specific transcriptional changes at later stages (5dpi).

***Cxcr3* and *Tlr1/2* pathway inhibition does not interfere with oligodendrocyte reactivity and proliferation**

Interference with *Cxcr3* and *Tlr1/2* signaling pathways following brain injury, did not result in the emergence of new cell types nor states, neither at 3 nor 5 dpi (Ext. Fig. 9a). Nevertheless, the inhibition of the above-mentioned pathways elicited an overall downregulation of various inflammatory-related genes in reactive glia clusters 'AG7', 'MG3' and 'OPCs2', especially at 3dpi (Fig. 5f). Furthermore, inhibition of *Cxcr3* and *Tlr1/2* pathways following injury in the zebrafish telencephalon interfered with oligodendrocyte proliferation, which resulted in a reduction of oligodendrocytes in the injury vicinity⁵⁴. To investigate the relevance of *Cxcr3* and *Tlr1/2* signaling also in the mammalian context, we first set out to examine the cluster distribution of oligodendroglial lineage cells between all conditions (INTACT, SW CTRL and SW INH) and timepoints (3 and 5 dpi) (Ext. Fig. 11a). Surprisingly, we detected no differences in the cluster distribution of reactive OPC clusters 'OPCs2' and 'OPCs3' between SW CTRL and SW INH cells, neither at 3 nor 5dpi (Ext. Fig. 11b). To further substantiate our scRNAseq findings, we determined the number of *Olig2*⁺ oligodendrocytes in stab wound-injured mice at 3dpi (Ext. Fig. 11c). In line with our bioinformatical analysis, we detected no differences in the number of *Olig2*⁺ cells in the injury surrounding between both experimental groups (Ext. Fig. 11d, e, f). Furthermore, we determined the proliferation capacity of *Olig2*⁺ cells between both experimental groups by labeling all cells in S-phase using the DNA base analogue EdU (0.05 mg/g 5-Ethynyl-2'-deoxyuridine i.p. injection 1hr before sacrifice) and did not observe any changes in the number of proliferating (*Olig2*⁺ and EdU⁺) oligodendrocytes (Ext. Fig. 11d, e, g).

In summary, the inhibition of *Cxcr3* and *Tlr1/2* signaling pathways following stab wound injury in the mouse cerebral cortex is not interfering with oligodendrocyte proliferation and is not affecting the overall number of oligodendrocyte lineage cells in the injury surrounding at early days post injury.

***Cxcr3* and *Tlr1/2* pathways regulate microglial activation in response to injury**

The expression of inflammatory genes in microglia is tightly linked with the activation state of this cell type^{7,58}. Therefore, we assessed if the downregulation of inflammatory genes induced by the *Cxcr3* and *Tlr1/2* pathway inhibition (Fig. 5f), might alleviate microglial reactivity. Hence, we examined the cluster distribution of subclustered microglia among all three conditions (INTACT, SW CTRL and SW INH) and timepoints (3 and 5 dpi) (Fig. 6a, b). As previously depicted in Ext. Fig. 9d, cells deriving from the intact condition are confined to the homeostatic clusters, whereas cells of the injured samples are primarily distributed in the reactive clusters at 3 dpi with a transition towards the homeostatic clusters noticeable at 5 dpi (Fig. 6b). Direct comparison of SW CTRL and SW INH samples exhibited differences in cell distribution with a higher proportion of cells being localized in the homeostatic clusters after *Cxcr3* and *Tlr1/2* signal inhibition (Fig. 6b). Although the discrepancy between both conditions was already detectable 3 dpi, the shift, was more pronounced 5 dpi (Fig.

6b). To further elucidate if the detected microglia cell distribution shift following *Cxcr3* and *Tlr1/2* pathway inhibition is accompanied by changes in the overall cell appearance, we determined microglia cell morphology characteristics using the automated morphological analysis tool published by Heindl et al. 2018⁵⁹. For that reason, brain sections of SW CTRL and SW INH animals were labelled with an anti-Iba1 antibody and areas in the vicinity of the injury site were analyzed (Fig. 6c). Microglia originating from SW INH animals displayed significantly smaller cell somata, reduced circular shape and at the same time increased branch length compared to microglia from SW CTRL animals (Fig. 6d-f, Ext. Fig. 12a). The inhibition of *Cxcr3* and *Tlr1/2* signaling pathways resulted in reduced branch volume without altering the total number of major branches (Ext. Fig. 12a). In addition, although not significantly altered, microglia from SW INH animals appeared to be more ramified than SW CTRL microglia as increased numbers of nodes per major branches were detected. (Ext. Fig. 12a).

In summary, our scRNA seq data implies that *Cxcr3* and *Tlr1/2* pathway inhibition accelerates the transition from a reactive to a homeostatic microglial cell state in the early days after injury. These findings are further supported by pronounced morphological changes of inhibitor-treated microglia, which are reminiscent of less reactive, activated cells.

Altered astrocyte response upon *Cxcr3* and *Tlr1/2* pathway inhibition

To address the impact of *Cxcr3* and *Tlr1/2* pathway inhibition on astrocytes after brain injury, we subclustered astrocytes (Fig. 7a) and investigated the cell distribution among all conditions and timepoints (Fig. 7b). Astrocytes originating from intact conditions were evenly distributed between all homeostatic clusters. However, cells from stab-wounded animals were initially localized in both, homeostatic and reactive clusters, at 3 dpi, whereas at 5 dpi most cells were distributed between all reactive clusters. By comparing astrocyte cell distribution of SW CTRL and SW INH samples, we detected noticeable differences at 5 dpi. Most cells originating from the SW CTRL condition were distributed among the reactive clusters 'AG5', 'AG6' and 'AG7', whereas cells originating from the SW INH condition were largely confined to the reactive cluster 'AG5' (Fig. 7b). Interestingly, cluster 'AG5' exhibited lower expression of reactivity markers, such as *Gfap* and *Lcn2*, in comparison to the reactive clusters 'AG6' and 'AG7' (Ext. Fig. 12b). In line with the shifted distribution of SW INH cells to cluster 'AG5', inhibitor-treated astrocytes displayed also lower expression levels of *Gfap* and *Lcn2* at 5 dpi (Ext. Fig. 12c). Additionally, to determine if astrocyte reactivity is overall altered, we generated 'astrocyte reactivity scores' (based on Hasel et al. 2021⁴⁶) and compared the reactivity gene set scores among intact, stab wound-injured control and inhibitor-treated samples (Ext. Fig. 12d). Generally, both reactivity scores ('CI4' and 'CI5' in Ext. Fig. 12d) were reduced in stab wound-injured inhibitor-treated samples at both timepoints (3 and 5dpi). However, although, both reactivity scores were decreased, the fraction of astrocytes expressing these distinct gene sets were not changed. Therefore, our analysis implies that the inhibitor-treatment overall reduces astrocyte reactivity, but this is not sufficient to revert these reactive astrocytes back to full homeostasis. In line with the scRNAseq analysis, also by our immunohistochemical measurements (Ext. Fig. 12e-i) we did not observe differences in the overall astrocyte reactivity state between stab-wounded control and inhibitor-treated mice at 5 dpi. We detected similar GFAP⁺ cell accumulation (Ext. Fig. 12f, g,

h), as well as comparable numbers of NGAL⁺ and GFAP⁺ positive astrocytes in the injury surrounding, between both experimental groups (Ext. Fig. 12f, g, i).

Furthermore, besides the reduced expression of reactive astrocyte markers in cluster 'AG5', this cluster was also devoted off proliferating cells as almost all cycling cells were confined to clusters 'AG6' and 'AG7', as depicted by the scRNAseq proliferation score (Ext. Fig. 12j, Ext. Table 5). Interestingly, based on the scRNAseq analysis, interference with Cxcr3 and Tlr1/2 signaling following stab wound injury reduced the fraction of proliferating astrocytes at both 3 and 5dpi, in line with the abundance of SW INH cells to cluster 'AG5' (Fig. 7b, Ext. Fig. 12k).

In order to investigate potential alterations in the proliferation capacity following inhibitor treatment, we assessed astrocyte proliferation using immunohistochemistry in combination with the DNA-base analogue EdU (0.05 mg/g 5-Ethynyl-2'-deoxyuridine i.p. injection 1hr before sacrifice) at 3 dpi (Fig. 7c). Indeed, inhibition of Cxcr3 and Tlr1/2 pathways following injury significantly decreased the number of proliferating (GFAP⁺ and EdU⁺) astrocytes in the injury vicinity (Fig. 7d, e, f), whereby the total number of EdU⁺ cells was not altered (Fig. 7d, e, g). In summary, our scRNAseq analysis implied reduced astrocyte reactivity alongside reduced proliferation rates following inhibitor treatment. However, although reduced astrocyte proliferation following Cxcr3 and Tlr1/2 pathway inhibition was evident *in vivo*, the signal interference did not completely revert astrocytes back to full homeostasis.

Discussion

TBI has complex pathophysiology, which involves the response of various types of cells^{3,4}. However, most studies have focused on the response of specific cell types, with few intended to evaluate the interplay between these cells⁶⁰⁻⁶² largely focusing on the single candidates mediating these interactions. In this manner, we developed a toolbox profiling the transcriptional changes across various cell types with providing spatial and temporal context. Our study used the stab-wound-injury model in mice^{23,63}, a mild injury model involving the breakdown of BBB and the activation of both glial and immune cells²³. The reproducibility of our model and the reactivity observed makes it perfect for studying the basic features of TBI pathophysiology.

Spatial transcriptomic analysis of the stab-wounded cortex 3dpi revealed a well-defined injury cluster, "cluster VI," around the injury core affecting only the surrounding area without detectable changes in the cortical regions distant from the injury. We observed the regulation of processes linked to angiogenesis, phagocytosis, and immune system-related processes. These are defense mechanisms featuring the early events following brain damage and wound healing, which involves clearing of dead cells and debris as well as re-establishing of the vasculature to ensure oxygen supply⁶⁴. Many observed local changes, represented by the Cluster's VI-enriched genes, are largely related to reactive astrocytes and microglia^{39-41,65,66}, indicating an overrepresentation of these populations in the injury milieu. Interestingly, we do not identify reactive OPC hallmarks despite clear evidence of reactive OPCs at the injury site^{67,68}. This could be partly explained by the missing signature of the reactive OPCs, as so far only an increase in proliferation and expression of proliferation-associated genes have been used as a hallmark of reactive OPCs⁶⁹. Our study now also provides the gene expression profile of the reactive OPCs that allows their mapping to the injury site of the spatial transcriptomic analysis, based on probabilistic mapping.

Additionally, by fitting the gene expression patterns in various mathematic models, we could categorize them based on their expression motive and identify

several genes with expression peaks at the injury core. Considering the limitations of the spatial transcriptomics analysis using the Visium platform, where the detected expression in each spot comes from multiple cells, we validated the expression patterns for some selected genes of interest (*Serpina3n*, *Lcn2*, and *Cd68*) with RNAscope and immunohistochemistry. Notably, the expression patterns detected with both methods were in line with the Visium analysis. This observation supports the use of Visium to detect global changes with spatial information.

Indeed, the combination of spatial transcriptomics with scRNA-seq analysis can become a great tool to reveal transcriptomic changes of specific cell types relative to their predicted location. This is of great interest for any focal pathology, as it has been described that the reaction of astrocytes¹⁶ OPCs^{10,70} and microglia^{70,71} depends on their distance to the pathology site. The anatomical similarity of the two data sets and the good representation of cell types in the scRNA-seq dataset are crucial for successfully integrating the two data sets. Thus, detecting the major, expected cell types in our scRNA-seq data was of great importance. We identified several neuronal and glial clusters, including astrocytes, microglia, and oligodendrocyte lineage cells, besides vascular cells, pericytes, and multiple types of immune cells. Particularly, some of the clusters we detected mainly in the injured datasets, highlighting the detection of specific cell types depending on the anatomical region and condition.

Integrating the scRNA-seq and the Visium data sets predicted the contribution of specific cell types to the injury environment. We detected multiple populations responding to the injury by enriched or decreased representation while others did not respond. Microglial clusters showed a more uniform response to injury as we could detect all microglia clusters accumulating at the injury, with cluster “11_Microglia” being the one with the highest correlation. On the other hand, astrocytes showed a heterogeneous response with clusters “12_Astrocytes” and “23_Astrocytes” responding to injury and accumulating around the injury area. In contrast, the remaining astrocytic clusters were underrepresented in the injury area compared to the rest of the cortex. Focusing on the injury-enriched astrocytic clusters “12_Astrocytes” and “23_Astrocytes,” we could see heterogeneity both at the location of the cells as well as the genes signature, with cluster “12_Astrocytes” being the one expressing high levels of *Gfap*. Cluster “23_Astrocytes,” on the contrary, could represent the recently described “atypical astrocytes,” which, after focal brain injury, rapidly downregulated GFAP together with other astrocytic proteins⁷². OPCs also responded to the injury, with cluster “15_OPCs” being the only one showing enrichment at the injury core. Finally, we could detect the response of peripheral infiltrating macrophages and monocytes, with clusters “13_Macrophages/Monocytes” and “18_Monocytes” contributing to the injury milieu. With the integration of the two datasets, we could identify the populations overrepresented in the injury core and require further investigation.

The addition of the dataset generated at 5dpi allowed us to analyze the temporal changes in reaction to injury. Microglia showed increased reactivity at 3dpi, whereas 5dpi cells shifted toward more homeostatic clusters. OPCs led a quick transition to reactivity at 3dpi, with very few cells residing in the reactive cluster at 5dpi. On the contrary, astrocytes reactivity peaked at 5dpi as most cells belonged in the reactive clusters, whereas, at 3dpi, we could still detect many cells in the homeostatic clusters. Importantly, no distinct time-point-dependent clusters appeared or disappeared for any analyzed glial cells. Hence, our data implies a continuous activation of glial cells accompanied by a partial return to homeostasis. Therefore, this

resource offers an excellent opportunity to investigate these processes more thoroughly.

To start with such analysis and as a proof of principle, we look at the genes characterizing each sub-cluster in a holistic approach. In this way, we could identify sub-clusters of microglia, astrocytes, and OPCs with shared enriched features, including proliferation and innate immune processes. Indeed, the proliferation is a hallmark of injury-induced reactivity, including microglia⁷³, astrocytes^{74,75}, and OPCs^{67,76} validating our approach. Surprisingly, we found several IFN-I pathway genes regulated in the reactive clusters MG4, AG5, and OPCs2. Among these genes, the Interferon regulatory factor 7 (*Irf7*), a transcription factor crucial for the IFN-I activity⁷⁷, and *Cxcl10*, a well-characterized ligand of the *Cxcr3* pathway⁵³, caught our attention. Previous studies have demonstrated that *Irf7* can induce type I IFNs through the activation of Tlr2, resulting in the transcription of several mediators, including *Cxcl10*^{78,79}. Furthermore, the Tlr2/*Irf7* signaling axis has been associated with microglia-mediated inflammation after subarachnoid hemorrhage in mice⁸⁰. Notably, we recently demonstrated that *Cxcr3* and Tlr1/2 regulate OPCs accumulation at the injury site in the zebrafish brain in a redundant and synergistic manner⁵⁴. Our data now support the entirely novel concept that the same innate immunity pathways trigger the initial response in injury-enriched reactive glial clusters.

As both pathways were regulated in several reactive populations, we decided to systemically inhibit the two pathways after brain injury by treating the animals with a specific antagonist for the *Cxcr3*⁵⁵ (NBI-74330) and a Tlr1/2 pathway inhibitor (CU CPT 22)⁵⁶. We then performed scRNA-seq analysis at both 3 and 5dpi, and by integrating the data sets with our control analysis, we could address the cell type-specific changes. Interestingly, we observed that multiple innate immunity genes, including *Irf7*, were downregulated after inhibition of the *Cxcr3* and Tlr1/2 pathways, with clusters AG7, MG3 and OPCs2 affected the most. Additionally, by performing differential gene expression analysis within each subcluster between SW CTRL and SW INH condition at each time-point, we addressed the changes induced in each cluster specifically. Notably, we observed an overall downregulation of innate immune processes shared between astrocytes, microglia, and OPCs at 3dpi, whereas at 5dpi became more specific for each population. These data suggest the shared initial regulation by different pathways that then diversify in specific populations to drive a specific reaction of each cell type. In conclusion, we demonstrated that inhibiting *Cxcr3* and Tlr1/2 pathways modulate innate immunity on a temporal basis in glial cells. However, further research is necessary to determine the role of each pathway for each population.

Next, we examined how the systemic inhibition of the two pathways affects the reactivity of glial cells. Thus, we addressed the accumulation of oligodendrocytes (Olig2⁺ cells) in combination with their proliferation. Surprisingly, we did not observe any difference between SW CTRL and SW INH conditions at 3dpi. This observation was in contrast to our study in zebrafish, where inhibiting the two pathways alleviated reactive gliosis by decreasing the accumulation of oligodendrocytes and their proliferation⁵⁴. That could be due to differences in the injury environment with additional pathways involved in the accumulation and proliferation of OPCs to the injury core in mice. Thus, the altered regulation of OPCs reactivity in mice and zebrafish could be one of possible difference between regeneration competent and regeneration incompetent species.

On the other hand, while addressing microglia reactivity via morphological analysis⁵⁹, we observed that inhibitor-treated microglia were in a less

reactive/activated state. Specifically, microglia originating from SW INH animals displayed significantly smaller cell somata, reduced circular shape, increased branch length, and appeared to be more ramified than in the SW CTRL. In combination with the cell distribution in the scRNA-seq clusters, this observation suggests that blocking Tlr1/2 and Cxcr3 pathways accelerates the transition from a reactive to a homeostatic state of microglial cells.

Similarly, astrocytes also demonstrated altered reactivity when Tlr1/2 and Cxcr3 pathways were inhibited, as evidenced by the reduction in the expression of markers associated with astrocyte reactivity. Additionally, we observed a reduction in the number of proliferating astrocytes in the injury vicinity at 3dpi. However, at 5dpi, we did not observe differences in the overall astrocyte reactivity state between SW CTRL and SW INH, as addressed with our transcriptomic analysis and the follow-up immunohistochemical measurements. These findings indicate the modular control of the astrocytic and possible glial reactivity in general with Tlr1/2 and Cxcr3 pathways controlling only some aspects (astrocyte proliferation for example). This is, indeed, well in line with specific pathology conditions inducing different glial response^{74,81–83}, further emphasizing the versatility of our data sets and analysis.

In conclusion, these data represent a comprehensive tool for analyzing early events following traumatic brain injury with respect to changes in time, space, and cell type. Additionally, it enables the examination of the interplay between cells in response to injury. A better understanding of the injury pathophysiology may open more opportunities for developing new therapeutic strategies.

Materials and Methods

Animals

All operations were performed on 8-12 weeks old C57BL/6 male mice, housed and handled under the German and European guidelines for the use of animals for research purposes. Experiments were approved by the institutional animal care committee and the government of Upper Bavaria (ROB-55.2-2532.Vet_02-20-158). Anaesthetized animals received a stab wound lesion in the cerebral cortex as previously described⁶³, by inserting a thin knife into the cortical parenchyma using the following coordinates from Bregma: RC: -1.2; ML: 1-1.2 and from Dura: DV: -0.6 mm. To produce stab lesions, the knife was moved over 1mm back and forth along the anteroposterior axis from -1.2 to -2.2 mm. Animals were sacrificed 3 and 5 days after the injury (dpi).

For the treatment experiments, animals received inhibitors by gavage feeding. NBI 74330 (100 mg/kg, R&D Systems #4528) and CU CPT 22 (3 mg/kg, R&D Systems #4884) were dissolved in DMSO and diluted in corn oil. The vehicle solution consisted of DMSO diluted in corn oil and was administered to all control animals. To analyze the proliferative capacity of glial cells we injected 5-Ethynyl-2'-deoxyuridine (EdU, 0.05 mg/g, Thermofisher #E10187) intraperitoneally and animals were sacrificed 1hr after injection.

For the induction of Cre-mediated recombination in NG2CreER^{T2} x CAG-eGFP mice, tamoxifen (40 mg/ml, Sigma #T5648) was administered orally. Animals received tamoxifen every second day (400 mg/kg) for a total of 3 times. Mice were injured two weeks after the last tamoxifen administration and sacrificed at 3dpi.

Tissue preparation

Mice were deeply anaesthetized and transcardially perfused with phosphate-buffered saline (PBS) followed by 4% paraformaldehyde (PFA) (wt/vol) dissolved in PBS. Brains were postfixed in 4% PFA overnight at 4°C, washed with PBS and cryoprotected in 30% sucrose at 4°C. Mouse brains used to assess microglia morphology were embedded in 3% agarose and cut coronally at 100 µm thickness using a vibratome (HM 650V, Microm). Otherwise, brains were embedded in frozen section medium Neg-50 (Eprelia #6502), frozen and subsequently sectioned using a cryostat (Thermo Scientific CryoStar NX50). Coronal sections were collected either at a thickness of 20µm on slides for RNAscope or 40µm for free-floating immunohistochemistry.

Immunohistochemistry

For immunohistochemistry, sections were blocked and permeabilized with 10% normal goat serum (NGS, vol/vol, Biozol, S-1000)/donkey serum (NDS, vol/vol, Sigma Aldrich 566460) and 0.5% Triton X-100 (vol/vol), dissolved in 1xPBS while being incubated overnight at 4°C with the corresponding primary antibodies. Following primary antibodies were used: anti-CD68 (rat 1:600, BioRad, MCA1957T), anti-Galactin1 (rabbit 1:200, Abcam, ab138513), anti-GFP (chick 1:400, Aves Labs, GFP-1020), anti-GFAP (goat 1:300, Abcam, ab53554), anti-GFAP (mouse 1:500, Sigma, G3893), anti-Iba1 (rabbit 1:500, Wako, 019-19741), anti-NGAL (rabbit 1:500, Thermofisher, PA5-79590), anti-Serpina3n (goat 1:500, R&D Systems AF4709-SP). Sections were washed with PBS and incubated with secondary antibodies dissolved in 1xPBS solution containing 0.5% Triton X for two hours at room temperature. Following secondary antibodies were used: donkey anti-chick IgY A488 (1:1000, Dianova 703-545-155), goat anti-mouse IgG1 A546 (1:1000, Thermofisher A-21123), goat anti-rabbit IgG A546 (1:1000, Thermofisher A-11010), goat anti-rabbit IgG A633 (1:1000, Thermofisher A-21070), goat anti-rat IgG A488 (1:1000, Thermofisher A-11006). For nuclear labeling, sections were incubated with DAPI (final concentration of 4 µg/mL, Sigma, D9542) for 10 min at room temperature. EdU incorporation was detected by Click-iT™ EdU Alexa Fluor™ 647 Imaging Kit (Thermo Fisher Scientific #C10340) according to the manufacturer's instructions. Staining procedure for microglia morphology analysis was performed as described in Heindl et al. 2018. Stained sections were mounted on glass slides with Aqua-Poly/Mount (Polysciences #18606).

In situ hybridization

RNA in situ hybridization was performed using RNAscope® Multiplex Fluorescent Reagent Kit (ACD) according to the manufacturer's instructions. Briefly, brain sections were fixed in 4% paraformaldehyde at 4 °C for 15 min, ethanol-dehydrated, deparaffinize with H₂O₂ and protease-permeabilized for 20min at 40 °C. Brain sections were then incubated for 2 h at 40 °C using the following probes: *S100a6*: 412981, *Tspo*: 422741, *Ifi2712a*: 88617, *Serpina3n*: 430191-C2, *Lcn2*: 313971-C3, *Lyz2*: 491621-C3, *Cd68*: 316611-C2, *Igfbp7*: 425741-C2, *Cxcr3*: 402511-C2, *Tlr2*: 317521, *Oasl2*: 534501, *Cxcl10*: 408921-C3. Signal was amplified according to the manufacturer's instructions (Cat.Nr: 320293). Subsequently, sections were

processed with immunohistochemistry analysis as described above. The primary antibodies used in combination with RNAscope® were as follows: chick antibody to GFP (1:500, Aves Lab, GFP-1020), goat antibody to GFAP (1:300, Abcam, ab53554), rabbit antibody to Iba1 (1:500, Wako, 019-19741)

Image acquisition, processing and quantitative analysis

Confocal microscopy was performed at the core facility bioimaging of the Biomedical Center (BMC) with an inverted Leica SP8 microscope using the LASX software (Leica). Overview images were acquired with a 10x/0.30 objective, higher magnification pictures with a 20x/0.75, 40x/1.30 or 63x/1.40 objective, respectively. Images utilized for the microglia morphology analysis were acquired with an 40x/1.30 objective with an image matrix of 1024x1024 pixel, a pixel scaling of 0.2 μm x 0.2 μm and a depth of 8-bit. Image processing was performed using the NIH ImageJ software (version 2.1.0/1.53f). To acquire overview images, single images were stitched using the ImageJ plug-in tool 'pairwise stitching' (Preibisch et al. 2009).

For all quantifications a minimum of three sections per animal were analyzed. In each section, an area of 300 μm (150 μm on each side of the injury) was selected and either the pixel covered area or the number of positive cells in all individual z-planes of an optical z-stack was quantified. Additionally, to account for variations in section thickness, total cell numbers were normalized to the section depth. Statistical analysis was performed using GraphPad Prism (version 9.3.1).

Spatial transcriptomics analysis

Mouse brains from 3dpi or intact C57Bl/6J mice were embedded and snap frozen in an isopentane and liquid nitrogen bath as recommended by 10x Genomics (Protocol: CG000240). During cryosectioning (Thermo Scientific CryoStar NX50) the brains were resected to generate a smaller sample (Fig. 1a) and two 10 μm thick coronal sections of the dorsal brain area were collected in one capture area. The tissue was stained using H&E staining and imaged with the Carl Zeiss Axio Imager.M2m Microscope using 10x objective (Protocol: CG0001600). The libraries were prepared with Visium Spatial Gene Expression Reagent Kits (CG000239) with 18min permeabilization time and sequenced on Illumina NextSeq 2000 system according to manufacturer protocol. Sequencing was performed in the Laboratory for Functional Genome Analysis (LAFUGA).

Data were mapped against the mouse reference genome mm10 (GENCODE vM23/Ensembl 98; builds versions 1.2.0 and 2020A from 10xGenomics) with Space Ranger 1.2.2. Both data sets were analyzed, and quality checked following the SCANPY³⁵ and Squidpy³⁶ pipeline, selecting spots with at least 1500 reads and a maximum 45% mitochondrial fraction. Normalization and log transformation was performed using the counts per million (CPM) strategy with a target count depth of 10,000 using SCANPY's³⁵ `normalize_total` and `log1p` functions. Following cell count normalization and scaling (function `scale` in SCANPY), experimental groups were integrated. Highly variable gene (HVGs) selection was performed via the function `highly_variable_genes` using the Cell Ranger flavor with default parametrization, obtaining 2000 HVGs. Unsupervised clustering of cells was done using the Leiden algorithm⁸⁴ as implemented in SCANPY. This allowed classification of multiple clusters based on marker genes selected using `test_overestim_var` between the normalized counts of

each marker gene in a cluster against all others (function rank_genes_groups in SCANPY). The layer marker score was performed using the function score_genes (as implemented in SCANPY) based on established marker genes (Ext. Table 3) described by Zeisel, A. et al 2018³⁷. Gene ontology enrichment analysis was performed using the function enrichGO (R package: clusterProfiler⁵⁷) on the marker genes for cluster VI (indicated above) selecting the genes with $pval < 0.05$ and $log_2fc > 1$ and the top 10 functions of the three aspects (MF: Molecular Function; CC: Cellular Component; BP: Biological Process) were presented on a dot plot.

Single-cell analysis

The lesioned grey matter of the somatosensory cortex of C57BL/6J mice at 3dpi and 5dpi or the corresponding region of the noninjured cortex were isolated using a biopsy punch (\varnothing 0.25cm) and the cortical cells were dissociated at a single cell level using the Papain Dissociation System (Worthington, # LK003153) followed by the Dead Cell Removal kit (Miltenyi Biotec # 130-090-101), according to manufacturer's instructions. Incubation with dissociating enzyme was performed for 60 min.

Single-cell suspensions were resuspended in 1xPBS with 0.04% BSA and processed using the Single-Cell 3' Reagent Kits v2 or v3.1 from 10xGenomics according to the manufacturer instructions. In brief, this included generation of single cell gel beads in emulsion (GEMs), post-GEM-RT cleanup, cDNA amplification and library construction. Illumina sequencing libraries were sequenced on a HiSeq 4000 or NovaSeq6000 system (with an average read depth of 30,000 raw reads per cell) according to the manufacturer's instructions for each version. Sequencing was performed in the genome analysis centre of the Helmholtz Center Munich

Transcriptome alignment of single-cell data was done using Cell Ranger v3.0.2 and v6.0.0 against the mouse reference genome mm10 (GENCODE vM23/Ensembl 98; builds versions 1.2.0 and 2020A from 10xGenomics). Quality Control (QC) of mapped cells was done using recommendations by Luecken and Theis⁸⁵ selecting cells with at least 1000 genes, maximum of 50000 reads and 25% mitochondrial fraction. Doublets were removed using the Scrublet framework⁸⁶. Normalization was performed using the scran³⁵ package (R package) followed by log-transformation using SCANPY's log1p functions⁸⁷. Highly variable gene (HVGs) selection was performed via the function highly_variable_genes using the Cell Ranger flavor with default parametrization, obtaining 2000 HVGs. Following cell count normalization and scaling, (function scale in SCANPY) experimental groups were integrated with scVI^{51,52}. Unsupervised clustering of cells was done using the Leiden algorithm⁸⁴ as implemented in SCANPY. This allowed classification of multiple main clusters based on marker genes selected using test_overestim_var between the normalized counts of each marker gene in a cluster against all others (function rank_genes_groups in SCANPY). The top 50 marker genes were used for the cluster annotation using the online available databases for the mouse brain (<http://mousebrain.org>) and the immune cells (http://rstats.immgen.org/MyGeneSet_New/index.html). Additionally, we generated gene expression scores using the function score_genes (as implemented in SCANPY) based on established marker genes (Table 2) of the main cell populations in the adult mouse brain to further confirm the cluster annotation. Visualization of cell groups is done using Uniform Manifold Approximation and Projection (UMAP)⁸⁸, as implemented in SCANPY. Differential gene expression analysis between treated and control conditions was performed using the tool diffxpy

(<https://diffxpy.readthedocs.io/en/latest/index.html>) using the Wald test. Of note, since some glial subclusters are comprised of only few cells, the differential gene analysis did not reveal differential expressed genes in these subclusters.

All the comparisons of the overlapping genes were performed using the R package UpSetR⁸⁹ which provides an efficient way to visualize the intersecting gene set in UpSet plot. For cluster comparison Additionally, the gene ontology (GO) analysis was performed using the R package clusterProfile⁵⁷, using the functions compareCluster (fun:enrichGO) or enrichGO. The visualisation of the functional enrichment results was done using the following visualization methods from the R package enrichplot⁵⁷: dot plot; enrichment map (function: emaplot) (based on the pairwise similarities of the enriched terms calculated by the pairwise_termsim function); and the Gene-Concept Network plot (function: cnetplot).

Spatial alignment of the scRNA-seq data

For the spatial localization of the scRNA-seq data, we used the Python package Tangram⁴⁹, focusing on the 3dpi control condition and using only the cortical cluster of the Visium data set in order to have the same anatomical region. We selected the training genes using the tool AutoGeneS⁵⁰ and used 439 training genes as the union of the top informative marker genes of each cluster in the scRNA-seq data that were detected in the Visium profiles. To find the spatial alignment for the scRNA-seq we used the Tangram⁴⁹ function map_cells_to_space which gave us the probabilistic mapping score. Additionally, we segmented the H&E image, using the Squidpy³⁶ function segment which was used for deconvolving the Visium data using the Tangram⁴⁹ functions count_cell_annotations and deconvolve_cell_annotations.

Reference:

1. Majdan, M. *et al.* Years of life lost due to traumatic brain injury in Europe: A cross-sectional analysis of 16 countries. *PLoS Med* **14**, e1002331 (2017).
2. Blennow, K. *et al.* Traumatic brain injuries. *Nat Rev Dis Primers* **2**, 1–19 (2016).
3. Mira, R. G., Lira, M. & Cerpa, W. Traumatic Brain Injury: Mechanisms of Glial Response . *Frontiers in Physiology* vol. 12 Preprint at <https://www.frontiersin.org/article/10.3389/fphys.2021.740939> (2021).
4. Puntambekar, S. S., Saber, M., Lamb, B. T. & Kokiko-Cochran, O. N. Cellular players that shape evolving pathology and neurodegeneration following traumatic brain injury. *Brain Behav Immun* **71**, 9–17 (2018).
5. Maas, A. I., Stocchetti, N. & Bullock, R. Moderate and severe traumatic brain injury in adults. *Lancet Neurol* **7**, 728–741 (2008).
6. Donat, C. K., Scott, G., Gentleman, S. M. & Sastre, M. Microglial Activation in Traumatic Brain Injury. *Front Aging Neurosci* **9**, (2017).
7. Kettenmann, H., Hanisch, U.-K., Noda, M. & Verkhratsky, A. Physiology of Microglia. *Physiol Rev* **91**, 461–553 (2011).
8. Dimou, L. & Götz, M. Glial Cells as Progenitors and Stem Cells: New Roles in the Healthy and Diseased Brain. *Physiol Rev* **94**, 709–737 (2014).
9. Simon, C., Dimou, L. & Gotz, M. Progenitors in the adult cerebral cortex - cell cycle properties and regulation by physiological stimuli and injury. *Glia* **59**(6), 869–881 (2011).

10. von Streitberg, A. *et al.* NG2-Glia Transiently Overcome Their Homeostatic Network and Contribute to Wound Closure After Brain Injury. *Front Cell Dev Biol* **9**, 662056 (2021).
11. Hughes, E. G., Kang, S. H., Fukaya, M. & Bergles, D. E. Oligodendrocyte progenitors balance growth with self-repulsion to achieve homeostasis in the adult brain. *Nat Neurosci* **16**, 668–676 (2013).
12. Escartin, C. *et al.* Reactive astrocyte nomenclature, definitions, and future directions. *Nat Neurosci* **24**, 312–325 (2021).
13. Robel, S., Berninger, B. & Götz, M. The stem cell potential of glia: lessons from reactive gliosis. *Nat Rev Neurosci* **12**, 88–104 (2011).
14. Buffo, A. *et al.* Origin and progeny of reactive gliosis: A source of multipotent cells in the injured brain. *Proceedings of the National Academy of Sciences* **105**, 3581–3586 (2008).
15. Sirko, S. *et al.* Focal laser-lesions activate an endogenous population of neural stem/progenitor cells in the adult visual cortex. *Brain* **132**, 2252–2264 (2009).
16. Bardehle, S. *et al.* Live imaging of astrocyte responses to acute injury reveals selective juxtavascular proliferation. *Nat Neurosci* **16**, 580–586 (2013).
17. Brenner, M. Role of GFAP in CNS injuries. *Neurosci Lett* **565**, 7–13 (2014).
18. Pekny, M., Wilhelmsson, U. & Pekna, M. The dual role of astrocyte activation and reactive gliosis. *Neurosci Lett* **565**, 30–38 (2014).
19. Sofroniew, M. v. Molecular dissection of reactive astrogliosis and glial scar formation. *Trends Neurosci* **32**, 638–647 (2009).
20. Anderson, M. A. *et al.* Astrocyte scar formation aids central nervous system axon regeneration. *Nature* **532**, 195–200 (2016).
21. Batiuk, M. Y. *et al.* Astrocyte Reactivity: Subtypes, States, and Functions in CNS Innate Immunity. *Trends Immunol* **41**, 758–770 (2020).
22. Sofroniew, M. v. & Vinters, H. v. Astrocytes: biology and pathology. *Acta Neuropathol* **119**, 7–35 (2010).
23. Frik, J. *et al.* Cross-talk between monocyte invasion and astrocyte proliferation regulates scarring in brain injury. *EMBO Rep* **19**, (2018).
24. Heimann, G. *et al.* Changes in the Proliferative Program Limit Astrocyte Homeostasis in the Aged Post-Traumatic Murine Cerebral Cortex. *Cerebral Cortex* **27**, 4213–4228 (2017).
25. Liddel, S. A. *et al.* Neurotoxic reactive astrocytes are induced by activated microglia. *Nature* **541**, 481–487 (2017).
26. Yun, S. P. *et al.* Block of A1 astrocyte conversion by microglia is neuroprotective in models of Parkinson's disease. *Nat Med* **24**, 931–938 (2018).
27. Marzan, D. E. *et al.* Activated microglia drive demyelination via CSF1R signaling. *Glia* **69**, 1583–1604 (2021).
28. George, K. K., Heithoff, B. P., Shandra, O. & Robel, S. Mild Traumatic Brain Injury/Concussion Initiates an Atypical Astrocyte Response Caused by Blood–Brain Barrier Dysfunction. *J Neurotrauma* **39**, 211–226 (2022).
29. Guttenplan, K. A. *et al.* Neurotoxic reactive astrocytes induce cell death via saturated lipids. *Nature* **599**, 102–107 (2021).
30. Shandra, O. *et al.* Repetitive Diffuse Mild Traumatic Brain Injury Causes an Atypical Astrocyte Response and Spontaneous Recurrent Seizures. *The Journal of Neuroscience* **39**, 1944–1963 (2019).
31. Munoz-Ballester, C., Mahmutovic, D., Rafiqzad, Y., Korot, A. & Robel, S. Mild Traumatic Brain Injury-Induced Disruption of the Blood-Brain Barrier Triggers an Atypical Neuronal Response. *Front Cell Neurosci* **16**, (2022).

32. Shechter, R. & Schwartz, M. CNS sterile injury: Just another wound healing? *Trends Mol Med* **19**, 135–143 (2013).
33. von Streitberg, A. *et al.* NG2-Glia Transiently Overcome Their Homeostatic Network and Contribute to Wound Closure After Brain Injury. *Front Cell Dev Biol* **9**, 662056 (2021).
34. Buffo, A. *et al.* Expression pattern of the transcription factor Olig2 in response to brain injuries: implications for neuronal repair. *Proc Natl Acad Sci U S A* **102**, 18183–18188 (2005).
35. Wolf, F. A., Angerer, P. & Theis, F. J. SCANPY: large-scale single-cell gene expression data analysis. *Genome Biol* **19**, 15 (2018).
36. Palla, G. *et al.* Squidpy: a scalable framework for spatial omics analysis. *Nat Methods* **19**, 171–178 (2022).
37. Zeisel, A. *et al.* Molecular Architecture of the Mouse Nervous System. *Cell* **174**, 999–1014.e22 (2018).
38. Sirko, S. *et al.* Astrocyte reactivity after brain injury—: The role of galectins 1 and 3. *Glia* **63**, 2340–2361 (2015).
39. Hasel, P., Rose, I. V. L., Sadick, J. S., Kim, R. D. & Liddelow, S. A. Neuroinflammatory astrocyte subtypes in the mouse brain. *Nat Neurosci* **24**, 1475–1487 (2021).
40. Escartin, C. *et al.* Reactive astrocyte nomenclature, definitions, and future directions. *Nat Neurosci* **24**, 312–325 (2021).
41. Zamanian, J. L. *et al.* Genomic analysis of reactive astrogliosis. *J Neurosci* **32**, 6391–6410 (2012).
42. Jurga, A. M., Paleczna, M. & Kuter, K. Z. Overview of General and Discriminating Markers of Differential Microglia Phenotypes. *Front Cell Neurosci* **14**, 1–18 (2020).
43. Kueckelhaus, J. *et al.* Inferring spatially transient gene expression pattern from spatial 2 transcriptomic studies 3 4. doi:10.1101/2020.10.20.346544.
44. Yu, F. *et al.* Phagocytic microglia and macrophages in brain injury and repair. *CNS Neurosci Ther* **28**, 1279–1293 (2022).
45. Ochocka, N. *et al.* Single-cell RNA sequencing reveals functional heterogeneity of glioma-associated brain macrophages. *Nat Commun* **12**, 1151 (2021).
46. Hasel, P., Rose, I. V. L., Sadick, J. S., Kim, R. D. & Liddelow, S. A. Neuroinflammatory astrocyte subtypes in the mouse brain. *Nat Neurosci* **24**, 1475–1487 (2021).
47. Baranek, T. *et al.* High Dimensional Single-Cell Analysis Reveals iNKT Cell Developmental Trajectories and Effector Fate Decision. *Cell Rep* **32**, (2020).
48. Tirosh, I. *et al.* Dissecting the multicellular ecosystem of metastatic melanoma by single-cell RNA-seq. *Science (1979)* **352**, 189–196 (2016).
49. Biancalani, T. *et al.* Deep learning and alignment of spatially resolved single-cell transcriptomes with Tangram. *Nat Methods* **18**, 1352–1362 (2021).
50. Aliee, H. & Theis, F. J. AutoGeneS: Automatic gene selection using multi-objective optimization for RNA-seq deconvolution. *Cell Syst* **12**, 706–715.e4 (2021).
51. Lopez, R., Regier, J., Cole, M. B., Jordan, M. I. & Yosef, N. Deep generative modeling for single-cell transcriptomics. *Nat Methods* **15**, 1053–1058 (2018).
52. Gayoso, A. *et al.* A Python library for probabilistic analysis of single-cell omics data. *Nature Biotechnology* vol. 40 163–166 Preprint at <https://doi.org/10.1038/s41587-021-01206-w> (2022).

53. Colvin, R. A., Campanella, G. S. V., Sun, J. & Luster, A. D. Intracellular domains of CXCR3 that mediate CXCL9, CXCL10, and CXCL11 function. *Journal of Biological Chemistry* **279**, 30219–30227 (2004).
54. Sanchez-Gonzalez, R. *et al.* Innate Immune Pathways Promote Oligodendrocyte Progenitor Cell Recruitment to the Injury Site in Adult Zebrafish Brain. *Cells* **11**, 520 (2022).
55. Torraca, V. *et al.* The CXCR3-CXCL11 signaling axis mediates macrophage recruitment and dissemination of mycobacterial infection. *DMM Disease Models and Mechanisms* (2015) doi:10.1242/dmm.017756.
56. Cheng, K., Wang, X., Zhang, S. & Yin, H. Discovery of Small-Molecule Inhibitors of the TLR1/TLR2 Complex. *Angewandte Chemie International Edition* **51**, 12246–12249 (2012).
57. Wu, T. *et al.* clusterProfiler 4.0: A universal enrichment tool for interpreting omics data. *The Innovation* **2**, 100141 (2021).
58. Villapol, S., Loane, D. J. & Burns, M. P. Sexual dimorphism in the inflammatory response to traumatic brain injury. *Glia* **65**, 1423–1438 (2017).
59. Heindl, S. *et al.* Automated morphological analysis of microglia after stroke. *Front Cell Neurosci* **12**, (2018).
60. Frik, J. *et al.* Cross-talk between monocyte invasion and astrocyte proliferation regulates scarring in brain injury. *EMBO Rep* **19**, (2018).
61. Han, R. T., Kim, R. D., Molofsky, A. v. & Liddelow, S. A. Astrocyte-immune cell interactions in physiology and pathology. *Immunity* vol. 54 Preprint at <https://doi.org/10.1016/j.immuni.2021.01.013> (2021).
62. Liddelow, S. A. *et al.* Neurotoxic reactive astrocytes are induced by activated microglia. *Nature* **541**, (2017).
63. Buffo, A. *et al.* Expression pattern of the transcription factor Olig2 in response to brain injuries: implications for neuronal repair. *Proc Natl Acad Sci U S A* **102**, 18183–18188 (2005).
64. Shechter, R. & Schwartz, M. CNS sterile injury: Just another wound healing? *Trends Mol Med* **19**, 135–143 (2013).
65. Sirko, S. *et al.* Astrocyte reactivity after brain injury-: The role of galectins 1 and 3. *Glia* **63**, 2340–2361 (2015).
66. Jurga, A. M., Paleczna, M. & Kuter, K. Z. Overview of General and Discriminating Markers of Differential Microglia Phenotypes. *Front Cell Neurosci* **14**, 1–18 (2020).
67. Dimou, L. & Gotz, M. Glial cells as progenitors and stem cells: new roles in the healthy and diseased brain. *Physiol Rev* **94**, 709–737 (2014).
68. Eugenín-von Bernhardt, J. & Dimou, L. NG2-glia, more than progenitor cells. *Adv Exp Med Biol* (2016) doi:10.1007/978-3-319-40764-7_2.
69. Simon, C., Dimou, L. & Gotz, M. Progenitors in the adult cerebral cortex - cell cycle properties and regulation by physiological stimuli and injury . *Glia* **59(6)**, 869–881 (2011).
70. Chen, W. T. *et al.* Spatial Transcriptomics and In Situ Sequencing to Study Alzheimer's Disease. *Cell* **182**, (2020).
71. Mazaheri, F. *et al.* TREM2 deficiency impairs chemotaxis and microglial responses to neuronal injury. *EMBO Rep* **18**, 1186–1198 (2017).
72. Shandra, O. *et al.* Repetitive Diffuse Mild Traumatic Brain Injury Causes an Atypical Astrocyte Response and Spontaneous Recurrent Seizures. *The Journal of Neuroscience* **39**, 1944–1963 (2019).

Acknowledgements

We are particularly grateful to Dr. Magdalena Götz and Dr. Stefan Stricker (Ludwig- Maximilians-University, Munich) for their valuable support toward this study, experimental suggestions, and critical reading of the manuscript. Lastly, we thank all the members of the Neurogenesis and Regeneration group for their experimental inputs, discussions, and critical reading of the manuscript. We acknowledge the support of the following core facilities: the Bioimaging Core Facility at the BioMedical Center of LMU Munich, the Laboratory for Functional Genome Analysis (LAFUGA), and the Sequencing Facility at the Helmholtz Zentrum München. This work was supported by the German research foundation (DFG) by the SFB 870; TRR274; SPP 1738 “Emerging roles of non-coding RNAs in nervous system development, plasticity & disease”, SPP1757 “Glial heterogeneity”; SPP2191 “Molecular mechanisms of functional phase separation” (ID 402723784) and the Excellence Strategy within the framework of the Munich Cluster for Systems Neurology (EXC 2145/1010 SyNergy – ID 390857198) and Ampro Helmholtz Alliance.

Author Contributions

C.K., V.S. and J.N. conceived the project and experiments. C.K., V.S., J.F.S., T.S.E. and R.B. performed the experiments and analyzed the data. C.K., H.A., and S.F. performed the bioinformatic analyses C.K., V.S. and J.N. wrote the manuscript with input from all authors. J.N., M.G., and F.J.T. supervised research and acquired funding.

Declaration of interests

The authors declare no conflict of interest.

Figure Legends

Figure 1. Spatially resolved transcriptomic changes induced by stab wound injury.

(a) Experimental scheme to conduct spatial transcriptomics in intact and stab wound-injured mouse cerebral cortices (3dpi). Brains were manually resected and selected areas highlighted in blue or red dashed boxes were positioned on Visium capture areas. (b) Brain sections of both conditions contain cortical-, hippocampal- and white matter regions. Dashed red line indicates injury core. (c) Clustering of gene expression data on spatial coordinates based on highly variable genes and subsequent dimensionality reduction. (d) Dot plot illustrating the expression of the 20 most enriched genes in the injury-induced cluster VI. (e) Image displaying the spatial trajectory along cluster VI in mediolateral direction. (f) Heatmap exhibits distinct expression patterns of genes (y-axis) along the spatial trajectory (x-axis). Dashed white line indicates injury core. (g,h) Gene expression of 'peaking genes' *Serpina3n*, *Lcn2* and *Cd68* in spatial context (g) and along the spatial trajectory (h). Dashed black line indicates injury core. (i,j) Images depicting expression of *Serpina3n*, *Lcn2* and *Cd68* on RNA (i) and protein level (j) in stab wound-injured cerebral cortices (3dpi). All images are full z-projections of confocal z-stacks. (k) Dot plots depicting GO-terms of over-represented cluster VI significant-enriched genes (pval < 0.05, log₂ fold change > 1). Scale bars: i,j: 150 μm. Abbreviations: CTX = cerebral cortex, WM = white matter, HPF = hippocampal formation, LV = lateral ventricle, CP = choroid plexus, V3 = third ventricle, TH = thalamus, fi = fimbria, dpi = days post injury, BP = biological processes, MF = molecular functions, CC = cellular components, GO = gene ontology.

Figure 2. Combination of spatial and single cell transcriptomics identifies cellular populations contributing to distinct transcriptional responses at the injury site.

(a) Experimental scheme to conduct single-cell RNA-sequencing of intact and stab wound-injured cerebral cortices (3dpi) using the 10x Genomics platform. (b) UMAP plot illustrates 6322 single cells distributed among 30 distinct clusters. Clusters are color-coded and annotated based on their transcriptional identities. (c) UMAP plot depicting distribution of cells isolated from intact (green) and injured (red) cerebral cortices. (d) Dot plot emphasizing strong correlation of post-hoc cluster annotation with established cell type-specific gene sets (see Ext. Table 3). (e,f) scRNAseq cluster localization on Visium based on probabilistic mapping (e) and single cell deconvolution (f) in spatial context. Abbreviations: UMAP = uniform manifold approximation and projection, dpi = days post injury, OPCs = oligodendrocyte progenitor cells, COPs = committed oligodendrocyte progenitors, MOL = mature oligodendrocytes, VECV = vascular endothelial cells (venous), VSMCs = vascular smooth muscle cells, VLMCs = vascular and leptomeningeal cells, DAM = disease-associated microglia, BAM = border-associated macrophages, NKT cells = natural killer T cells, DC/DCs = dendritic cells.

Figure 3. Stab wound injury induces defined transcriptional changes in glial subpopulations.

(a) Experimental scheme to conduct single-cell RNA-sequencing of intact and stab wound-injured cerebral cortices (3 and 5dpi) using the 10x Genomics platform. (b) UMAP embedding of integrated and batch-corrected single cell transcriptomes of 35240 cells distributed among 35 distinct clusters. Clusters were color-coded and annotated based on their transcriptional identities. (c-e) UMAPs depicting subclustering of astrocytes (9 clusters) (c), microglia (8 clusters) (d) and oligodendrocytes (10 clusters) (e). Cells were further assigned to homeostatic (blue) or reactive (red) clusters based on cell origin (see Ext. Fig. 6), distribution (pink cells) and distinct marker expression. Abbreviations: UMAP = uniform manifold approximation and projection, dpi = days post injury, OPCs = oligodendrocyte progenitor cells, COPs = committed oligodendrocyte progenitors, MOL = mature oligodendrocytes, VECV = vascular endothelial cells (venous), VSMCs = vascular smooth muscle cells, VLMCs = vascular and leptomeningeal cells, BAM = border-associated macrophages, NKT cells = natural killer T cells, DC/DCs = dendritic cells.

Figure 4. Stab wound injury induces common transcriptional changes in reactive glial subpopulations.

(a) UpSet plot depicting unique and overlapping DEGs (p val < 0.05, \log_2 fold change > 1.6 or \log_2 fold change < -1.6) induced in reactive glial subclusters 'MG4' 'AG5' and 'OPCs2' compared to all other clusters of the respective cell type. 192 commonly shared genes between these clusters are highlighted by red bar. (b) GO-term network analysis of the 192 commonly shared genes associates shared DEGs to the biological processes proliferation (green dashed line) and innate immunity (orange dashed line). (c) Chord diagram illustrates innate immunity GO-terms of Fig. 4b and the corresponding genes. Abbreviations: DEGs = differentially expressed genes, GO = gene ontology, BP = biological processes.

Figure 5. Cxcr3 and Tlr1/2 pathways orchestrate innate immune response shared between reactive glial cells.

(a) Experimental scheme to conduct single-cell RNA-sequencing of intact, stab wound-injured control (3/5dpi_CTRL) and stab wound-injured inhibitor-treated (3/5dpi_INH) cerebral cortices using the 10x Genomics platform. (b) UMAP embedding of integrated and batch-corrected single cell transcriptomes of 53813 cells. Cells were distributed among 36 distinct clusters, color-coded and annotated based on their transcriptional identities. (c-e) UMAPs illustrating subclustering of astrocytes (9 clusters) (c), microglia (8 clusters) (d) and oligodendrocytes (13 clusters) (e). Cells were further assigned to homeostatic (blue) or reactive (red) clusters based on cell origin (see Ext. Fig. 9). (f) Dot plots depict reduced expression of various shared inflammatory genes (see Fig. 4c) in reactive glial clusters 'AG7', 'MG3' and 'OPCs2' following inhibitor-treatment. (g-h) GO-term networks illustrate common and unique downregulated biological processes of glial subclusters in response to Cxcr3 and Tlr1/2 pathway inhibition at 3dpi (g) and 5dpi (h) (see Ext. Table 8). Common downregulation of innate immunity-associated GO-terms (highlighted by red dashed lines) can be observed at 3 but not at 5dpi. Abbreviations: UMAP = uniform manifold

approximation and projection, dpi = days post injury, OPCs = oligodendrocyte progenitor cells, COPs = committed oligodendrocyte progenitors, MOL = mature oligodendrocytes, VECV = vascular endothelial cells (venous), VSMCs = vascular smooth muscle cells, VLMCs = vascular and leptomeningeal cells, BAM = border-associated macrophages, NKT cells = natural killer T cells, DC/DCs = dendritic cells.

Figure 6. Cxcr3 and Tlr1/2 pathway inhibition following stab wound injury reduces microglial reactivity.

(a,b) UMAPs illustrating subclusters of microglia (a) and cell distributions (b) among those subclusters at all timepoints (intact, 3 and 5dpi) and conditions (CTRL and INH). (c) Experimental paradigm to assess microglia morphology characteristics according to Heindl et al. 2018. Grey box on mouse brain scheme highlights analyzed area. Red line indicates injury core. (d,e) Representative images of Iba1⁺ microglia (yellow) in CTRL (d) and INH-treated (e) mice. Dashed white boxes indicate selected microglia used for 3D reconstruction. All images are full z-projections of confocal z-stacks. (f) Scatter plot depicting morphological features of analyzed microglial cells. Each data point represents one microglial cell and in total 450 cells per condition were analyzed. Data are displayed as median \pm interquartile range. p-values were determined using Mann-Whitney U-test. Scale bars: d,e: 20 μ m. Abbreviations: UMAP = uniform manifold approximation and projection, dpi = days post injury, CTRL = stab wound-injured control animals, INH = stab wound-injured inhibitor-treated animals.

Figure 7. Proliferation of reactive astrocytes is decreased upon Cxcr3 and Tlr1/2 pathway inhibition.

(a,b) UMAPs illustrating subclusters of astrocytes (a) and cell distributions (b) among those subclusters at all timepoints (intact, 3 and 5dpi) and conditions (CTRL and INH). (c) Experimental paradigm to address astrocyte proliferation. Dashed grey box on mouse brain scheme refers to analyzed area. Red line displays injury core. (d,e) Representative overview images of proliferating GFAP⁺ (green) and EdU⁺ (magenta) astrocytes in CTRL (d) and INH-treated (e) animals. White dashed lines highlight injury cores. Micrographs (d'-e'') are magnifications of white boxed areas in (d) and (e), respectively. White arrowheads in micrographs depict colocalization of EdU (d',e') with GFAP⁺ astrocytes (d'',e''). All images are full z-projections of confocal z-stacks. (f,g) Dot plots depicting percentage of proliferating (GFAP⁺ and EdU⁺) astrocytes (f) and total density of proliferating (EdU⁺) cells (g) in CTRL and INH-treated animals. Data are shown as mean \pm standard error of the mean. Each data point represents one animal. p-values were determined using unpaired t-test. Scale bars: d,e: 50 μ m (overview), d'-e'': 20 μ m (micrographs). Abbreviations: UMAP = uniform manifold approximation and projection, dpi = days post injury, EdU = 5-Ethynyl-2'-deoxyuridine, i.p. = intraperitoneal injection, CTRL = stab wound-injured control animals, INH = stab wound-injured inhibitor-treated animals.

Ext. Figure 1. Spatial transcriptome of intact and grey matter stab wound-injured mice.

(a) Experimental scheme to conduct spatial transcriptomics of intact and stab wound-injured mice (3dpi). Brains were manually resected (selected areas highlighted in blue and red dashed boxes) and positioned on Visium capture areas. (b) In each capture area, two brain sections of either intact or stab wound-injured cortices were collected. Dashed red lines indicate injury core. (c) Clustering of gene expression data on spatial coordinates based on highly variable genes and subsequent dimensionality reduction. Clusters are color-coded and annotated based on their transcriptional identities. (d) Dot plot depicting 5 most enriched genes in each of the 16 identified clusters. (e) Expression of neuronal layer scores 2/3, 4, 5 and 6 in intact and injured brain sections on spatial coordinates. Neuronal layer gene set scores are listed in Ext. Table 2 (f) Heatmap shows genes (y-axis) with highest expression in injury vicinity ('peaking genes') along the spatial trajectory (x-axis). Dashed white line indicates injury core. Abbreviations: dpi = days post injury.

Ext. Figure 2. scRNA-seq clustering of intact and brain-injured mice (3dpi) and cell-type identification.

(a) UMAP plots depicting clustering of cells originating from intact (2676 cells) and injured (3646 cells) condition among 30 defined clusters. Clusters are color-coded and annotated based on their transcriptional identities. Note that clusters '13_Macrophages/Monocytes', '17_DCs' and '23_Astrocytes' are absent in the intact condition. (b) Dot plot depicting the expression of the 3 most enriched genes in each of the 30 identified clusters (see Ext. Table 4). (c-e) UMAPs highlighting example marker genes to identify microglia/macrophages (c), astrocytes (d) and OPCs (e). G2M gene set score is listed in Ext. Table 5. Abbreviations: UMAP = uniform manifold approximation and projection, dpi = days post injury, OPCs = oligodendrocyte progenitor cells, COPs = committed oligodendrocyte progenitors, MOL = mature oligodendrocytes, VECV = vascular endothelial cells (venous), VSMCs = vascular smooth muscle cells, VLMCs = vascular and leptomeningeal cells, BAM = border-associated macrophages, NKT cells = natural killer T cells, DCs = dendritic cells.

Ext. Figure 3. Probabilistic mapping of in scRNA-seq identified cellular clusters on Visium data set.

(a,b) Probabilistic mapping of in Fig. 2b identified scRNA-seq clusters on spatial transcriptome dataset (3 dpi). Stab wound injury elicits different mode of reaction in injury vicinity: Injury-induced enrichment and accompanied depletion of distinct clusters (a) or non-responding clusters (b). Abbreviations: OPCs = oligodendrocyte progenitor cells, NKT cells = natural killer T cells, DCs = dendritic cells, MOL = mature oligodendrocytes, VSMCs = vascular smooth muscle cells, COPs = committed oligodendrocyte progenitors, BAM = border-associated macrophages, VLMCs = vascular and leptomeningeal cells, VECV = vascular endothelial cells (venous).

Ext. Figure 4. Single-cell deconvolution-based mapping of in scRNA-seq identified cellular clusters on Visium data set.

(a,b) Deconvolution based mapping of in Fig. 2b identified scRNA-seq clusters on spatial transcriptome dataset (3 dpi). Abbreviations: OPCs = oligodendrocyte progenitor cells, NKT cells = natural killer T cells, DCs = dendritic cells, MOL = mature oligodendrocytes, VSMCs = vascular smooth muscle cells, COPs = committed oligodendrocyte progenitors, BAM = border-associated macrophages, VLMCs = vascular and leptomeningeal cells, VECV = vascular endothelial cells (venous).

Ext. Figure 5. Integration of scRNA-seq datasets of intact and brain-injured mice (3 and 5dpi), cluster distribution and cell type identification.

(a,b) UMAP plots depicting clustering (a) and cell distribution of integrated and batch-corrected intact (16567 cells), 3 dpi (3637 cells) and 5dpi (13658 cells) cells among 35 defined clusters (b). Clusters were color-coded and annotated based on their transcriptional identities. (c) Dot plot depicting expression of the 3 most enriched genes in each of the 35 identified clusters (see Ext. Table 6). Abbreviations: UMAP = uniform manifold approximation and projection, dpi = days post injury, VECV = vascular endothelial cells (venous), MOL = mature oligodendrocytes, DAM = disease-associated microglia, OPCs = oligodendrocyte progenitor cells, NKT cells = natural killer T cells, BAM = border-associated macrophages, VSMCs = vascular smooth muscle cells, COPs = committed oligodendrocyte progenitors, VLMCs = vascular and leptomeningeal cells, DC = dendritic cells.

Ext. Figure 6. Stab wound injury elicits unique gene expression in distinct glial subpopulations.

(a) UMAP depicting subclustered astrocytes of integrated and batch-corrected intact, 3 and 5dpi datasets. (b) Dot plot depicting expression of the 5 most enriched genes in each of the 9 identified clusters. (c) UMAP displaying cell distribution of intact (green), 3dpi (red) and 5dpi (orange) cells among all 9 astrocytic clusters. Note that clusters 'AG5', 'AG6' and 'AG8' are mainly composed of cells originating from injured cortices. (d) UMAP displaying localization of injury-enriched cluster '12_Astrocytes' (turquoise, Ext. Fig. 4b) on subclustered astrocytes. (e) UMAPs highlighting expression of example marker genes *Gfap*, *Vim* and *Lcn2* to identify reactive astrocyte clusters. (f) UMAP depicting subclustered microglia of integrated and batch-corrected intact, 3 and 5dpi datasets. (g) Dot plot depicting expression of the 5 most enriched genes in each of the 8 identified clusters. (h) UMAP displaying cell distribution of intact (green), 3dpi (red) and 5dpi (orange) cells among all 8 microglial clusters. Note that clusters 'MG4' and 'MG6' are mainly composed of cells originating from injured cortices. (i) UMAP displaying localization of injury-enriched cluster '11_Microglia' (peach, Ext. Fig. 4b) on subclustered microglia. (j) UMAPs highlighting expression of example marker genes *Aif1*, *Tmem119* and *P2ry12* to identify reactive microglial clusters. (k) UMAP depicting subclustered oligodendrocytes of integrated and batch-corrected intact, 3 and 5dpi datasets. (l) Dot plot depicting expression of the 5 most enriched genes in each of the 10 identified clusters. (m) UMAP displaying cell distribution of intact (green), 3dpi (red) and 5dpi (orange) cells among all 10 clusters. Note that cluster 'OPCs2' is mainly composed of cells originating from both injured conditions. (n) UMAP displaying localization of injury-enriched cluster '15_OPCs' (pink, Ext. Fig. 4b) on subclustered

oligodendrocytes. **(o)** Dot plot depicting expression of the 30 most enriched genes in cluster 'OPCs2'. Note comparable gene expression between clusters 'OPCs1' and 'OPCs2' prevent identification of unique reactive OPC markers. Abbreviations: UMAP = uniform manifold approximation and projection, dpi = days post injury, OPCs = oligodendrocyte progenitor cells, COPs = committed oligodendrocyte progenitors, MFOL = myelin-forming oligodendrocytes, MOL = mature oligodendrocytes.

Ext. Figure 7. Reactive glial subpopulations share injury-induced transcriptomic signature.

(a,b) UpSet plots depicting unique and overlapping down-regulated **(a)** and up-regulated DEGs **(b)** ($p_{\text{val}} < 0.05$, \log_2 fold change > 1.6 or \log_2 fold change < -1.6) between different glial subclusters of integrated and batch-corrected intact, 3 and 5 dpi datasets (Fig. 5c-e). Wherever applicable, DEGs are determined by comparing each glial subcluster to all other subclusters within the respective cell type (see methods). Red bars in **(b)** highlight commonly shared genes between reactive astrocytic, microglial and oligodendroglial subclusters. Abbreviations: DEGs = differentially expressed genes.

Ext. Figure 8. Reactive glial subpopulations display shared gene expression following injury.

(a) Experimental paradigm to identify shared gene expression in astrocytes, OPCs and microglia. Dashed grey box on mouse brain scheme refers to highlighted area. Red line displays injury core. **(b-d)** Representative overview images depicting Galectin1 expression in GFAP⁺ astrocytes **(b)**, NG2⁺ glia **(c)** and Iba1⁺ microglia **(d)**. Micrographs **(b'-d')** are magnifications of white boxed areas in corresponding overview images. White dashed lines highlight injury cores. White arrowheads in micrographs depict colocalization of Galectin1 **(b'-d')** with GFAP⁺ **(b'')**, NG2⁺ **(c'')** and Iba1⁺ **(d'')** cells. All images are full z-projections of confocal z-stacks. **(e)** Dot plot depicting gene expression of components associated with Tlr1/2 and Cxcr3 signaling pathways. Genes are adapted and complemented based on Sanchez-Gonzalez et al. 2022⁵⁴. Scale bars: **b-d**: 50 μm (overview), **b'-d'**: 20 μm (micrographs).

Ext. Figure 9. scRNA-seq data integration of intact and stab wound-injured cortices.

(a) UMAP plots depicting cell distribution of integrated and batch-corrected intact (green, 16649 cells), 3dpi CTRL (red, 3637 cells), 3dpi INH (pink, 4613 cells), 5dpi CTRL (orange, 13766 cells) and 5dpi INH (peach, 15146 cells) datasets. **(b)** Heatmap displaying high cluster similarity of integrated intact and injured CTRL conditions ('control', y-axis) and integrated intact, injured CTRL and injured INH conditions ('control and inhibitor-treatment' x-axis). **(c)** UMAP displaying cell distribution of intact (green), 3dpi CTRL (red), 3 dpi INH (pink), 5dpi CTRL (orange) and 5dpi INH (peach) cells among 9 identified astrocytic clusters as depicted in Fig. 5c. Clusters 'AG5', 'AG6', 'AG7' and 'AG8' are mainly formed by cells originating from injured CTRL and INH animals. **(d)** UMAP displaying cell distribution of intact (green), 3dpi CTRL (red), 3dpi INH (pink), 5dpi CTRL (orange) and 5dpi INH (peach) cells among 8 identified microglial clusters as depicted in Fig. 5d. Clusters 'MG3' and 'MG6' are mainly formed by cells originating from injured CTRL and INH animals. **(e)** UMAP displaying cell

distribution of intact (green), 3dpi CTRL (red), 3dpi INH (pink), 5dpi CTRL (orange) and 5 dpi INH (peach) cells among 13 identified oligodendroglial clusters as depicted in Fig. 5e. Clusters 'OPCs1' and 'OPCs2' are mainly formed by cells originating from injured CTRL and INH animals. Abbreviations: UMAP = uniform manifold approximation and projection, dpi = days post injury, CTRL = stab wound-injured control mice, INH = stab wound-injured inhibitor-treated mice, VECV = vascular endothelial cells (venous), MOL = mature oligodendrocytes, OPCs = oligodendrocyte progenitor cells, NKT cells = natural killer T cells, BAM = border-associated macrophages, VSMCs = vascular smooth muscle cells, COPs = committed oligodendrocyte progenitors, VLMCs = vascular and leptomeningeal cells, DC = dendritic cells.

Ext. Figure 10. Cxcr3 and Tlr1/2 pathway inhibition following brain injury induces subcluster-specific changes.

(a-d) UpSet plots depicting unique and overlapping down-regulated (a,c) and up-regulated (b,d) DEGs (p val < 0.05, \log_2 fold change > 0.7 or \log_2 fold change < -0.7) between different glial subclusters in response to Cxcr3 and Tlr1/2 inhibition at 3 (a,b) and 5dpi (c,d). (e,f) GO-term networks illustrate distinct, subcluster-specific biological processes enriched in the set of genes up-regulated in response to Cxcr3 and Tlr1/2 pathway inhibition at 3dpi (e) and 5dpi (f) (see Ext. Table 8). Abbreviations: DEGs = differentially expressed genes, dpi = days post injury.

Ext. Figure 11. OPC reactivity after injury is not altered by Cxcr3 and Tlr1/2 pathway inhibition.

(a,b) UMAPs illustrating subclusters of oligodendrocytes (a) and cell distributions among these subclusters (b) at all timepoints (intact, 3 and 5dpi) and conditions (CTRL and INH). (c) Experimental paradigm to address number of oligodendrocytes and OPC proliferation in injury vicinity. Dashed grey box on mouse brain scheme refers to analyzed area. Red line displays injury core. (d,e) Representative overview images of proliferating Olig2⁺ (grey) and EdU⁺ (magenta) oligodendrocytes in CTRL (d) and INH-treated (e) animals. White dashed lines highlight injury cores. Micrographs (d'-e'') are magnifications of white boxed areas in (d) and (e), respectively. White arrowheads in micrographs depict colocalization of EdU (d',e') with Olig2⁺ (d'',e'') cells. All images are full z-projections of confocal z-stacks. (f,g) Dot plots depicting number of oligodendrocytes (Olig2⁺ cells) (f) and proliferating OPCs (Olig2⁺ and EdU⁺) (g) in CTRL and INH-treated animals. Data are shown as mean \pm standard error of the mean. Each data point represents one animal. p-values were determined using unpaired t-test. Scale bars: d,e: 50 μ m (overview), d',e'': 20 μ m (micrographs). Abbreviations: UMAP = uniform manifold approximation and projection, dpi = days post injury, EdU = 5-Ethynyl-2'-deoxyuridine, i.p. = intraperitoneal injection, CTRL = stab wound-injured control animals, INH = stab wound-injured inhibitor-treated animals, OPCs = oligodendrocyte progenitor cells, COPs = committed oligodendrocyte progenitors, MFOL = myelin-forming oligodendrocytes, MOL = mature oligodendrocytes.

Ext. Figure 12. Reaction of microglia and astrocytes to stab wound injury in absence of *Cxcr3* and *Tlr2* signaling.

(a) Scatter plots depicting morphological microglial features. Each data point represents one microglial cell and in total 450 cells per condition were analyzed. Data are displayed as median \pm interquartile range. p-values were determined using Mann-Whitney U-test. (b) UMAPs highlighting expression of *Gfap* and *Lcn2* among all astrocytic subclusters. (c) Dot plots depicting expression levels of *Gfap* and *Lcn2* in astrocytes. (d) Dot plot depicting 'astrocyte reactivity scores' among all timepoints (intact, 3 and 5dpi) and conditions (CTRL and INH). Genes defining 'astrocyte reactivity scores' in Ext. Fig. 12d were extracted from 'Cluster_4' and 'Cluster_8' astrocytes of Hasel et al. 2021⁴⁶ (e) Experimental paradigm to investigate astrocyte reactivity in injury vicinity. Dashed grey box on mouse brain scheme refers to analyzed area. Red line displays injury core. (f,g) Representative overview images of GFAP⁺ astrocytes (green) and NGAL⁺ cells (magenta) in CTRL (f) and INH-treated (g) animals. White dashed lines highlight injury cores. Micrographs (f'-g'') are magnifications of white boxed areas in (f) and (g), respectively. White arrowheads in micrographs depict colocalization of NGAL (f',g') with GFAP⁺ astrocytes (f'',g''). All images are full z-projections of confocal z-stacks. (h,i) Dot plots depicting percentage of area covered with GFAP⁺ signal (h) and density of GFAP⁺ NGAL⁺ double positive astrocytes (i) in injury vicinity of CTRL and INH-treated mice. Data are shown as mean \pm standard error of the mean. Each data point represents one animal. p-values were determined using unpaired t-test. (j) UMAPs highlighting localization of proliferating astrocytes (pink) to subclusters 'AG6' and 'AG7'. (k) Histogram illustrating percentage of proliferating astrocytes between all timepoints (intact, 3 and 5dpi) and condition (CTRL and INH). Proliferating astrocytes were identified in scRNAseq data sets by S+G2/M score expression (see Ext. Table 5). Scale bars: f,g: 50 μ m (overview), f'-g'': 20 μ m (micrographs). Abbreviations: UMAP = uniform manifold approximation and projection, dpi = days post injury, INT = intact mice, CTRL = stab wound-injured control animals, INH = stab wound-injured inhibitor-treated animals.

Fig. 2

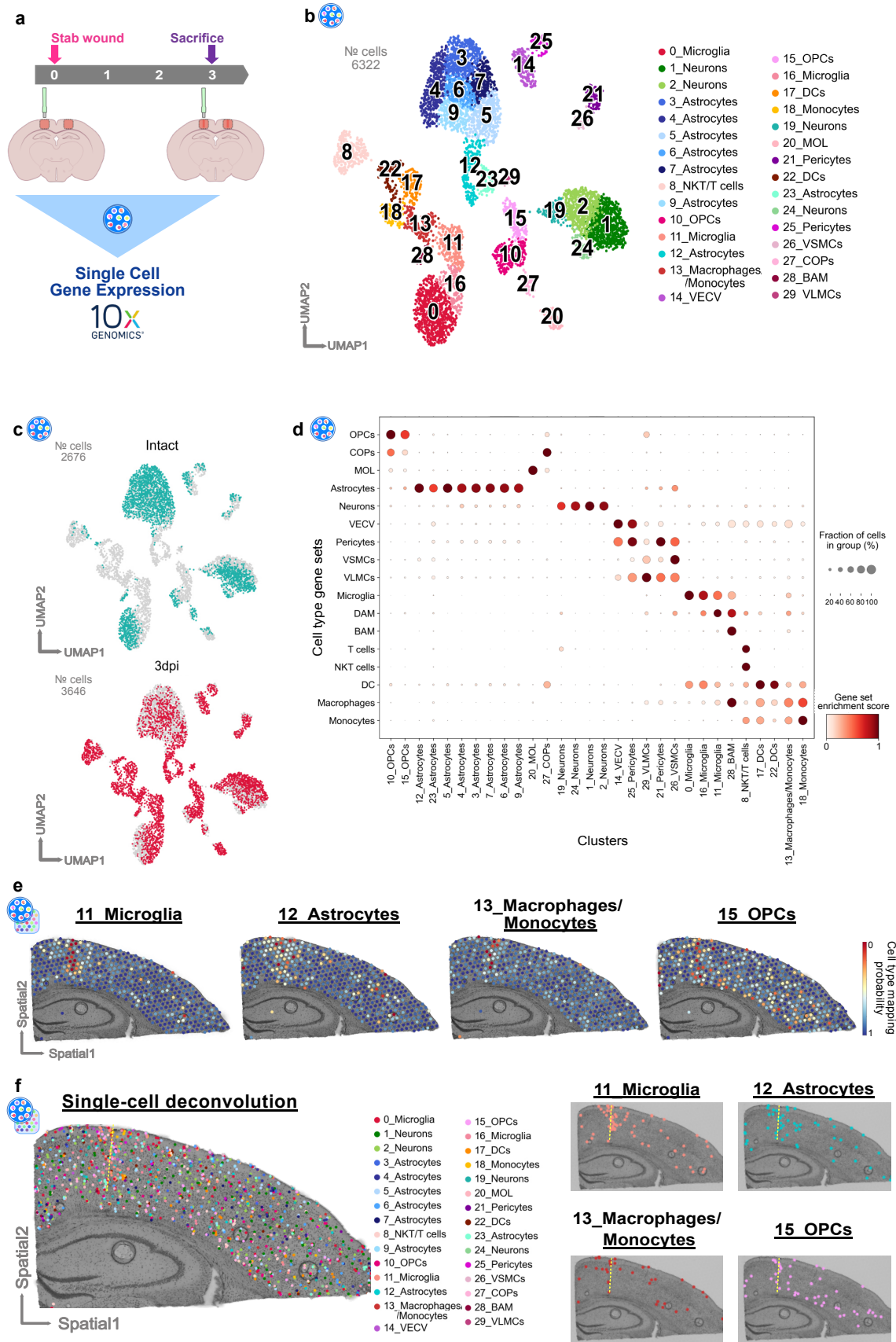


Fig. 3

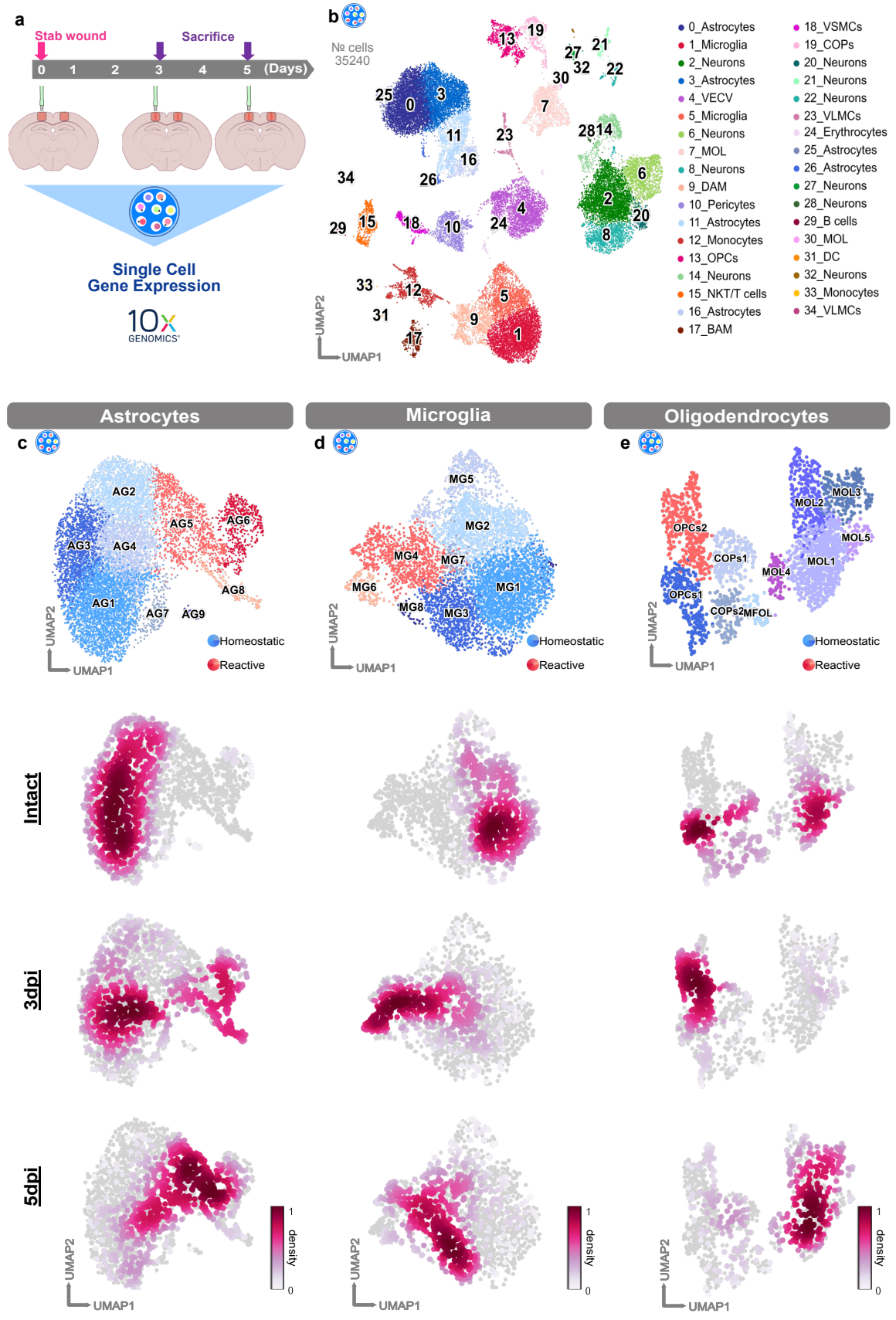


Fig. 4

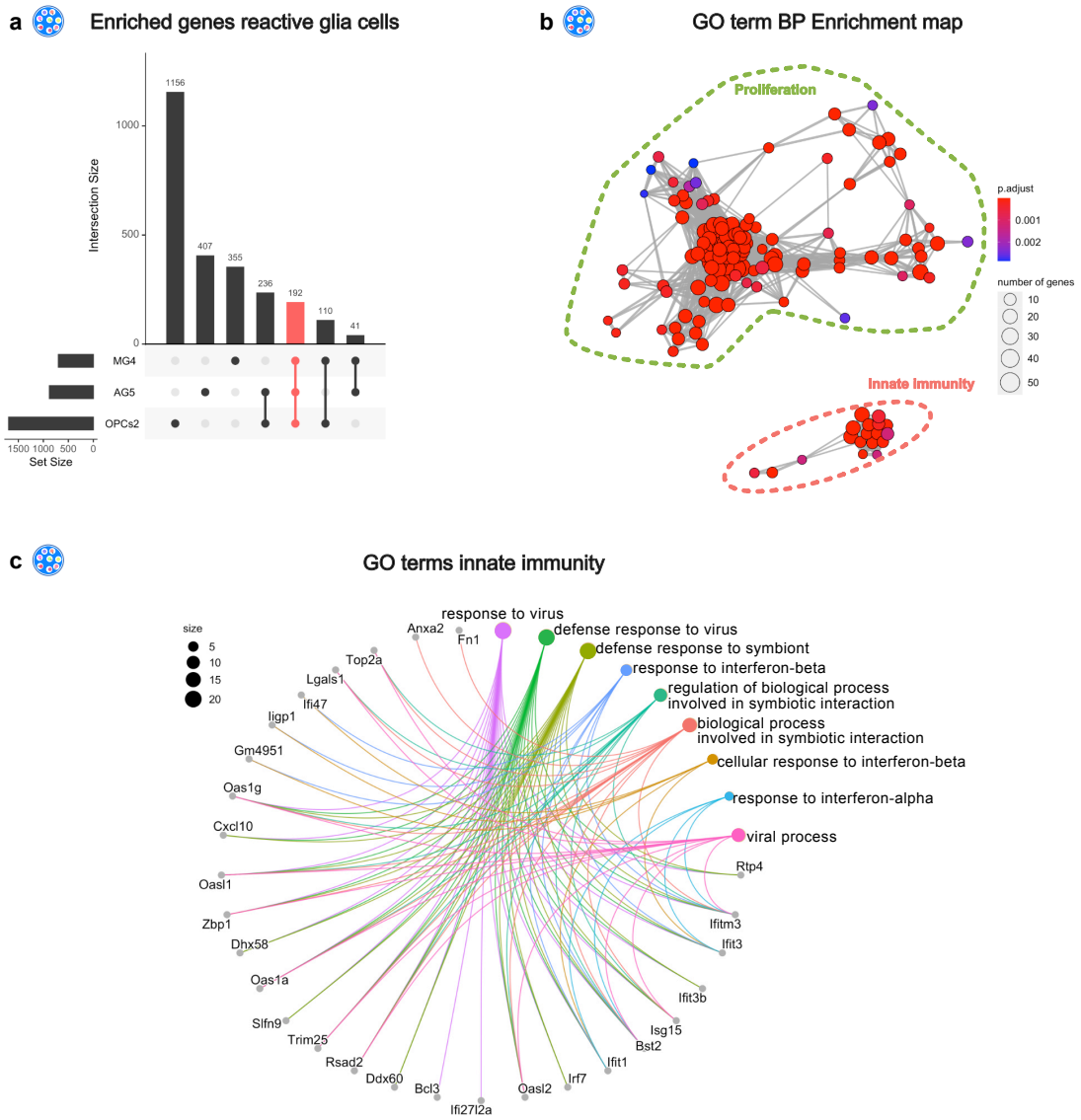


Fig. 5

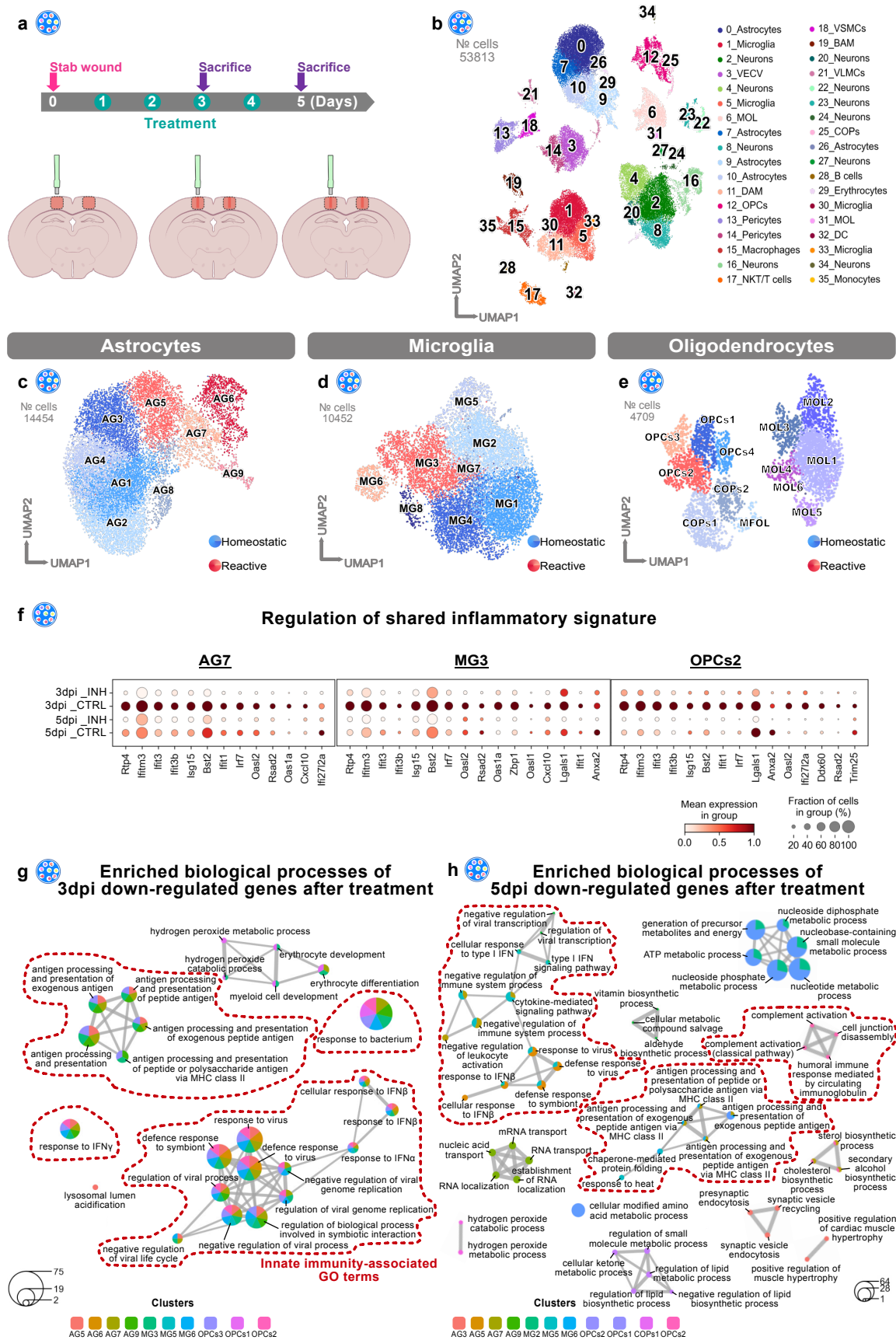


Fig.6

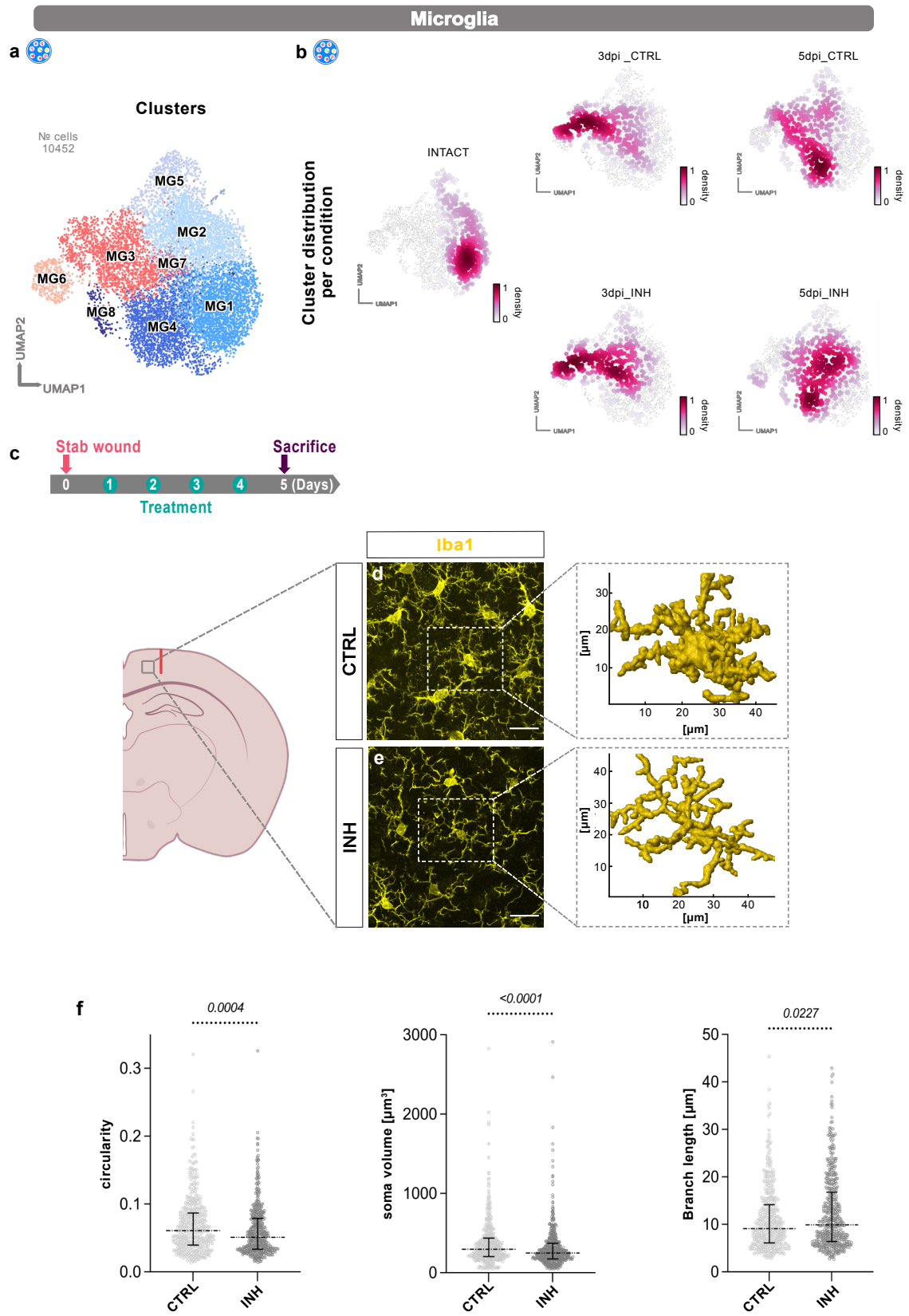
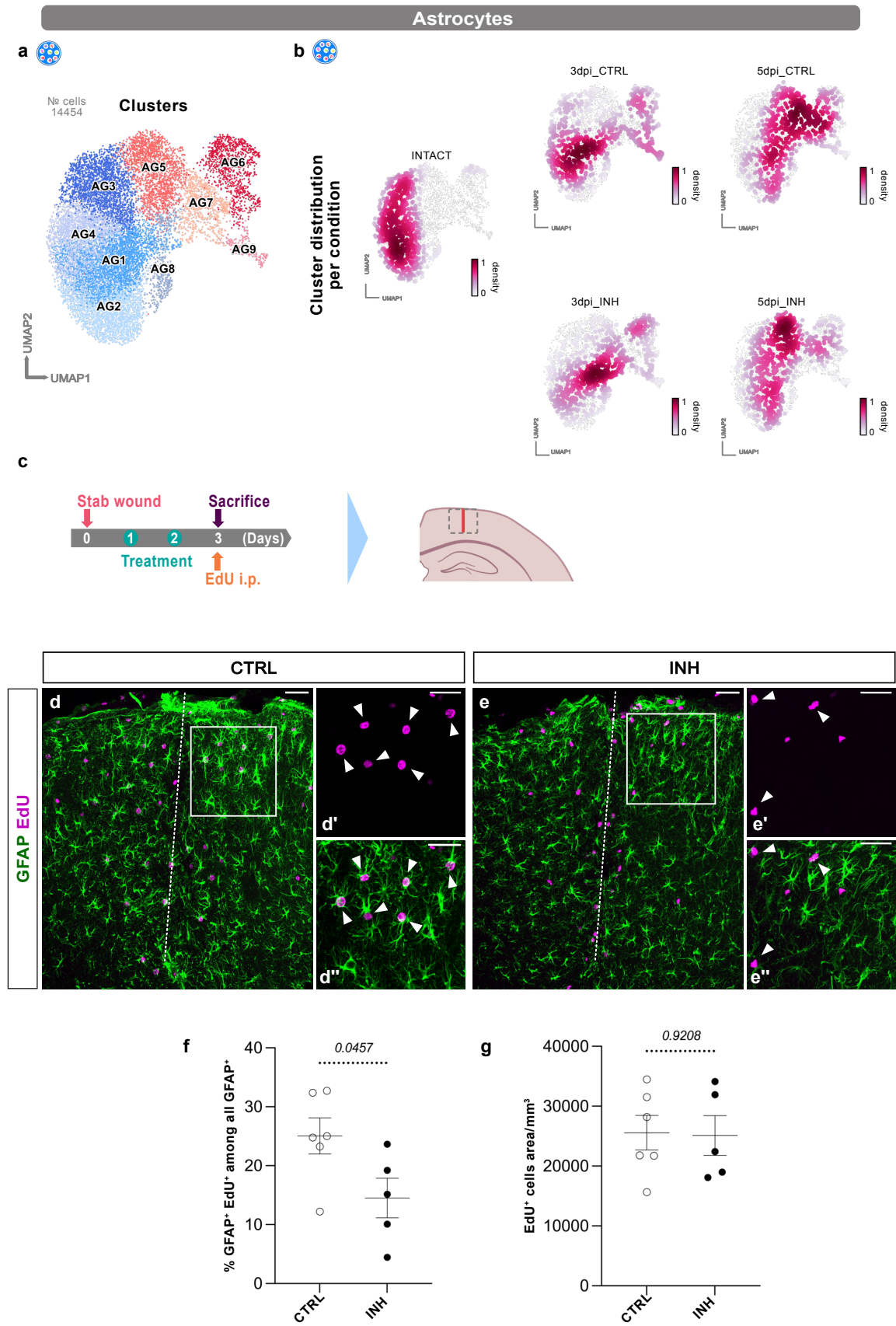
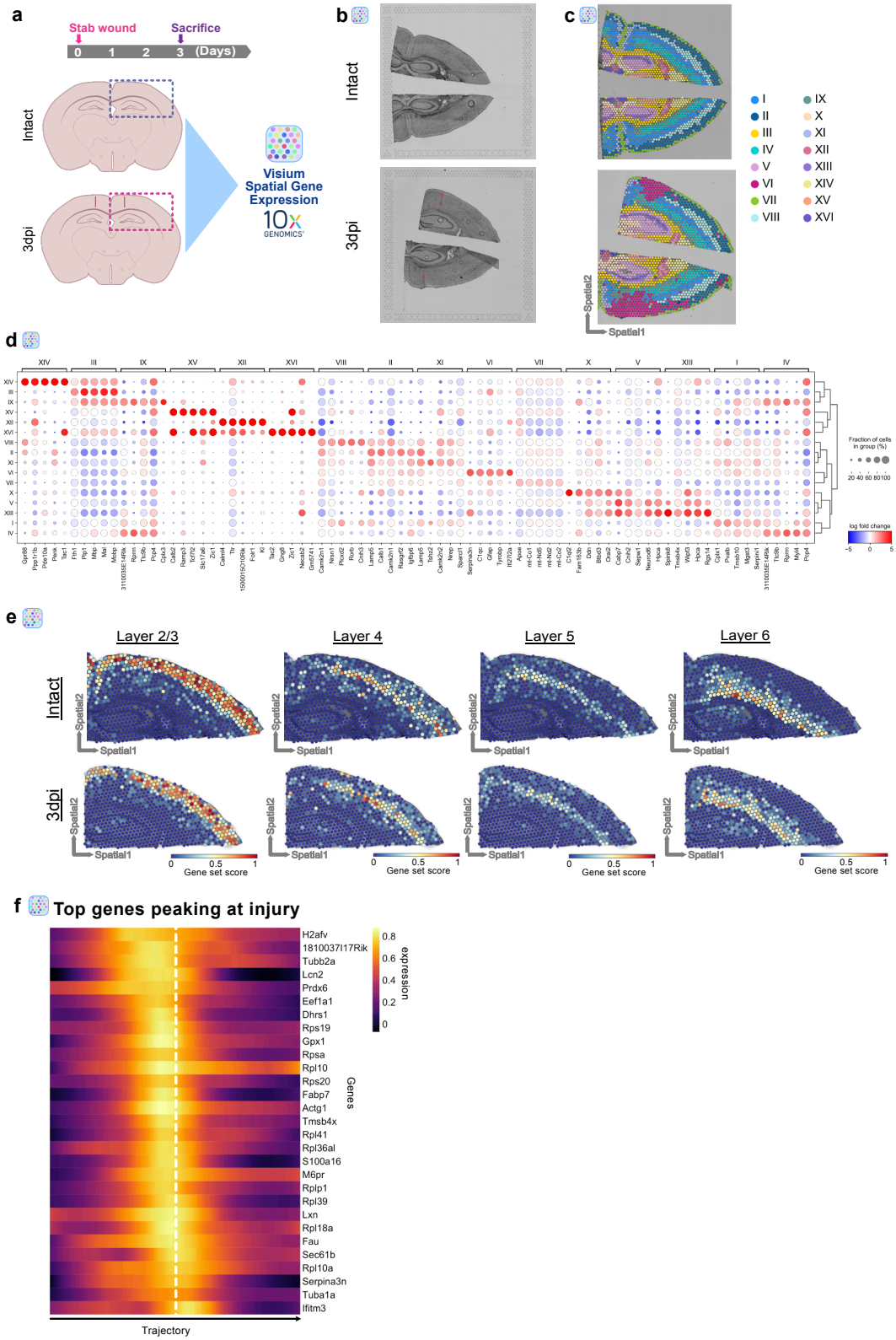


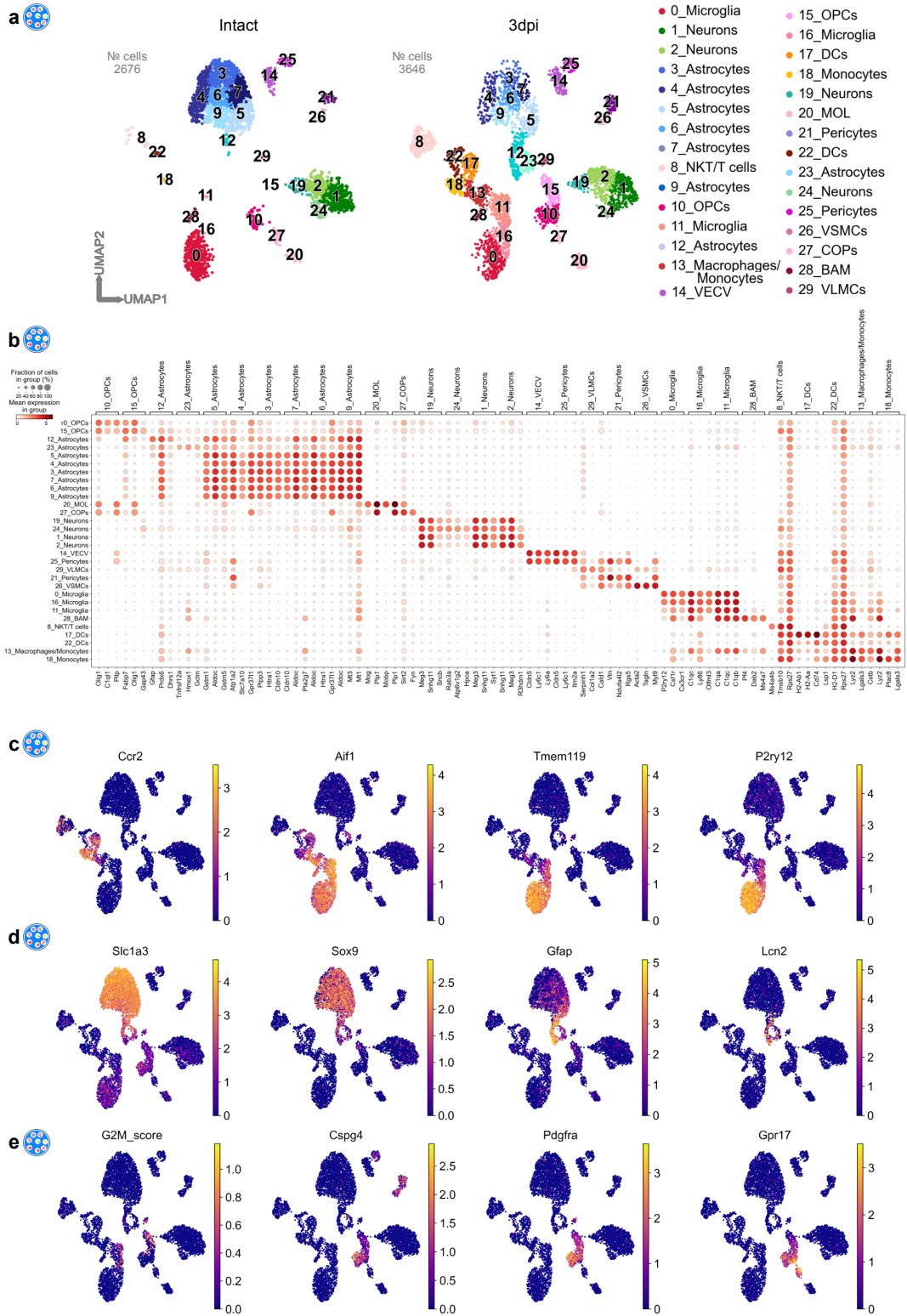
Fig.7



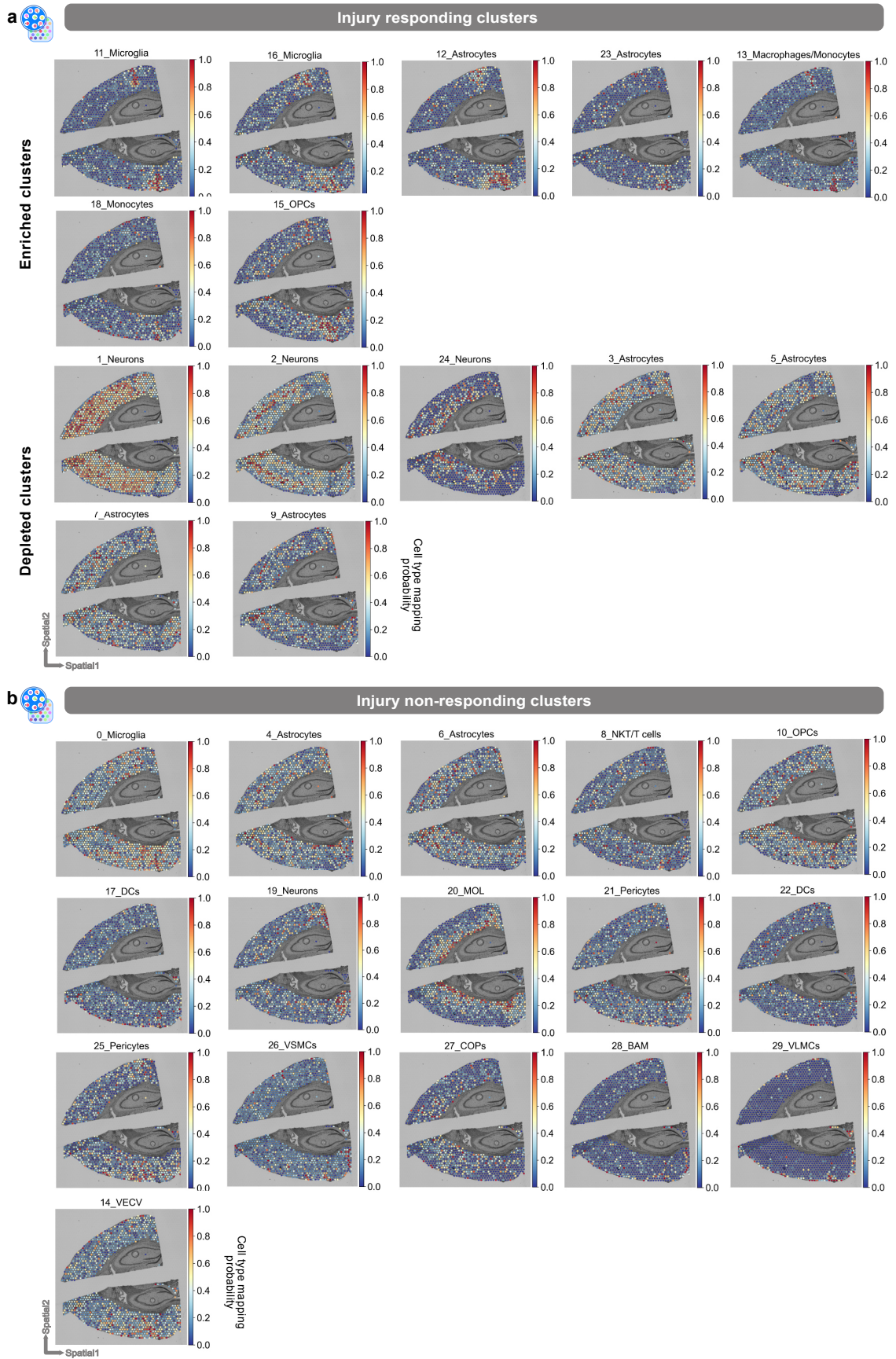
Ext.Fig. 1



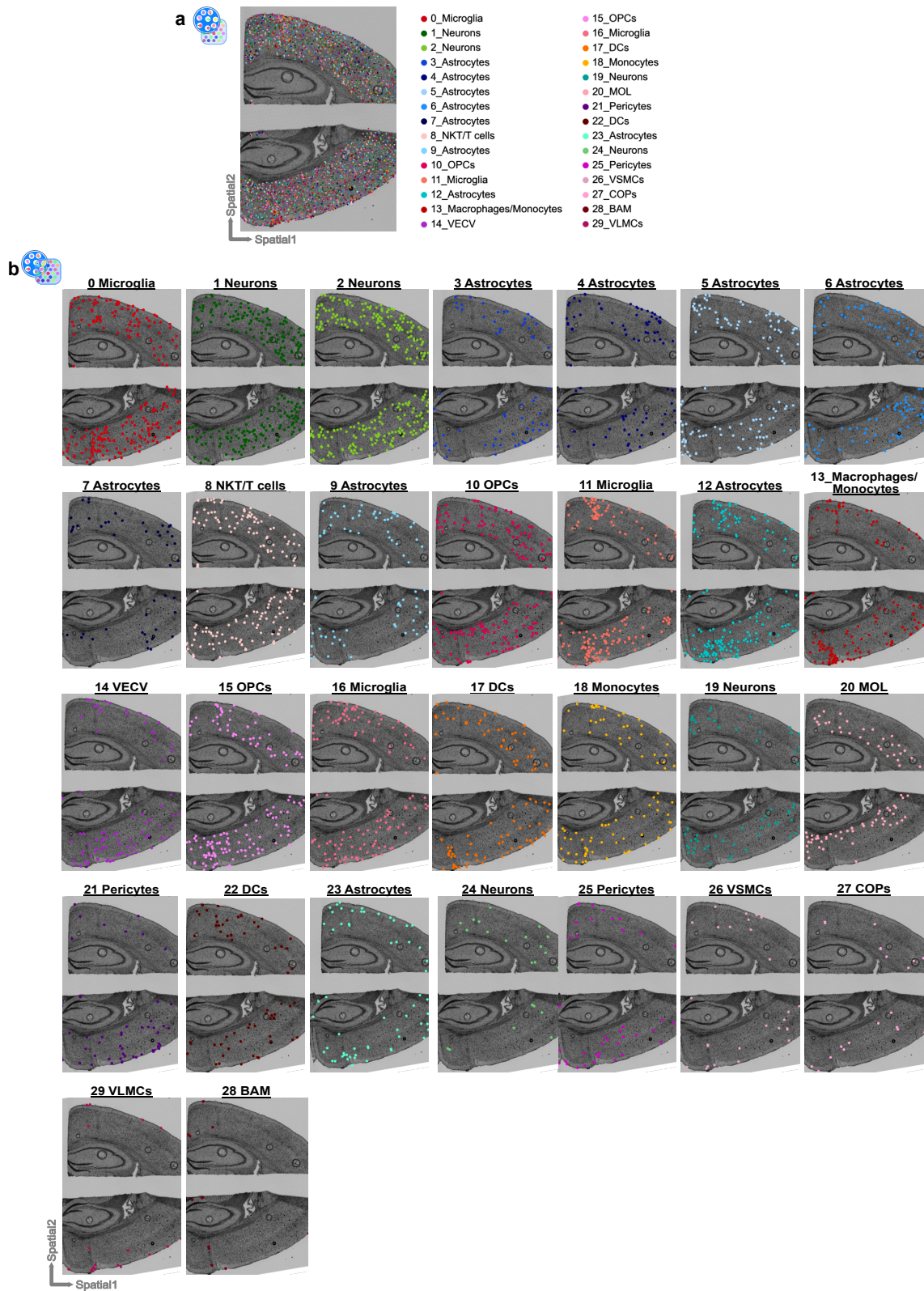
Ext.Fig. 2



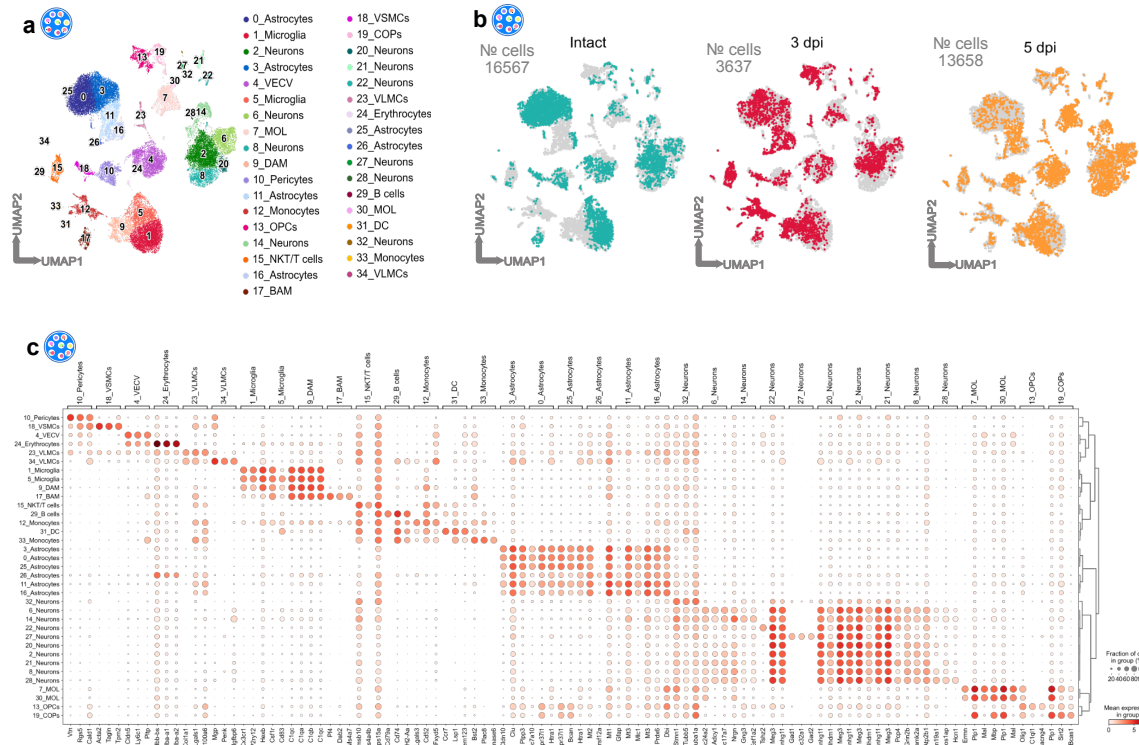
Ext.Fig. 3



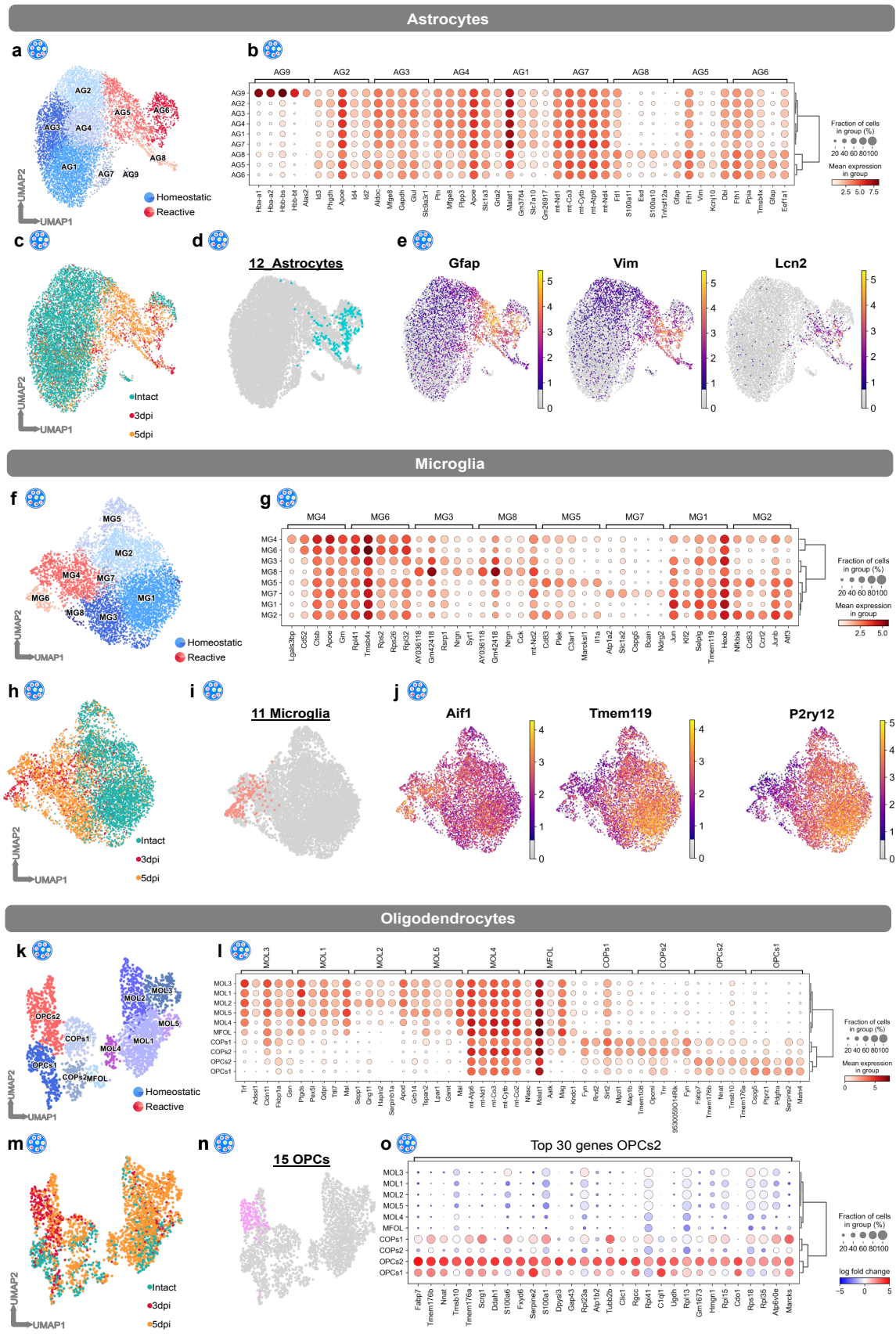
Ext. Fig.4



Ext.Fig. 5

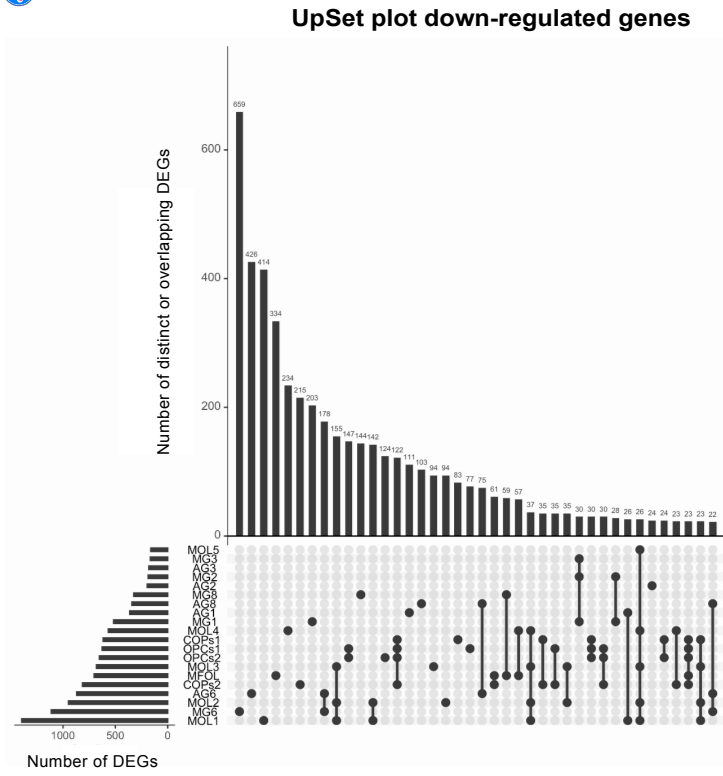


Ext.Fig. 6

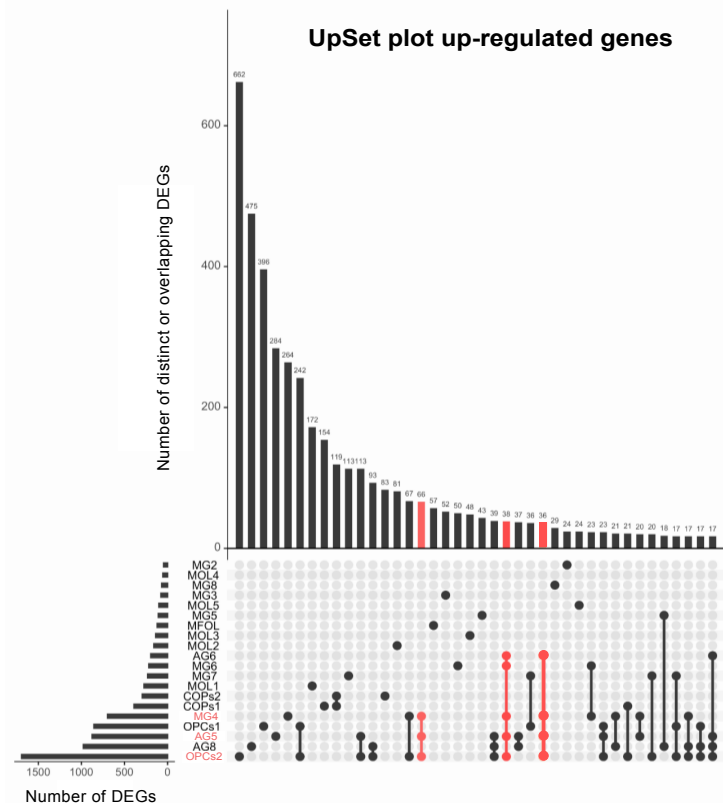


Ext. Fig. 7

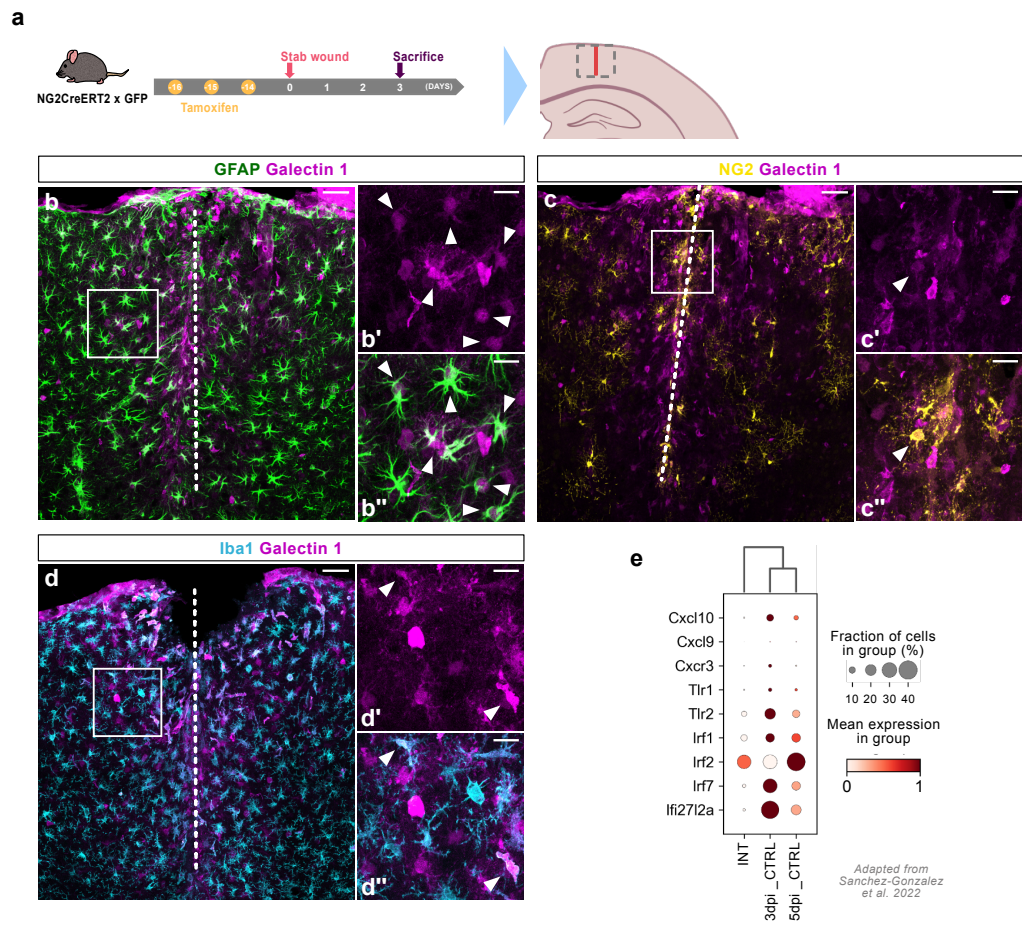
a



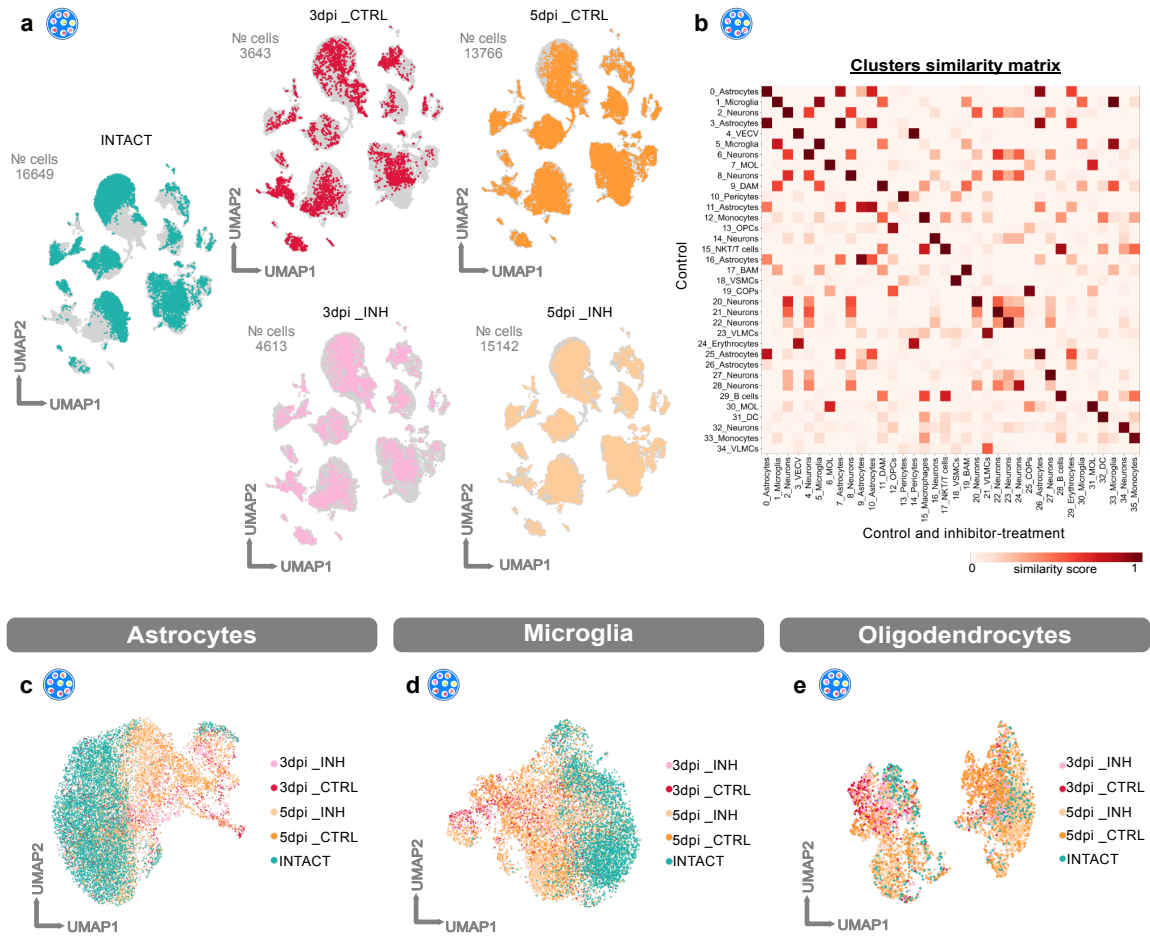
b



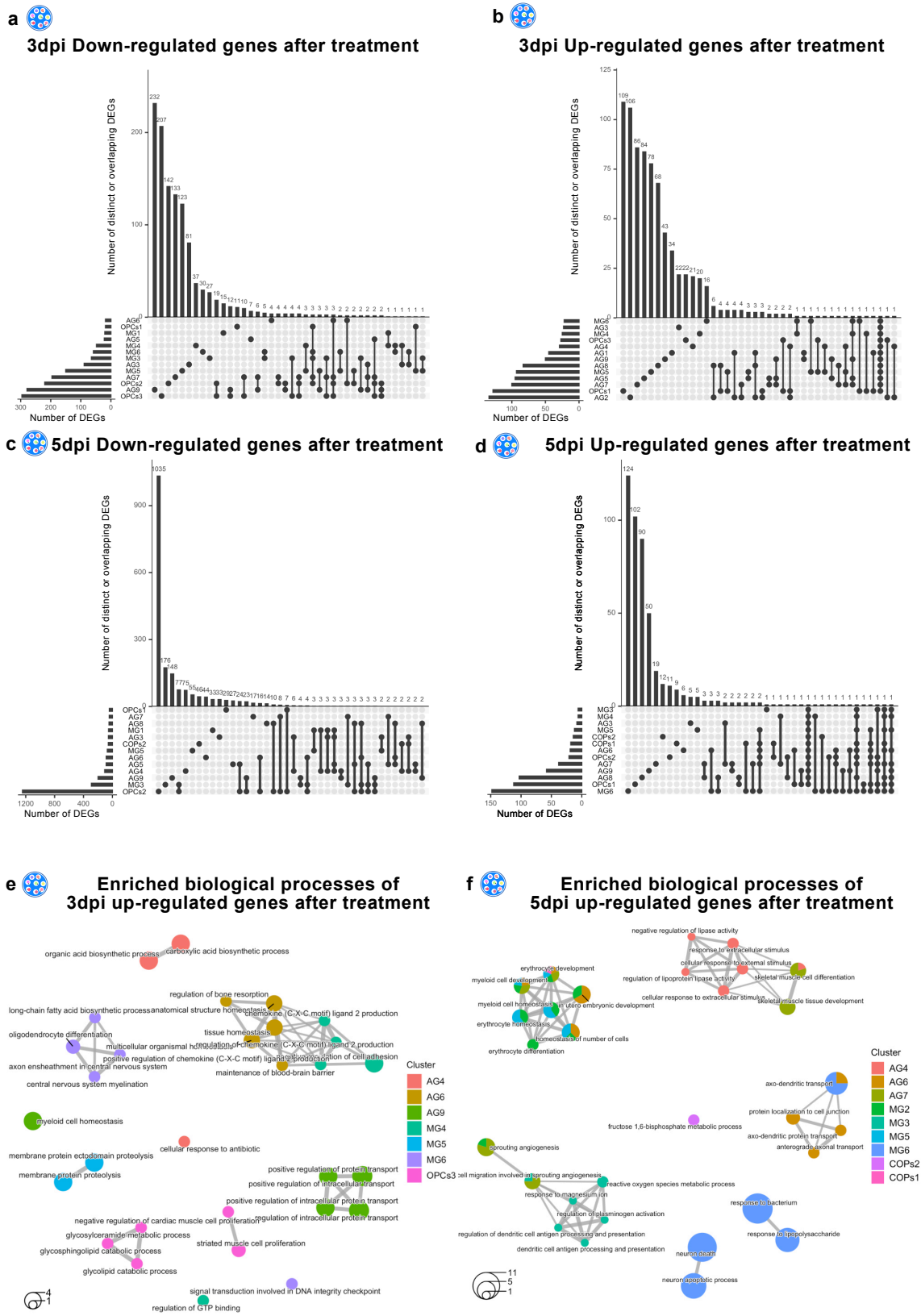
Ext.Fig. 8



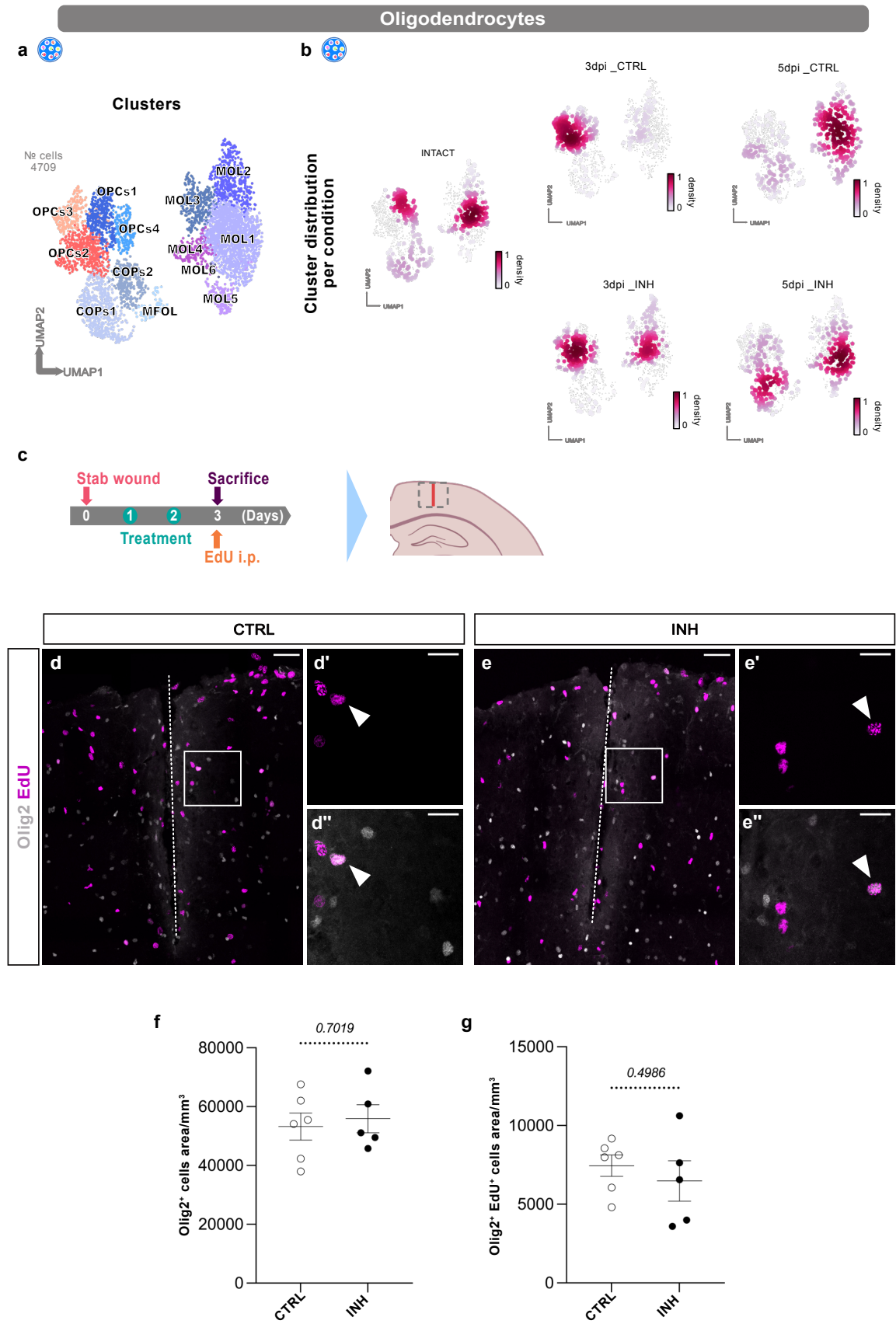
Ext. Fig. 9



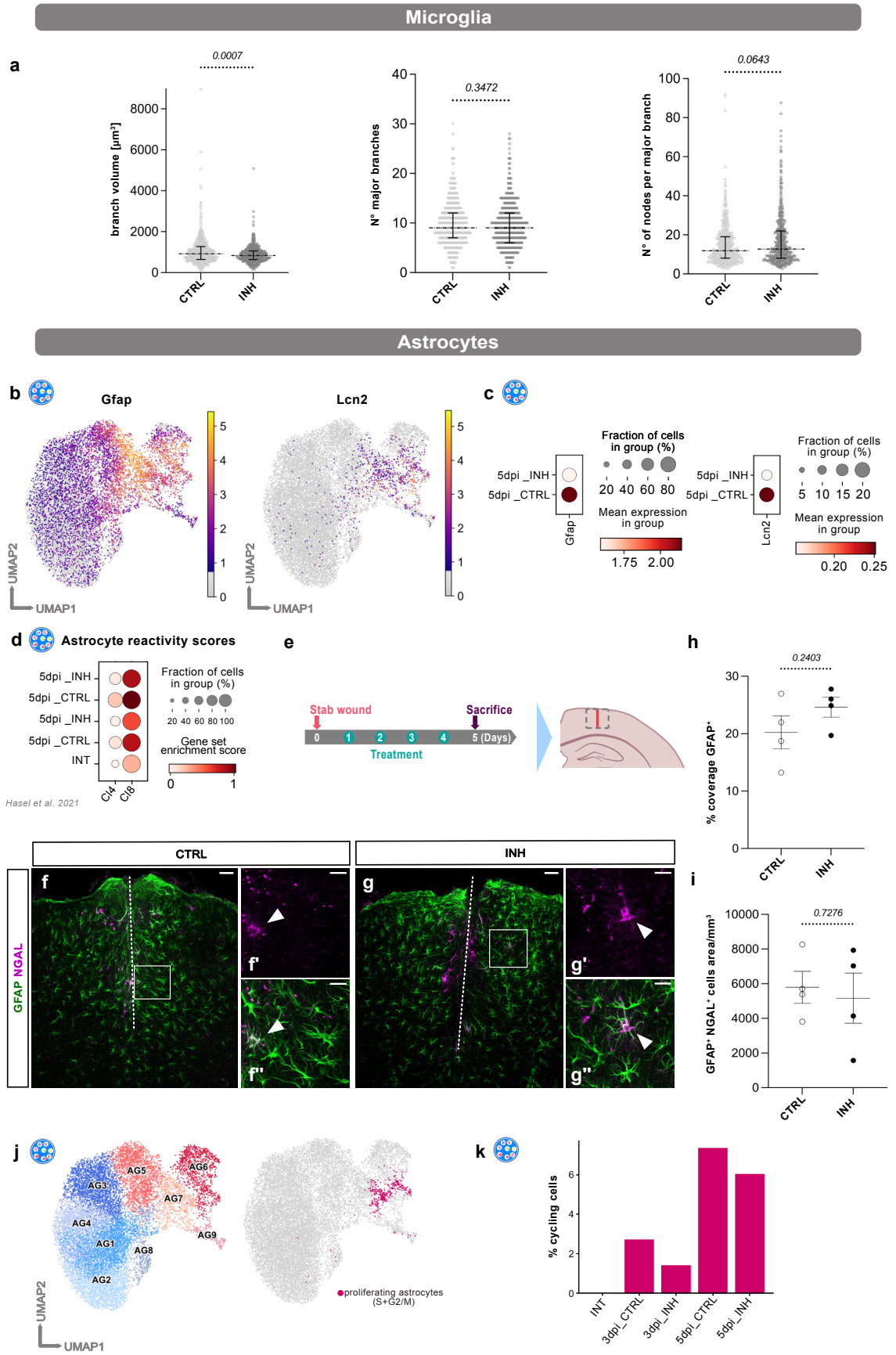
Ext.Fig. 10



Ext. Fig.11



Ext. Fig.12



3 Discussion

TBI is one of the leading causes of disability and mortality in western societies, and it is associated with increased risk for the development of additional pathologies, including neurodegenerative disorders (Maas et al., 2008; Puntambekar et al., 2018). Despite damages from the initial trauma, subsequent secondary cascades are thought to be a pivotal contributor to the subsequent detrimental outcomes. Glial cells are a critical contributor to secondary injury, having a dual role in TBI pathology. Initially, they associate with important protective aspects which promote recovery (Anderson et al., 2016). However, during the disease progression, they promote neuroinflammation, excitotoxicity, and extracellular matrix (ECM) changes, contributing to further damage to the CNS (George & Geller, 2018; Karve et al., 2016; Mira et al., 2021). This transition from a protective to a detrimental phenotype may present a time window for therapeutic interventions targeting glial cells, aiming to improve the adverse outcomes following TBI.

Overall, my Ph.D. project aimed to determine the mechanisms involved in glial cells' reactivity and glial border formation. In this line, I aimed to identify detrimental pathways involved in the prolonged glial border formation linked with the detrimental secondary phase of TBI pathophysiology. For my study, I used the stab-wound-injury model in mice (Buffo et al., 2005; Frik et al., 2018), a mild injury model involving the breakdown of BBB and the activation of both glial and immune cells (Frik et al., 2018). The reproducibility of the model and the reactivity observed, also long-term, make it perfect for studying the basic features of TBI pathophysiology. To address the changes in multiple populations and to profile the injury milieu, I performed transcriptomic analysis using the single-cell and spatial approach upon stab wound injury in the murine cerebral cortex. Thus, generating a molecular toolbox that could help us understand the changes following TBI. This analysis revealed specific subpopulations of glial cells with shared inflammatory signatures as part of the injury milieu. In addition, our zebrafish research revealed multiple components of the inflammatory system responsible for the prolonged accumulation of glial cells in the injury core (Sanchez-Gonzalez et al., 2022; Zambusi et al., 2022), highlighting the importance of tightly regulation of neuroinflammation for successful regeneration. Consequently, I utilize a trans-species approach by comparing our findings from zebrafish (Sanchez-Gonzalez et al., 2022) and mouse TBI models (Koupourtidou, Schwarz et al., unpublished data) and predicted Tlr2 and

Cxcr3 signaling pathways as a target to modulate glial reactivity in response to stab wound injury in the murine cerebral cortex. The transcriptomic analysis and the role of Tlr2 and Cxcr3 signaling pathways upon TBI in mice will be discussed in depth in the following section.

3.1 Molecular mapping of the injury milieu using spatial transcriptomics

TBI has complex pathophysiology, which involves the response of various types of cells (Mira et al., 2021; Puntambekar et al., 2018). In addition, an adequate border establishment requires distinct reactions of glial cells at a relative distance from the injury site. Indeed, it has already been demonstrated that astrocytes and OPCs respond differently based on their distance from the injury site. (Bardehle et al., 2013; Sofroniew & Vinters, 2010; von Streitberg et al., 2021). A better understanding of the global changes following TBI is critical as it can open new avenues in developing therapeutic approaches. However, most transcriptomic studies investigating cell states are independent of their location and mainly focus on the response of specific cell types, with few intended to evaluate the interplay between these cells. In this manner, I developed a toolbox profiling the transcriptional changes across various cell types with providing spatial and temporal context.

Spatial transcriptomic analysis of the stab-wounded cortex 3dpi revealed a well-defined injury cluster, “cluster VI,” around the injury core affecting only the surrounding area without altering the rest of the cortex. A remarkable observation was the extent of the injury milieu, which was restricted to a very close distance from the initial trauma, with the upper layer being more affected than the deeper layers. This could be explained by the V shape of the surgical tool used for the injury, which leads to more extensive damage to the upper layers. Interestingly, the cortical layer patterning was not altered by the injury as I could observe similar expression of the cortical gene sets (based on Zeisel et al., 2018) for each layer, with only a slight downregulation of these gene sets around the injury core.

Cluster’s VI-enriched genes are involved in glial reactivity, indicating an overrepresentation of these populations in the injury milieu. Indeed, among the top enriched genes for cluster VI, I detected genes specifically describing reactive astrocytes like *Gfap*, *Lcn2*, *Serpina3n*, *Vim*, *Lgals1*, *Fabp7*, and *Tspo* (Escartin et al., 2021; Hasel et al.,

2021; Jurga et al., 2020; Sirko et al., 2015; Zamanian et al., 2012) and genes specific for microglia/macrophages such as *Aif1*, *Csf1r*, *Cd68* and *Tspo* (Hammond et al., 2019; Jurga et al., 2020).

Looking at the processes characterizing the enriched genes of cluster VI, I observed the regulation of processes linked to angiogenesis and phagocytosis, known features of the early events following brain damage and wound healing in general (Shechter & Schwartz, 2013). These involve clearing dead cells and debris as well as re-establishing of vascular properties to ensure oxygen supply. In addition, I observed many genes linked to immune processes. Among them, I detected progranulin (*Grn*), which is important for microglia activation regulating its return to homeostasis and has a neuroprotective role (Zambusi et al., 2022; X. Zheng et al., 2022). Additionally, components of the complement system, which is also involved in the inflammatory reaction, were also enriched at the injury core. Specifically, I detected the Complement component 1q (C1q), subunits a, b, and c (*C1qa*, *b*, *c*), the recognition component of the classical complement activation pathway, which can regulate reactive astrocytes and microglia (Färber et al., 2009; Kettenmann et al., 2011; Liddelow et al., 2017)

To validate the accuracy of the spatial transcriptomics analysis in predicting gene expression in spatial context, I confirmed the expression of several cluster VI-specific genes (*Serpina3n*, *Lcn2*, and *Cd68*) using RNAscope. This enabled me to address if the expression patterns detected with the Visium correlate with the gene expression around the injury. Notably, the expression patterns detected were in line with the Visium analysis. This observation supports the use of Visium to detect global changes with spatial information.

3.2 Specific glial subpopulations contribute to the injury milieu

Even though the Visium platform offers the possibility to profile transcriptomic changes by preserving spatial information, the profile itself arises from multiple cells. In this regard, the combination of spatial transcriptomics with scRNA-seq analysis can become a great tool to reveal transcriptomic changes of specific cell types relative to their predicted location. This is of great interest in our injury model as it has been described that the reaction of especially astrocytes (Bardehle et al., 2013) and OPCs (von Streitberg et al., 2021) depends on their location. These observations are mainly based on live imaging studies, and until now, it has not been possible to study the transcriptomic profile

of these cells. Thus, we combined the spatial transcriptomic with scRNA-seq analysis aiming to generate a transcriptomic profile of multiple cells and predict their spatial localization.

However, for the successful integration of the two data sets, it is essential to consider some pre-requirements. For example, the samples should be from a similar anatomical location. Additionally, it is critical that the scRNA-seq dataset accurately represents the cell types of the region. Therefore, it was important to detect the predominant expected cell types in the scRNA-seq data. An important factor that can alter the detected cell types is the dissociation protocol. In my case, after trying different dissociation protocols, I decided to use an enzymatic dissociation protocol using papain (Papain Dissociation System-Worthington, used before by Zeisel et al., 2018). Using this protocol, I identified several neuronal and glial clusters, including astrocytes, microglia, and oligodendrocyte lineage cells. Additionally, vascular cells, pericytes, and multiple types of immune cells were also detected. Importantly, some of the clusters were detected mainly in the injured datasets, highlighting the detection of specific cell types depending on the anatomical region and condition.

Nowadays, there are several bioinformatic ways to integrate spatial and single-cell transcriptomic data (B. Li et al., 2022). As part of this study, I choose to use Tangram (Biancalani et al., 2021), a deep learning framework that uses non-convex optimization to learn a spatial alignment for scRNA-seq data and can assign cells to spatial locations using histological sections. Integrating the scRNA-seq and the Visium data sets predicted the contribution of specific cell subtypes to the injury environment. Indeed, I detected multiple populations responding to the injury by enriched or decreased representation, while others did not respond.

As I am interested in the populations accumulating at the injury milieu and forming the glial border, I focused on the populations with enriched representation in the injury area. Among them, microglial clusters showed a more uniform response to injury as I could detect all microglia clusters accumulating at the injury, with cluster “11_Microglia” being the one with the highest correlation. The cluster “11_Microglia” was mainly present in the 3dpi sample and had low expression of the homeostatic microglial genes, such as *P2ry12* and *Tmem119* (Masuda et al., 2019), whereas it had an enriched

score for the genes detected in disease-associated microglia (DAM) (Deczkowska et al., 2018; Hammad et al., 2018; Keren-Shaul et al., 2017; Masuda et al., 2020)

On the other hand, astrocytes showed a heterogeneous response, with most clusters being under-represented around the injury area compared to the rest of the cortex. Interestingly, only clusters “12_Astrocytes” and “23_Astrocytes” respond to injury by accumulating around the injury area. Focusing on the injury-enriched astrocytic clusters “12_Astrocytes” and “23_Astrocytes,” I could see heterogeneity both at the location of the cells as well as the genes signature, with cluster “12_Astrocytes” being the one expressing high levels of *Gfap* and “occupying” a larger area around the injury. Cluster “23_Astrocytes”, on the contrary, had low expression of several astrocytic markers, including *Gfap*, and could represent the recently described “atypical astrocytes,” which, after focal brain injury, rapidly downregulated GFAP together with other astrocytic proteins (Shandra et al., 2019). OPCs also responded to the injury, with cluster “15_OPCs” being the only one showing enrichment at the injury core. Finally, I could detect the response of peripheral infiltrating macrophages and monocytes, with clusters “13_Macrophages/Monocytes” and “18_Monocytes” contributing to the injury milieu.

With the integration of the two datasets, I could identify multiple populations overrepresented in the injury core. Interestingly, each cell type has subclusters that show variable responses to injury. The combination of the single cell and spatial transcriptomics helped us to better identify the subpopulations of glial cells, which require further investigation.

3.3 Shared inflammatory signature of reactive glial cells

Furthermore, it is essential to consider the temporal aspects of the cellular response to injury. It has been described based on immunohistochemical analysis that upon stab wound injury, microglia and OPCs rapidly respond to injury with their reactivity peak ranging from 2-3dpi, whereas astrocyte reactivity peaks at 5dpi (Frik et al., 2018; Robel et al., 2011; von Streitberg et al., 2021). Since our interest is mainly in glial cells, in addition to the 3dpi time point, I included the 5dpi to capture the early events following injury adequately, which could help us better characterize the cellular reactivity in response to injury.

To be able to unravel how each population transitioned from a resting, homeostatic to an activated, reactive state, I merged all conditions and analyzed them together. Focusing on glial cells, I identified distinct clusters in each of the investigated cell populations consisting mainly of cells from the injured samples; thus, I termed them reactive clusters. Besides that, they consisted of cells from the injury-responding clusters, as identified by the single-cell deconvolution analysis ('11_Microglia', '12_Astrocytes', '15_OPCs'). The classification was also in line with their gene expression patterns as the reactive astrocytic clusters ('AG5', 'AG6' and 'AG8') expressed high levels of *Gfap*, *Vim*, and *Lcn2* (Hasel et al., 2021; Sirko et al., 2015), reactive microglia ('MG4' and 'MG6') displayed high expression of *Aif1* and low expression of the homeostatic markers *Tmem119* and *P2ry12* (Ochocka et al., 2021) and reactive OPCs2 showed increased expression of proliferation genes (C. Simon et al., 2011).

Even though no distinct time-point-dependent clusters appeared, I could observe changes in the distribution of glial cells. Indeed, microglia showed increased reactivity at 3dpi, whereas 5dpi cells were shifting toward more homeostatic clusters. OPCs led a quick transition to reactivity at 3dpi, with very few cells residing in the reactive cluster at 5dpi. On the contrary, astrocytes reactivity peaked at 5dpi as most cells belonged in the reactive clusters, whereas, at 3dpi, I could still detect many cells in the homeostatic clusters. My observations were in line with previous literature regarding the kinetics of glial response (Frik et al., 2018; Robel et al., 2011; von Streitberg et al., 2021).

These temporal changes in the distribution of glial cells among the clusters prompted us to look at the genes characterizing each subcluster in a holistic approach. In this way, I could identify subclusters of microglia, astrocytes, and OPCs with shared enriched features, including proliferation and innate immune processes. As discussed in the introduction, proliferation is indeed one of the main processes which are activated in glial cells upon CNS insult and highly contributes to the accumulation of glial cells at the injury area and the formation of the glial border (Mira et al., 2021; Robel et al., 2011; C. Simon et al., 2011). The innate immune response is also important for the response of glial cells and their accumulation to the injury site, being crucial to recovery after TBI. However, when the immune response is dysregulated can result in excessive neuroinflammation and secondary injury (Mira et al., 2021; D. W. Simon et al., 2017).

Limiting the inflammatory response to the level needed for clearance and isolation of the damaged area and prohibiting its excessive activation could prevent secondary injury and promote regeneration.

Aiming to better understand the innate immune response induced by glial cells, I investigated further the genes of these processes. Among them, I found several IFN-I pathway genes regulated in the reactive clusters MG4, AG5, and OPCs2. Interestingly, the Interferon regulatory factor 7 (*Irf7*), a transcription factor crucial for the IFN-I activity (Ning et al., 2011), and *Cxcl10*, a well-characterized ligand of the Cxcr3 pathway (Colvin et al., 2004), got our attention. Previous studies have demonstrated that *Irf7* can induce type I IFNs through the activation of Tlr2, resulting in the transcription of several mediators, including *Cxcl10* (Dietrich et al., 2010; Perkins & Vogel, 2015). Furthermore, the Tlr2/*Irf7* signaling axis has been associated with microglia-mediated inflammation after subarachnoid hemorrhage in mice (Xu et al., 2021).

Notably, we recently demonstrated that Cxcr3 and Tlr1/2 regulate OPCs accumulation at the injury site in the zebrafish brain in a redundant and synergistic manner (Sanchez-Gonzalez et al., 2022). More specifically, we could show that activation of Tlr2 and Cxcr3 innate immunity pathways lead to increased OPC proliferation and long-lasting OPC accumulation even after the ablation of microglia and infiltrating monocytes. Thus, suggesting that OPCs can sense and react to injury-induced innate immunity signals independently from immune cells (Sanchez-Gonzalez et al., 2022).

However, both receptors are not exclusively expressed in OPCs, and the reduced proliferation of OPCs could be a consequence of Cxcr3 and Tlr2 misregulation in other populations. Therefore, I assessed their role in pure primary OPC cultures isolated from P0 mouse cerebral cortex using Moloney murine leukemia virus (MLV) based clonal analysis. OPCs are permanently labeled with GFP expressing retrovirus, and the size of clones produced by transduced progenitors within 5 days is measured in the vehicle and double inhibitor treated cultures. The treatment reduced the clone size produced by OPCs, supporting a cell-autonomous role of Tlr1/2&Cxcr3 pathways in OPC proliferation. Additionally, as CRISPR/Cas9 mediated knock out of Tlr2 and Cxcr3 in an OPC cell line (Oli-neu) (Sohl et al., 2013) reduced proliferation, this corroborates a direct role of these receptors in regulating OPC proliferation and rules out pharmacological off-target effects

(Sanchez-Gonzalez et al., 2022). Supporting the ability of OPCs to sense innate immunity signals, it recently was demonstrated that activation of Tlr1/2 via HMGB1 leads to decrease differentiation of OPCs in purified primary OPC cultures (Rouillard et al., 2022).

Taken together, these data reveal the importance of OPCs during the glial border formation, supporting the hypothesis that OPCs could directly sense injury-generated signals and regulate their proliferation rate in Tlr2- and Cxcr3-dependent manner both in the zebrafish and mouse forebrain. Our findings add to the recently investigated field of OPCs as a sensor and mediator of inflammation in CNS disorders which is mainly presented in studies of multiple sclerosis (MS) (Boccazzi et al., 2022). Indeed, it has been shown that OPCs can maintain immune homeostasis and modulate inflammatory reactions interacting with microglia (Boccazzi et al., 2022; Desu et al., 2021; Jäkel et al., 2019).

3.4 Cxcr3 and Tlr1/2 regulate distinct aspects of glial reactivity

Aiming to address the role of Cxcr3 and Tlr1/2 in response to injury in mice, I decided to systemically inhibit the two pathways after brain injury by treating the animals with a specific antagonist for the Cxcr3 (Torraca et al., 2015) (NBI-74330) and a Tlr1/2 pathway inhibitor (CU CPT 22) (Cheng et al., 2012), similarly to our zebrafish analysis (Sanchez-Gonzalez et al., 2022). I sought to address the changes in multiple populations and decided to perform scRNA-seq analysis at both 3 and 5 dpi. By integrating the data sets with our control analysis, I could address the cell type-specific changes by looking into specific subclusters. Focusing on glial cells and the shared inflammatory signature that I detected in the reactive glial clusters MG4, AG5, and OPCs2, I first addressed the expression of these genes in each glial subcluster. Interestingly, I could observe that multiple of these genes, including *Irf7*, were downregulated after inhibition of the Cxcr3 and Tlr1/2 pathways. The downregulation of the shared inflammatory genes was detected at both time points, with clusters AG7, MG3, and OPCs2 affected the most. This interesting observation indicates that the two pathways have a role in regulating glial-induced inflammation upon stab wound injury and can modulate microglia, astrocytes, and OPCs.

Additionally, by performing differential gene expression analysis within each subcluster between SW CTRL and SW INH condition at each time-point, I addressed the

changes induced in each cluster specifically. Notably, I observed an overall downregulation of innate immune processes shared between astrocytes, microglia, and OPCs at 3dpi, which were present mainly in the reactive clusters of each population. Downregulation of immune response-related genes was also detected at 5dpi, however, these processes were not shared between the different glial populations. Furthermore, the biological processes induced by the inhibitor treatment are cluster-specific, independent of the analysis timepoint. In conclusion, I demonstrated that inhibiting Cxcr3 and Tlr1/2 pathways modulate innate immunity on a temporal basis in specific glial subpopulations.

In conclusion, the scRNA-seq analysis implies that Cxcr3 and Tlr1/2 signaling pathways regulate similar processes to initially activate (3dpi) different glial cells. This activation, however, is followed by cell type-specific transcriptional changes at later stages (5dpi). Following the gene expression changes, we further looked at specific reactivity features of glial cells, where we detected changes in astrocytes and microglia reactivity (Koupourtidou, Schwarz et al., unpublished data). These findings indicate that Tlr1/2 and Cxcr3 pathways control specific aspects of glial reactivity and that perturbing these pathways does not entirely restore glial cell homeostasis. However, further research is necessary to determine the role of each pathway for each population.

3.5 Summary and conclusions

In summary, the data generated in my thesis represent a comprehensive tool for analyzing early events following traumatic brain injury with respect to changes in time, space, and cell type. The advantage of single transcriptomic analysis gave us the power to study multiple populations at a specific time of the disease progression. This way, we were able to identify multiple cell states of each glial population and identify rare cell states that otherwise, e.g., with bulk analysis, would be hard to identify. This way, I observed specific glial subclusters with a shared innate immunity signature. Understanding the role and function of these processes could help us distinguish between the detrimental and beneficial aspects of glial reactivity and neuroinflammation.

My data also contribute to the characterization of OPCs as part of the cellular response to CNS insult, their contribution to the glial border formation, and

neuroinflammation. Besides their increased proliferation in response to injury, we can now provide the gene expression profile of the reactive OPCs. Even though there is no specific marker expressed exclusively by reactive OPCs, there were several genes that show higher expression in reactive compared to homeostatic OPCs. Among them, there were also genes related to innate immune response supporting the contribution of OPCs in controlling and modulating neuroinflammation in CNS disorders (Boccazzi et al., 2022; Desu et al., 2021; Jäkel et al., 2019). Additionally, I could show in vitro that innate immune responses via Tlr1/2 and Cxcr3 can modulate the proliferation capacity of OPCs (Sanchez-Gonzalez et al., 2022). These two observations indicate a cross-regulation of the two features that OPCs acquire in response to injury.

Additionally, I mediated a trans-species approach comparing our findings from zebrafish and mice in response to injury. Our knowledge from zebrafish, where we identified Tlr1/2 and Cxcr3 as important mediators of OPCs proliferation and accumulation at the injury site, in combination with the shared inflammatory signature detected in subclusters of glial cells prompted us to investigate the role of the two pathways upon injury in the murine cerebral cortex. Overall, we could detect downregulation of innate immune response upon inhibition of Tlr1/2 and Cxcr3 however, this was only modulating some aspects of reactive astrocytes and microglia and did not entirely restore them to homeostasis.

This observation contrasted with our zebrafish data, where we could see that glial cells had a faster transition to homeostasis when Tlr1/2 and Cxcr3 were inhibited (Sanchez-Gonzalez et al., 2022). This could be due to differences in the injury environment with additional cell types and pathways involved in the accumulation of glial cells in the injury core in mice and could be one of the possible differences between regeneration competent and regeneration incompetent species.

A better comparison of the cellular response to injury between zebrafish and mice may help us understand the difference between the two species and allow us to extract the pro-regenerative mechanism of zebrafish CNS. In this line, it could be useful the integrations of the scRNA-seq data sets after injury in the two species (Zambusi et al., 2022, Koupourtidou, Schwarz et al., unpublished data). A better understanding of the

injury pathophysiology and the identification of beneficial and detrimental pathways may open more opportunities for developing new therapeutic strategies.

4 Bibliography

- Abbott, N. J., Patabendige, A. A. K., Dolman, D. E. M., Yusof, S. R., & Begley, D. J. (2010). Structure and function of the blood-brain barrier. In *Neurobiology of Disease* (Vol. 37, Issue 1, pp. 13–25). <https://doi.org/10.1016/j.nbd.2009.07.030>
- Akira, S., Uematsu, S., & Takeuchi, O. (2006). Pathogen recognition and innate immunity. In *Cell* (Vol. 124, Issue 4, pp. 783–801). <https://doi.org/10.1016/j.cell.2006.02.015>
- Alam, A., Thelin, E. P., Tajsic, T., Khan, D. Z., Khellaf, A., Patani, R., & Helmy, A. (2020). Cellular infiltration in traumatic brain injury. *Journal of Neuroinflammation*, *17*(1), 328. <https://doi.org/10.1186/s12974-020-02005-x>
- Allen, N. J., & Lyons, D. A. (2018). Glia as architects of central nervous system formation and function. *Science*, *362*(6411), 181–185. <https://doi.org/10.1126/science.aat0473>
- Anderson, M. A., Burda, J. E., Ren, Y., Ao, Y., O’Shea, T. M., Kawaguchi, R., Coppola, G., Khakh, B. S., Deming, T. J., & Sofroniew, M. v. (2016). Astrocyte scar formation aids central nervous system axon regeneration. *Nature*, *532*(7598), 195–200. <https://doi.org/10.1038/nature17623>
- Barbosa, J. S. S., Sanchez-Gonzalez, R., di Giaimo, R., Baumgart, E. V. v, Theis, F. J. J., Gotz, M., & Ninkovic, J. (2015). Live imaging of adult neural stem cell behavior in the intact and injured zebrafish brain. *Science*, *348*(6236), 789–793. <https://doi.org/10.1126/science.aaa2729>
- Bardehle, S., Krüger, M., Buggenthin, F., Schwausch, J., Ninkovic, J., Clevers, H., Snippert, H. J., Theis, F. J., Meyer-Luehmann, M., Bechmann, I., Dimou, L., & Götz, M. (2013). Live imaging of astrocyte responses to acute injury reveals selective juxtavascular proliferation. *Nature Neuroscience*, *16*(5), 580–586. <https://doi.org/10.1038/nn.3371>
- Batiuk, M. Y., de Vin, F., Duqué, S. I., Li, C., Saito, T., Saido, T., Fiers, M., Belgard, T. G., & Holt, M. G. (2017). An immunoaffinity-based method for isolating ultrapure adult astrocytes based on ATP1B2 targeting by the ACSA-2 antibody. *Journal of Biological Chemistry*, *292*(21), 8874–8891. <https://doi.org/10.1074/jbc.M116.765313>
- Batiuk, M. Y., Martirosyan, A., Wahis, J., de Vin, F., Marneffe, C., Kusserow, C., Koeppen, J., Viana, J. F., Oliveira, J. F., Voet, T., Ponting, C. P., Belgard, T. G., & Holt, M. G. (2020). Astrocyte Reactivity: Subtypes, States, and Functions in CNS Innate Immunity. *Trends in Immunology*, *41*(9), 758–770. <https://doi.org/10.1016/j.it.2020.07.004>
- Baumgart, E. V., Barbosa, J. S., Bally-cuif, L., Götz, M., & Ninkovic, J. (2012). Stab wound injury of the zebrafish telencephalon: A model for comparative analysis of reactive gliosis. *Glia*, *60*(3), 343–357. <https://doi.org/10.1002/glia.22269>
- Becker, C. G., & Becker, T. (2008). Adult zebrafish as a model for successful central nervous system regeneration. *Restor Neurol Neurosci*, *26*(2–3), 71–80. http://www.ncbi.nlm.nih.gov/entrez/query.fcgi?cmd=Retrieve&db=PubMed&dopt=Citation&list_uids=18820403

- Bergles, D. E., Roberts, J. D. B., Somogyi, P., & Jahr, C. E. (2000). Glutamatergic synapses on oligodendrocyte precursor cells in the hippocampus. *Nature*, *405*(6783), 187–191. <https://doi.org/10.1038/35012083>
- Biancalani, T., Scalia, G., Buffoni, L., Avasthi, R., Lu, Z., Sanger, A., Tokcan, N., Vanderburg, C. R., Segerstolpe, Å., Zhang, M., Avraham-Davidi, I., Vickovic, S., Nitzan, M., Ma, S., Subramanian, A., Lipinski, M., Buenrostro, J., Brown, N. B., Fanelli, D., ... Regev, A. (2021). Deep learning and alignment of spatially resolved single-cell transcriptomes with Tangram. *Nature Methods*, *18*(11), 1352–1362. <https://doi.org/10.1038/s41592-021-01264-7>
- Biber, K., Dijkstra, I., Trebst, C., de Groot, C. J. A., Ransohoff, R. M., & Boddeke, H. W. G. M. (2002). Functional expression of CXCR3 in cultured mouse and human astrocytes and microglia. *Neuroscience*, *112*(3), 487–497. [https://doi.org/10.1016/S0306-4522\(02\)00114-8](https://doi.org/10.1016/S0306-4522(02)00114-8)
- Blennow, K., Brody, D. L., Kochanek, P. M., Levin, H., McKee, A., Ribbers, G. M., Yaffe, K., & Zetterberg, H. (2016). Traumatic brain injuries. *Nature Reviews Disease Primers*, *2*, 1–19. <https://doi.org/10.1038/nrdp.2016.84>
- Bocazzi, M., Raffaele, S., & Fumagalli, M. (2022). Not only myelination: the immune-inflammatory functions of oligodendrocytes. *Neural Regeneration Research*, *17*(12), 2661–2663. <https://doi.org/10.4103/1673-5374.342678>
- Brenner, M. (2014). Role of GFAP in CNS injuries. *Neuroscience Letters*, *565*, 7–13. <https://doi.org/10.1016/j.neulet.2014.01.055>
- Bsibsi, M., Ravid, R., & van Noort, J. M. (2002a). Broad Expression of Toll-Like Receptors in the Human Central Nervous System. In *Journal of Neuropathology and Experimental Neurology* (Vol. 61, Issue 11). <https://academic.oup.com/jnen/article/61/11/1013/2916258>
- Bsibsi, M., Ravid, R., & van Noort, J. M. (2002b). Broad Expression of Toll-Like Receptors in the Human Central Nervous System. In *Journal of Neuropathology and Experimental Neurology* (Vol. 61, Issue 11). <https://academic.oup.com/jnen/article/61/11/1013/2916258>
- Buffo, A., Rite, I., Tripathi, P., Lepier, A., Colak, D., Horn, A.-P., Mori, T., & Götz, M. (2008). Origin and progeny of reactive gliosis: A source of multipotent cells in the injured brain. *Proceedings of the National Academy of Sciences*, *105*(9), 3581–3586. <https://doi.org/10.1073/pnas.0709002105>
- Buffo, A., Vosko, M. R., Erturk, D., Hamann, G. F., Jucker, M., Rowitch, D., & Gotz, M. (2005). Expression pattern of the transcription factor Olig2 in response to brain injuries: implications for neuronal repair. *Proc Natl Acad Sci U S A*, *102*(50), 18183–18188. <https://doi.org/10.1073/pnas.0506535102>
- Cardona-Alberich, A., Tourbez, M., Pearce, S. F., & Sibley, C. R. (2021). Elucidating the cellular dynamics of the brain with single-cell RNA sequencing. In *RNA Biology* (Vol. 18, Issue 7, pp. 1063–1084). Bellwether Publishing, Ltd. <https://doi.org/10.1080/15476286.2020.1870362>
- Cartier, L., Hartley, O., Dubois-Dauphin, M., & Krause, K. H. (2005). Chemokine receptors in the central nervous system: Role in brain inflammation and neurodegenerative

- diseases. In *Brain Research Reviews* (Vol. 48, Issue 1, pp. 16–42). Elsevier. <https://doi.org/10.1016/j.brainresrev.2004.07.021>
- Chapouton, P., Jagasia, R., & Bally-Cuif, L. (2007). Adult neurogenesis in non-mammalian vertebrates. *Bioessays*, 29(8), 745–757. <https://doi.org/10.1002/bies.20615>
- Cheng, K., Wang, X., Zhang, S., & Yin, H. (2012). Discovery of Small-Molecule Inhibitors of the TLR1/TLR2 Complex. *Angewandte Chemie International Edition*, 51(49), 12246–12249. <https://doi.org/10.1002/anie.201204910>
- Colvin, R. A., Campanella, G. S. V., Sun, J., & Luster, A. D. (2004). Intracellular domains of CXCR3 that mediate CXCL9, CXCL10, and CXCL11 function. *Journal of Biological Chemistry*, 279(29), 30219–30227. <https://doi.org/10.1074/jbc.M403595200>
- Davalos, D., Grutzendler, J., Yang, G., Kim, J. v., Zuo, Y., Jung, S., Littman, D. R., Dustin, M. L., & Gan, W. B. (2005). ATP mediates rapid microglial response to local brain injury in vivo. *Nature Neuroscience*, 8(6), 752–758. <https://doi.org/10.1038/nn1472>
- Deczkowska, A., Keren-Shaul, H., Weiner, A., Colonna, M., Schwartz, M., & Amit, I. (2018). Disease-Associated Microglia: A Universal Immune Sensor of Neurodegeneration. *Cell*, 173(5), 1073–1081. <https://doi.org/10.1016/j.cell.2018.05.003>
- Desu, H. L., Illiano, P., Choi, J. S., Ascona, M. C., Gao, H., Lee, J. K., & Brambilla, R. (2021). TNFR2 signaling regulates the immunomodulatory function of oligodendrocyte precursor cells. *Cells*, 10(7). <https://doi.org/10.3390/cells10071785>
- Dewan, M. C., Rattani, A., Gupta, S., Baticulon, R. E., Hung, Y.-C., Punchak, M., Agrawal, A., Adeleye, A. O., Shrimel, M. G., Rubiano, A. M., Rosenfeld, J. v., & Park, K. B. (2019). Estimating the global incidence of traumatic brain injury. *Journal of Neurosurgery JNS*, 130(4), 1080–1097. <https://doi.org/10.3171/2017.10.JNS17352>
- di Giaimo, R., Durovic, T., Barquin, P., Kociaj, A., Lepko, T., Aschenbroich, S., Breunig, C. T., Irmeler, M., Cernilogar, F. M., Schotta, G., Barbosa, J. S., Trümbach, D., Baumgart, E. V., Neuner, A. M., Beckers, J., Wurst, W., Stricker, S. H., & Ninkovic, J. (2018). The Aryl Hydrocarbon Receptor Pathway Defines the Time Frame for Restorative Neurogenesis. *Cell Reports*, 25(12), 3241–3251.e5. <https://doi.org/10.1016/j.celrep.2018.11.055>
- Diaz-Aparicio, I., Paris, I., Sierra-Torre, V., Plaza-Zabala, A., Rodríguez-Iglesias, N., Márquez-Roper, M., Beccari, S., Huguet, P., Abiega, O., Alberdi, E., Matute, C., Bernales, I., Schulz, A., Otrókocsi, L., Sperlagh, B., Happonen, K. E., Lemke, G., Maletic-Savatic, M., Valero, J., & Sierra, A. (2020). Microglia actively remodel adult hippocampal neurogenesis through the phagocytosis secretome. *Journal of Neuroscience*, 40(7), 1453–1482. <https://doi.org/10.1523/JNEUROSCI.0993-19.2019>
- Dietrich, N., Lienenklaus, S., Weiss, S., & Gekara, N. O. (2010). Murine Toll-Like Receptor 2 Activation Induces Type I Interferon Responses from Endolysosomal Compartments. *PLoS ONE*. <https://doi.org/10.1371/journal.pone.0010250>
- Dimou, L., & Götz, M. (2014). Glial Cells as Progenitors and Stem Cells: New Roles in the Healthy and Diseased Brain. *Physiological Reviews*, 94(3), 709–737. <https://doi.org/10.1152/physrev.00036.2013>

- Dimou, L., Simon, C., Kirchhoff, F., Takebayashi, H., & Gotz, M. (2008). Progeny of Olig2-expressing progenitors in the gray and white matter of the adult mouse cerebral cortex. *J Neurosci*, *28*(41), 10434–10442. <https://doi.org/28/41/10434> [pii] 10.1523/JNEUROSCI.2831-08.2008
- Diotel, N., Lübke, L., Strähle, U., & Rastegar, S. (2020). Common and Distinct Features of Adult Neurogenesis and Regeneration in the Telencephalon of Zebrafish and Mammals. In *Frontiers in Neuroscience* (Vol. 14). Frontiers Media S.A. <https://doi.org/10.3389/fnins.2020.568930>
- Donat, C. K., Scott, G., Gentleman, S. M., & Sastre, M. (2017). Microglial Activation in Traumatic Brain Injury. *Frontiers in Aging Neuroscience*, *9*(JUN). <https://doi.org/10.3389/fnagi.2017.00208>
- El-Zayat, S. R., Sibaii, H., & Mannaa, F. A. (2019). Toll-like receptors activation, signaling, and targeting: an overview. *Bulletin of the National Research Centre*, *43*(1). <https://doi.org/10.1186/s42269-019-0227-2>
- Endo, F., Kasai, A., Soto, J. S., Yu, X., Qu, Z., Hashimoto, H., Gradinaru, V., Kawaguchi, R., & Khakh, B. S. (2022). Molecular basis of astrocyte diversity and morphology across the CNS in health and disease. *Science*, *378*(6619). <https://doi.org/10.1126/science.adc9020>
- Escartin, C., Galea, E., Lakatos, A., O’Callaghan, J. P., Petzold, G. C., Serrano-Pozo, A., Steinhäuser, C., Volterra, A., Carmignoto, G., Agarwal, A., Allen, N. J., Araque, A., Barbeito, L., Barzilai, A., Bergles, D. E., Bonvento, G., Butt, A. M., Chen, W. T., Cohen-Salmon, M., ... Verkhratsky, A. (2021). Reactive astrocyte nomenclature, definitions, and future directions. *Nature Neuroscience*, *24*(3), 312–325. <https://doi.org/10.1038/s41593-020-00783-4>
- Eugenín-von Bernhardt, J., & Dimou, L. (2016). NG2-glia, More Than Progenitor Cells. In *Advances in Experimental Medicine and Biology* (pp. 27–45). https://doi.org/10.1007/978-3-319-40764-7_2
- Färber, K., Cheung, G., Mitchell, D., Wallis, R., Weibe, E., Schwaeble, W., & Kettenmann, H. (2009). C1q, the recognition subcomponent of the classical pathway of complement, drives microglial activation. *Journal of Neuroscience Research*, *87*(3), 644–652. <https://doi.org/10.1002/jnr.21875>
- Finnie, J. W., & Blumbergs, P. C. (2002). ANIMAL MODELS Traumatic Brain Injury. In *Vet Pathol* (Vol. 39).
- Fitch, M. T., & Silver, J. (2008). CNS injury, glial scars, and inflammation: Inhibitory extracellular matrices and regeneration failure. *Exp Neurol*, *209*(2), 294–301. <https://doi.org/10.1016/j.expneurol.2007.05.014>
- Frik, J., Merl-Pham, J., Plesnila, N., Mattugini, N., Kjell, J., Kraska, J., Gómez, R. M., Hauck, S. M., Sirko, S., & Götz, M. (2018). Cross-talk between monocyte invasion and astrocyte proliferation regulates scarring in brain injury. *EMBO Reports*, *19*(5). <https://doi.org/10.15252/embr.201745294>
- Gadea, A., Schinelli, S., & Gallo, V. (2008). Endothelin-1 Regulates Astrocyte Proliferation and Reactive Gliosis via a JNK/c-Jun Signaling Pathway. *Journal of Neuroscience*, *28*(10), 2394–2408. <https://doi.org/10.1523/JNEUROSCI.5652-07.2008>

- Galichet, C., Clayton, R. W., & Lovell-Badge, R. (2021). Novel Tools and Investigative Approaches for the Study of Oligodendrocyte Precursor Cells (NG2-Glia) in CNS Development and Disease. In *Frontiers in Cellular Neuroscience* (Vol. 15). Frontiers Media S.A. <https://doi.org/10.3389/fncel.2021.673132>
- George, N., & Geller, H. M. (2018). Extracellular matrix and traumatic brain injury. In *Journal of Neuroscience Research* (Vol. 96, Issue 4, pp. 573–588). John Wiley and Sons Inc. <https://doi.org/10.1002/jnr.24151>
- Ginhoux, F., Greter, M., Leboeuf, M., Nandi, S., See, P., Gokhan, S., Mehler, M. F., Conway, S. J., Ng, L. G., Stanley, E. R., Samokhvalov, I. M., & Merad, M. (2010). Fate Mapping Analysis Reveals That Adult Microglia Derive from Primitive Macrophages. *Science*, *330*(6005), 841–845. <https://doi.org/10.1126/science.1194637>
- Gong, T., Liu, L., Jiang, W., & Zhou, R. (2020). DAMP-sensing receptors in sterile inflammation and inflammatory diseases. In *Nature Reviews Immunology* (Vol. 20, Issue 2, pp. 95–112). Nature Research. <https://doi.org/10.1038/s41577-019-0215-7>
- Gyoneva, S., & Ransohoff, R. M. (2015). Inflammatory reaction after traumatic brain injury: therapeutic potential of targeting cell–cell communication by chemokines. *Trends in Pharmacological Sciences*, *36*(7), 471–480. <https://doi.org/10.1016/j.tips.2015.04.003>
- Hammad, A., Westacott, L., & Zaben, M. (2018). The role of the complement system in traumatic brain injury: A review. In *Journal of Neuroinflammation* (Vol. 15, Issue 1). BioMed Central Ltd. <https://doi.org/10.1186/s12974-018-1066-z>
- Hammond, T. R., Dufort, C., Dissing-Olesen, L., Giera, S., Young, A., Wysoker, A., Walker, A. J., Gergits, F., Segel, M., Nemesh, J., Marsh, S. E., Saunders, A., Macosko, E., Ginhoux, F., Chen, J., Franklin, R. J. M., Piao, X., McCarroll, S. A., & Stevens, B. (2019). Single-Cell RNA Sequencing of Microglia throughout the Mouse Lifespan and in the Injured Brain Reveals Complex Cell-State Changes. *Immunity*, *50*(1), 253-271.e6. <https://doi.org/10.1016/J.IMMUNI.2018.11.004/ATTACHMENT/2B359AF0-8A8C-47BC-8540-0C02E6E771D3/MMC4.XLSX>
- Hanke, M. L., & Kielian, T. (2011). Toll-like receptors in health and disease in the brain: mechanisms and therapeutic potential. In *Clinical Science* (Vol. 121, Issue 9, pp. 367–387). <https://doi.org/10.1042/CS20110164>
- Hasel, P., Rose, I. V. L., Sadick, J. S., Kim, R. D., & Liddelow, S. A. (2021). Neuroinflammatory astrocyte subtypes in the mouse brain. *Nature Neuroscience*, *24*(10), 1475–1487. <https://doi.org/10.1038/s41593-021-00905-6>
- Heidari, A., Yazdanpanah, N., & Rezaei, N. (2022). The role of Toll-like receptors and neuroinflammation in Parkinson’s disease. In *Journal of Neuroinflammation* (Vol. 19, Issue 1). BioMed Central Ltd. <https://doi.org/10.1186/s12974-022-02496-w>
- Ho, M. S., Verkhatsky, A., Duan, S., & Parpura, V. (2019). Editorial: Glia in health and disease. In *Frontiers in Molecular Neuroscience* (Vol. 12). Frontiers Media S.A. <https://doi.org/10.3389/fnmol.2019.00063>
- Hughes, E. G., Kang, S. H., Fukaya, M., & Bergles, D. E. (2013). Oligodendrocyte progenitors balance growth with self-repulsion to achieve homeostasis in the adult brain. *Nature Neuroscience*, *16*(6), 668–676. <https://doi.org/10.1038/nn.3390>

- Hwang, B., Lee, J. H., & Bang, D. (2018). Single-cell RNA sequencing technologies and bioinformatics pipelines. In *Experimental and Molecular Medicine* (Vol. 50, Issue 8). Nature Publishing Group. <https://doi.org/10.1038/s12276-018-0071-8>
- Jäkel, S., Agirre, E., Mendanha Falcão, A., van Bruggen, D., Lee, K. W., Knuesel, I., Malhotra, D., French-Constant, C., Williams, A., & Castelo-Branco, G. (2019). Altered human oligodendrocyte heterogeneity in multiple sclerosis. *Nature*, *566*(7745), 543–547. <https://doi.org/10.1038/s41586-019-0903-2>
- Jakel, S., & Dimou, L. (2017). Glial Cells and Their Function in the Adult Brain: A Journey through the History of Their Ablation. *Front Cell Neurosci*, *11*, 24. <https://doi.org/10.3389/fncel.2017.00024>
- Jiang, H., Wang, Y., Liang, X., Xing, X., Xu, X., & Zhou, C. (2018). Toll-Like Receptor 4 Knockdown Attenuates Brain Damage and Neuroinflammation After Traumatic Brain Injury via Inhibiting Neuronal Autophagy and Astrocyte Activation. *Cellular and Molecular Neurobiology*, *38*(5), 1009–1019. <https://doi.org/10.1007/s10571-017-0570-5>
- Jurga, A. M., Paleczna, M., & Kuter, K. Z. (2020). Overview of General and Discriminating Markers of Differential Microglia Phenotypes. *Frontiers in Cellular Neuroscience*, *14*(August), 1–18. <https://doi.org/10.3389/fncel.2020.00198>
- Kang, K., Lee, S.-W., Han, J. E., Choi, J. W., & Song, M.-R. (2014). The complex morphology of reactive astrocytes controlled by fibroblast growth factor signaling. *Glia*, *62*(8), 1328–1344. <https://doi.org/10.1002/glia.22684>
- Karin, N. (2020). CXCR3 Ligands in Cancer and Autoimmunity, Chemoattraction of Effector T Cells, and Beyond. In *Frontiers in Immunology* (Vol. 11). Frontiers Media S.A. <https://doi.org/10.3389/fimmu.2020.00976>
- Karve, I. P., Taylor, J. M., & Crack, P. J. (2016). The contribution of astrocytes and microglia to traumatic brain injury. *British Journal of Pharmacology*, *173*(4), 692–702. <https://doi.org/10.1111/bph.13125>
- Kaslin, J., Ganz, J., & Brand, M. (2008). Proliferation, neurogenesis and regeneration in the non-mammalian vertebrate brain. *Philos Trans R Soc Lond B Biol Sci*, *363*(1489), 101–122. <https://doi.org/CL63TV282MH44466> [pii] 10.1098/rstb.2006.2015
- Kawasaki, T., & Kawai, T. (2014). Toll-like receptor signaling pathways. In *Frontiers in Immunology* (Vol. 5, Issue SEP). Frontiers Media S.A. <https://doi.org/10.3389/fimmu.2014.00461>
- Keaney, J., & Campbell, M. (2015). The dynamic blood–brain barrier. *The FEBS Journal*, *282*(21), 4067–4079. <https://doi.org/https://doi.org/10.1111/febs.13412>
- Keren-Shaul, H., Spinrad, A., Weiner, A., Matcovitch-Natan, O., Dvir-Szternfeld, R., Ulland, T. K., David, E., Baruch, K., Lara-Astaiso, D., Toth, B., Itzkovitz, S., Colonna, M., Schwartz, M., & Amit, I. (2017). A Unique Microglia Type Associated with Restricting Development of Alzheimer’s Disease. *Cell*, *169*(7), 1276–1290.e17. <https://doi.org/10.1016/j.cell.2017.05.018>

- Kettenmann, H., Hanisch, U.-K., Noda, M., & Verkhratsky, A. (2011). Physiology of Microglia. *Physiological Reviews*, *91*(2), 461–553. <https://doi.org/10.1152/physrev.00011.2010>
- Kettenmann, H., & Verkhratsky, A. (2022). Glial Cells: Neuroglia. In *Neuroscience in the 21st Century* (pp. 825–860). Springer International Publishing. https://doi.org/10.1007/978-3-030-88832-9_19
- Kiefer, F., & Siekmann, A. F. (2011). The role of chemokines and their receptors in angiogenesis. In *Cellular and Molecular Life Sciences* (Vol. 68, Issue 17, pp. 2811–2830). <https://doi.org/10.1007/s00018-011-0677-7>
- Kielian, T., Mayes, P., & Kielian, M. (2002). Characterization of microglial responses to *Staphylococcus aureus*: effects on cytokine, costimulatory molecule, and Toll-like receptor expression. *Journal of Neuroimmunology*, *130*(1–2), 86–99. [https://doi.org/10.1016/S0165-5728\(02\)00216-3](https://doi.org/10.1016/S0165-5728(02)00216-3)
- Kishimoto, N., Shimizu, K., & Sawamoto, K. (2012). Neuronal regeneration in a zebrafish model of adult brain injury. *Disease Models & Mechanisms*, *5*(2), 200–209. <https://doi.org/10.1242/dmm.007336>
- Konat, G. W., Kielian, T., & Marriott, I. (2006). The role of Toll-like receptors in CNS response to microbial challenge. In *Journal of Neurochemistry* (Vol. 99, Issue 1, pp. 1–12). <https://doi.org/10.1111/j.1471-4159.2006.04076.x>
- Kreisel, T., Wolf, B., Keshet, E., & Licht, T. (2019). Unique role for dentate gyrus microglia in neuroblast survival and in VEGF-induced activation. *Glia*, *67*(4), 594–618. <https://doi.org/https://doi.org/10.1002/glia.23505>
- Kuo, P. T., Zeng, Z., Salim, N., Mattarollo, S., Wells, J. W., & Leggatt, G. R. (2018). The role of CXCR3 and its chemokine ligands in skin disease and cancer. In *Frontiers in Medicine* (Vol. 5, Issue SEP). Frontiers Media S.A. <https://doi.org/10.3389/fmed.2018.00271>
- Kyritsis, N., Kizil, C., Zocher, S., Kroehne, V., Kaslin, J., Freudenreich, D., Iltzsche, A., & Brand, M. (2012). Acute Inflammation Initiates the Regenerative Response in the Adult Zebrafish Brain. *Science*, *338*(6112), 1353–1356. <https://doi.org/10.1126/science.1228773>
- Laird, M. D., Shields, J. S., Sukumari-Ramesh, S., Kimbler, D. E., Fessler, R. D., Shakir, B., Youssef, P., Yanasak, N., Vender, J. R., & Dhandapani, K. M. (2014). High mobility group box protein-1 promotes cerebral edema after traumatic brain injury via activation of toll-like receptor 4. *Glia*, *62*(1), 26–38. <https://doi.org/https://doi.org/10.1002/glia.22581>
- Li, B., Zhang, W., Guo, C., Xu, H., Li, L., Fang, M., Hu, Y., Zhang, X., Yao, X., Tang, M., Liu, K., Zhao, X., Lin, J., Cheng, L., Chen, F., Xue, T., & Qu, K. (2022). Benchmarking spatial and single-cell transcriptomics integration methods for transcript distribution prediction and cell type deconvolution. *Nature Methods*, *19*(6), 662–670. <https://doi.org/10.1038/s41592-022-01480-9>
- Li, Y. H., Zhang, C. L., Zhang, X. Y., Zhou, H. X., & Meng, L. L. (2015). Effects of mild induced hypothermia on hippocampal connexin 43 and glutamate transporter 1 expression

- following traumatic brain injury in rats. *Molecular Medicine Reports*, 11(3), 1991–1996. <https://doi.org/10.3892/mmr.2014.2928>
- Li, Y., He, X., Kawaguchi, R., Zhang, Y., Wang, Q., Monavarfeshani, A., Yang, Z., Chen, B., Shi, Z., Meng, H., Zhou, S., Zhu, J., Jacobi, A., Swarup, V., Popovich, P. G., Geschwind, D. H., & He, Z. (2020). Microglia-organized scar-free spinal cord repair in neonatal mice. *Nature*. <https://doi.org/10.1038/s41586-020-2795-6>
- Liddel, S. A., Guttenplan, K. A., Clarke, L. E., Bennett, F. C., Bohlen, C. J., Schirmer, L., Bennett, M. L., Münch, A. E., Chung, W.-S., Peterson, T. C., Wilton, D. K., Frouin, A., Napier, B. A., Panicker, N., Kumar, M., Buckwalter, M. S., Rowitch, D. H., Dawson, V. L., Dawson, T. M., ... Barres, B. A. (2017). Neurotoxic reactive astrocytes are induced by activated microglia. *Nature*, 541(7638), 481–487. <https://doi.org/10.1038/nature21029>
- Long, X., Yao, X., Jiang, Q., Yang, Y., He, X., Tian, W., Zhao, K., & Zhang, H. (2020). Astrocyte-derived exosomes enriched with miR-873a-5p inhibit neuroinflammation via microglia phenotype modulation after traumatic brain injury. *Journal of Neuroinflammation*, 17(1), 89. <https://doi.org/10.1186/s12974-020-01761-0>
- Louveau, A., Harris, T. H., & Kipnis, J. (2015). Revisiting the Mechanisms of CNS Immune Privilege. In *Trends in Immunology* (Vol. 36, Issue 10, pp. 569–577). Elsevier Ltd. <https://doi.org/10.1016/j.it.2015.08.006>
- Maas, A. I., Stocchetti, N., & Bullock, R. (2008). Moderate and severe traumatic brain injury in adults. *The Lancet Neurology*, 7(8), 728–741. [https://doi.org/10.1016/S1474-4422\(08\)70164-9](https://doi.org/10.1016/S1474-4422(08)70164-9)
- Majdan, M., Plancikova, D., Maas, A., Polinder, S., Feigin, V., Theadom, A., Rusnak, M., Brazinova, A., & Haagsma, J. (2017). Years of life lost due to traumatic brain injury in Europe: A cross-sectional analysis of 16 countries. *PLOS Medicine*, 14(7), e1002331. <https://doi.org/10.1371/journal.pmed.1002331>
- Marz, M., Schmidt, R., Rastegar, S., & Strahle, U. (2011). Regenerative response following stab injury in the adult zebrafish telencephalon. *Dev Dyn*, 240(9), 2221–2231. <https://doi.org/10.1002/dvdy.22710>
- Masuda, T., Sankowski, R., Staszewski, O., Böttcher, C., Amann, L., Sagar, Scheiwe, C., Nessler, S., Kunz, P., van Loo, G., Coenen, V. A., Reinacher, P. C., Michel, A., Sure, U., Gold, R., Grün, D., Priller, J., Stadelmann, C., & Prinz, M. (2019). Spatial and temporal heterogeneity of mouse and human microglia at single-cell resolution. *Nature*, 566(7744), 388–392. <https://doi.org/10.1038/s41586-019-0924-x>
- Masuda, T., Sankowski, R., Staszewski, O., & Prinz, M. (2020). Microglia Heterogeneity in the Single-Cell Era. *Cell Reports*, 30(5), 1271–1281. <https://doi.org/10.1016/j.celrep.2020.01.010>
- McKee, C. A., & Lukens, J. R. (2016). Emerging roles for the immune system in traumatic brain injury. In *Frontiers in Immunology* (Vol. 7, Issue DEC). Frontiers Media S.A. <https://doi.org/10.3389/fimmu.2016.00556>
- Mira, R. G., Lira, M., & Cerpa, W. (2021). Traumatic Brain Injury: Mechanisms of Glial Response. In *Frontiers in Physiology* (Vol. 12). <https://www.frontiersin.org/article/10.3389/fphys.2021.740939>

- Mishra, B. B., Mishra, P. K., & Teale, J. M. (2006). Expression and distribution of Toll-like receptors in the brain during murine neurocysticercosis. *Journal of Neuroimmunology*, 181(1–2), 46–56. <https://doi.org/10.1016/j.jneuroim.2006.07.019>
- Müller, M., Carter, S., Hofer, M. J., & Campbell, I. L. (2010). Review: The chemokine receptor CXCR3 and its ligands CXCL9, CXCL10 and CXCL11 in neuroimmunity – a tale of conflict and conundrum. *Neuropathology and Applied Neurobiology*, 36(5), 368–387. <https://doi.org/https://doi.org/10.1111/j.1365-2990.2010.01089.x>
- Murphy, P. M. (2002). International Union of Pharmacology. XXX. Update on Chemokine Receptor Nomenclature. *Pharmacological Reviews*, 54(2), 227–229. <https://doi.org/10.1124/pr.54.2.227>
- Ning, S., Pagano, J. S., & Barber, G. N. (2011). IRF7: activation, regulation, modification and function. *Genes and Immunity*, 12(6), 399–414. <https://doi.org/10.1038/GENE.2011.21>
- Nishiyama, A., Komitova, M., Suzuki, R., & Zhu, X. (2009). Polydendrocytes (NG2 cells): multifunctional cells with lineage plasticity. *Nat Rev Neurosci*, 10(1), 9–22. <https://doi.org/nrn2495> [pii] 10.1038/nrn2495
- Nomiyama, H., Osada, N., & Yoshie, O. (2011). A family tree of vertebrate chemokine receptors for a unified nomenclature. In *Developmental and Comparative Immunology* (Vol. 35, Issue 7, pp. 705–715). <https://doi.org/10.1016/j.dci.2011.01.019>
- Ochocka, N., Segit, P., Walentynowicz, K. A., Wojnicki, K., Cyranowski, S., Swatler, J., Mieczkowski, J., & Kaminska, B. (2021). Single-cell RNA sequencing reveals functional heterogeneity of glioma-associated brain macrophages. *Nature Communications*, 12(1), 1151. <https://doi.org/10.1038/s41467-021-21407-w>
- Ohlig, S., Clavreul, S., Thorwirth, M., Simon-Ebert, T., Bocchi, R., Ulbricht, S., Kannayian, N., Rossner, M., Sirko, S., Smialowski, P., Fischer-Sternjak, J., & Götz, M. (2021). Molecular diversity of diencephalic astrocytes reveals adult astrogenesis regulated by Smad4. *The EMBO Journal*, 40(21). <https://doi.org/10.15252/embj.2020107532>
- Oliveira-Nascimento, L., Massari, P., & Wetzler, L. M. (2012). The role of TLR2 in infection and immunity. In *Frontiers in Immunology* (Vol. 3, Issue APR). <https://doi.org/10.3389/fimmu.2012.00079>
- Oosenbrug, T., van de Graaff, M. J., Haks, M. C., van Kasteren, S., & Rensing, M. E. (2020). An alternative model for type I interferon induction downstream of human TLR2. *Journal of Biological Chemistry*, 295(42), 14325–14342. <https://doi.org/10.1074/jbc.RA120.015283>
- Ozerdem, U., Grako, K. A., Dahlin-Huppe, K., Monosov, E., & Stallcup, W. B. (2001). NG2 proteoglycan is expressed exclusively by mural cells during vascular morphogenesis. *Developmental Dynamics*, 222(2), 218–227. <https://doi.org/https://doi.org/10.1002/dvdy.1200>
- Pekny, M., Wilhelmsson, U., & Pekna, M. (2014). The dual role of astrocyte activation and reactive gliosis. *Neuroscience Letters*, 565, 30–38. <https://doi.org/10.1016/j.neulet.2013.12.071>

- Pérez-Rodríguez, D. R., Blanco-Luquin, I., & Mendioroz, M. (2021). The participation of microglia in neurogenesis: A review. In *Brain Sciences* (Vol. 11, Issue 5). MDPI AG. <https://doi.org/10.3390/brainsci11050658>
- Perkins, D. J., & Vogel, S. N. (2015). Space and time: New considerations about the relationship between Toll-like receptors (TLRs) and type I interferons (IFNs). In *Cytokine* (Vol. 74, Issue 2, pp. 171–174). Academic Press. <https://doi.org/10.1016/j.cyto.2015.03.001>
- Petersen, A., Soderstrom, M., Saha, B., & Sharma, P. (2021). Animal models of traumatic brain injury: a review of pathophysiology to biomarkers and treatments. In *Experimental Brain Research* (Vol. 239, Issue 10, pp. 2939–2950). Springer Science and Business Media Deutschland GmbH. <https://doi.org/10.1007/s00221-021-06178-6>
- Puntambekar, S. S., Saber, M., Lamb, B. T., & Kokiko-Cochran, O. N. (2018). Cellular players that shape evolving pathology and neurodegeneration following traumatic brain injury. *Brain, Behavior, and Immunity*, 71, 9–17. <https://doi.org/10.1016/j.bbi.2018.03.033>
- Qi Xia, M., Bacskai, B. J., Knowles, R. B., Xin Qin, S., & Hyman, B. T. (2000). Expression of the chemokine receptor CXCR3 on neurons and the elevated expression of its ligand IP-10 in reactive astrocytes: in vitro ERK1 / 2 activation and role in Alzheimer's disease. In *Journal of Neuroimmunology* (Vol. 108). www.elsevier.com/locate/jneuroin
- Réaux-Le Goazigo, A., van Steenwinckel, J., Rostène, W., & Mélik Parsadaniantz, S. (2013). Current status of chemokines in the adult CNS. In *Progress in Neurobiology* (Vol. 104, pp. 67–92). <https://doi.org/10.1016/j.pneurobio.2013.02.001>
- Robel, S., Berninger, B., & Götz, M. (2011). The stem cell potential of glia: lessons from reactive gliosis. *Nature Reviews Neuroscience*, 12(2), 88–104. <https://doi.org/10.1038/nrn2978>
- Rouillard, M. E., Hu, J., Sutter, P. A., Kim, H. W., Huang, J. K., & Crocker, S. J. (2022). The Cellular Senescence Factor Extracellular HMGB1 Directly Inhibits Oligodendrocyte Progenitor Cell Differentiation and Impairs CNS Remyelination. *Frontiers in Cellular Neuroscience*, 16. <https://doi.org/10.3389/fncel.2022.833186>
- Sanchez-Gonzalez, R., Koupourtidou, C., Lepko, T., Zambusi, A., Novoselc, K. T., Durovic, T., Aschenbroich, S., Schwarz, V., Breunig, C. T., Straka, H., Huttner, H. B., Irmeler, M., Beckers, J., Wurst, W., Zwergal, A., Schauer, T., Straub, T., Czopka, T., Trümbach, D., ... Ninkovic, J. (2022). Innate Immune Pathways Promote Oligodendrocyte Progenitor Cell Recruitment to the Injury Site in Adult Zebrafish Brain. *Cells*, 11(3), 520. <https://doi.org/10.3390/cells11030520>
- Scheller, A., Bai, X., & Kirchhoff, F. (2017). The Role of the Oligodendrocyte Lineage in Acute Brain Trauma. *Neurochemical Research*, 42(9), 2479–2489. <https://doi.org/10.1007/s11064-017-2343-4>
- Shandra, O., Winemiller, A. R., Heithoff, B. P., Munoz-Ballester, C., George, K. K., Benko, M. J., Zuidhoek, I. A., Besser, M. N., Curley, D. E., Edwards, G. F., Mey, A., Harrington, A. N., Kitchen, J. P., & Robel, S. (2019). Repetitive Diffuse Mild Traumatic Brain Injury

- Causes an Atypical Astrocyte Response and Spontaneous Recurrent Seizures. *The Journal of Neuroscience*, 39(10), 1944–1963. <https://doi.org/10.1523/JNEUROSCI.1067-18.2018>
- Shechter, R., & Schwartz, M. (2013). CNS sterile injury: Just another wound healing? *Trends in Molecular Medicine*, 19(3), 135–143. <https://doi.org/10.1016/j.molmed.2012.11.007>
- Silver, J., & Miller, J. H. (2004). Regeneration beyond the glial scar. *Nat Rev Neurosci*, 5(2), 146–156. <http://dx.doi.org/10.1038/nrn1326>
- Simon, C., Dimou, L., & Gotz, M. (2011). Progenitors in the adult cerebral cortex - cell cycle properties and regulation by physiological stimuli and injury. *Glia*, 59(6), 869–881.
- Simon, D. W., McGeachy, M. J., Bayir, H., Clark, R. S. B., Loane, D. J., & Kochanek, P. M. (2017). The far-reaching scope of neuroinflammation after traumatic brain injury. *Nature Reviews Neurology* 2017 13:3, 13(3), 171–191. <https://doi.org/10.1038/nrneurol.2017.13>
- Sirko, S., Behrendt, G., Johansson, P. A., Tripathi, P., Costa, M. R., Bek, S., Heinrich, C., Tiedt, S., Colak, D., Dichgans, M., Fischer, I. R., Plesnila, N., Staufenbiel, M., Haass, C., Snapyan, M., Saghatelian, A., Tsai, L.-H., Fischer, A., Grobe, K., ... Götz, M. (2013). Reactive Glia in the Injured Brain Acquire Stem Cell Properties in Response to Sonic Hedgehog. *Cell Stem Cell*, 12(4), 426–439. <https://doi.org/10.1016/j.stem.2013.01.019>
- Sirko, S., Irmeler, M., Gascón, S., Bek, S., Schneider, S., Dimou, L., Obermann, J., de Souza Paiva, D., Poirier, F., Beckers, J., Hauck, S. M., Barde, Y., & Götz, M. (2015). Astrocyte reactivity after brain injury—: The role of galectins 1 and 3. *Glia*, 63(12), 2340–2361. <https://doi.org/10.1002/glia.22898>
- Sirko, S., Neitz, A., Mittmann, T., Horvat-Bröcker, A., Holst, A. von, Eysel, U. T., & Faissner, A. (2009). Focal laser-lesions activate an endogenous population of neural stem/progenitor cells in the adult visual cortex. *Brain*, 132(8), 2252–2264. <https://doi.org/10.1093/brain/awp043>
- Sofroniew, M. v. (2009). Molecular dissection of reactive astrogliosis and glial scar formation. *Trends in Neurosciences*, 32(12), 638–647. <https://doi.org/10.1016/j.tins.2009.08.002>
- Sofroniew, M. v. (2015). Astrocyte barriers to neurotoxic inflammation. *Nature Reviews Neuroscience*, 16(5), 249–263. <https://doi.org/10.1038/nrn3898>
- Sofroniew, M. v. (2020). Astrocyte Reactivity: Subtypes, States, and Functions in CNS Innate Immunity. In *Trends in Immunology* (Vol. 41, Issue 9, pp. 758–770). <https://doi.org/10.1016/j.it.2020.07.004>
- Sofroniew, M. v., & Vinters, H. v. (2010). Astrocytes: biology and pathology. *Acta Neuropathologica*, 119(1), 7–35. <https://doi.org/10.1007/s00401-009-0619-8>
- Sohl, G., Hombach, S., Degen, J., & Odermatt, B. (2013). The oligodendroglial precursor cell line Oli-neu represents a cell culture system to examine functional expression of the mouse gap junction gene connexin29 (Cx29). *Front Pharmacol*, 4, 83. <https://doi.org/10.3389/fphar.2013.00083>

- Szepesi, Z., Manouchehrian, O., Bachiller, S., & Deierborg, T. (2018). Bidirectional Microglia–Neuron Communication in Health and Disease. In *Frontiers in Cellular Neuroscience* (Vol. 12, p. 323). Frontiers Media S.A. <https://doi.org/10.3389/fncel.2018.00323>
- Tan, Y. L., Yuan, Y., & Tian, L. (2020). Microglial regional heterogeneity and its role in the brain. In *Molecular Psychiatry* (Vol. 25, Issue 2, pp. 351–367). Springer Nature. <https://doi.org/10.1038/s41380-019-0609-8>
- Tang, F., Barbacioru, C., Wang, Y., Nordman, E., Lee, C., Xu, N., Wang, X., Bodeau, J., Tuch, B. B., Siddiqui, A., Lao, K., & Surani, M. A. (2009). mRNA-Seq whole-transcriptome analysis of a single cell. *Nature Methods*, 6(5), 377–382. <https://doi.org/10.1038/nmeth.1315>
- Thau, L., Reddy, V., & Singh, P. (2022, January). *Anatomy, Central Nervous System*. StatPearls [Internet]. Treasure Island (FL): StatPearls Publishing. <https://www.ncbi.nlm.nih.gov/books/NBK542179/>
- Torraca, V., Cui, C., Boland, R., Bebelman, J. P., van der Sar, A. M., Smit, M. J., Siderius, M., Spaink, H. P., & Meijer, A. H. (2015). The CXCR3-CXCL11 signaling axis mediates macrophage recruitment and dissemination of mycobacterial infection. *DMM Disease Models and Mechanisms*. <https://doi.org/10.1242/dmm.017756>
- Verkhatsky, A., & Nedergaard, M. (2018). Physiology of Astroglia. *Physiological Reviews*, 98(1), 239–389. <https://doi.org/10.1152/physrev.00042.2016>
- Verkhatsky, A., & Parpura, V. (2014). General pathophysiology of neuroglia: Neurological and psychiatric disorders as gliopathies. In *Pathological Potential of Neuroglia: Possible New Targets for Medical Intervention* (Vol. 9781493909742, pp. 1–12). Springer New York. https://doi.org/10.1007/978-1-4939-0974-2_1
- von Streitberg, A., Jäkel, S., Eugenin von Bernhardt, J., Straube, C., Buggenthin, F., Marr, C., & Dimou, L. (2021). NG2-Glia Transiently Overcome Their Homeostatic Network and Contribute to Wound Closure After Brain Injury. *Frontiers in Cell and Developmental Biology*, 9, 662056. <https://doi.org/10.3389/fcell.2021.662056>
- Wallace, J., Lord, J., Dissing-Olesen, L., Stevens, B., & Murthy, V. N. (2020). Microglial depletion disrupts normal functional development of adult-born neurons in the olfactory bulb. *ELife*, 9, e50531. <https://doi.org/10.7554/eLife.50531>
- Wang, C., Yue, H., Hu, Z., Shen, Y., Ma, J., Li, J., Wang, X.-D., Wang, L., Sun, B., Shi, P., Wang, L., & Gu, Y. (2020). Microglia mediate forgetting via complement-dependent synaptic elimination. *Science*, 367(6478), 688–694. <https://doi.org/10.1126/science.aaz2288>
- Wang, Y., Ge, P., & Zhu, Y. (2013). TLR2 and TLR4 in the brain injury caused by cerebral ischemia and reperfusion. In *Mediators of Inflammation* (Vol. 2013). <https://doi.org/10.1155/2013/124614>
- Wu, Y., Dissing-Olesen, L., MacVicar, B. A., & Stevens, B. (2015). Microglia: Dynamic Mediators of Synapse Development and Plasticity. In *Trends in Immunology* (Vol. 36, Issue 10, pp. 605–613). Elsevier Ltd. <https://doi.org/10.1016/j.it.2015.08.008>

- Xiong, Y., Mahmood, A., & Chopp, M. (2013). Animal models of traumatic brain injury. In *Nature Reviews Neuroscience* (Vol. 14, Issue 2, pp. 128–142). <https://doi.org/10.1038/nrn3407>
- Xiong, Y., Mahmood, A., & Chopp, M. (2018). Current understanding of neuroinflammation after traumatic brain injury and cell-based therapeutic opportunities. *Chinese Journal of Traumatology*, 21(3), 137–151. <https://doi.org/10.1016/j.cjtee.2018.02.003>
- Xu, S., Mei, S., Lu, J., Wu, H., Dong, X., Shi, L., Zhou, J., & Zhang, J. (2021). Transcriptome Analysis of Microglia Reveals That the TLR2/IRF7 Signaling Axis Mediates Neuroinflammation After Subarachnoid Hemorrhage. *Frontiers in Aging Neuroscience*, 13. <https://doi.org/10.3389/fnagi.2021.645649>
- Zamanian, J. L., Xu, L., Foo, L. C., Nouri, N., Zhou, L., Giffard, R. G., & Barres, B. A. (2012). Genomic Analysis of Reactive Astrogliosis. *Journal of Neuroscience*, 32(18), 6391–6410. <https://doi.org/10.1523/JNEUROSCI.6221-11.2012>
- Zambusi, A., & Ninkovic, J. (2020). Regeneration of the central nervous system-principles from brain regeneration in adult zebrafish. *World Journal of Stem Cells*, 12(1), 8–24. <https://doi.org/10.4252/wjsc.v12.i1.8>
- Zambusi, A., Novoselc, K. T., Hutten, S., Kalpazidou, S., Koupourtidou, C., Schieweck, R., Aschenbroich, S., Silva, L., Yazgili, A. S., van Bebber, F., Schmid, B., Möller, G., Tritscher, C., Stigloher, C., Delbridge, C., Sirko, S., Günes, Z. I., Liebscher, S., Schlegel, J., ... Ninkovic, J. (2022). TDP-43 condensates and lipid droplets regulate the reactivity of microglia and regeneration after traumatic brain injury. *Nature Neuroscience*. <https://doi.org/10.1038/s41593-022-01199-y>
- Zeisel, A., Hochgerner, H., Lönnerberg, P., Johnsson, A., Memic, F., van der Zwan, J., Häring, M., Braun, E., Borm, L. E., la Manno, G., Codeluppi, S., Furlan, A., Lee, K., Skene, N., Harris, K. D., Hjerling-Leffler, J., Arenas, E., Ernfors, P., Marklund, U., & Linnarsson, S. (2018). Molecular Architecture of the Mouse Nervous System. *Cell*, 174(4), 999–1014.e22. <https://doi.org/10.1016/j.cell.2018.06.021>
- Zhang, X., Lu, P., & Shen, X. (2022). Applications of single-cell multi-omics sequencing in deep understanding of brain diseases. *Clinical and Translational Discovery*, 2(3). <https://doi.org/10.1002/ctd2.95>
- Zheng, R. Z., Lee, K. Y., Qi, Z. X., Wang, Z., Xu, Z. Y., Wu, X. H., & Mao, Y. (2022). Neuroinflammation Following Traumatic Brain Injury: Take It Seriously or Not. In *Frontiers in Immunology* (Vol. 13). Frontiers Media S.A. <https://doi.org/10.3389/fimmu.2022.855701>
- Zheng, X., Mi, T., Wang, R., Zhang, Z., Li, W., Zhao, J., Yang, P., Xia, H., & Mao, Q. (2022). Progranulin deficiency promotes persistent neuroinflammation and causes regional pathology in the hippocampus following traumatic brain injury. *GLIA*, 70(7), 1317–1336. <https://doi.org/10.1002/glia.24175>
- Zlotnik, A., & Yoshie, O. (2012). The Chemokine Superfamily Revisited. In *Immunity* (Vol. 36, Issue 5, pp. 705–716). Cell Press. <https://doi.org/10.1016/j.immuni.2012.05.008>

5 Curriculum Vitae

6 Publications

- Zambusi A, Novoselc KT, Hutten S, Kalpazidou S, **Koupourtidou C**, Schieweck R, Aschenbroich S, Silva L, Yazgili AS, van Bebber F, Schmid B, Möller G, Tritscher C, Stigloher C, Delbridge C, Sirko S, Günes ZI, Liebscher S, Schlegel J, Aliee H, Theis F, Meiners S, Kiebler M, Dormann D, Ninkovic J. **TDP-43 condensates and lipid droplets regulate the reactivity of microglia and regeneration after traumatic brain injury.** Nat Neurosci. 2022 Nov 24. doi: 10.1038/s41593-022-01199-y.
- Liebich A*, Schmid N*, **Koupourtidou C***, Herrmann C, Dietrich KG, Welter H, Ninkovic J, Mayerhofer A. **The Molecular Signature of Human Testicular Peritubular Cells Revealed by Single-Cell Analysis.** Cells. 2022 Nov 19;11(22):3685. doi: 10.3390/cells11223685.
- Giehl-Schwab J, Giesert F, Rauser B, Lao CL, Hembach S, Lefort S, Ibarra IL, **Koupourtidou C**, Luecken MD, Truong DJ, Fischer-Sternjak J, Masserdotti G, Prakash N, Ninkovic J, Hölter SM, Vogt Weisenhorn DM, Theis FJ, Götz M, Wurst W. **Parkinson's disease motor symptoms rescue by CRISPRa-reprogramming astrocytes into GABAergic neurons.** EMBO Mol Med. 2022 May 9;14(5):e14797. doi: 10.15252/emmm.202114797.
- Sanchez-Gonzalez R, **Koupourtidou C**, Lepko T, Zambusi A, Novoselc KT, Durovic T, Aschenbroich S, Schwarz V, Breunig CT, Straka H, Huttner HB, Irmeler M, Beckers J, Wurst W, Zwergal A, Schauer T, Straub T, Czopka T, Trümbach D, Götz M, Stricker SH, Ninkovic J. **Innate Immune Pathways Promote Oligodendrocyte Progenitor Cell Recruitment to the Injury Site in Adult Zebrafish Brain.** Cells. 2022 Feb 2;11(3):520. doi: 10.3390/cells11030520.
- Vangopoulou C, Bourmpoula MT, **Koupourtidou C**, Giompres P, Stamatakis A, Kouvelas ED, Mitsacos A. **Effects of an early life experience on rat brain cannabinoid receptors in adolescence and adulthood.** IBRO Rep. 2018 May 28;5:1-9. doi: 10.1016/j.ibror.2018.05.002.

7 Eidesstattliche Versicherung/Affidavit

Christina Koupourtidou

(Studierende / Student)

Hiermit versichere ich an Eides statt, dass ich die vorliegende Dissertation "**Molecular profiling of glial reactivity in response to CNS injury**" selbstständig angefertigt habe, mich außer der angegebenen keiner weiteren Hilfsmittel bedient und alle Erkenntnisse, die aus dem Schrifttum ganz oder annähernd übernommen sind, als solche kenntlich gemacht und nach ihrer Herkunft unter Bezeichnung der Fundstelle einzeln nachgewiesen habe.

I hereby confirm that the dissertation "**Molecular profiling of glial reactivity in response to CNS injury**" is the result of my own work and that I have only used sources or materials listed and specified in the dissertation.

München / Munich

30.11.2022

(Datum / Date)

Christina Koupourtidou

(Unterschrift / Signature)

8 Declaration of author contributions

Publication 1: Sanchez-Gonzalez, R., **Koupourtidou, C.**, Lepko, T., Zambusi, A., Novoselc, K. T., Durovic, T., Aschenbroich, S., Schwarz, V., Breunig, C. T., Straka, H., Huttner, H. B., Irmeler, M., Beckers, J., Wurst, W., Zwergal, A., Schauer, T., Straub, T., Czopka, T., Trümbach, D., Götz, M., Stricker, S., Ninkovic, J. Innate Immune Pathways Promote Oligodendrocyte Progenitor Cell Recruitment to the Injury Site in Adult Zebrafish Brain. *Cells* (2022) <https://doi.org/10.3390/cells11030520>

The contribution of the authors is as follows:

Conceptualization, R.S.-G., J.N. and M.G.; methodology, R.S.-G., J.N., C.K., T.L., A.Z. (Alessandro Zambusi), K.T.N., T.D., M.I., S.A., V.S., C.T.B. and S.H.S.; software, D.T. and W.W.; formal analysis, T.S. (Tamas Schauer), R.S.-G., T.S. (Tobias Straub), M.I., J.B. and J.N.; resources, H.S., H.B.H., A.Z. (Andreas Zwergal) and T.C.; writing—original draft preparation, R.S.-G. and J.N.; writing—review and editing, all authors. All authors have read and agreed to the published version of the manuscript.

My contribution to this publication in detail:

For this paper, I was involved in the experiment validating the role of Cxcr3 and Tlr1/2 in OPCs using two *in vitro* approaches. First, with the primary OPC culture and clonal analysis, I assessed the role of the two pathways in the proliferation capacity of OPCs. Furthermore, with the generation of the Oli-neu cell line deficient for Cxcr3 and Tlr2 using the CRISPR/Cas9 approach I addressed the direct role of the pathways in the proliferation capacity of OPCs and ruled out any pharmacological off-targets. Additionally, I assisted in the preparation of RNA-Seq libraries from FACs-isolated cells. I was also involved in editing and reviewing the paper.

Confirmation of author contributions:

Prof. Dr. Jovica Ninković

Dr. Rosario Sanchez-Gonzalez

Christina Koupourtidou

.....

.....

.....

Publication 2: Zambusi, A., Novoselc, K. T., Hutten, S., Kalpazidou, S., **Koupourtidou, C.**, Schieweck, R., Aschenbroich, S., Silva, L., Yazgili, A. S., van Bebber, F., Schmid, B., Möller, G., Tritscher, C., Stigloher, C., Delbridge, C., Sirko, S., Günes, Z. I., Liebscher, S., Schlegel, J., Aliee H., Theis F., Meiners S., Kiebler M., Dormann D., Ninkovic, J. TDP-43 condensates and lipid droplets regulate the reactivity of microglia and regeneration after traumatic brain injury. Nat Neurosci (2022).

<https://doi.org/10.1038/s41593-022-01199-y>

The contribution of authors is as follows:

A.Z., K.T.N. and J.N. conceived the project and experiments. A.Z., K.T.N., S.H., S.K., R.S., S.A., L.S., A.S.Y., F.v.B., G.M., C.T., C.S., S.S., Z.I.G. and C.D. performed the experiments and analyzed the data. A.Z., K.T.N., C.K., H.A. and F.T. performed the bioinformatic analyses. A.Z., K.T.N. and J.N. wrote the manuscript with input from all authors. J.N., D.D., M.K., B.S., J.S., S.M. and S.L. supervised research and acquired funding.

My contribution to this publication in detail:

For this paper, I was involved in the scRNA-seq and snRNA-seq experiments and bioinformatic analysis. More specifically, I was assisting from the step of cell/nuclei preparation until the library preparation, aligned the data, established the bioinformatic analysis pipeline and supported the downstream bioinformatic analysis. I was also involved in editing and reviewing the paper.

Confirmation of author contributions:

Prof. Dr. Jovica Ninković

Dr. Alessandro Zambusi

Klara Tereza Novoselc

.....

.....

.....

Christina Koupourtidou

.....

Publication 3: Koupourtidou C.*, Schwarz V.*, Aliee H., Frerich S., Fischer-Sternjak J., Simon-Ebert T., Bocchi R., Götz M., Theis F.J., Ninkovic J. Spatial, temporal and cell-type-specific profiling of the injured brain. Manuscript ready for submission

The contribution of authors is as follows:

C.K., V.S. and J.N. conceived the project and experiments. C.K., V.S., J.F.S., T.S.E. and R.B. performed the experiments and analyzed the data. C.K., H.A. and S.F. performed the bioinformatic analyses C.K., V.S. and J.N. wrote the manuscript with input from all authors. J.N., M.G., and F.T. supervised research and acquired funding.

My contribution to this publication in detail:

For this manuscript, I performed all animal experiments for the experiments mentioned below. I performed the scRNA-seq and spatial transcriptomics including wet-bench and bioinformatic analysis of the data. I also was responsible for the validations with RNA scope. Furthermore, I contributed to the writing and editing of the manuscript.

Confirmation of author contributions:

Prof. Dr. Jovica Ninković

Christina Koupourtidou

Veronika Schwarz

.....

.....

.....

9 Acknowledgments

This journey cannot end without reminiscing and acknowledging all the people who supported me over these years. A journey that started many years ago mainly drove my motivation to study abroad. Of course, all this wouldn't have been possible without my supervisor's support Jovica, who gave me a chance to work at a high-quality lab and the freedom to perform all experiments. He was the one encouraging me to continue with my academic career, and at this point, I must say it was a good decision. Thank you, Jovica, for always being supportive, for your guidance, and for giving me the freedom to perform all these different types of experiments but also for getting involved in the bioinformatic analysis and finding what I really like to do. You were always there when needed and always gave me chances to prove myself and become better. In this line, I would also like to thank Magdalena for all her experimental feedback throughout my Ph.D. and her valuable support, which allowed me to contribute to many projects. Also, Tatiana and Judith, for all the transcriptomic experiments, it was always nice doing experiments with you. Of course, I cannot forget all the discussions with Judith. Thank you for always being honest with me and supporting me during the tough periods of my Ph.D.!

Thanks to all the people I collaborated with, to my TAC members for all the precious inputs and suggestions, as well as to the GSN for all the support provided during my Ph.D.

Special thank goes to my dear Friend Veronika. Without her, all this wouldn't have been possible. I couldn't have asked for a better collaborator; thank you for always supporting me, keeping a record of all our experiments, spending additional hours in the mouse house, and always being there for a coffee. I'm really glad that this journey gave me you as a friend!

Thanks to all the people from the Ninkovic group. Of course, I have to mention the core members of the group during my time here, Anita, Tamara, Tjasa, Alessandro, Sven, Klara, Finja, Sofia, and Priya, with whom I spent most of my time during the past years. Thank you all for your help and for creating a wonderful environment. It was always a pleasure to come to work and have a good time with you.

Acknowledgments

My greatest thanks go to my family, my parents, and my sisters, Sina and Aggeliki, for inspiring my scientific fascination, as well as for encouraging and supporting my decisions and career. Thank you to my relatives in Germany for all the support and help I've received throughout my stay here. Also, to my Greek friends, specially Haido and Sofia, for all the nice moments during these years and for making Munich feel like home. My greatest gratitude goes to Dimitris for changing his entire life to support me, for motivating me and being there for me when I needed him. Throughout this journey, we faced many obstacles together, but now we are finding our Ithaka.